



HAL
open science

Nuclear structure in the vicinity of Ni: in-beam gamma-ray spectroscopy of Cu through proton knockout

Louis Olivier

► **To cite this version:**

Louis Olivier. Nuclear structure in the vicinity of Ni: in-beam gamma-ray spectroscopy of Cu through proton knockout. Nuclear Experiment [nucl-ex]. Université Paris-Saclay, 2017. English. NNT : 2017SACLS212 . tel-01637435

HAL Id: tel-01637435

<https://theses.hal.science/tel-01637435>

Submitted on 17 Nov 2017

HAL is a multi-disciplinary open access archive for the deposit and dissemination of scientific research documents, whether they are published or not. The documents may come from teaching and research institutions in France or abroad, or from public or private research centers.

L'archive ouverte pluridisciplinaire **HAL**, est destinée au dépôt et à la diffusion de documents scientifiques de niveau recherche, publiés ou non, émanant des établissements d'enseignement et de recherche français ou étrangers, des laboratoires publics ou privés.



Nuclear structure in the vicinity of ^{78}Ni : In-beam γ -ray spectroscopy of ^{79}Cu through proton knockout

Thèse de doctorat de l'Université Paris-Saclay
préparée à l'Université Paris-Sud

École doctorale n°576 PHENIICS
Particules, Hadrons, Énergie, Noyau,
Instrumentation, Imagerie, Cosmos et Simulation

Spécialité de doctorat : Structure et réactions nucléaires

Thèse présentée et soutenue à Orsay, le 8 septembre 2017, par

Louis OLIVIER

Composition du Jury :

Pr Elias Khan Professeur, Institut de Physique Nucléaire d'Orsay	Président
Dr Giacomo de Angelis Directeur de recherche, Laboratori Nazionali di Legnaro	Rapporteur
Pr Jonathan Billowes Professeur, The University of Manchester	Rapporteur
Dr Beatriz Fernández Domínguez Chargée de recherche, Universidad de Santiago de Compostela	Examinatrice
Dr Jonathan Wilson Directeur de recherche, Institut de Physique Nucléaire d'Orsay	Directeur de thèse
Dr Serge Franchoo Chargé de recherche, Institut de Physique Nucléaire d'Orsay	Co-Directeur de thèse

Remerciements

Les remerciements sont loin d'être la partie la plus facile à rédiger dans une thèse, mais ils offrent au jeune docteur l'unique opportunité d'exprimer comme il se doit sa gratitude aux personnes qui ont compté pendant ces trois années.

Je tiens tout d'abord à remercier les membres de mon jury : Giacomo de Angelis, Jonathan Billowes, Beatriz Fernández Domínguez, Elias Khan et Jonathan Wilson. Merci pour nos échanges et pour vos commentaires. En particulier, merci à vous Giacomo et Jonathan B. d'avoir été les rapporteurs de ce travail.

Bien sûr, un grand merci à toi Serge pour ton encadrement. Tu étais présent quand j'en avais besoin et tu m'as fait confiance du début à la fin de la thèse. J'ai beaucoup apprécié de travailler avec toi, nos discussions étaient toujours enrichissantes, même lorsqu'il ne s'agissait pas de physique. J'espère qu'à l'avenir nous continuerons d'échanger, voire de travailler ensemble.

C'est au sein du groupe NESTER que j'ai effectué cette thèse, dans un environnement propice à l'épanouissement scientifique. Je remercie tous mes collègues, on se croisait de temps à autre dans le couloir ou pendant le déjeuner et c'était toujours un plaisir de discuter avec vous. En particulier, un grand merci à toi Freddy, pour nos très nombreux échanges, nos visites de Montréal et Denver, nos discussions politiques et j'en passe. Je pouvais débarquer dans ton bureau à n'importe quel moment et tu me recevais toujours avec le sourire. De même, tu as relu toute ma thèse et tes commentaires m'ont été précieux. Merci David pour nos nombreuses discussions sur le modèle en couches qui m'ont beaucoup apporté et pour m'avoir aidé dans la préparation de ma soutenance. Merci également à toi Andrea, pour nos discussions de physique et pour m'avoir régulièrement demandé des nouvelles de l'avancée de mon article. Pierre, tu passais souvent nous voir dans notre bureau pour parler de politique et d'actualité, merci pour ces moments de réflexion que tu nous offrais. Merci Fairouz, pour tes encouragements suite à mes présentations en réunion de groupe ou en répétition de soutenance. Fadi, merci pour le soutien que tu apportes aux doctorants pour l'organisation d'événements. Iulian, merci pour nos discussions de physique qui m'ont beaucoup appris, ainsi que pour tes conseils de programmation lors des shifts au Riken. Céline, tu étais toujours disponible pour m'aider dans mes petits soucis administratifs, un grand merci pour ta patience et ta bonne humeur.

Je remercie tous les membres de la collaboration Seastar dont je faisais partie, et en particulier merci à vous Alexandre et Pieter pour votre accueil chaleureux. Vous étiez toujours à l'écoute des différents problèmes que je pouvais rencontrer, que ce soit dans la compréhension du dispositif expérimental ou dans l'analyse des données. Merci également à vous Anna, César, Clémentine, Eda, Kasia, Nancy, Taras et Valérie, pour nos discussions pendant les shifts au Riken ou pendant les workshops Seastar. De même, je remercie Ogata-san, Otsuka-san et Tsunoda-san pour nos échanges à propos des calculs théoriques qu'ils ont effectués.

L'institut de physique nucléaire d'Orsay est une grande maison où il fait bon travailler et je tiens à remercier toutes les personnes qui participent au bon déroulement des thèses, du service informatique au service administratif. Un grand merci en particulier à toi Pascale, pour toute l'aide que tu as pu m'apporter, notamment concernant les réservations de salle et l'organisation d'événements pour les doctorants. Merci également à vous Luc et Valérie, pour votre disponibilité et votre coup de main pour l'organisation de la freshers' day. Enfin, merci à la direction du laboratoire qui est à l'écoute des problèmes que peuvent rencontrer les doctorants.

Bien évidemment, les principaux interlocuteurs d'un thésard sont les autres thésards. Et s'il y a une doctorante – maintenant docteure ! – qui mérite toute ma reconnaissance, c'est bien toi Claire. Ce fut un plaisir de partager le bureau avec toi pendant ces trois années. Je me souviendrai toujours de ton légendaire “rire de Dirac”¹ et de nos discussions sur tout et n'importe quoi lors de nos nombreuses pauses thé. Tu as été mon principal soutien au laboratoire dans les moments désagréables et tu m'as donné de précieux conseils sur ce que j'entreprenais autour de ma thèse (D2I2, Pheniics Days, etc.). Si j'ai autant apprécié cette thèse et si la fin ne m'a pas semblé si difficile qu'on le dit, c'est en partie grâce à toi. Un grand merci également à toi Benjamin. Nos conversations politiques, parfois animées, étaient toujours passionnantes, surtout autour d'un jap' à volonté. Il m'a fallu un peu de temps pour m'habituer à ton départ, au milieu de ma thèse, et c'est la pauvre Claire qui s'est récupéré toutes les piques qui auparavant t'étaient destinées... Mais heureusement, tu revenais régulièrement nous rendre visite ! Enfin, pour en terminer avec mon trio préféré de compagnons d'escape games, merci à toi Anne pour nos sorties culturelles (vive la Sainte-Chapelle !) et ludiques, ainsi que pour tes succulents gâteaux au chocolat. J'espère qu'un jour nous aurons l'occasion de disputer un match de badminton ! Clément, c'était toujours sympa de te voir débarquer dans notre bureau en traînant des pieds quand tu passais à l'imprimante chercher tes spectres. Anastasia, merci pour ta bonne humeur et ton humour. Liqiang, mon deuxième collègue de bureau,

¹Capacité à rire très fort pendant un très court laps de temps, à l'image d'un delta de Dirac donc l'abscisse serait le temps et l'ordonnée l'intensité du rire.

j'adorais ton air amusé quand tu me demandais pourquoi, pour la énième fois, Claire parlait du bureau sans pouvoir s'arrêter de rire. Je n'ai jamais pu te dire pourquoi, je ne le sais pas moi-même... Julien, c'était toujours un plaisir de te voir autour d'un café, et ça se terminait souvent par des conversations d'une heure ou deux. Tu fais partie des gens avec qui j'aurais aimé travailler, vu ton esprit d'équipe et ta détermination impressionnante. Raphaël, tu descendais régulièrement dans notre bureau où nous aimions t'y recevoir les bras ouverts. J'ai été ravi d'être secrétaire de D2I2 pendant ta présidence. Alice, merci de ton implication dans la vie du labo et dans le conseil de Pheniics, c'était très encourageant. Merci aux autres doctorants avec qui j'étais toujours content de discuter lors des différents événements du labo, notamment vous Antoine, Liss, Olivier et Quentin. Il y a également les anciens doctorants, ceux qu'on voit soutenir puis partir. Pierre, merci pour ton aide pendant mon stage de M2 et une partie de ma première année de thèse, quand tu étais encore au labo. Aurélie, merci pour nos discussions sur les différentes voies possibles après le doctorat. Noël, même après ton départ du labo tu continuais à passer nous rendre visite de temps en temps. J'aimais beaucoup nos discussions de politique et celles concernant D2I2. Maud, merci pour les mémorables pauses ludiques, nos premiers escape games et autres mails formels.

Je remercie tous mes collègues médiateurs de la Cité des sciences, où j'effectuais ma mission doctorale pendant ces trois ans, pour leurs conseils m'ayant permis d'être plus à l'aise à l'oral et d'améliorer ma pédagogie. Cela m'aura servi tout au long de ma thèse, de ma première conférence à ma soutenance, et je ne doute pas que cela me servira encore longtemps. Merci en particulier à toi Olivier, pour m'avoir accueilli dans ton équipe, et à vous Anaïs, Lisa et Nadège, pour nos discussions aussi bien de politique et de sciences que sur le déroulement de ma thèse, vous étiez toujours là pour me remonter le moral dans les petits moments de cafard. Merci également aux doctorants de la Cité, grâce à vous j'ai appris plein de choses sur les comètes, les virus et autres réseaux de neurones artificiels (même si j'ai dû en oublier une bonne partie...).

Il y a (heureusement) une vie en dehors de la thèse – même en dernière année – avec des potes qui sont toujours de la partie. Merci en particulier à vous Alexis et Zack, vous m'avez été d'un grand soutien pendant ces trois ans et votre présence à ma soutenance m'a vraiment fait plaisir. Des amis comme vous deux, c'est rare. Merci également à vous Frédo et Guigui, bon courage pour votre fin de thèse qui approche à grands pas. Jean-François, je suis content qu'on ait gardé contact malgré ton exil en terre belge. Enfin, je n'oublie pas non plus mes camarades de l'impro, vous qui me demandiez régulièrement des nouvelles de l'avancement de mon travail (alors que vous savez parfaitement qu'il ne faut jamais demander ça à un thésard !).

Je remercie toute ma famille qui depuis le début de mes études supérieures suit attentivement mon cheminement vers le doctorat. Vous êtes nombreux à être venus à ma soutenance ou à m'avoir envoyé des messages de soutien ce jour-là, merci de vos encouragements. En particulier un immense merci à vous mes chers parents et à toi Élise, ma sœur adorée. Vous avez toujours cru en moi et m'avez soutenu tout au long de mes études sans jamais rechigner malgré mes cinq déménagements ! C'est principalement grâce à vous que je suis arrivé jusque là.

Pour finir, je tiens à remercier chaleureusement Tania, artisane officieuse de cette thèse. Tu mériterais un prix Nobel de la paix pour ta patience et ton soutien sans faille pendant ces trois années. Me supporter n'a pas dû être facile tous les jours ! Je n'étais jamais seul quand je rentrais d'une journée difficile, tu étais là pour me remonter le moral quand j'en avais besoin et tu partageais ma joie à chaque succès. Merci pour ces nombreux bons moments passés ensemble, et même si nos routes se sont séparées depuis, j'espère que nous continuerons à nous croiser dans le futur.

S'entourer de gens formidables est un art dans lequel j'ai la prétention d'exceller, puissent ces remerciements en témoigner.

Louis

Contents

Introduction	1
1 Shell evolution towards ^{78}Ni	3
1.1 Nuclear shell-model and exotic nuclei	3
1.1.1 Independent-particle picture	3
1.1.2 Effective NN interaction	5
1.1.3 Multipole decomposition of the Hamiltonian	6
1.2 Magicity in the vicinity of ^{78}Ni	8
1.2.1 Separation energies	9
1.2.2 Half-lives	9
1.2.3 Systematics of the 2_1^+ state	10
1.2.4 $B(E2; 2^+ \rightarrow 0^+)$ in nickel isotopes	11
1.3 The neutron-rich copper isotopic chain	12
1.3.1 Monopole drift	12
1.3.2 $\pi f_{7/2}^{-1}$ single-hole strength	13
1.3.3 Low-lying collective states	14
1.3.4 Summary	15
1.4 Summary of theoretical studies for copper	16
1.5 Study proposed in the present work	18
1.5.1 Spectroscopic factors	18
1.5.2 In-beam γ -ray spectroscopy	19
2 Experimental setup	23
2.1 Beam production	23
2.1.1 Heavy-ion accelerating system	23
2.1.2 BigRIPS	24
2.2 MINOS	27
2.2.1 Liquid-hydrogen target	27
2.2.2 Vertex tracker	27
2.2.3 Beam tracker	28
2.3 DALI2	28
2.3.1 Geometry	28
2.3.2 Typical response function	30
2.4 ZeroDegree	32
2.5 Data acquisition	33

3	Data analysis	35
3.1	Particle identification	35
3.1.1	Trajectory reconstruction	35
3.1.2	TOF- $B\rho$ - ΔE method	36
3.1.3	Identification in BigRIPS	36
3.1.4	Identification in ZeroDegree	40
3.2	MINOS calibration	42
3.2.1	Tracking algorithm	42
3.2.2	Drift velocity	43
3.3	DALI2 calibration	45
3.3.1	Energy calibration	45
3.3.2	Time alignment	47
3.3.3	Add-back	49
3.4	Doppler correction	49
3.4.1	Doppler effect	49
3.4.2	β corrections	50
3.5	Geant4 simulations	52
3.5.1	Simulation code	52
3.5.2	DALI2 energy resolution and efficiency	52
3.5.3	Energy errors	54
3.6	Two reference cases: $^{78,80}\text{Zn}$	55
3.7	Beam-line transmission	57
3.7.1	Principle	57
3.7.2	Efficiency of the beam-line detectors	58
3.7.3	Losses from scattering in the target	58
3.7.4	Number of nuclei	60
3.8	Limit of the analysis	61
4	Procedure for building level schemes	63
4.1	General overview	63
4.1.1	Method of fit	63
4.1.2	Criteria for peaks identification	66
4.1.3	Steps of the procedure	66
4.2	Application to a known case: ^{81}Ga	67
4.2.1	$^{82}\text{Ge}(p,2p)^{81}\text{Ga}$ from the first campaign	67
4.2.2	Multi-channel to ^{81}Ga from the second campaign	74
4.3	Comparison with literature	82

5	Results	85
5.1	γ -ray energy spectrum	85
5.2	Application of the procedure	86
5.2.1	γ - γ coincidences without background subtraction	86
5.2.2	Decays to the ground state	90
5.2.3	Intensities estimation	91
5.2.4	γ - γ coincidences with background subtraction	93
5.2.5	Summary	98
5.3	Level scheme	99
5.3.1	Placement of the transitions	99
5.3.2	Influence of levels half-lives	102
5.3.3	Knockout feeding	103
5.4	Cross sections calculation	103
5.4.1	Inclusive cross sections	103
5.4.2	Exclusive cross sections	104
6	Interpretation and discussion	107
6.1	Monte-Carlo shell-model calculations	107
6.1.1	Valence space and interaction	107
6.1.2	Results for ^{79}Cu	108
6.2	Interpretation of the level scheme	110
6.2.1	Ground state and first excited state	110
6.2.2	Second excited state	111
6.2.3	Multiplet of states	113
6.2.4	Higher-energy levels	115
6.3	Exclusive cross sections	116
6.4	^{79}Cu : a valence proton outside a ^{78}Ni core	118
	Conclusion and outlook	121
	A Publication	127
	B Résumé en français	133
B.1	Motivation physique	134
B.2	Dispositif expérimental	134
B.3	Analyse et construction des schémas de niveaux	135
B.4	Résultats et interprétation	137
B.5	Conclusion	138
	Bibliography	139

Introduction

The atomic nucleus is one of the most complex and fascinating physical systems, presenting a large variety of behaviors like deformation, collective excitation or particle emission. An intense competition between the electromagnetic, strong and weak interactions occurs within it. Since its discovery by E. Rutherford [1], more than a century ago, great experimental and theoretical efforts have been achieved to understand its numerous properties. And yet, even now, there is no unified theory that would explain all nuclear phenomena.

Early, it has been proposed that the nucleus has a shell structure, similar to the electrons in the atom. Indeed, the nucleus components, the protons and the neutrons, may arrange themselves in such ways that some interesting features arise. One of the most famous examples is the extra binding energy for nuclei having special numbers of protons and/or neutrons, the magic numbers. Some of these numbers were first identified in 1934 from isotopic and isotonic abundances by K. Guggenheimer [2], and from binding energies by W. M. Elsasser [3]. The latter tried to establish for the first time an independent-particle model, where each nucleon moves independently from the others in a global potential, but neither his model nor the similar ones that followed could establish the correct list of magic numbers. The solution to this problem was found in 1949 by Goeppert Mayer [4] and Haxel, Jensen and Suess [5], who introduced a spin-orbit term in the potential which gave rise to the well-known magic numbers: 2, 8, 20, 28, 50, 82, 126. However, although these numbers are valid for the nuclei in the valley of stability, they are not universal throughout the nuclear chart [6].

One of the greatest challenges in nuclear structure nowadays is to understand the shell evolution for extreme neutrons over protons N/Z ratios. The observation of the strong rearrangements of nuclear structure far from stability help to have a better knowledge of the forces at stake. With the developement of radioactive-ion beams facilities worldwide over the last few decades, more and more exotic regions of the nuclear chart can be reached. We show this nuclear chart in figure 1. Many techniques were developed in order to access to the multiple facets of the nucleus, like laser spectroscopy, mass measurement, β -decay studies and of course plenty of nuclear reactions involving a wide range of energies. All these techniques are complementary.

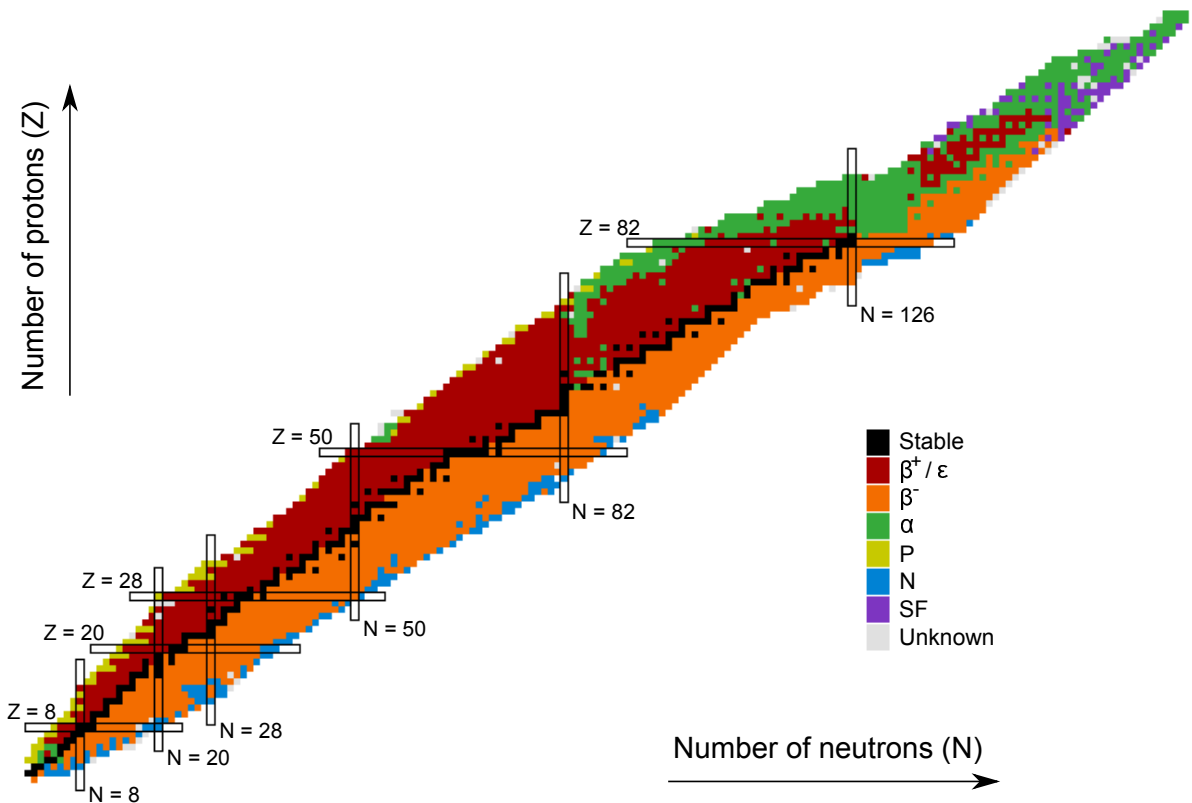


Figure 1 – The chart of nuclides. The colors represent the different decay modes and the conventional magic numbers are indicated.

In this thesis, we are interested in the proton-shell evolution towards the supposedly doubly-magic ^{78}Ni nucleus ($Z = 28$, $N = 50$). The evolution of the $Z = 28$ gap towards $N = 50$ can be studied by probing the single-particle character of the states in the copper isotopic chain, having one proton more than nickel. Our work focuses on ^{79}Cu , at $N = 50$, produced through the (p,2p) proton-knockout reaction and studied by means of in-beam γ -ray spectroscopy. The physics motivations for such a study are described in chapter 1. The setup of the experiment and the different analysis steps are explained in chapters 2 and 3, respectively. In chapter 4, we describe the procedure we established for building level schemes from our data and test it on a known case for validation. We apply this procedure to ^{79}Cu in chapter 5. Finally, the interpretation of our results and their comparison with shell-model calculations is done in chapter 6.

Chapter 1

Shell evolution towards ^{78}Ni

1.1 Nuclear shell-model and exotic nuclei

The nuclear shell-model remains one of the major tools to treat the many-body problem that represents the atomic nucleus. We present here the main features of this model, proven to be robust for nuclei close to the valley of stability, and the mechanisms at work in exotic nuclei.

1.1.1 Independent-particle picture

The properties of a nucleus with a A -body wave function ψ_A are given by the Schrödinger equation,

$$\left[\sum_{i=1}^A -\frac{\hbar^2}{2m} \Delta_i + \sum_{i<j}^A W(i,j) \right] \psi_A = E \psi_A \quad (1.1)$$

with W the many-body interaction. Here we show only the two-body part, but the reasoning that follows is the same including more-body terms.

The fundamental hypothesis of the nuclear shell-model is that each nucleon moves independently in a mean-field describing the average interaction with the other nucleons and represented by a one-body potential $U(i)$. Then, the Hamiltonian is rewritten as

$$\hat{H} = \left[\sum_{i=1}^A \left(-\frac{\hbar^2}{2m} \Delta_i + U(i) \right) \right] + \left[\sum_{i<j}^A W(i,j) - \sum_{i=1}^A U(i) \right] = \hat{H}^{(0)} + \hat{V} \quad (1.2)$$

where \hat{V} is the residual interaction. By using an appropriate U , this residual interaction may be small and is neglected in the independent-particle model. The facts that in stable nuclei there is a nearly constant nucleon density and that nuclear forces are short-range interactions lead legitimately to choose a Woods-Saxon potential for U , or an approximation as a harmonic oscillator potential. The nucleon orbitals that can be built from such a U are shown in figure 1.1, on the left and central parts. The large gaps between

shells correspond to the harmonic oscillator magic numbers, which are 2, 8, 20, 40, 70. Independently, Goeppert Mayer [4] and Haxel, Jensen and Suess [5] proposed to add a spin-orbit term in the potential, like for electrons in atoms, and the spin-orbit splitting led to the set of magic numbers that we know, as shown in figure 1.1 on the right.

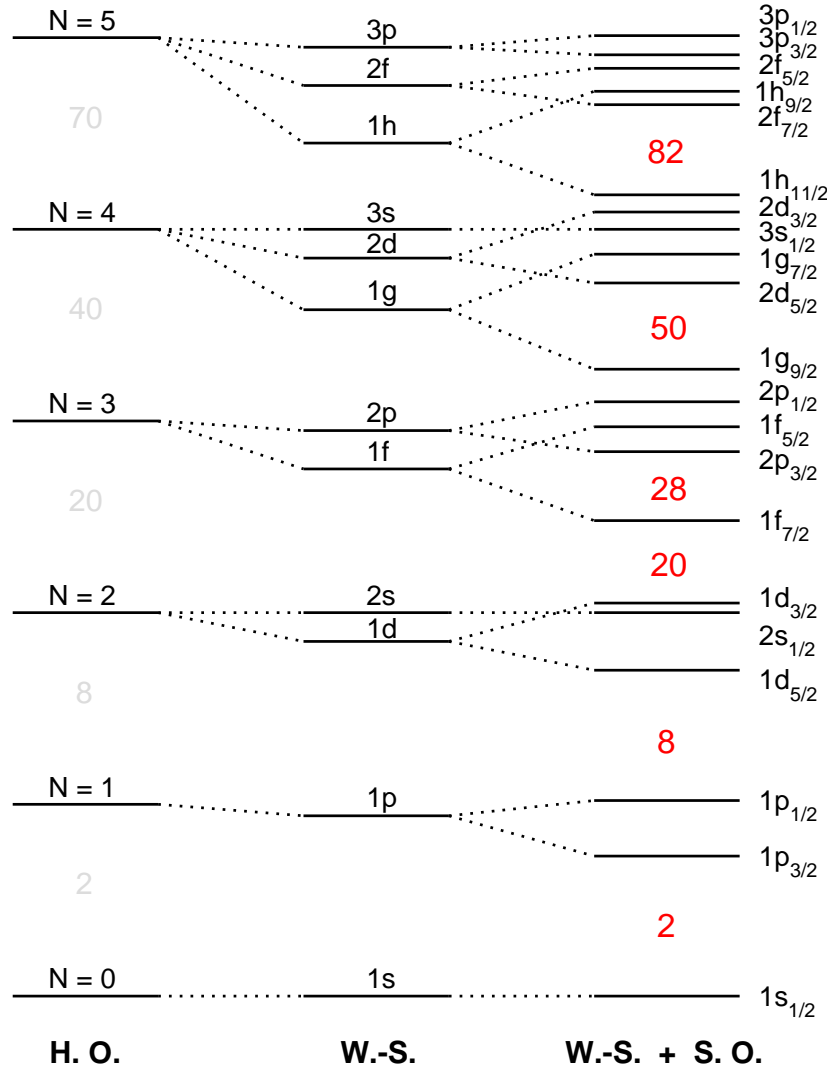


Figure 1.1 – Orbital scheme from the single-particle Hamiltonian $\hat{H}^{(0)}$ of equation 1.2, using a harmonic oscillator potential (left), a Woods-Saxon potential (center), and a Woods-Saxon potential plus a spin-orbit term (right).

The validity of this independent-particle model is limited to closed-shell nuclei with one particle or one hole, but for a number of protons or neutrons getting away from the magic numbers, the residual interaction cannot be neglected anymore: the two-body interaction plays a significant role. Moreover, these magic numbers are not universal throughout the nuclear chart, as the nuclear forces far from stability may induce strong structure rearrangements. Some of them can disappear, like $N = 28$ in silicon isotopes [7], while new magic numbers arise, like $N = 34$ in calcium isotopes [8]. We can therefore wonder what happens to the $Z = 28$ gap in exotic regions of the nuclear chart.

1.1.2 Effective NN interaction

The properties of the force between two nucleons can be derived from nucleon-nucleon scattering experiments and from the study of the deuteron, the only two-nucleon system that is bound. From these observations, we can obtain some general properties of the NN interaction:

- It is attractive but with a hard core component that prevents the nuclear matter from collapsing;
- It is of short range, of the order of 1 fm;
- It is strongly spin-dependent, since no pair of nucleons with $S = 0$ is bound contrary to the $S = 1$ ground-state of the deuteron;
- It comprises a non-central part, i.e. a part that has not a spherical symmetry, made of the spin-orbit term $\vec{L} \cdot \vec{S}$ and the tensor term, written as:

$$S_{12} = \frac{3(\vec{\sigma}_1 \cdot \vec{r})(\vec{\sigma}_2 \cdot \vec{r})}{r^2} - \vec{\sigma}_1 \cdot \vec{\sigma}_2 \quad (1.3)$$

with $r = |\vec{r}_1 - \vec{r}_2|$ the distance between the two nucleons;

- It is charge-independent.

Then, different potentials can be built by combining spin ($\vec{\sigma}_1 \cdot \vec{\sigma}_2$), isospin ($\vec{\tau}_1 \cdot \vec{\tau}_2$), spin-orbit ($\vec{L} \cdot \vec{S}$) and tensor (S_{12}) terms in order to reproduce the experimental observations. We can notice that the spin-orbit and tensor terms of the interaction act only between nucleons having a relative spin $S = 1$.

In order to simplify the many-body problem, shell-model calculations are based on a truncated space, i.e. a space reduced to several valence orbitals above an inert core, as explained in section 1.4. Therefore, one deals with an effective NN interaction within the valence space. To derive this effective interaction, one generally starts from the free nucleon-nucleon interaction to which are added in-medium effects, because a core is in reality never totally inert, and the Pauli principle, as a nucleon cannot move to states already occupied by other nucleons. The in-medium effects are taken into account using perturbation theory, and the Pauli principle requires the strong repulsive component in the NN interaction at very short range. Due to the latter, a renormalization procedure has to be applied because otherwise the repulsive part of the interaction, which tends towards infinity when r goes to zero, would make the perturbation treatment meaningless [9].

Such an effective interaction that one builds from the bare NN potential fails to reproduce saturation properties of nuclei and spin-orbit magic numbers [9]. The limitation to two-body forces is probably the cause of this problem and the addition of a three-body term has been argued to give a better agreement with the experimental data [10]. For

example, an effective interaction with a three-body term has been developed in the oxygen isotopes region [11], leading to a correct neutron drip-line at ^{24}O , while the use of only a two-body interaction puts it wrongly at ^{28}O . For the valence spaces where no effective three-body interaction is available yet, a solution was found in the multipole decomposition of the Hamiltonian.

1.1.3 Multipole decomposition of the Hamiltonian

Historically, the multipole decomposition of the Hamiltonian was done to overcome the insufficiency of two-body effective interactions described just before [12]. The decomposition is done in the following way [13]:

$$\hat{H} = \hat{H}_m + \hat{H}_M \quad (1.4)$$

with \hat{H}_m the monopole part and \hat{H}_M the multipole part. The problem of the two-body interaction was bypassed by adjusting the monopole part to experimental data.

Monopole part

The monopole part of the Hamiltonian depicts a spherical mean field. It is responsible for global saturation properties and single-particle behavior [13]. Considering a two-body interaction V , the monopole part of the Hamiltonian can be written as follows [14]:

$$\hat{H}_m = \sum_j \varepsilon_j^\pi \hat{n}_j^\pi + \sum_j \varepsilon_j^\nu \hat{n}_j^\nu + \sum_{j,j'} V_{jj'}^{\pi\nu} \hat{n}_j^\pi \hat{n}_{j'}^\nu + \sum_{j \leq j'} V_{jj'}^{\nu\nu} \frac{\hat{n}_j^\nu (\hat{n}_{j'}^\nu - \delta_{jj'})}{1 + \delta_{jj'}} + \sum_{j \leq j'} V_{jj'}^{\pi\pi} \frac{\hat{n}_j^\pi (\hat{n}_{j'}^\pi - \delta_{jj'})}{1 + \delta_{jj'}} \quad (1.5)$$

with $\varepsilon^{\pi,\nu}$ the proton and neutron single-particle energies, $\hat{n}^{\pi,\nu}$ the proton and neutron number operators, j the set of quantum numbers of a given orbital, and $V_{ij}^{\tau\tau'}$ the monopole component of V , corresponding to an average of the two-body interaction over all possible magnetic substates of the two nucleons in the orbits j and j' :

$$V_{jj'}^{\tau\tau'} = \frac{\sum_J \langle jj' | V | jj' \rangle_J (2J + 1)}{\sum_J (2J + 1)} \quad (1.6)$$

with J the angular momentum of a two-body state, that takes all allowed values, and τ the type of nucleon. Terms with higher-order of $n^{\pi,\nu}$ have to be added to take into account more-body interactions.

In the shell-model framework, the monopole Hamiltonian is used for the calculation of effective single-particle energies (ESPE), which quantify the effects of the other nucleons on a nucleon in a given orbital. These ESPE are defined for an occupied orbit as the opposite of the nucleon separation-energy of this orbit and for an unoccupied orbit as the

opposite of the gain of binding energy by putting a nucleon into this orbit [15]. The ESPE are linear functions of the occupation numbers $\langle \hat{n}_{j'}^{\tau'} \rangle$ of the orbitals j' above a core A_0 ,

$$\tilde{\varepsilon}_j^{\tau}(A) = \varepsilon_j^{\tau}(A_0) + \sum_{j',\tau'} V_{jj'}^{\tau\tau'} \langle \hat{n}_{j'}^{\tau'} \rangle \quad (1.7)$$

where the sum runs over all valence orbitals, and

$$\Delta\varepsilon_j = \tilde{\varepsilon}_j^{\tau}(A) - \varepsilon_j^{\tau}(A_0) = \sum_{j',\tau'} V_{jj'}^{\tau\tau'} \langle \hat{n}_{j'}^{\tau'} \rangle \quad (1.8)$$

is the so-called monopole drift. An illustration of such an effect is shown in figure 1.2(a). The monopole drift is responsible of shell-structure modifications that can be strong enough to make disappear some magic numbers and give rise to new ones, like for example in ^{24}O [15, 16], illustrated in figure 1.2(b). Unfortunately, the ESPE are not observables [17]: they are uncorrelated energies while the nucleus is a correlated system.

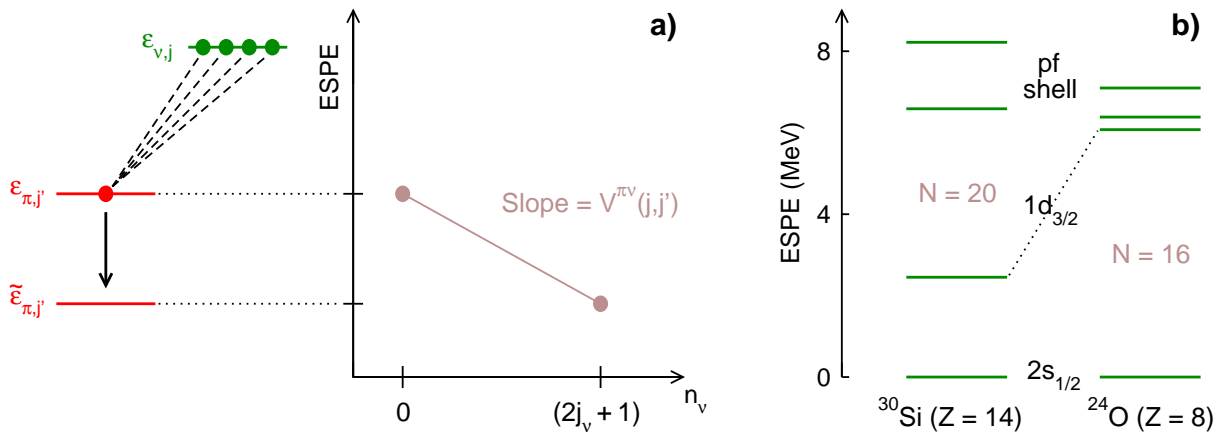


Figure 1.2 – Monopole drift. (a) Linear decrease of the $\pi j'$ -orbital ESPE as a function of the neutron occupation in the νj orbital. (b) Example of a monopole drift for the neutron $1d_{3/2}$ orbital between ^{30}Si and ^{24}O , relatively to the $2s_{1/2}$ orbital. The magic number $N = 20$ disappears and is replaced by $N = 16$ [15, 16].

The contribution to the shell evolution of the different components of the monopole part of the NN interaction has been much discussed [14, 15, 18–22]. This is not a straightforward question because of the renormalization of the bare NN force and the adjustment of the monopole part to experimental data. In several studies, the effective interaction was decomposed into central, spin-orbit and tensor parts, allowing to trace them separately. Various effective interactions and different shells were considered. The conclusion of these works is that the central part of the NN interaction mainly drives the global trend of the ESPE, while the tensor part can significantly modify the ESPE splitting between spin-orbit partners [14, 18–21]. The tensor force, when filling a neutron (proton) orbital

$j' = l \pm 1/2$, impacts proton (neutron) spin-orbit partners $j_> = l + 1/2$ and $j_< = l - 1/2$ as follows [19]:

$$(2j_> + 1)V_{j_>,j'}^{\pi\nu} + (2j_< + 1)V_{j_<,j'}^{\pi\nu} = 0 \quad (1.9)$$

meaning that the monopole part of the tensor force acts in an opposite way on spin-orbit partners, but also that it vanishes when both $j_>$ and $j_<$ orbitals are full. Moreover, $j'_< - j_>$ and $j'_> - j_<$ interactions are attractive while $j'_> - j_>$ and $j'_< - j_<$ interactions are repulsive. As explained in section 1.4, this has strong implications on the shell gaps that are delimited by spin-orbit orbit partners, which is the case of the $Z = 28$ gap in ^{78}Ni .

Multipole part

The multipole part of the Hamiltonian describes the correlations between the valence nucleons, like pairing and quadrupole interactions. It is responsible for the particle-hole excitations across shell gaps. The decrease of a shell gap, due to a monopole drift that brings closer the two orbitals defining the gap, can induce the presence of intruder deformed configurations at low energy if the correlation energy of such configurations is larger than energy needed to create them [14]. In some cases, the correlations may be important enough so that the typical signatures of a magic nucleus disappear, while the magic gap is only weaker but still existing [12]. There is therefore competition between the monopole part, that tends to make the nucleus spherical, and the multipole part, that leads it into a deformed shape. The disentanglement between correlations and pure monopole effect is non-trivial.

1.2 Magicity in the vicinity of ^{78}Ni

In the shell model as it was initially formulated, the proton $\pi f_{7/2}$ orbital separates from the $3\hbar\omega$ harmonic oscillator shell because of the spin-orbit splitting and forms the $Z = 28$ gap. The neutron $\nu g_{9/2}$ orbital splits off from the $4\hbar\omega$ shell to join the $3\hbar\omega$ orbits and creates a magic number at $N = 50$. With 28 protons and 50 neutrons, the ^{78}Ni nucleus is thus expected to be one of the most neutron-rich doubly magic nuclei, making it of great interest for nuclear structure.

Up to now, no evidence has been found for the disappearance of the shell closures at $Z = 28$ and $N = 50$, even if some studies hint at a possible weakening of the $Z = 28$ magic number towards $N = 50$, as explained in the following, and more recently of the $N = 50$ magic number below ^{78}Ni [23]. The mechanisms at work far from stability, described in the previous section, may influence these two gaps, in particular through monopole drifts of single-particle energies. So far no information about the spectroscopy of ^{78}Ni is available, but we present here the status of experimental knowledge regarding the magicity towards this key nucleus, focusing more on the $Z = 28$ gap.

1.2.1 Separation energies

Mass measurements are a key tool in the identification of shell closures, as they give access to properties like the two-proton separation energy, defined as

$$S_{2p}(Z, N) = M(Z - 2, N) + 2M(^1\text{H}) - M(Z, N) = B(Z, N) - B(Z - 2, N) \quad (1.10)$$

with M the mass and B the binding energy of the nuclei considered. In other words, this quantity corresponds to the energy required to remove the last pair of protons, which is much higher in the case of a closed shell than for a pair of protons above a gap. In figure 1.3(a), one can see the evolution of S_{2p} as a function of the number of protons in the nickel region. The drop when passing $Z = 28$ that can be observed in the $N = 40$ and $N = 42$ isotonic chains is characteristic of a shell closure. The latter is even more visible when looking at the evolution of S_{2p} as a function of the neutron number, shown in figure 1.3(b), where there is a gap between the nickel and zinc isotopic chains. Unfortunately, $S_{2p}(^{78}\text{Ni})$ and $S_{2p}(^{80}\text{Zn})$ are not known, they require to measure the masses of ^{76}Fe and ^{78}Ni that are not accessible so far.

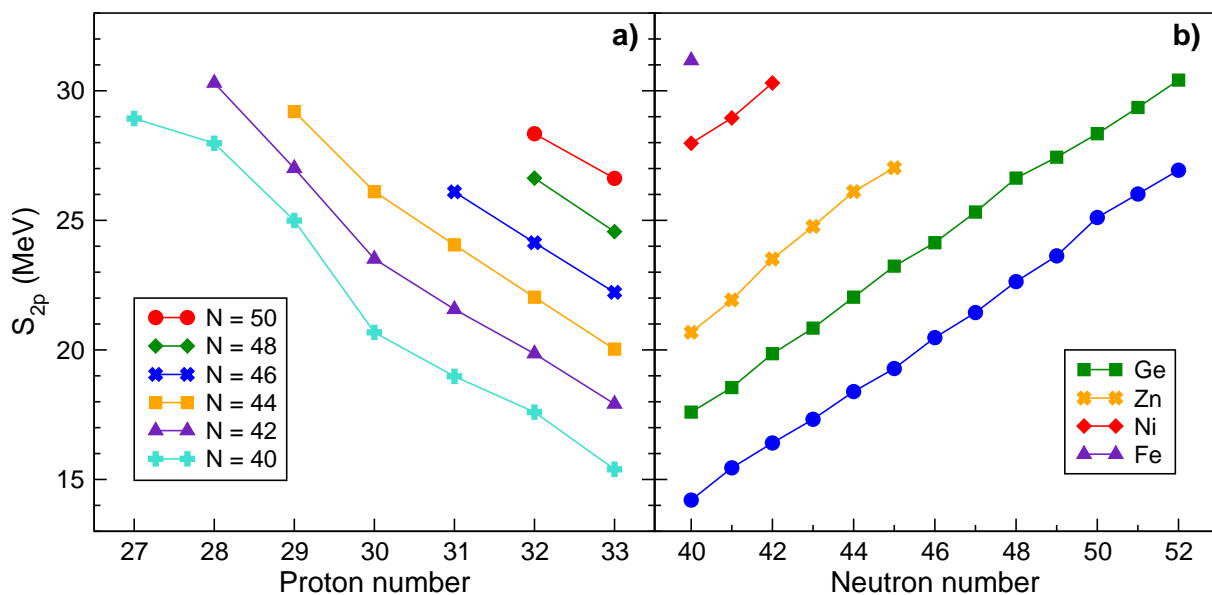


Figure 1.3 – Two-proton separation energies of (a) the $N = 40$ to 50 isotonic and (b) the $Z = 26$ to 32 isotopic chains. Data taken from reference [24].

1.2.2 Half-lives

Experimental indications of a doubly-magic ^{78}Ni can also be found looking at the half-lives of the surrounding isotopes. The systematics of the β -decay half-lives for the $Z = 27$ to 31 isotopic chains is shown in figure 1.4.

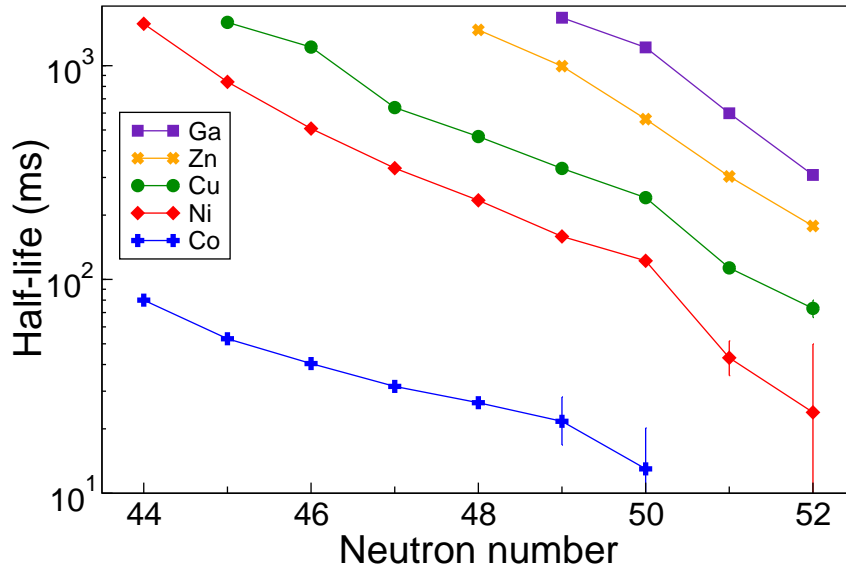


Figure 1.4 – β -decay half-lives of the $Z = 27$ to 31 isotopic chains above $N = 44$. Data taken from references [25, 26].

Half-lives beyond ^{78}Ni were measured at RIKEN [25]. The fast drop of the half-life for the $N > 50$ nickel isotopes was interpreted by the authors as suggesting the magicity of the $N = 50$ neutron number: if the $N = 50$ gap is large, the 51^{th} neutron that is above will strongly increase the Q_β value and therefore strongly decrease the half-life. As regards the gap between the cobalt and nickel chains, a similar reasoning is made but this time concerning the $Z = 28$ gap: in a $\text{Co} \rightarrow \text{Ni}$ decay, the proton produced can fill the last proton orbital before the gap, while a $\text{Ni} \rightarrow \text{Cu}$ decay can only fill an orbital above, decreasing Q_β especially if the gap is large.

1.2.3 Systematics of the 2_1^+ state

One of the signatures of a shell gap is a high first 2^+ state in the magic nucleus compared to its neighbors. This can be understood within the shell-model framework as follows: (i) if the nucleus is doubly magic, i.e. with a closed shell for both protons and neutrons, at least one nucleon has to be excited across a shell gap to generate a 2^+ state, which requires an important amount of energy; (ii) in a nucleus with one closed shell and one open shell, the creation of an excited state costs only the energy of breaking a pair in the open shell; (iii) when both proton and neutron shells are open, we can have an important deformation of the nucleus that leads to even lower excited states.

The evolution of the 2_1^+ state in the $N = 44$ to 52 isotonic chains is shown in figure 1.5(a). The magic character of $Z = 28$ is reflected by a higher energy of the 2_1^+ state in nickel compared to the other isotopes. The same observation can be done for the $N = 50$ isotonic chain that is higher in energy than the others, showing the magic character of $N = 50$. Similar conclusions can be drawn from the systematics of the 2_1^+ state

in the iron, nickel, zinc, germanium and selenium isotopic chains, shown in figure 1.5(b): when passing the $N = 50$ neutron number, the 2_1^+ state suddenly rises, and the nickel isotopic chain is significantly above the others.

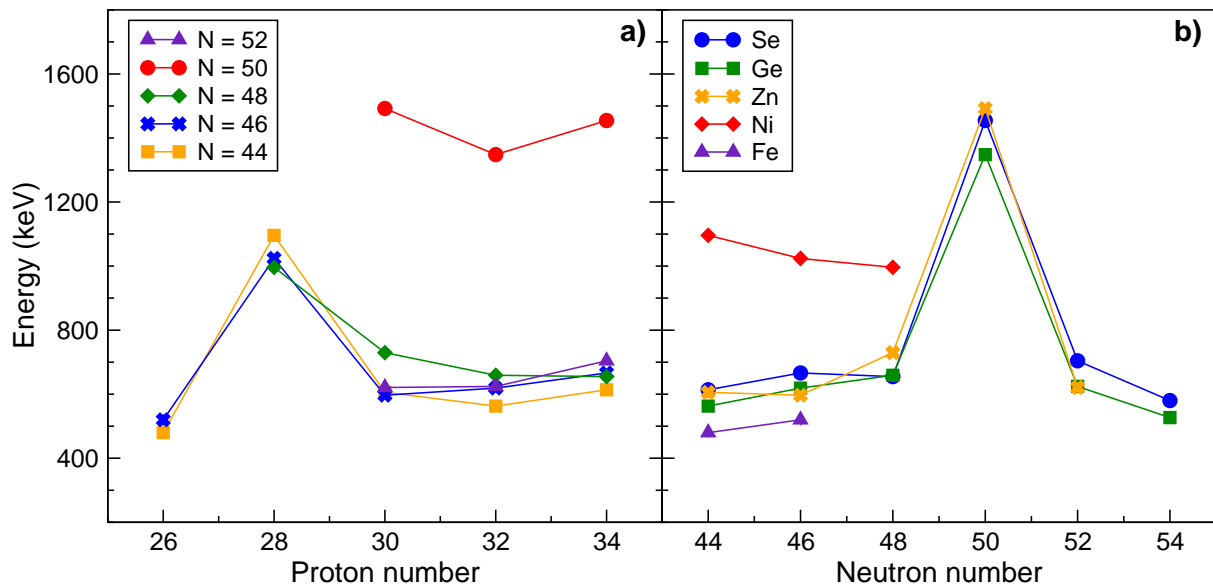


Figure 1.5 – Systematics of the 2_1^+ state in (a) the $N = 44$ to 52 isotonic and (b) the $Z = 26$ to 34 isotopic chains. The $Z = 28$ and $N = 50$ numbers clearly show a magic character, but no information is available for ^{78}Ni so far. Data taken from references [26–37].

Up to now, no information about the spectroscopy of ^{78}Ni has been published, but one can see that its 2_1^+ -state energy would be a crucial information to ascertain the persistence of the $Z = 28$ and $N = 50$ gaps at such a high exoticity.

1.2.4 $B(E2; 2^+ \rightarrow 0^+)$ in nickel isotopes

The ^{70}Ni nucleus ($N = 42$) was found to have a reduced transition probability $B(E2; 2^+ \rightarrow 0^+)$, defined in section 1.5.2, three times larger [38] than for ^{68}Ni [39]. While it is somewhat normal that the addition of two neutrons above a subshell closure, like at $N = 40$, increases the collectivity, such an abrupt rise of the $B(E2)$ in ^{70}Ni was unexpected and was interpreted as an indication of a reduction of the $Z = 28$ gap [38]. This was also suggested as a possible explanation for the slight decrease of the first 2^+ -state energy above ^{70}Ni [30], that can be seen in figure 1.5(b). The enhancement of collectivity was confirmed in ^{74}Ni by measuring its deformation length, but this time the authors concluded that it could be also due to the weakening of the $N = 50$ gap and not necessarily of the $Z = 28$ one [40]. More recently, two experiments were performed to measure the $B(E2)$ value in $^{72,74}\text{Ni}$, one through Coulomb excitation [41] and the other one through a lifetime measurement [42]. The results show that the enlargement of collectivity above $N = 40$ is not as pronounced as previously said and the authors concluded that the

quenching of the $Z = 28$ gap does not happen. But no other explanation for such a high $B(E2)$ in ^{70}Ni was given so far. As a consequence, the study of the proton magicity close to ^{78}Ni is of primary importance to disentangle the ambiguity on the possible weakening of the $Z = 28$ gap.

1.3 The neutron-rich copper isotopic chain

Neutron-rich copper isotopes, having one proton more than nickel isotopes, provide an interesting way of probing the nuclear structure in the vicinity of ^{78}Ni , in particular to characterize its proton single-particle nature. We present here the latest status of the experimental knowledge in this isotopic chain. The orbitals of interest for protons are $1f_{7/2}$, supposedly full, and $2p_{3/2}$, $1f_{5/2}$, $2p_{1/2}$. As regards neutrons, we are concerned about the $1g_{9/2}$ orbital, which is empty at $N = 40$ and full at $N = 50$.

1.3.1 Monopole drift

When adding neutrons in the $\nu g_{9/2}$ orbital above the $N = 40$ subshell gap, there is a sudden decrease of the energy of the first $5/2^-$ excited state relative to the $3/2^-$ ground state in $^{71,73}\text{Cu}$, compared to lighter copper isotopes. This was established from β decay of $^{69,71,73}\text{Ni}$ [43, 44] and the authors assumed a $\pi f_{5/2}$ and $\pi p_{3/2}$ single-particle characters for these two states, respectively. The $\pi f_{5/2}$ single-particle character of the $5/2^-$ state in $^{69,71,73}\text{Cu}$ was confirmed by Coulomb excitation [45], in which the fall of the reduced transition probability $B(E2; 5/2_1^- \rightarrow 3/2_{gs}^-)$ from more than 10 W.u. ($N < 40$) to less than 5 W.u. ($N \geq 40$) was observed. The inversion of these $3/2^-$ and $5/2^-$ states above $N = 44$ was evidenced from collinear laser spectroscopy, where it was shown that the ground state of ^{75}Cu has a spin $5/2^-$ [46]. Two nearly degenerate states were observed in ^{75}Cu , at 61.7(4) and 66.2(4) keV [47], and based on the systematics and the $B(M1)$ and $B(E2)$ transition rates, the authors concluded that one of them is a $3/2^-$ state with a significant single-particle character. The inversion of the first $3/2^-$ and $5/2^-$ states in ^{75}Cu was found to be maintained in ^{77}Cu by laser spectroscopy [48], and the first $3/2^-$ level was assigned very recently to a state at 293 keV in a β -decay experiment [49]. But no information is available for ^{79}Cu .

The systematics of the first $3/2^-$ and $5/2^-$ states in the copper isotopic chain is shown in figure 1.6. The important single-particle character of these levels means that the gap between the $\pi p_{3/2}$ and $\pi f_{5/2}$ orbitals decreases when filling the $\nu g_{9/2}$ orbital, due to a monopole drift [43, 44]. If the $\pi f_{5/2}$ orbital is inverted with the $\pi p_{3/2}$ one, it becomes the upper orbital defining the $Z = 28$ gap, and therefore a continuation of the monopole drift could affect the size of the gap.

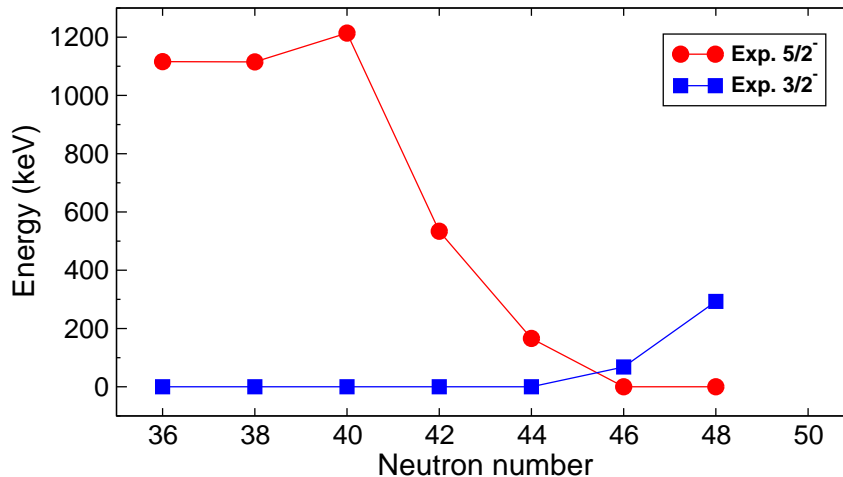


Figure 1.6 – Systematics of the first $3/2^-$ and $5/2^-$ states in neutron-rich copper isotopes. The ground-state spin changes at $N = 46$. Data taken from references [26, 43, 46–50].

It is interesting to note that a similar behavior was observed in the gallium isotopes, that have two protons more than copper. Indeed, the ground state of ^{71}Ga ($N = 40$) has a spin $3/2^-$ and when starting to fill the $\nu g_{9/2}$ orbital, there is a drop in energy of the first $5/2^-$ excited state, although less sudden than for copper. The inversion between the $3/2^-$ and $5/2^-$ states happens in ^{81}Ga [51, 52]. The authors concluded that the same mechanism as for copper is at work in gallium. But studying single-particle behaviors in gallium is more difficult as the three protons in the $\pi p_{3/2} f_{5/2}$ orbitals, instead of one for copper, may couple and give rise to states that mix with the single-particle ones.

1.3.2 $\pi f_{7/2}^{-1}$ single-hole strength

The behavior of the $\pi f_{7/2}$ spin-orbit partner is more difficult to determine. This orbital is of primary importance as it is the lower orbital defining the $Z = 28$ gap. Access to this hole state is possible through proton transfer or knockout reactions. The $\pi f_{7/2}^{-1}$ strength can be fragmented over several $7/2^-$ levels and it is therefore necessary to extract the spectroscopic factor, defined in section 1.5.1, of each level in order to calculate the centroid of the strength.

In ^{69}Cu , two $7/2^-$ states were observed a few decades ago [50] and another one was discovered recently [53], from experiments using the $^{70}\text{Zn}(d, ^3\text{He})^{69}\text{Cu}$ pick-up reaction. These three states lie at 1.71, 1.87 and 3.35 MeV and were found to have spectroscopic factors equal to 2.50(14), 0.50(10) and 2.40(15), implying the important $\pi f_{7/2}^{-1}$ character of the first and third ones. 67(3)% of the $\pi f_{7/2}^{-1}$ strength have been observed and the rest must lie at higher energy than 3.35 MeV, meaning that the centroid found at 2.45 MeV has to be seen as a lower limit [53].

A $7/2^-$ state was observed at 1.19 MeV in ^{71}Cu , fed by the $E2$ cascade from the decay of a $19/2^-$ isomeric state [28, 54], for which a single-hole character was excluded by the

large $B(E2)$ value (10.7(12) W.u.) measured in the Coulomb-excitation experiment [45]. Based on the $\log ft$ values, a $7/2^-$ spin was assigned to the 0.98-MeV state observed in the β -decay experiment [43,44]. In the $^{72}\text{Zn}(d,^3\text{He})^{71}\text{Cu}$ pick-up reaction performed lately [55], none of these two levels was observed but three new $7/2^-$ states were discovered at 1.86, 3.24 and 4.36 MeV with a spectroscopic factor of 1.4(2), 1.5(3) and 3.7(6), respectively. An experimental centroid of 3.8 MeV for the $\pi f_{7/2}^{-1}$ strength was determined from the latter experiment, based on the 86(12)% of the total strength observed. Comparing with ^{69}Cu , it is not possible to clarify in what direction or to what extent the energy of the centroid shifts, but the $\pi f_{7/2}^{-1}$ strength remains sufficiently high to conclude that the $Z = 28$ gap does not collapse when starting to fill the $\nu g_{9/2}$ orbital [55].

The first spectroscopic information for ^{73}Cu was obtained in the β -decay experiment, in which a $7/2^-$ spin has been tentatively assigned to two states, at 0.96 and 1.01 MeV, and a $(7/2^-, 9/2^-)$ spin to another one at 1.30 MeV [44]. The Coulomb-excitation experiment excludes the single-hole character of the 0.96-MeV level because of its high $B(E2)$ value (14.9(18) W.u.) [45]. A multinucleon-transfer experiment was performed recently, in which the lifetime of several states was extracted [56]. The authors concluded that only the 1.30-MeV state could have a $\pi f_{7/2}^{-1}$ single-hole character, in contradiction with the core-coupling character suggested earlier [44], but mentioning that this state could also have a spin $5/2^-$. The situation is not clear in this nucleus and no spectroscopic factor was extracted, preventing from firm conclusions.

As regards the isotopes heavier than ^{73}Cu , no $7/2^-$ state has ever been observed in ^{75}Cu , while two of them were possibly identified in ^{77}Cu in a recent β -decay experiment [49]: one at 1.15 MeV, interpreted as a core-coupling state, and another one tentatively placed at 2.07 MeV, mentioned as a possible candidate for the $\pi f_{7/2}^{-1}$ hole state. For ^{79}Cu , there is not even a partial level scheme. The situation is therefore not clear in this region, and spectroscopic information in such an exotic isotope as ^{79}Cu is crucial in order to know more about the behavior of the $Z = 28$ gap when reaching $N = 50$.

1.3.3 Low-lying collective states

One of the major discoveries in the Coulomb-excitation experiment was the observation of a strongly collective low-lying state in $^{71,73}\text{Cu}$ [45]. Indeed, a $1/2^-$ level was observed with a large $B(E2; 1/2_1^- \rightarrow 3/2_{gs}^-)$ value, above 20 W.u., in both isotopes, at 454 and 135 keV, respectively. In comparison, the first $1/2^-$ in ^{69}Cu was measured at 1.1 MeV [50] and the corresponding $B(E2)$ value is 10.4 W.u. [45], meaning that there is a significant increase of the collectivity at low energy beyond $N = 40$. This coexistence of single-particle and collective states was also observed in ^{75}Cu , with the discovery of nearly degenerate isomeric states at 61.7(4) and 66.2(4) keV [47]. Although it was not possible to attribute firmly a spin to each state, the authors suggested a spin $3/2^-$ and $1/2^-$, based on the systematics. They determined the $B(E2)$ of each transition assuming these

spins and they found that the $3/2^-$ state has a $\pi p_{3/2}$ single-particle character while the $1/2^-$ state, with $B(E2; 1/2_1^- \rightarrow 5/2_{gs}^-) > 16$ W.u., is strongly collective. These low-energy collective states might be linked to the possible increase of collectivity in nickel isotopes, discussed in section 1.2.4. It would be interesting to see the evolution of the energy and nature of this first $1/2^-$ state when reaching $N = 50$.

1.3.4 Summary

The systematics of the first $1/2^-$, $3/2^-$ and $5/2^-$ states as well as the known or suggested $7/2^-$ ones for $N \geq 40$ is shown in figure 1.7. The spectroscopic factors extracted for the $7/2^-$ states are indicated, knowing that in this precise case their sum is at most equal to 8 (i.e. $2j + 1$, the number of protons expected in the $\pi f_{7/2}$ orbital in the extreme shell-model representation) for a given copper isotope. The two lowest $7/2^-$ states were not observed in the $^{72}\text{Zn}(d, ^3\text{He})^{71}\text{Cu}$ reaction, meaning that their spectroscopic factor is low [55], and no spectroscopic factors were measured in heavier copper isotopes. The systematics of the 2_1^+ state in nickel isotopes is also shown, and it can be noted that it follows closely the $7/2^-$ states of copper for which a core-coupling nature was determined [45, 55, 56] or at least suggested [49].

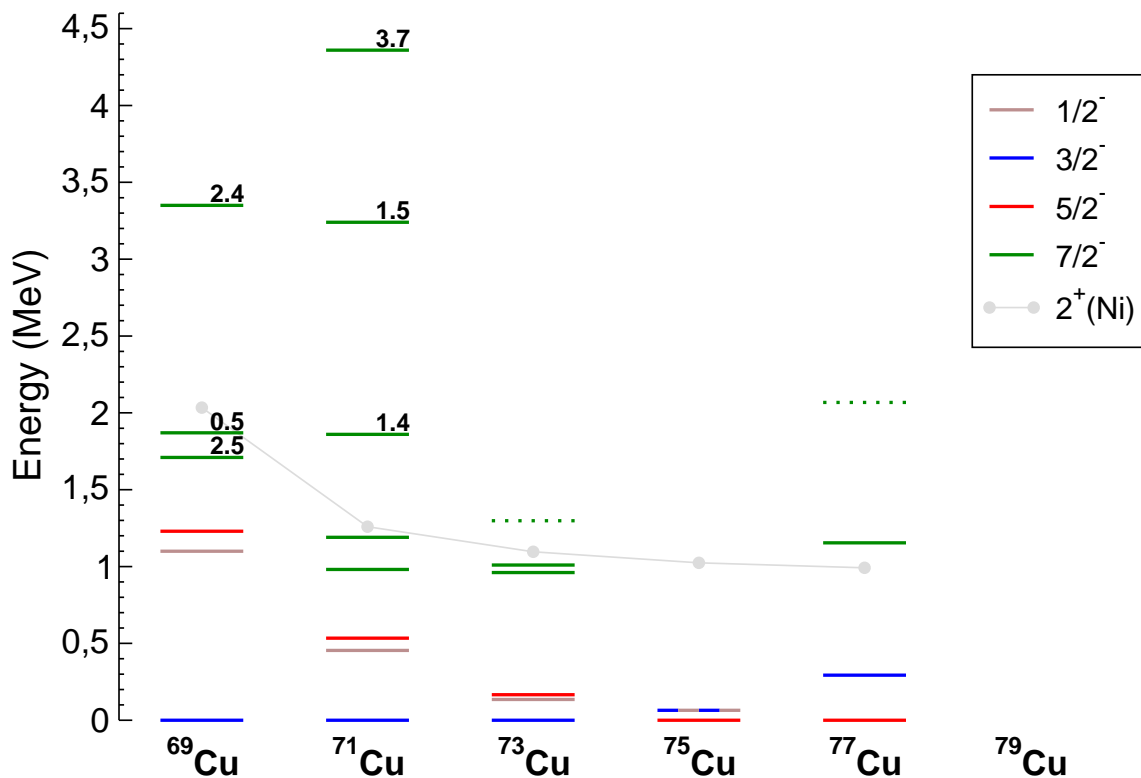


Figure 1.7 – Systematics of the first $1/2^-$, $3/2^-$, $5/2^-$ and $7/2^-$ states of neutron-rich copper isotopes, as well as the 2_1^+ state of nickel isotopes. The spectroscopic factors known for the $7/2^-$ states are indicated. Data taken from references [27–30, 43–50, 53–55].

1.4 Summary of theoretical studies for copper

Shell-model calculations in the full space, i.e. considering all possible single-particle orbitals, is numerically impossible for medium-mass and heavy nuclei, and one has to use a truncated space. The model space is then divided into:

- An inert closed-shell core, whose orbitals are always full (no exchange of particles with upper orbitals);
- A valence space, composed of several orbitals where the valence nucleons may evolve;
- A forbidden space, including orbitals energetically higher than the valence space, which is always empty.

These three components are chosen depending on the region of interest in the nuclear chart and the total dimension of the valence space is given by

$$D = \begin{pmatrix} \Omega_\pi \\ N_\pi \end{pmatrix} \begin{pmatrix} \Omega_\nu \\ N_\nu \end{pmatrix} \quad (1.11)$$

with $N_{\pi,\nu}$ the number of valence protons and neutrons evolving in a space of dimension $\Omega_{\pi,\nu}$ and $\Omega = \sum_j (2j + 1)$.

One of the first shell-model calculation dedicated to the copper isotopic chain beyond $N = 40$ was performed after the β -decay study but before the Coulomb excitation and laser spectroscopy experiments, using a realistic interaction developed by the Strasbourg group in a valence space composed of the $p_{3/2}f_{5/2}p_{1/2}g_{9/2}$ orbitals, both for protons and neutrons, above a ^{56}Ni core [57]. The main component of the wave functions of the $3/2^-$ and $5/2^-$ states above $N = 40$ is found to correspond to the $\pi p_{3/2}$ and $\pi f_{5/2}$ single-particle states, respectively. The calculations show a monopole shift, as observed experimentally, but the $5/2^-$ lies too high in energy and the inversion of the $\pi p_{3/2}$ and $\pi f_{5/2}$ orbitals is predicted at $N = 50$.

This monopole drift implies the strong attraction between the $\nu g_{9/2}$ and $\pi f_{5/2}$ orbitals, that has been later explained by the tensor force by the Tokyo group in a study where the inversion of the $\pi p_{3/2}$ and $\pi f_{5/2}$ orbitals is found to happen at mid-shell [19]. The authors also predicted a weakening of the $Z = 28$ gap in ^{78}Ni because of the repulsion between $\nu g_{9/2}$ and $\pi f_{7/2}$ orbital, due to the same tensor force. The effect of such an interaction between the $\nu g_{9/2}$ and the $\pi f_{7/2}f_{5/2}$ orbitals is illustrated in figure 1.8(a), while an example of the predicted evolution of proton ESPE is shown in figure 1.8(b). Further calculations within the $p_{3/2}f_{5/2}p_{1/2}g_{9/2}$ valence space were then performed using the JUN45 interaction [58]. They reproduce the inversion of the $3/2^-$ and $5/2^-$ states in ^{75}Cu but failed to explain the lowering of the $1/2^-$ one.

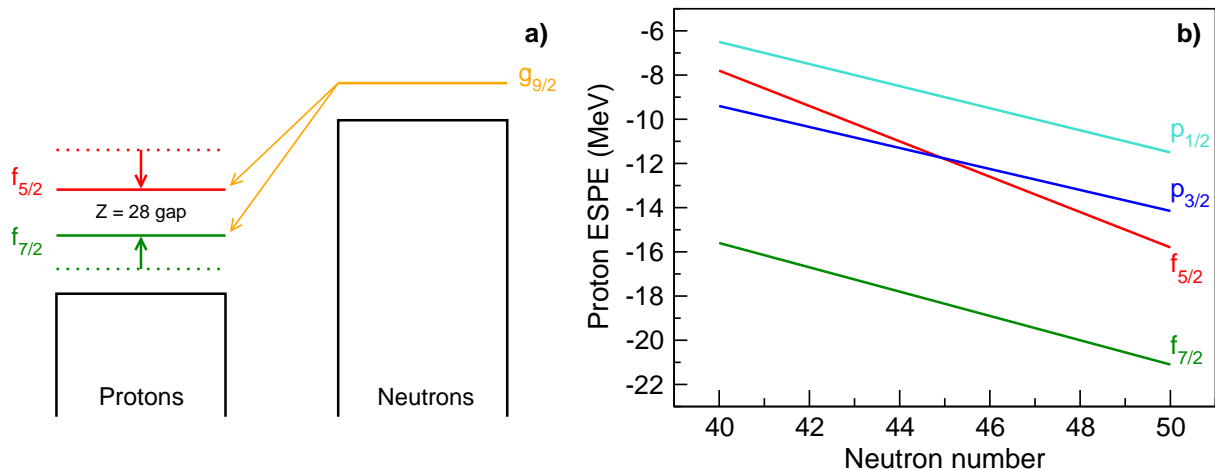


Figure 1.8 – (a) Schematic representation of the interaction due to the tensor force between the $\nu g_{9/2}$ and $\pi f_{5/2}, f_{7/2}$ orbitals. (b) Evolution of the proton ESPE in nickel isotopes, showing the inversion between the $\pi p_{3/2}$ and $\pi f_{5/2}$ orbitals. Values taken from [20].

A possible weakening of the $Z = 28$ gap towards $N = 50$ was also stressed by calculations performed by the Strasbourg group, including the $\pi f_{7/2}$ orbital in the valence space [59], which allows proton excitations across the $Z = 28$ gap. In agreement with the experimental evidences [45] and the previous calculation for copper [57, 58], the authors showed the important single-particle character of the first $3/2^-$ and $5/2^-$ states, while the first $1/2^-$ level is found to be more and more collective when adding neutrons in the $\nu g_{9/2}$ orbital, except at $N = 50$ where there is a restoration of its single-particle character. In these calculations, the inversion of the $\pi p_{3/2}$ and $\pi f_{5/2}$ orbitals was found at $N = 46$ and the systematics of the low-lying levels, known up to ^{73}Cu at that time, was correctly reproduced. The authors explained the impossibility for previous calculations to have a fair agreement with the experimental systematics by the lack of proton degrees of freedom due to the non-inclusion of the $\pi f_{7/2}$ orbital in the valence space. Later on, the same authors showed that using a larger model space, with the addition of the $\nu d_{5/2}$ orbital that allows neutron excitations across the $N = 50$ gap, the $Z = 28$ shell closure appears to be robust [60]. The latter work was performed using the LNPS interaction [61].

The tensor force seems to play a major role in the evolution of the $Z = 28$ gap, delimited by the $\pi f_{7/2}$ and $\pi p_{3/2} - \pi f_{5/2}$ orbitals. The strength of this interaction reaches its maximum when the $\nu g_{9/2}$ orbital is full, at $N = 50$, i.e. for ^{78}Ni . The lack of data in the very close vicinity of the latter nucleus prevents both experimental and theoretical firm conclusions about its magicity. The study of ^{79}Cu can therefore provide significant information on the evolution of nuclear structure in such an exotic region of the nuclear chart.

1.5 Study proposed in the present work

In the experiment, described in the next chapter, we are dealing with inverse kinematics and the nucleus of interest is produced through proton-removal of the projectile: $^{80}\text{Zn}(p,2p)^{79}\text{Cu}$. Nucleon-removal reactions, also referred as knockout reactions, are part of the direct reactions. A direct reaction is a fast process occurring at the surface of the nuclei where a few nucleons may be exchanged or removed from the projectile and the target, and in which the populated final states keep memory of the initial state [62]. This property leads to the notion of spectroscopic factor, a powerful tool that links direct reactions and nuclear structure. The γ rays emitted in-flight by the final nucleus are detected to obtain information on its levels.

1.5.1 Spectroscopic factors

In a knockout reaction, hole states can be populated. The probability to populate a final state f depends on the overlap between this state f and the initial state i of the projectile. The overlap between a nucleus with A nucleons in the initial state $|\psi_i^A\rangle$ and a nucleus with $A - 1$ nucleons in the final state $|\psi_f^{A-1}\rangle$ is given by the spectroscopic factor:

$$S_k = |\langle \psi_i^A | a_k^\dagger | \psi_f^{A-1} \rangle|^2 \quad (1.12)$$

with a_k^\dagger the creation operator. Said in a different way, this spectroscopic factor S_k quantifies the degree of likeness between a nucleus $|\psi_f^{A-1}\rangle$ and a core $|\psi_i^A\rangle$ plus a hole in the $k = (nlj)$ orbital. Therefore, S_k informs us about the single-hole nature of each populated state in the final nucleus. S_k goes from 0 (no likeness at all) to 1 (full likeness, i.e. pure single-hole state). Of course, due to the correlations in the nucleus, pure single-hole states do not exist and the spectroscopic strength is fragmented over several levels. The challenge resides in finding all these fragments in order to reconstruct the energy centroid of the considered orbital, given as follows:

$$E_k^{centroid} = \frac{\sum_i S_k^i E_k^i}{\sum_i S_k^i} \quad (1.13)$$

with E_k^i the energy of each level i with a spin and parity $j^{(-1)^l}$ carrying a spectroscopic strength S_k^i . Often, and it will be the case in the following, the spectroscopic factors regarding nucleon-removal are multiplied by the occupation number of the orbital k in the initial nucleus, which corresponds at most to $(2j + 1)$.

Unfortunately, spectroscopic factors are not observables [17], they are model dependent, but they can be extracted from the reaction cross sections. Indeed, the cross section to populate a given final bound state with a spin $J_f^{\pi_f}$, called exclusive cross section $\sigma_{exc}(J_f^{\pi_f})$, is given by [63]:

$$\sigma_{exc}(J_f^{\pi_f}) = \sum_k S_k \sigma_{sp}^k \quad (1.14)$$

with σ_{sp}^k the calculated single-particle cross-section to remove a particle in the $k = (nlj)$ orbital. In our case, we remove a proton from a ^{80}Zn in its ground state, which means $J_i^{\pi_i} = 0^+$. If one considers that the proton can be removed either from the $\pi 1f_{7/2}$, $\pi 1f_{5/2}$ or $\pi 2p_{3/2}$ orbitals, we expect to populate final states in ^{79}Cu with a spin $J_f^{\pi_f}$ that corresponds to a proton removed in an orbital k with $j_k^{(-1)^{l_k}} = J_f^{\pi_f}$. Therefore, equation 1.14 reduces to one term and we obtain

$$S_k = \frac{\sigma_{exc}(J_f^{\pi_f})}{\sigma_{sp}^k} \quad \text{with } j_k^{(-1)^{l_k}} = J_f^{\pi_f} \quad (1.15)$$

giving access to the spectroscopic factor. One has to be careful as S_k depends on the model of reaction used. And of course, it necessary to know the spin and parity of a state for calculating its spectroscopic factor, as σ_{sp} depends on the orbital where the nucleon is removed. In the ideal case, the spin determination is done by measuring the momentum distribution of the knocked-out proton. As regards the exclusive cross sections, they can be obtained from γ -ray tagging, as shown in the next section.

Finally, the cross section to populate any final bound state, called inclusive cross section, is simply the sum of all exclusive cross sections:

$$\sigma_{inc} = \sum_{J_f^{\pi_f}} \sigma_{exc}(J_f^{\pi_f}) = \sum_{J_f^{\pi_f}} S_k \sigma_{sp}^k \quad \text{with } j_k^{(-1)^{l_k}} = J_f^{\pi_f} \quad (1.16)$$

but it can also be determined independently by measuring the number of reactions in the target, as explained in section 5.4.1.

1.5.2 In-beam γ -ray spectroscopy

The knockout reaction often populates a final excited state of the residue which will decay through γ -ray emission so quickly that there is not enough time to stop the nucleus: the γ rays are emitted in flight. Using an appropriate detector, it is possible to efficiently perform the necessary Doppler correction and to build the level scheme of the nucleus, using the intensity of the transitions and looking at γ - γ coincidence relations, when several γ rays are emitted in cascade. We recall here some useful properties of γ emissions.

Selection rules

In the nucleus frame, the energy of the emitted γ ray is equal to the energy difference between the energies of the final and initial states (the recoil of the emitting nucleus can be neglected here). For angular-momentum conservation reasons, the angular momentum L transferred by the photon satisfies

$$|J_i - J_f| \leq L \leq J_i + J_f \quad (L \neq 0) \quad (1.17)$$

with J_i (J_f) the spin of the initial (final) state. The transitions can be of two types: electric (E), where the parity between the initial and final states is changed by $(-1)^L$, and magnetic (M), for which the parity associated is $(-1)^{L+1}$. Therefore, depending on the parity of the initial (π_i) and final (π_f) states, we can have the following transitions:

$$\begin{aligned} \pi_i = \pi_f & \quad \text{even electric, odd magnetic (M1, E2, M3, E4, ...)} \\ \pi_i = -\pi_f & \quad \text{odd electric, even magnetic (E1, M2, E3, M4, ...)} \end{aligned} \quad (1.18)$$

and generally, the kind of transition with the lower L is dominant.

Transition probability and nature of states

The probability of a transition of type $\sigma = E$ or M and angular momentum L between two states is given by [64]

$$\lambda(\sigma L; i \rightarrow f) = \frac{8\pi}{\hbar} \frac{L+1}{L[(2L+1)!!]^2} k^{2L+1} B(\sigma L; i \rightarrow f) \quad (1.19)$$

with $k = \frac{E_\gamma}{\hbar c}$, E_γ the energy of the emitted photon, and $B(\sigma L; i \rightarrow f)$ the reduced transition probability. The latter depends on the nature of the initial and final states: while single-particle transitions involve only one nucleon by definition, collective states entail in general several particles, making the transition probability larger in the second case than in the first one. As a consequence, the degree of collectivity of the states in a given transition can be quantified by comparing the observed transition probability to the single-particle transition probability, the latter being given by the Weisskopf estimates [64]:

$$\begin{aligned} B(E L; i \rightarrow f) &= \frac{1}{4\pi} \left(\frac{3}{L+3} \right)^2 (1.2 A^{1/3})^{2j} \\ B(M L; i \rightarrow f) &= \frac{10}{\pi} \left(\frac{3}{L+3} \right)^2 (1.2 A^{1/3})^{2j-2} \left(\frac{\hbar}{2m_p c} \right)^2 \end{aligned} \quad (1.20)$$

with m_p the proton mass. The probability of a transition in Weisskopf units (W.u.) is the ratio between the experimental value and the Weisskopf estimate. A pure single-particle

transition has a transition probability close to 1 W.u., while collective transitions have a much higher value.

Branching ratios

The intensity of the γ rays emitted is a crucial information as it allows to calculate the branching ratios, i.e. the knockout feeding to each level, which is directly linked to the exclusive cross section. The relative branching ratio of a state J^π is given by the intensity of the outgoing γ -rays ($I_{\gamma_{out}}$) minus the intensity of the incoming ones ($I_{\gamma_{in}}$), divided by N_{nuclei} , the number of nuclei produced:

$$b.r. (J^\pi) = \frac{\sum_{\gamma_{out}} I_{\gamma_{out}}(J^\pi) - \sum_{\gamma_{in}} I_{\gamma_{in}}(J^\pi)}{N_{nuclei}} \quad (1.21)$$

with $\sum b.r. (J^\pi) = 100\%$, and the exclusive cross section can be derived from the inclusive one as follows:

$$\sigma_{exc} (J^\pi) = b.r. (J^\pi) \times \sigma_{inc} \quad (1.22)$$

Therefore, this gamma-tagging technique is a key tool in knockout experiments to find the different levels of the nucleus, make assumption on their spin and extract the spectroscopic factors.

Chapter 2

Experimental setup

The experiment was part of the first Seastar (Shell evolution and search for two-plus energies at the RIBF) campaign, an experimental program that aims at investigating very neutron-rich nuclei produced through proton knockout by means of in-beam γ -ray spectroscopy. It was performed during 5 days at the Radioactive Isotope Beam Factory (RIBF) of RIKEN, Japan, combining the MINOS device, a liquid-hydrogen target coupled to a vertex tracker, and the DALI2 scintillator array. The different parts of the setup are described in this chapter.

2.1 Beam production

The beam production is based on the in-flight separation technique. A ^{238}U primary beam collides with a ^9Be target, producing a cocktail of exotic nuclei sorted in flight by a magnetic spectrometer, creating the secondary beam used for the experiment.

2.1.1 Heavy-ion accelerating system

The RIBF accelerating system [65] as used in the experiment for the production of a high-energy ^{238}U primary beam is shown in figure 2.1.

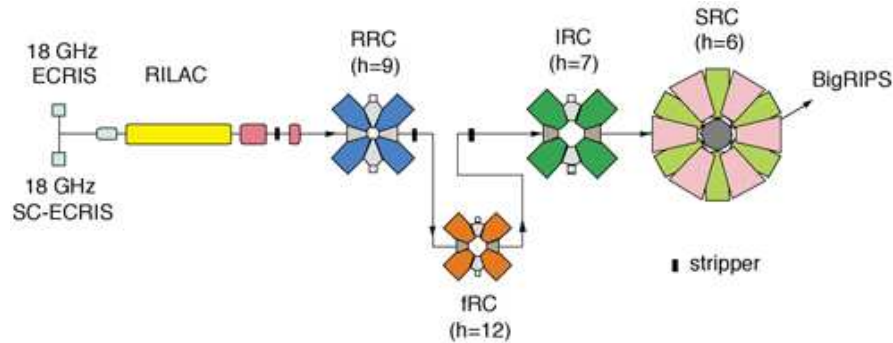


Figure 2.1 – Schematic diagram of the RIBF heavy-ion accelerator system for the radioactive-ions beam generation at 345 MeV per nucleon. Image taken from reference [66].

The ^{238}U ions are extracted in an Electron Cyclotron Resonance Ion Source (ECRIS) and go into the RILAC linear accelerator. The latter is used as a first injector for the four-cyclotron sequence constituted of RCC, fRC, IRC and finally SRC, a superconducting cyclotron driving the beam up to 345 MeV per nucleon. Two strippers are placed upstream and downstream fRC. Once the beam leaves the SRC, it is sent on the primary target at the entrance of the BigRIPS separator. The intensity of the ^{238}U beam was 12 pA, which corresponds to 7.5×10^{10} particles per second (pps).

2.1.2 BigRIPS

The BigRIPS spectrometer [67] is a two-stage radioactive ion beam separator, placed after the accelerating system. It is made of fourteen superconducting triplet quadrupoles (STQs) that focus the beam and six room-temperature dipoles with a bending angle of 30° , distributed between eight foci (F0 to F7) over a length of 78.2 m. Its horizontal and vertical angular acceptances are ± 40 and ± 50 mrad, respectively, and its momentum acceptance is $\pm 3\%$.

The first stage of BigRIPS, from F0 to F2, consists in producing the secondary RI-beam and selecting the nuclei of interests with the $B\rho-\Delta E-B\rho$ method. The identification of the isotopes is performed in the second stage, from F3 to F7, with the TOF- $B\rho-\Delta E$ method. The secondary beam is then sent into the different experimental beam-lines of the RIBF, as shown in figure 2.2.

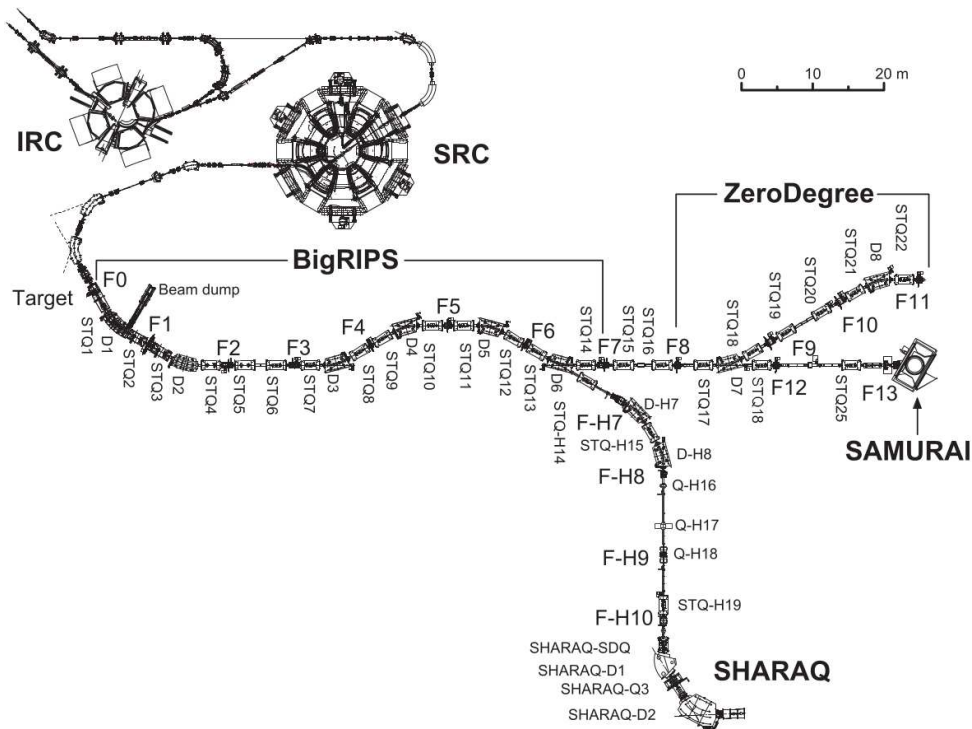


Figure 2.2 – Schematic view of the RIBF experimental lines. Image taken from reference [67].

Production and selection of the secondary beam

The ^{238}U primary beam is sent on a 3-mm thick ^9Be primary target set at the entrance of BigRIPS (F0) for in-flight fission, creating a wide range of nuclei. These nuclei are fully stripped, meaning that their charge corresponds to their proton number Z . The selection of the nuclei of interest is made through a technique called momentum-loss achromat [68], based on a $B\rho$ - ΔE - $B\rho$ selection using two dipoles (D1 and D2) separated by a degrader placed at F1. An illustration of this method is shown in figure 2.3.

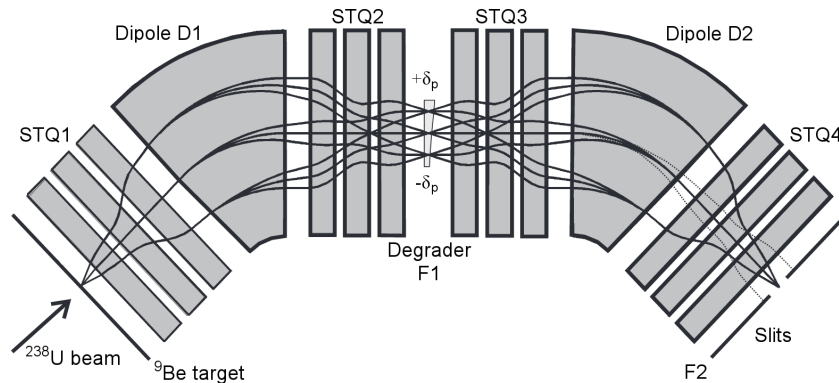


Figure 2.3 – Schematic representation of the momentum-loss achromat technique. The beam can be purified by stopping unwanted isotopes (dashed line) in the F2 slits after $B\rho$ - ΔE - $B\rho$ selection. Image taken from reference [69] and modified.

In a constant magnetic field \vec{B} , the trajectory of an ion with a mass number A , charge $Q = Ze$ and momentum P is described by the magnetic rigidity

$$B\rho = \frac{P}{Q} = \frac{\gamma m v}{Ze} = \frac{u c}{e} \beta \gamma \frac{A}{Z} \quad (2.1)$$

where ρ is the curvature radius of the ion, $v = \beta c$ its velocity, $m \approx Au$ its mass, $u \approx 931.5$ MeV the atomic mass unit, c the speed of light and $\gamma = (1 - \beta^2)^{-1/2}$. Then, the first dipole (D1) separates the beam through $\beta\gamma A/Z$ selection. A beam dump is placed just after D1 in order to stop the remaining primary beam.

This selection in $B\rho$ is not enough as several nuclei can have a similar $\beta\gamma A/Z$. Therefore, an aluminium degrader is placed in F1, where the beam is going to lose energy as described by the relativistic Bethe formula

$$\Delta E = \frac{4\pi e^4 n z Z^2}{m_e \beta^2 c^2} \left[\ln \frac{2m_e \beta^2 c^2}{I} - \ln(1 - \beta^2) - \beta^2 \right] \quad (2.2)$$

with z , n and I the atomic number, atomic density and mean excitation potential of the aluminium degrader. The energy loss of the fragments in the degrader depends on (A, Z, β) in a different manner than $B\rho$. Thus, two different isotopes with the same $B\rho$

will be discriminated thanks to the degrader because they will not lose the same amount of energy. Finally, another selection in $B\rho$ is done after the degrader, through the second dipole (D2). The thickness of the degrader varies with the horizontal position at F1. This ensures that the full D1-degrader-D2 setup is achromatic: the position of the isotopes in the F2 focal plane does not depend on their momentum, only on their nature. Slits are then adjusted in F2 to purify the beam.

Identification of the secondary beam

The second stage of BigRIPS, from F3 to F7, serves to identify the fragments leaving the first stage. Another degrader is located at F5 to improve the separation of the secondary beam. The particle identification is made through the TOF- $B\rho$ - ΔE method: the time of flight, magnetic rigidity and energy loss of the isotopes are measured to deduce their mass-to-charge ratio A/Q and their atomic number Z . More details about this method are given in section 3.1.2.

The time of flight of each nucleus is calculated thanks to two plastic scintillation counters located at F3 and F7, corresponding to a flight path of 46.6 m. The time resolution is approximately 40 ps [70]. This corresponds to a relative time-of-flight resolution of 0.016% for the ^{80}Zn secondary beam of interest at 270 MeV per nucleon. The positions (x, y) of the fragments in F3, F5 and F7 focal planes are measured by two sets of double position-sensitive parallel plate avalanche counters (PPACs) [71,72]. This gives the angles (θ, ϕ) of the ion trajectory with respect to the optical axis (z -axis) in the (xz) and (yz) planes, respectively. These (x, θ, y, ϕ) coordinates are necessary to determine the $B\rho$ of the ions, as explained in section 3.1.1. Finally, the energy loss of the isotopes is measured with a tilted electrode gas ionization chamber [73] located at F7.

After the second stage of BigRIPS, the nuclei went to the MINOS target, placed in F8, at the entrance of the ZeroDegree spectrometer.

Beam intensity and energy

The mean intensity and energy of the primary and secondary beams are given in table 2.1. The beam setting in BigRIPS was tuned for ^{79}Cu but in our case, the nucleus of interest is ^{80}Zn . Both total and ^{80}Zn values are indicated for the secondary beam.

Beam	Intensity (pps)	Energy (MeV/n)
Primary (^{238}U)	7.5×10^{10}	345
Secondary (^{80}Zn)	$\sim 2.6 \times 10^2$	270
Secondary (Total)	$\sim 5.5 \times 10^3$	250 to 280

Table 2.1 – Mean intensity and energy of the primary and secondary beams.

2.2 MINOS

MINOS (MagIc Numbers Off Stability) [74] is a liquid-hydrogen target used for nucleon-removal from very exotic nuclei, coupled to a proton tracker made for reaction-vertex reconstruction. The principle of this device is described in figure 2.4.

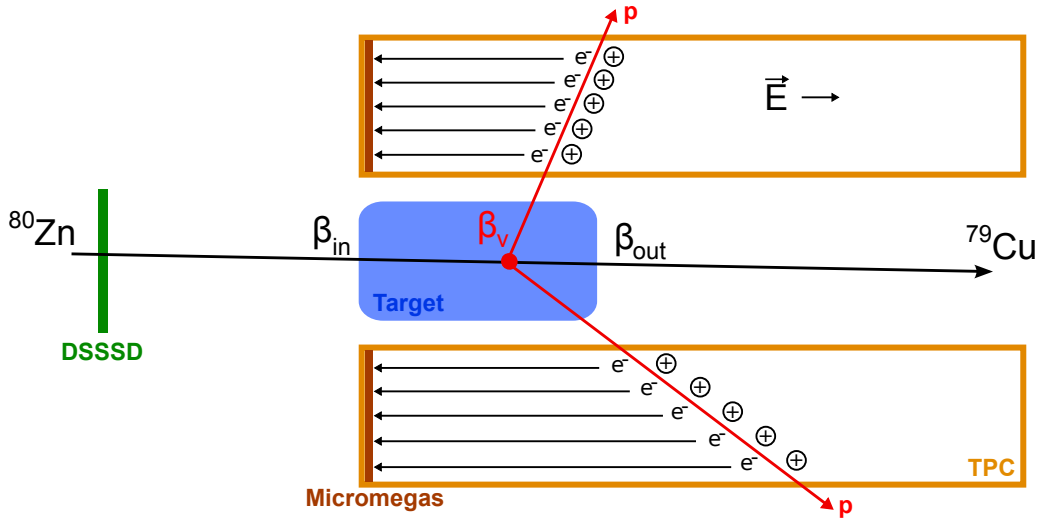


Figure 2.4 – Schematic view of the MINOS device.

2.2.1 Liquid-hydrogen target

The cylindrical target cell is made of polyethylene terephthalate (PET) and is filled with pure liquid hydrogen at 20 K. The entrance window has an effective diameter of 38 mm and is 110- μm thick, while the diameter of the exit window is 52 mm for a 150- μm thickness. The cell was placed in a 2-mm thick aluminum pipe of 72-mm inner diameter with two PET windows of 150 μm thickness at each end, allowing a vacuum of $\sim 10^{-6}$ mbar in the reaction chamber.

In this experiment, the target length was measured to be 100(1) mm when it was empty. An additional 2 to 3 mm has to be taken into account because of the deformation of the entrance window when the target is filled, due to the pressure difference. The density of the liquid hydrogen was 70.97 kg/m^3 .

2.2.2 Vertex tracker

The target chamber is surrounded by a cylindrical time-projection chamber (TPC) of 300-mm length, with an inner diameter of 80 mm and an outer diameter of 178.8 mm. The TPC is filled with a gas mixture of Ar (82%), CF_4 (15%) and $\text{isoC}_4\text{H}_{10}$ (3%) at room temperature and atmospheric pressure. This mixture was found to be the best compromise between low average energy to produce an electron/ion pair, high drift velocity of the

electrons and amplification of the avalanche process at the anode. The gas flow in the TPC was from 7 to 10 liters per hour, in order to avoid a rise of water and oxygen impurities as they decrease the electron drift velocity. An electric field of 185 V/cm was applied alongside the beam direction.

After the proton knockout of the secondary beam in the liquid-hydrogen target, the scattered proton and the removed one leave the reaction chamber and pass through the TPC, ionizing the atoms of the gas. The released electrons drift towards the anode following straight lines due to the applied electric field. The electron signal is amplified at the anode by a bulk-Micromegas detector [75,76]: a thin micro-mesh is placed at 128 μm from the anode and a strong electric field of 36 kV/cm is applied in this gap, inducing electron avalanches whose charge is collected by the anode. This anode is segmented into 4608 pads equally divided into 18 rings and each pad has an area of about 4 mm². This segmentation allows to reconstruct the proton trajectory in the (xy) plane. The information about the z -coordinate is given by the drift time of the electrons in the TPC.

From two proton trajectories or from one proton trajectory and the beam direction, it is possible to reconstruct the reaction vertex in the MINOS target. The efficiency of reconstruction for events with one or two protons is 95%, while the vertex position resolution along the beam axis is 5 mm FWHM (full width at half maximum).

2.2.3 Beam tracker

When only one proton is seen in the TPC, the vertex can still be reconstructed if the trajectory of the nucleus in the target is known. The beam trajectory can be extracted from the position information given by the two PPACs placed at F8. In order to increase the precision and efficiency of this trajectory measurement, a double sided silicon strip detector (DSSSD) was set 458-mm upstream from the target. This DSSSD was 300- μm thick and had 128 strips both horizontally and vertically, for an area of 10 \times 10 cm². The beam direction is then given by the DSSSD and one of the two F8 PPACs.

2.3 DALI2

DALI2 (Detector Array for Low Intensity radiation 2) [77] is a γ -ray detector made of 186 NaI(Tl) scintillators. It has been designed for in-beam γ -ray spectroscopy experiments with high-velocity beams ($\beta \sim 0.6$).

2.3.1 Geometry

In the geometry used in the experiment, shown in figure 2.5, the crystals were arranged into ten cylindrical layers plus a wall for forward-angle measurements. Each layer was made of 10 to 14 crystals with dimensions of 45 \times 80 \times 160 mm³ or 40 \times 80 \times 160 mm³ and

the wall was formed by 64 crystals, half measuring $40 \times 80 \times 160 \text{ mm}^3$ and half measuring $60 \times 60 \times 120 \text{ mm}^3$. This geometry has been chosen to maximize the detection efficiency, especially at forward angles because of the Lorentz boost, and the segmentation allows to reduce the angular resolution to 7° FWHM. The angular resolution is crucial for an accurate Doppler correction. The MINOS device was placed at the entrance of DALI2: the beginning of the target was 8 mm upstream the edge of the first layer of the array. The angular coverage of DALI2 in this configuration went from 11° to 95° at the center of the MINOS target. An energy threshold of about 150 keV was set in order to reduce background events.

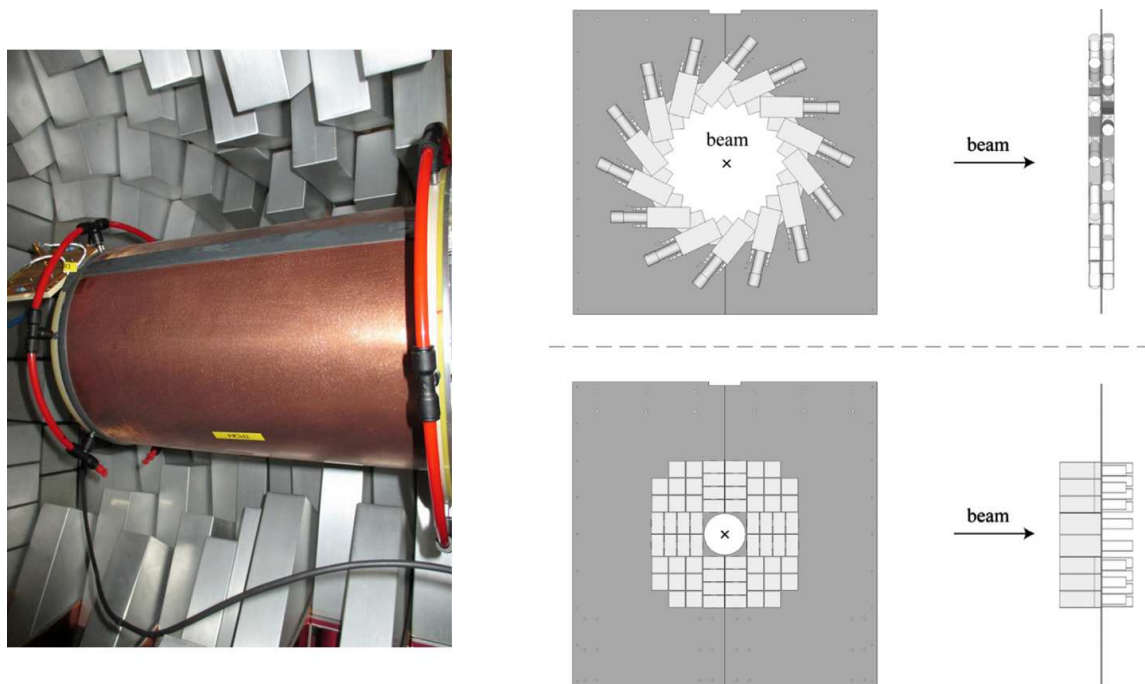


Figure 2.5 – DALI2 configuration. (Left) Picture of DALI2 with MINOS inside. (Top right) Layout of the layers, that are made of 10 to 14 crystals, and (bottom right) placement of the 64 crystals of the wall, at forward angles. The image on the right is taken from reference [77].

The performances of this configuration have been obtained with Geant4 simulations [78], described in section 3.5, using experimental conditions. For a velocity $\beta_{in} = 0.62$ at the entrance of the target, the energy resolution at 500 keV (1 MeV) is found to be $\sigma_E/E = 5.4\%$ (4.3%) and the photopeak efficiency is 30% (19%). We show in section 3.3.3 how this efficiency can be increased up to 38% (27%) with the add-back procedure, by summing the energies received by neighboring crystals.

2.3.2 Typical response function

The response of DALI2 to radiations depends on the detector geometry and resolution, and on the three main interactions between the γ rays and the crystals: photoelectric absorption, Compton scattering and pair production. We present here the case of an emitting source at rest and a moving source, using experimental conditions.

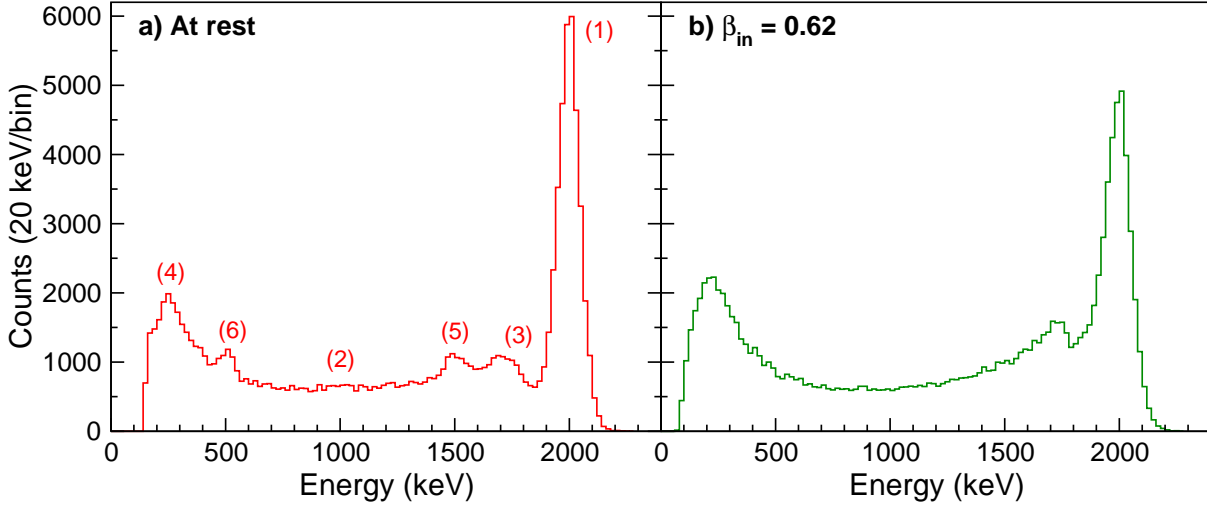


Figure 2.6 – DALI2 response functions for a 2-MeV transition emitted by (a) a source at rest and (b) a moving source entering the 102-mm thick target with $\beta_{in} = 0.62$. In the latter case the Doppler correction is done, and the add-back procedure is used for both. The different parts of the spectra are described in the text.

Source at rest

A typical response function of DALI2 after add-back for a 2-MeV transition emitted by a source at rest is shown in figure 2.6(a). It has been obtained from simulations including the 150-keV energy threshold.

The photopeak (1) is named after the photoelectric effect, in which the γ ray is fully absorbed by an atom of the crystal. Its width depends on the intrinsic resolution of the detector. The photoelectric absorption dominates for energies up to about 200 keV.

Above 200 keV, the Compton scattering prevails and is responsible of the continuum (2). This continuum is not uniform as the cross section of Compton scattering, given by the Klein-Nishina formula, depends on the scattering angle and the initial energy. From the Compton-scattering formula, that we recall:

$$E'_\gamma = \frac{E_\gamma}{1 + \frac{E_\gamma}{m_e c^2} (1 - \cos \theta)} \quad (2.3)$$

it can be seen that the scattered photon has an energy E'_γ in the range from the initial energy E_γ ($\theta = 0^\circ$, meaning no interaction) down to $E_\gamma / (1 + \frac{2E_\gamma}{m_e c^2}) = 227$ keV in our

case. Therefore, the continuum goes from $E_\gamma - E_\gamma'^{max} = 0$ to $E_\gamma - E_\gamma'^{min} = 1773$ keV, the latter value corresponding to the Compton edge (3). The fact that the photopeak is not fully separated from the Compton edge has two origins: the resolution of the crystals, that induces a significant width of both the photopeak and the Compton edge, and the multiple Compton events, when two or more Compton interactions happen in the same crystal or in two neighboring crystals whose energies are summed in the add-back procedure. Also from equation 2.3, we can note that scattering angles greater than 120° lead to scattered photons with a similar energy, between 227 and 291 keV. Due to the geometry of DALI2, these backscattered photons can be detected and they form the backscatter peak (4) around 250 keV.

Although not predominant below several MeV, the pair-production process plays a role in the interaction of γ rays when $E_\gamma \geq 2m_e c^2$, like in our example. After the pair production, the positron will annihilate with an electron in the crystal, creating two photons of 511 keV. Sometimes one or two of these photons escape from the crystal, inducing an incomplete detection and creating the so-called single ($E_\gamma - 511$ keV) and double ($E_\gamma - 1022$ keV) escape peaks. The single escape peak (5) can be clearly seen at 1489 keV. Once again, because of the array geometry, the escaping 511-keV γ ray (6) can be detected. As regards the double escape peak, that should be at 978 keV, nothing emerges clearly from the continuum. But as both 511-keV photons are emitted in opposite directions, it is very likely that one of them is detected in a neighboring crystal, whose collected energy will be summed to the first-interaction crystal with the add-back procedure, reducing the intensity of the double escape peak.

Moving source

Concerning the response of DALI2 in experimental conditions, a simulated energy-spectrum after add-back and Doppler correction for a 2-MeV transition emitted by a moving source, with a velocity at the entrance of the target $\beta_{in} = 0.62$, is shown in figure 2.6(b).

Due to the Doppler effect, the energy E_γ seen by the detector is shifted from the energy E_0 in the nucleus reference frame by a factor that depends on the angle of emission θ in the laboratory frame and on the nucleus velocity β . Considering the geometry of the setup, a 2-MeV γ ray in the nucleus frame reaches DALI2 with an energy between 1.5 and 4.0 MeV. This effect can be corrected with the Doppler formula:

$$E_0 = E_\gamma \frac{1 - \beta \cos \theta}{\sqrt{1 - \beta^2}} \quad (2.4)$$

Consequently, all events that are not subject to the Doppler effect will be wrongly shifted, using the velocity of the nucleus and an emission angle that is not relevant. For example, the 511-keV peak is spread between 250 and 700 keV. As regards the backscatter

peak, whose energy is almost constant when the incident-photon energy is above 1 MeV as it can be noted from equation 2.3, it is shifted and broader but it is not spread like the 511-keV one because at such a low energy (~ 250 keV), the wrong shift is only between about -120 to +100 keV.

The non-observation of a single escape peak and the persistence of the Compton edge are directly linked to the previous explanations. The Compton edge corresponding to the incident energy E_γ (1.5 to 4.0 MeV) minus $E_\gamma/(1 + \frac{2E_\gamma}{m_e c^2})$ (218 to 240 keV), after Doppler correction it is equal to the true corrected energy E_0 minus a wrongly shifted 218 to 240 keV transition: we are in the same case than for the backscatter peak and therefore the Compton edge is simply shifted and broader. At the contrary, the single escape peak is equal to E_γ minus 511 keV, meaning that after Doppler correction it corresponds to E_0 minus 250 to 700 keV and is spread over the continuum.

Finally, the width of the photopeak is larger for two reasons. The first one is that due to the Lorentz boost, most of the γ rays are emitted forward, i.e. with a higher energy in the laboratory frame, and the intrinsic resolution σ_E increases with the energy. Secondly, as explained in section 3.5.3, the errors made on the Doppler correction deteriorate the resolution.

2.4 ZeroDegree

The identification of the reaction products after MINOS is done with the ZeroDegree spectrometer [67], shown in figure 2.2. ZeroDegree is made of six STQs and two dipoles of the same type as those of BigRIPS. It has four foci (F8 to F11) for a total length of 36.5 m. In the Seastar campaign, ZeroDegree was used in its large acceptance mode: the angular acceptance was ± 45 mrad horizontally and ± 30 mrad vertically, while the momentum acceptance was $\pm 3\%$. The setting in ZeroDegree was tuned for ^{78}Ni . The mean rate and energy of nuclei arriving at the end of ZeroDegree are given in table 2.2. Both total and $^{80}\text{Zn}(p,2p)^{79}\text{Cu}$ rates are mentioned.

Nucleus in F11	Nucleus selected in BR	Intensity (pps)	Energy (MeV/n)
^{79}Cu	^{80}Zn	~ 0.5	180
All	None	~ 380	180 to 200

Table 2.2 – Mean rate and energy of the isotopes arriving at the end of ZeroDegree (F11). For ^{79}Cu , it takes into account a selection on ^{80}Zn in BigRIPS.

Like for BigRIPS, the TOF- $B\rho$ - ΔE method is used for the identification. The time of flight is measured between two plastic scintillator counters placed at F8 and F11, the trajectory is determined by two double PPACs at F8, F9 and F11, and the energy loss is recorded into the ionization chamber located at F11.

2.5 Data acquisition

The recording of the events is done using the RIBF data-acquisition system [79]. For dead time and disk-space saving reasons, it is necessary to optimize the data acquisition to focus on the interesting events only. In the experiment, this was done according to the logic described as follows.

When a nucleus passes through the F7 plastic scintillator, it creates a F7-trigger signal. If this nucleus, or the reaction product if a reaction happened in the target, reaches the F11 plastic scintillator, a F11-trigger signal is created and combined to the F7-trigger one, giving the F7×F11 signal. When a γ ray is detected in DALI2, the output signal from the photomultipliers of the crystals is sent into an amplifier and split in two branches, one for the energy and one for the time. In the time branch, the signal goes through a constant fraction discriminator (CFD) where an energy threshold of around 150 keV is applied in order to reduce low-energy background events. For an energy above this threshold, the signal output of the CFD is used as a γ -trigger signal and is combined to the F7×F11 one if it exists. Finally, the data acquisition starts if either one or both of the following conditions is fulfilled:

- The F7 plastic scintillator triggered, disregarding if the nucleus reaches the end of ZeroDegree or not. This is the F7DS trigger, downscaled (DS) by a factor 40 for avoiding to record too many events. This trigger is used for the transmission measurement and cross section calculation, as explained in section 3.7.
- Both F7 and F11 plastic scintillators triggered and at least one γ ray was detected in DALI2. This is the F7×F11× γ trigger, used for the γ -spectroscopy analysis.

The acquisition system works with a common-dead-time system, i.e. the detector with the largest dead time determines the dead time of the whole setup. The mean dead time τ of DALI2 is about 100 μ s and is similar for MINOS, while it can go up to 200 μ s for some of the beam detectors. The average rate of events recorded per second was $R = 400$ Hz. The fraction of events lost due to the dead time being given by $R\tau$ [80], we can therefore estimate it at 8%.

Chapter 3

Data analysis

In this chapter, we describe how we reconstruct the variables of interest from the raw data recorded during the experiment. Firstly, the identification of the nuclei is done to select the reaction channel of interest. Secondly, the MINOS TPC is calibrated to reconstruct the knocked-out proton trajectories and obtain the interaction vertex. Thirdly, the calibration of DALI2 is performed and the simulation of its response, used in a later stage for fitting the γ -ray energy spectra, is described. Two reference cases, $^{78,80}\text{Zn}$, are used to benchmark the whole analysis procedure. Finally, we measure the ZeroDegree spectrometer transmission, needed to calculate cross sections.

3.1 Particle identification

The first step of the analysis is to identify the isotopes in the BigRIPS and ZeroDegree spectrometers. This identification is done event by event, by reconstructing the trajectory of the particles and using the TOF- $B\rho$ - ΔE method.

3.1.1 Trajectory reconstruction

The trajectory reconstruction in the spectrometers is necessary to determine $B\rho$. The path of an ion in a spectrometer is described by an ion-optical transfer matrix that links the input and output coordinates. For example, the position coordinate in the horizontal plane at F5 depends on the coordinates at F3 through a power series [81]:

$$x_5 = \sum_{i,j,k,l,m} T_{ijklm} x_3^i \theta_3^j y_3^k \phi_3^l \delta_{35}^m \quad (3.1)$$

where the T_{ijklm} coefficients are the transfer matrix elements, x and θ the position and angle in the horizontal plane, y and ϕ the position and angle in the vertical plane, and $\delta_{35} = (B\rho_{35} - B\rho_0)/B\rho_0$ the relative $B\rho$ deviation of the ion from the central value $B\rho_0$ between F3 and F5. Then, by measuring $(x_3, \theta_3, y_3, \phi_3, x_5)$ with the PPACs in F3 and F5, we can deduce δ_{35} and so $B\rho_{35}$. The first-order matrix elements ($i + j + k + l + m = 1$)

have been determined in previous experiments, while higher-order corrections are applied empirically in order to improve the mass-to-charge ratio (A/Q) resolution, as explained further in this section.

3.1.2 TOF- $B\rho$ - ΔE method

The particle identification in the BigRIPS and ZeroDegree spectrometers is based on the TOF- $B\rho$ - ΔE method [70]. On an event-by-event basis, the atomic number Z and the mass-to-charge ratio A/Q of the nuclei are deduced from the measurement of their time of flight (TOF), magnetic rigidity $B\rho$ and energy loss ΔE , using the following equations:

$$\text{TOF} = \frac{L}{\beta c} \quad (3.2)$$

$$B\rho = \frac{\gamma m_u \beta A}{c Q} \quad (3.3)$$

$$\Delta E = \frac{4\pi e^4 n z Z^2}{m_e \beta^2 c^2} \left[\ln \frac{2m_e \beta^2 c^2}{I} - \ln(1 - \beta^2) - \beta^2 \right] \quad (3.4)$$

with L the flight-path length, $\beta = v/c$ the velocity of the particle, c the speed of light, $\gamma = 1/\sqrt{1 - \beta^2}$ the Lorentz factor, $m_u = 931.494$ MeV the atomic mass unit, m_e the electron mass, e the elementary charge. In the Bethe formula, describing the energy loss in equation 3.4, z , n and I are the atomic number, atomic density and mean excitation potential of the material penetrated by the particle.

3.1.3 Identification in BigRIPS

In the BigRIPS spectrometer, the particle identification is performed from F3 to F7, as shown in figure 3.1. Two sets of PPAC detectors in F3, F5 and F7, are used for the trajectory reconstruction and $B\rho$ calculation. The time of flight is measured between two plastic scintillation counters in F3 and F7. The energy loss is recorded in the ionization chamber located in F7.

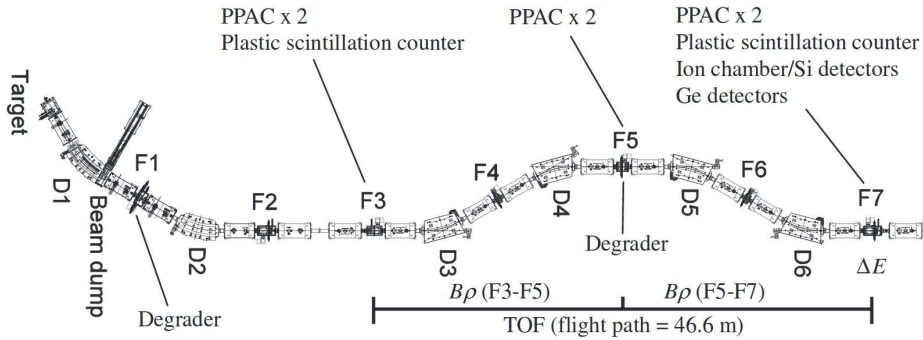


Figure 3.1 – Schematic view of the BigRIPS spectrometer. The section from F3 to F7 is used for particle identification. Image taken from [70].

Z and A/Q reconstruction

Because of the degrader placed in F5, there is an important energy loss during the flight path. As a consequence, it is necessary to measure $B\rho$ before and after the degrader. Then, from equations 3.2 and 3.3, we have:

$$\text{TOF} = \frac{L_{35}}{\beta_{35}c} + \frac{L_{57}}{\beta_{57}c} \quad (3.5)$$

$$\left(\frac{A}{Q}\right)_{35} = \frac{c}{m_u} \frac{B\rho_{35}}{\gamma_{35}\beta_{35}} \quad (3.6)$$

$$\left(\frac{A}{Q}\right)_{57} = \frac{c}{m_u} \frac{B\rho_{57}}{\gamma_{57}\beta_{57}} \quad (3.7)$$

where subscripts 35 and 57 correspond to a variable measured in F3-F5 and F5-F7 parts of BigRIPS, respectively. If we assume no charge change at F5, we have $(A/Q)_{35} = (A/Q)_{57}$ and from equations 3.6 and 3.7 we deduce:

$$\frac{\beta_{35}\gamma_{35}}{\beta_{57}\gamma_{57}} = \frac{B\rho_{35}}{B\rho_{57}} \quad (3.8)$$

Thanks to equations 3.5 and 3.8, we can obtain the velocities β_{35} and β_{57} before and after the degrader, from the $B\rho_{35}$, $B\rho_{57}$ and time of flight values that were measured. The A/Q value is then derived using equation 3.3 and the atomic number Z from equation 3.4, using the measured ΔE and β_{57} values. These two variables, A/Q and Z , allow an unambiguous identification of the incoming nuclei.

Background removal

Some background events can appear on the identification diagram due to reactions in the materials of the beam line, incorrect detector responses or charge changes in the F5 degrader. Their removal is discussed in the following.

Plastic scintillation counters

When a particle passes through a plastic scintillation counter, the scintillation signal is detected by two photomultipliers (PMs) located on each side of the detector. It can be shown, as for example in reference [70], that there is following correlation:

$$\ln\left(\frac{q_L}{q_R}\right) \propto t_R - t_L \quad (3.9)$$

with q_L and q_R the charge-integrated signals and t_L and t_R the timing information obtained from the left and right PMs, respectively. Consequently, a correlation plot of $\ln(q_L/q_R)$ versus $t_R - t_L$ can be used to remove inconsistent events, as shown in figure 3.2(a).

PPAC detectors

As described in reference [72], the PPAC detectors use the delay-line read-out method. The signal induced by the passage of a particle is split and collected at both ends of the delay-line, giving two timing signals T_1 and T_2 . The sum of the delay times, $T_{sum} = T_1 + T_2$ is constant and does not depend on the position of the incident particle. Inconsistent events like events caused by δ -rays can be removed as their T_{sum} value is different from the T_{sum} value of normal events, as shown in figure 3.2(b).

Correlation between ΔE_{IC} and the signal of the plastic scintillation counters

The correlation between the energy loss in the ionization chamber and the charge-integrated signal in the plastic scintillator counter in F7 can also be used for rejecting background events. Such a correlation is shown in figure 3.2(c), where we can see pileup events in the ionization chamber.

Charge changes in the F5 degrader

If there is a change of the charge state in the F5 degrader, the equation 3.8 is not valid anymore and the β_{35} and β_{57} values are not correctly reconstructed. In order to avoid such events, the correlation between $B\rho_{35}$ and $B\rho_{57}$ is checked. In the degrader, when

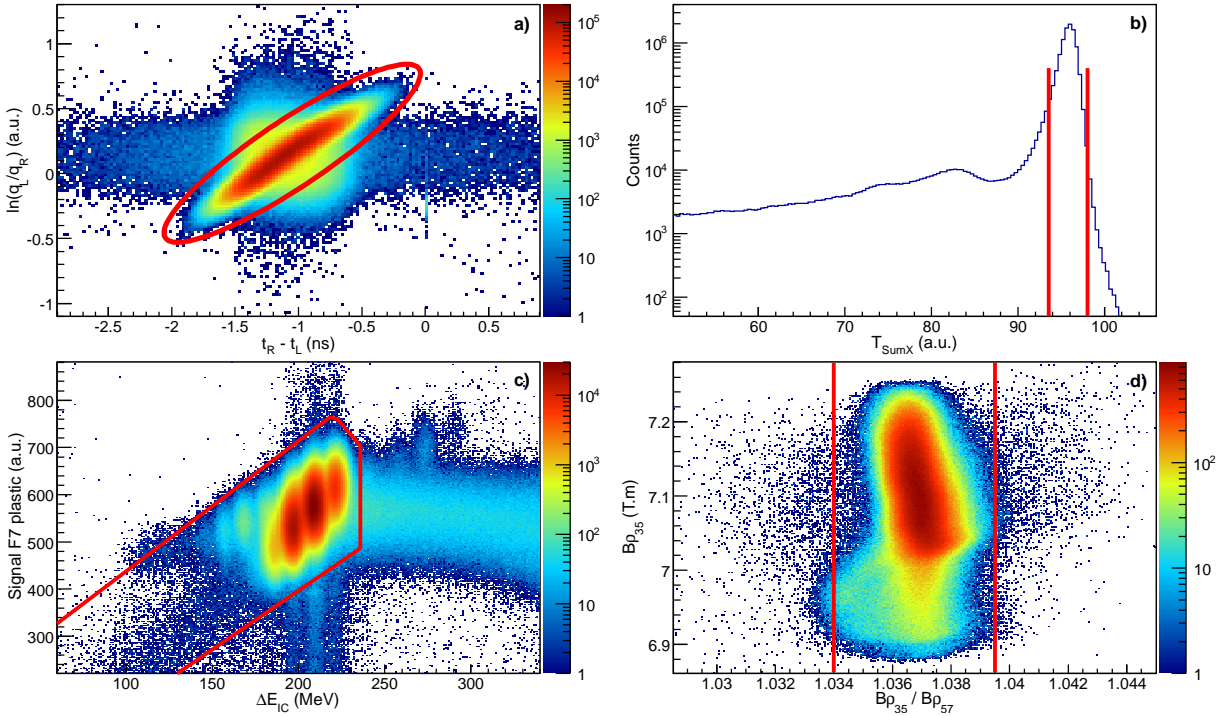


Figure 3.2 – Background removal techniques for the particle identification. (a) Removal of inconsistent events in the F3 plastic scintillation counter. (b) T_{sum} peak selection in the F3 PPAC detector, $\pm 3\sigma$. (c) Charge-integrated signal in the F7 plastic scintillator counter versus energy loss in the ionization chamber. The tail on the right part corresponds to pileup events. (d) Diagram of $B\rho_{35}$ versus $B\rho_{35}/B\rho_{57}$.

there is no charge change, the particle $B\rho$ is modified only by a decrease of the velocity. For a given isotope, we therefore expect the ratio of $B\rho$ before and after the degrader to be constant. Inconsistent events having different ratio can be removed. A diagram of $B\rho_{35}$ versus $B\rho_{35}/B\rho_{57}$ for ^{80}Zn is shown in figure 3.2(d) as an example.

Final identification diagram and A/Q resolution

The Z versus A/Q identification diagrams for BigRIPS before and after background reduction are shown in figure 3.3. Although the background reduction is very important in some regions, there is only a decrease of 7% of the statistics in the part corresponding to ^{80}Zn .

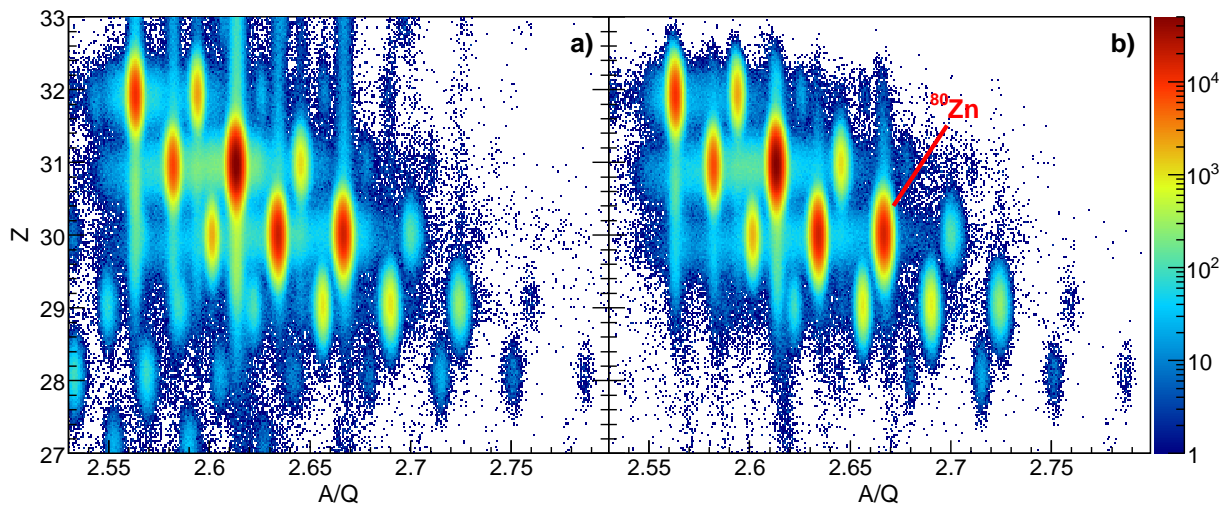


Figure 3.3 – Particle identification in BigRIPS, before (a) and after (b) background reduction.

A projection in A/Q is done for the zinc isotopes and shown in figure 3.4. For ^{80}Zn , we find a A/Q sigma resolution of 0.073(1)%, good enough to clearly separate it from other isotopes.

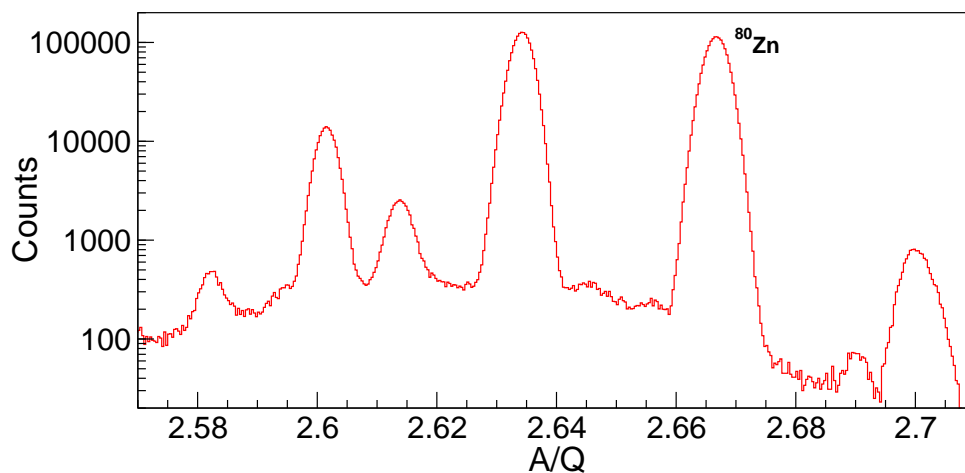


Figure 3.4 – A/Q projection for zinc isotopes in BigRIPS.

3.1.4 Identification in ZeroDegree

The particle identification in the ZeroDegree spectrometer is done between F8 and F11, in the same way than for BigRIPS. But this time, corrections have to be applied for a better isotope separation, i.e. to reach a sufficient A/Q resolution.

A/Q corrections

Empirical corrections are made to improve the A/Q resolution, following the method explained in reference [70]. This method is equivalent to an adjustment of the transfer matrix elements in equation 3.1: if the trajectory is correctly reconstructed, the A/Q value of an isotope should not depend on its position nor on the angle of its trajectory.

The applied corrections focus on the copper isotopes, in particular ^{79}Cu . In a first phase, we check the dependence of A/Q with the x -position in the F9 focal plane (called F9X), shown in figure 3.5(a). This dependence is reduced by applying corrections in F9X up to the third order, as shown in figure 3.5(b). In this case, we have the following correction: $(A/Q)_{corr.} = A/Q - 0.00000045 \times (F9X)^2 + 0.000000004 \times (F9X + 10)^3$.

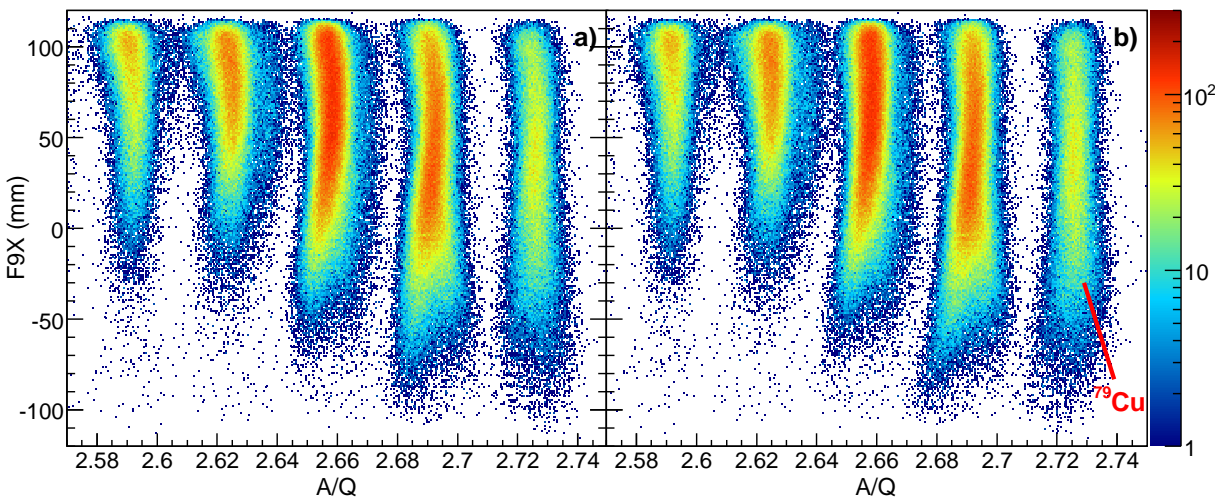


Figure 3.5 – (a) F9X dependence of A/Q for the copper isotopes. (b) Reduction of this dependence after corrections up to the third order in F9X.

This procedure is also applied to the F9 trajectory angle, as well as to the position and angle in the F11 focal plane. The Z versus A/Q identification diagrams for ZeroDegree before and after optical corrections are shown in figure 3.6.

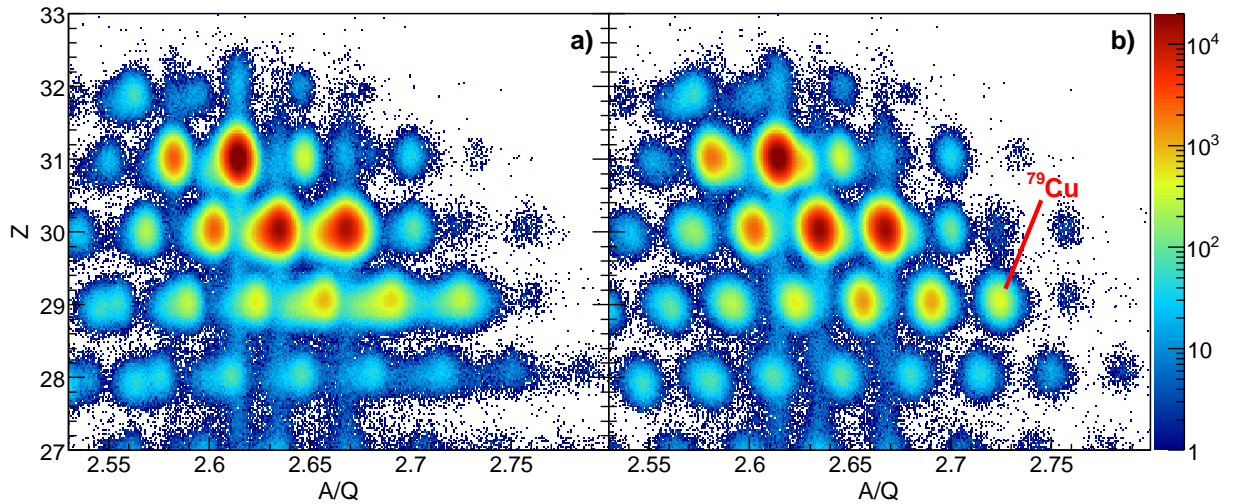


Figure 3.6 – ZeroDegree particle identification diagrams, before (a) and after (b) corrections in A/Q . The background removal methods have been applied on both diagrams.

A/Q resolution

The projection in A/Q is done for the copper isotopes before and after corrections, and is shown in figure 3.7. For ^{79}Cu , we find a A/Q sigma resolution of 0.134(1)% after corrections, sufficient to separate it from other isotopes.

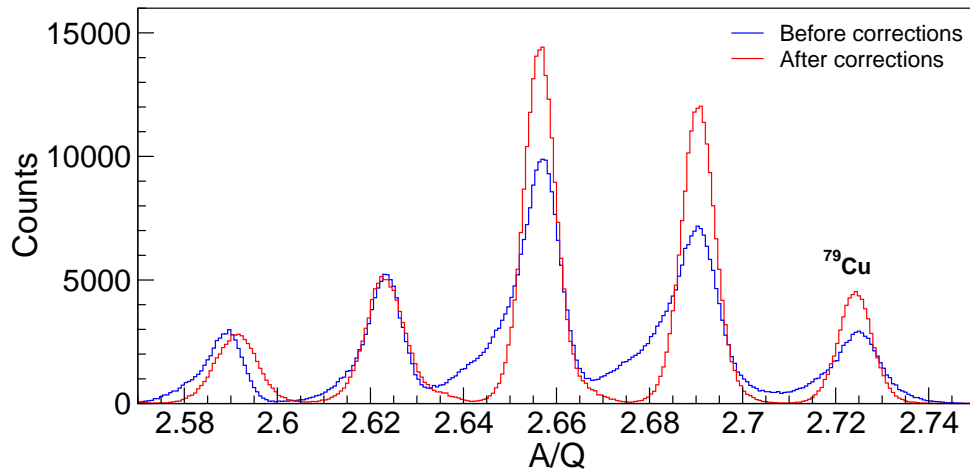


Figure 3.7 – A/Q projection for copper isotopes before (blue) and after (red) optical projections. The corrections have been optimized on ^{79}Cu , inducing a shift for some other isotopes like ^{75}Cu , on the left of the figure.

We can now select the reaction channel of interest by applying a cut on ^{80}Zn in BigRIPS and on ^{79}Cu in ZeroDegree.

3.2 MINOS calibration

The next analysis step is the reconstruction of the interaction vertex in the MINOS target. The principle of the tracking algorithm used is briefly described here, as well as the method for determining the drift velocity of the electrons in the TPC along the experiment.

3.2.1 Tracking algorithm

When a proton passes through the TPC, it ionizes the atoms of the gas and the ionization electrons drift towards the anode following straight lines, due to the applied electric field. The signals recorded from each pad of the anode allow the reconstruction of the proton trajectory thanks to a tracking algorithm. This algorithm was part of the PhD work of C. Santamaria (CEA, France) [82]. It works on an event by event basis and is made of four main steps: (i) identification of tracks in the (x, y) anode-plane, (ii) determination of the z -coordinate along the TPC associated to each fired pad, (iii) track filtering and (iv) interaction-vertex reconstruction.

(i) In the first step, the x and y coordinates of the pads that received a signal above a given threshold are collected. A modified Hough transform [83], whose principle is described in figure 3.8, is applied to all (x_{pad}, y_{pad}) points. This transform is used to

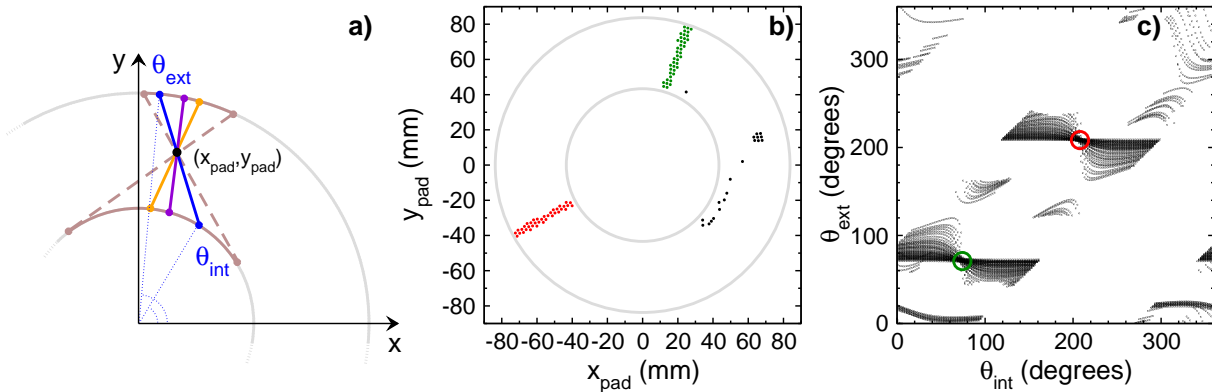


Figure 3.8 – Example of a modified Hough transform for an event with two tracks in the TPC. (a) Principle of the modified Hough transform. All the possible tracks passing through each (x_{pad}, y_{pad}) point (like the blue, orange and violet tracks) are determined by a set of $(\theta_{int}, \theta_{ext})$ parameters. The range of θ_{int} and θ_{ext} is in brown, it delimits the tracks crossing the inner and outer cylinders of the TPC. (b) The two tracks (red and green) and some background (black) in the (x, y) plane. (c) The same event in the $(\theta_{int}, \theta_{ext})$ Hough space. A point and a straight line in the (x, y) space correspond respectively to a line and a point in the Hough space. The two tracks correspond to the intersection of most of the lines (red and green circles) while noise in the (x, y) space is represented by uncorrelated $(\theta_{int}, \theta_{ext})$ lines.

recognize straight lines in an image and allow us both to identify the projection of the tracks on the anode and to reject background events. Each of these 2D-tracks must be formed by least 10 fired pads, including more than 2 of them in the four first inner rings, otherwise it is rejected and considered as noise.

(ii) In the second step, the electronic signal of each pad that is part of the 2D-tracks found in the first step is fitted by the following formula [74]:

$$q(t) = q_a \exp\left(-3 \frac{t-t_{pad}}{\tau}\right) \sin\left(\frac{t-t_{pad}}{\tau}\right) \left(\frac{t-t_{pad}}{\tau}\right)^3 + q_b \quad (3.10)$$

with q_a the signal amplitude, t_{pad} the pad trigger time, τ the shaping time and q_b the signal baseline. t_{pad} is relative to the acquisition trigger time and is delayed by a time t_0 that depends on the acquisition electronics. It can be converted in a drift distance:

$$z_{pad} = (t_{pad} - t_0) v_{drift} \quad (3.11)$$

with v_{drift} the drift velocity of the electrons in the gas, determined in the next section. z_{pad} is the coordinate along the beam axis of the place where the ionization electrons that reached the pad were created.

(iii) This step allows to discard wrong tracks created by δ -electrons. Standard Hough transforms are applied in the (xy) , (xz) and (yz) planes for each identified tracks. A track is rejected if less than 15 of the 18 anode rings were fired. The latter condition does not apply in case of low scattering-angle protons, which cross the cathode, as they do not pass through all the rings.

(iv) In the last step, the final tracks are fitted by straight lines. The interaction vertex is taken as the middle of the minimum distance between them. If only one proton trajectory is reconstructed, the beam trajectory is used. The tracking of the beam is done by using the PPAC detectors in F8 and the DSSSD.

3.2.2 Drift velocity

The drift velocity of the electrons in the TPC is affected by the rate of impurities in the gas, which is not constant. Therefore, the drift velocity has to be monitored along the experiment. For a given run, we plot the measured trigger times t_{pad} of every pad and for all the events, with the condition to have less than ten pads hit per ring in order to reduce background events. This gives the drift-time distribution shown in figure 3.9(a).

Electron ionizations that happen near the Micromegas have a drift time equal to zero, while the maximum drift time corresponds to an electron that went across the whole 300-mm TPC. Therefore, the minimum trigger time t_0 , already mentioned in equation 3.11, depends only on the acquisition electronics and is constant over the experiment. It is defined by the nub at the beginning of the rise of the drift-time distribution. The

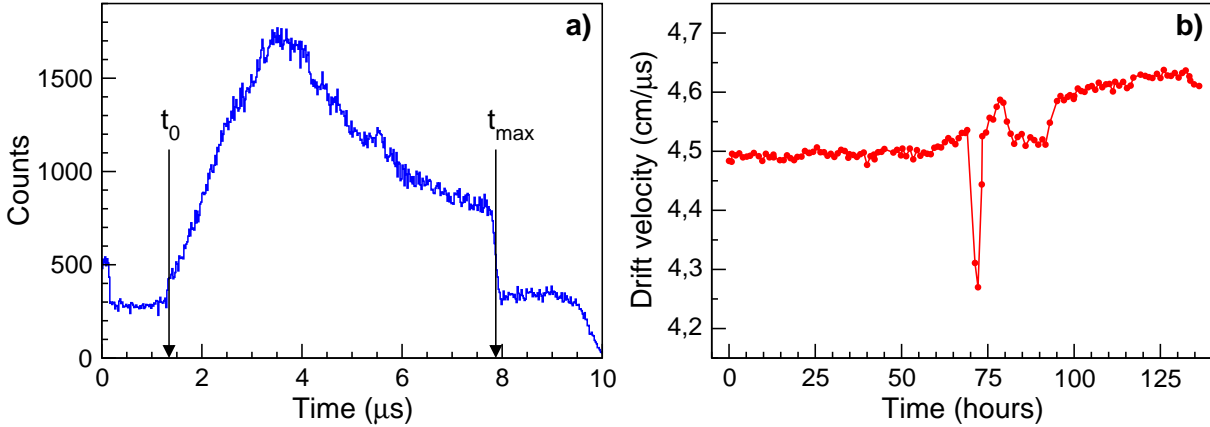


Figure 3.9 – (a) Drift-time distribution in the MINOS TPC for a run of one hour, with the t_0 and t_{max} values used for calculating the drift velocity. (b) Evolution of the drift velocity over time during the experiment, each point corresponding to one run. The uncertainty is of the order of the hundredth of $\text{cm}/\mu\text{s}$. The drop of the drift velocity after 70 hours corresponds to a change of the gas bottle: the impurity rate increased for a moment because of this change, slowing down the electrons.

maximum drift time t_{max} corresponds to the midpoint of the sharp drop of the distribution and is determined by fitting the slope with a Fermi function:

$$f(t) = \frac{p_0}{\exp[(t-t_{max})/p_1] + 1} + p_2 \quad (3.12)$$

This process is applied to find t_{max} for each run. The corresponding drift velocity is simply calculated as follow:

$$v_{drift} = \frac{L_{TPC}}{t_{max} - t_0} \quad (3.13)$$

and its evolution over the experiment is shown in figure 3.9(b). One can note that there is a drop of the drift velocity after 70 hours: this corresponds to a change of the gas bottle that increased the rate of impurities in the TPC, slowing down the electrons. Then, the gas flow has been adjusted to come back to a stable drift velocity.

Once the drift velocity is determined, the interaction vertex can be reconstructed with the tracking algorithm described in the previous section. The coordinate of the vertex along the beam axis z_{vertex} , needed for the Doppler correction, can also be used to check the consistency of the reconstructed target length over the experiment. An example of a z_{vertex} distribution is shown in figure 3.10(a). Each side of the distribution can be fitted by a Fermi function in order to find the midpoint of the slope, corresponding to the edges of the target. The difference between z_{max} and z_{min} gives the reconstructed target length, whose evolution over time is shown in figure 3.10(b).

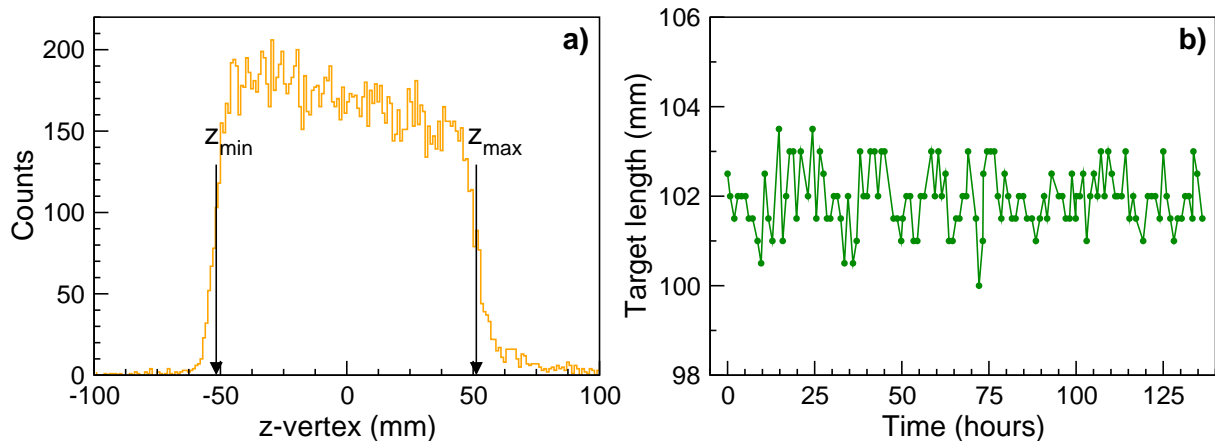


Figure 3.10 – (a) Example of a z_{vertex} distribution with z_{min} and z_{max} used for reconstructing the target length. (b) Reconstructed target length over the experiment. For each point, the uncertainty is of the order of 1 mm.

For most of the runs, the reconstructed target length is found in the interval 102 ± 1 mm, which is consistent with the 100(1)-mm value measured for the empty target plus the target window deflection of two to three millimeters induced by the pressure when the target is filled. At most, the reconstructed target length differs by 2 mm from this 102-mm central value, but this is below the 5-mm FWHM vertex resolution mentioned in section 2.2.2.

3.3 DALI2 calibration

Energy and time calibrations of DALI2 are needed, as we use both information. Once the crystals are calibrated, the add-back procedure is applied in order to increase the efficiency of the array.

3.3.1 Energy calibration

The 186 crystals of DALI2 are calibrated in energy by using three reference γ -ray sources, for a total of five γ -ray transitions: one transition at 662 keV from ^{137}Cs , two transitions at 898 and 1836 keV from ^{88}Y and two transitions at 1173 and 1332 keV from ^{60}Co . The sources were placed at the end of the MINOS pipe. Seven sets of calibration runs were performed, one per day from the beginning to the end of the experiment. Each set comprises a run of at least thirty minutes per source.

The gain of the ADC modules was adjusted to reach energies up to around 8 MeV and the energy information was distributed over 4096 channels. For every crystal, each photopeak of the calibration transitions is fitted with a Gaussian function and an exponential background. The five centroids obtained are then associated to their corresponding energy and a linear fit is performed to determine the calibration relation between ADC channel and energy. An example of the procedure is shown in figure 3.11.

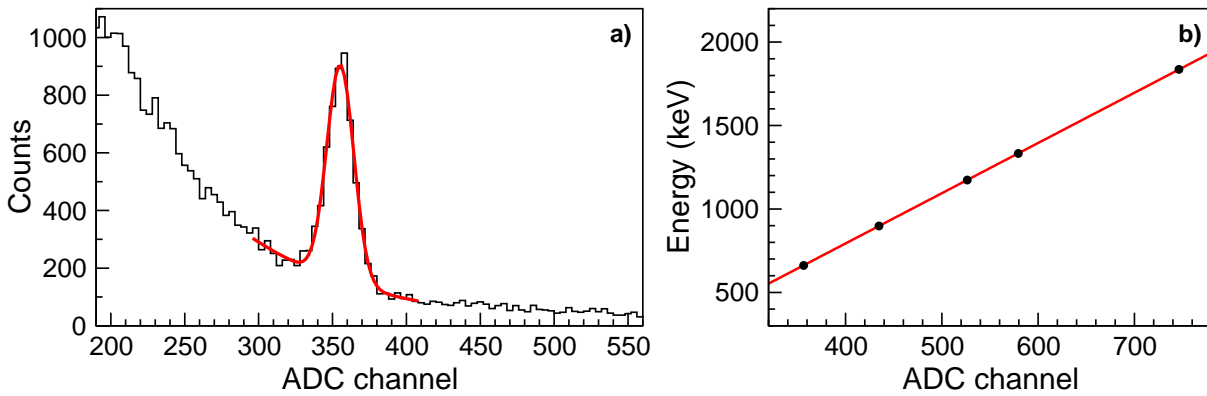


Figure 3.11 – DALI2 energy-calibration procedure. (a) Raw spectrum of ^{137}Cs after a calibration run, whose photopeak is fitted with a Gaussian function and an exponential background. (b) Linear relation between ADC channel and energy obtained from the five calibration points.

Once the energy calibration is applied to all crystals, the photopeaks of the calibrated spectra are fitted with a Gaussian function and an exponential background. A verification of the quality of the calibration is done by plotting the difference between the measured energy of the five transitions and the value from literature, i.e. the residuals, as shown in figure 3.12(a). For most of the crystals, this difference is lower than 1%. A projection of the energy difference over all crystals is done for estimating the deviation of its distribution. From figure 3.12(b), we find that more than 80% of the energy differences are within ± 5 keV. The latter value is then used as an overall calibration error for the measured energies of the experiment. A last check of the calibration is done using the 2734-keV transition from the ^{88}Y source: it is not possible to fit it for each crystal because its intensity is too low, but when summing all crystals after calibration, a fit can be performed and we find an energy of 2732(3) keV, which is in good agreement with the

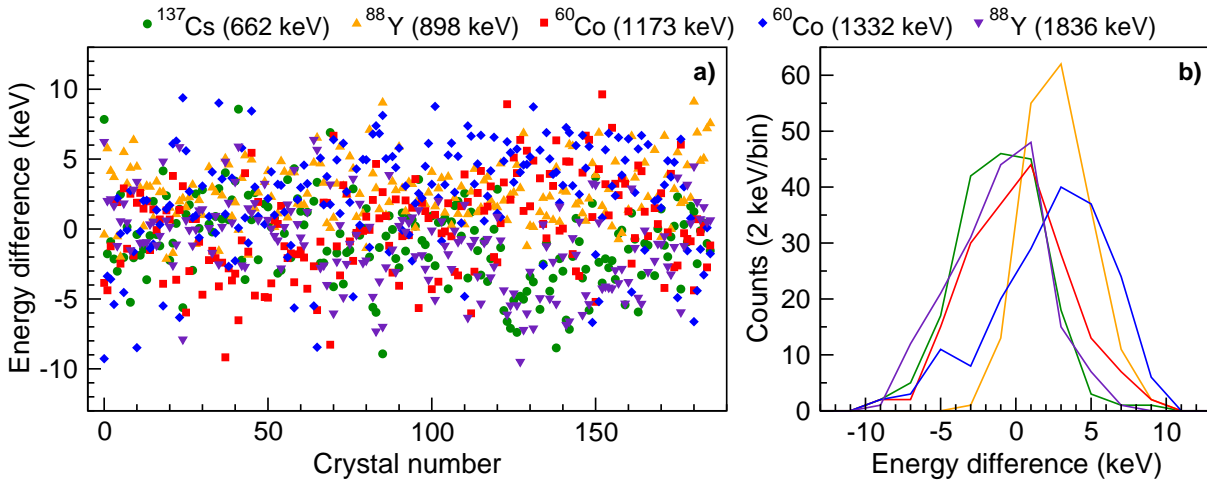


Figure 3.12 – (a) Difference between measured and literature energies of the calibration transitions for each crystal. The uncertainty of each point is of the order of 1 keV. (b) Projection of the energy difference over all crystals.

tabulated value. Finally, five crystals (31, 48, 63, 132 and 167) have been removed from the analysis because either they had a strong non-linear behavior or the gain drift was too important.

The energy resolution of the photopeaks for each crystal is shown in figure 3.13(a). The first 20 crystals have the worst resolution and have been placed backward, where the Doppler shift reduces the energy in the laboratory frame. Crystals 125 to 144 also have a worse resolution than the others. They are located on the outer part of the forward wall and are shadowed by other crystals. Therefore, they receive much less γ -rays and their contribution to the overall resolution is small. The overall σ_E/E resolution of the DALI2 array is found to be 3.3% and 2.8% at 898 and 1173 keV, respectively, in good agreement with the expected value of 3.0% at 1 MeV [77].

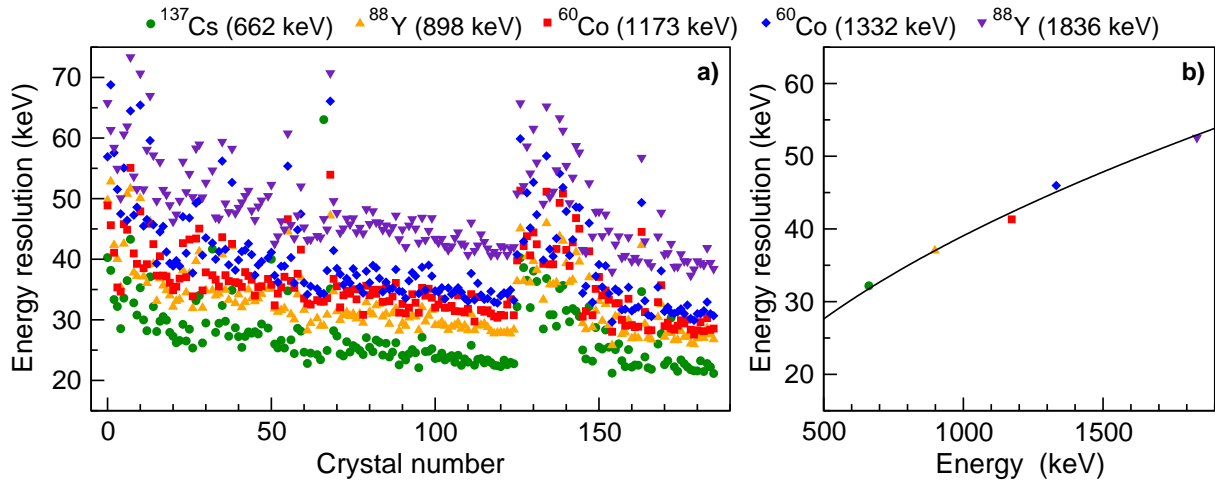


Figure 3.13 – (a) Energy resolution (σ) of each crystal for the calibration transitions. The uncertainty of each point is below 2 keV. (b) σ resolution as a function of the energy for one crystal, with a fit using equation 3.14.

As the resolution is proportional to the square-root of the energy [80], the evolution of the resolution as function of the energy, shown in figure 3.13(b), is fitted by the following function:

$$\sigma_E = k \sqrt{E} \quad (3.14)$$

and the k -value of each crystal will be used as an input in the simulation described in section 3.5.

3.3.2 Time alignment

The time information given by DALI2 can be used to remove γ rays uncorrelated in time from the beam. When a nucleus passes through the F7 plastic scintillator, the acquisition starts to record the information from the DALI2 crystals. The nuclei need a time $t \pm \Delta t$ to reach the target, Δt depending of $\Delta\beta$ between the fastest and the slowest nuclei. If a γ ray is detected before $t - \Delta t$ or after $t + \Delta t$, it is rejected. t is the

difference between the starting time given by the F7 plastic scintillator and the stopping time from the crystal hit by a γ -ray, with an additional delay that depends on the crystal electronics. Therefore, it is necessary to align all crystals. In figure 3.14(a) is shown a time spectrum obtained from one crystal, taking into account γ energies above 200 keV. This spectrum is fitted by a Landau function in order to determine the centroid. Then, by convention, the mean value of each crystal is set to zero by applying an offset. Once this alignment is done for the whole array, we can plot the time information versus the energy of the detected γ -rays, as shown in figure 3.14(b). This allows us to check that there is no energy dependence of the time. Such a dependence can be observed below 200 keV, this must be an electronic effect but not a physical one as there is a sharp cutoff at 200 keV. A time gate $\pm 3\sigma_t$, with σ_t the time resolution given below, is then applied to remove uncorrelated events.

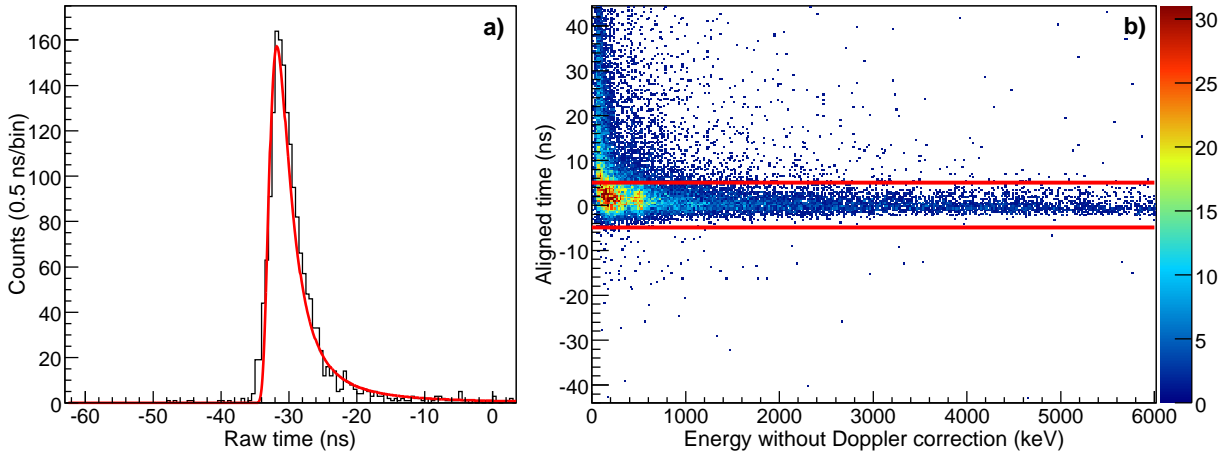


Figure 3.14 – DALI2 time alignment. (a) Time spectrum of one crystal for energies above 200 keV, fitted with a Landau function in order to determine the centroid. (b) DALI2 time after alignment as a function of the energy. A time cut in the interval from -5 ns to +5 ns, i.e. $\pm 3\sigma_t$, is applied to remove uncorrelated events.

Although the time spectrum shown in figure 3.14(a) is not Gaussian, we can estimate the time distribution width by fitting the left part of the distribution with a Gaussian. We find $\sigma_t \sim 1.7$ ns. This width depends on Δt , mentioned above, and on the time resolutions of the crystal considered and the F7 plastic scintillator. The β distribution of the incoming nuclei has a width $\sigma_{\beta_{in}} \sim 0.004$ centered on $\beta = 0.63$ and the flight path between the F7 plastic scintillator and the target is 12 m. This corresponds to a time width $\sigma_t^{\beta_{in}} \sim 0.8$ ns. The time resolution of the plastic scintillator, a few tens of picoseconds [70], can be neglected. The time resolution of the crystal can therefore be estimated as:

$$\sigma_t^{crystal} = \sqrt{(\sigma_t)^2 - (\sigma_t^{\beta_{in}})^2} \sim 1.5 \text{ ns} \quad (3.15)$$

which is of course only an order of magnitude as it may vary from one crystal to another. Such a value is in agreement with the time resolution of a NaI(Tl) crystal, of the order of one to a few nanoseconds, found in the literature [80].

3.3.3 Add-back

In the range of energies we are looking at, from a few hundreds of keV up to some MeV, Compton scattering is the dominant interaction of γ -rays with the detector. As a consequence, the crystals will often receive only a part of the γ -ray energy. If a γ ray deposits its energy in several crystals close enough to each other, the energies will be summed to reconstruct the initial energy: this is the add-back procedure.

The mean interaction point in each crystal has been determined by simulations of DALI2, described in section 3.5. When a crystal is fired by a γ ray, all other crystals whose mean interaction point is distant by less than 15 cm are taken into account for the add-back. This maximum distance has been chosen as a compromise between gain of photopeak efficiency and inclusion of crystals hit by another γ ray. The first interaction is assumed to take place in the crystal receiving the largest part of the reconstructed energy.

Below 400 keV, NaI crystals have a non-linear behavior [84]. The effect of the non-linearity on the add-back has been studied in reference [85] and was evaluated to induce a shift up to 5 keV on the reconstructed photopeak. In our case, the shift should be lower as we limit the add-back for energies above 200 keV, to exclude the important low-energy background described in section 3.6. This error due to non-linearity is neglected because the peaks that are well resolved can be fitted without add-back, and statistical error dominates in the case of high-energy peaks, as we discuss in section 3.5.3.

The difference of photopeak efficiencies with and without add-back is discussed in section 3.5.2.

3.4 Doppler correction

The energies seen by DALI2 are Doppler-shifted due to the velocity of the nuclei. This effect is corrected using MINOS tracking information.

3.4.1 Doppler effect

When light is emitted by a moving source, its wavelength in the laboratory frame is subjected to a shift that depends on the source velocity and the emission angle. In our case, the nuclei are fast ($\beta \sim 0.6$) and the energy measured by DALI2 are strongly Doppler-shifted. A Doppler correction is applied as follow:

$$E_0 = E_\gamma \frac{1 - \beta \cos \theta}{\sqrt{1 - \beta^2}} \quad (3.16)$$

with E_0 the corrected energy (i.e. the energy in the nucleus frame), E_γ the energy measured, β the velocity of the nucleus when emitting the γ ray and θ the emission angle in the laboratory frame.

As there is no information about the half-lives of the emitting levels, all decays are considered to be prompt: the emission point is taken as the interaction vertex, reconstructed by MINOS, and β is taken at the velocity β_v at this vertex. Therefore, the direction of the γ -ray emission corresponds to the line between the interaction vertex and the mean interaction point of the crystal hit. θ is the angle between this direction and the direction of the emitting nucleus, the latter being taken as the beam direction because the residue angle from the reaction is neglected. β_v is calculated using the following linear interpolation:

$$\beta_v = \beta_{in} - \left(\frac{z_{vertex}}{L_{target}} + 0.5 \right) (\beta_{in} - \beta_{out}) \quad (3.17)$$

with β_{in} and β_{out} the velocities at the entrance and exit of the target, respectively, L_{target} the target length and z_{vertex} going from $-L_{target}/2$ to $L_{target}/2$. As shown in figure 3.15, we calculate a difference of less than 1% between this linear interpolation and β_v estimated from energy-loss calculations performed with LISE++ [86].

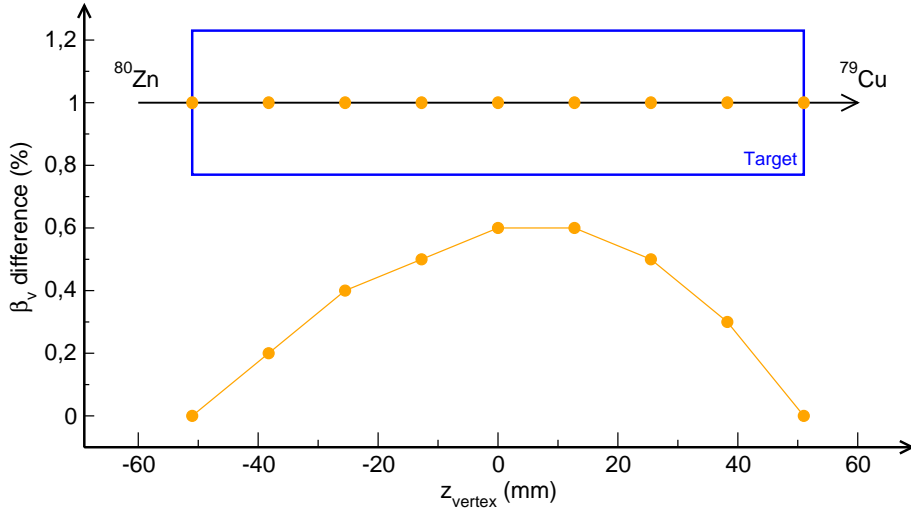


Figure 3.15 – Differences in β_v between the linear interpolation from equation 3.17 and the energy-loss calculations, depending on z_{vertex} . The change of atomic number Z at the reaction vertex is taken into account in the calculations.

A non-zero half-life of the emitting levels would affect both the emission angle and the velocity, as the produced nucleus travels before emitting a γ ray, inducing a bias in the correction. Such an effect on the corrected energy is discussed in sections 3.5.2.

3.4.2 β corrections

As seen in equation 3.17, we need the velocities of the nuclei at the entrance and exit of the target, β_{in} and β_{out} , in order to determine β_v for the Doppler correction. In the experiment, we only measure β_{BR} in BigRIPS and β_{ZD} in ZeroDegree, and so we have to take into account the extra materials before and after the target. β_{BR} corresponds to the velocity after the F5 degrader and is higher than β_{in} because between the degrader

and the target, the nuclei pass for example through the DSSSD and the entrance window of the target. β_{ZD} corresponds to the velocity at the D7 dipole and is lower than β_{out} as there are materials between the target and the D7 dipole, such as the exit window of the target.

The corrections on the β values are estimated using LISE++ [86]. First, we take the mean value of the β_{BR} distribution. Then we calculate the energy loss of a ^{80}Zn nucleus with a velocity β_{BR}^{Mean} in the extra materials before the target. This gives $\beta_{in}^{Calc.}$. Then, the energy loss of a ^{80}Zn nucleus with a velocity $\beta_{in}^{Calc.}$ in half the liquid-hydrogen target is calculated, giving $\beta_{middle}^{Calc.}$. We use the latter value for the velocity of a ^{79}Cu nucleus of which we compute the energy loss in the other half of the liquid-hydrogen target. This time, we obtain $\beta_{out}^{Calc.}$. Finally, β_{in} and β_{out} are calculated as follow:

$$\beta_{in} = \beta_{BR} - \beta_{BR}^{Mean} + \beta_{in}^{Calc.} < \beta_{BR} \quad (3.18)$$

$$\beta_{out} = \beta_{ZD} - \beta_{ZD}^{Mean} + \beta_{out}^{Calc.} > \beta_{ZD} \quad (3.19)$$

which is basically a shift of the experimental β_{BR} and β_{ZD} distributions.

We verified the consistency of the energy-loss calculation: the final velocity calculated for a nucleus with an initial velocity β_{BR} after passing through the extra materials and the target must correspond to the measured β_{ZD} . A run without target was performed and used to check the energy loss in the extra materials only. The result of this verification is shown in table 3.1. In all cases, the difference is below 0.2%, lower than the error due the linear extrapolation of β_v , indicating that both target and material energy-losses are well reproduced.

In BR	In ZD	Target	$\beta_{ZD}^{Meas.}$	$\beta_{ZD}^{Calc.}$	$\Delta\beta$
^{80}Zn	^{80}Zn	no	0.6148	0.6158	0.16%
^{79}Cu	^{79}Cu	no	0.6085	0.6096	0.18%
^{80}Zn	^{80}Zn	yes	0.5517	0.5521	0.07%
^{79}Cu	^{79}Cu	yes	0.5462	0.5453	- 0.16%
^{80}Zn	^{79}Cu	yes	0.5484	0.5487	0.05%

Table 3.1 – Measured and calculated values of β_{ZD} for different reaction channels, with or without the target. $\Delta\beta = (\beta_{ZD}^{Calc.} - \beta_{ZD}^{Meas.})/\beta_{ZD}^{Meas.}$ is the difference in percent.

Once this verification is done, we can extract $\beta_{in}^{Calc.}$ and $\beta_{out}^{Calc.}$. The measured and computed β values are given in table 3.2. The mean value of the β_{BR} and β_{ZD} distributions are shifted by -1.8% and 1.5%, respectively.

β_{BR}^{Mean} (^{80}Zn)	$\beta_{in}^{Calc.}$ (^{80}Zn)	$\beta_{out}^{Calc.}$ (^{79}Cu)	β_{ZD}^{Mean} (^{79}Cu)
0.6342	0.6228	0.5566	0.5484

Table 3.2 – Calculated velocities at the entrance and exit of the target compared to the values measured in BigRIPS and ZeroDegree.

3.5 Geant4 simulations

DALI2 simulations using Geant4 [78] are performed in order to obtain the response functions of the array at different energies. These response functions will be used to fit the γ -ray spectra and extract the intensities of the transitions.

3.5.1 Simulation code

The DALI2 simulation code [87] has been developed by P. Doornenbal (RIKEN, Japan). It takes into account experimental conditions like the geometry of the detector, the target thickness and the beam energy, as well as the lifetime of excited states. These simulations are crucial as they take into account the anisotropy of the γ rays emitted by the moving nuclei, due to the Lorentz boost. The code is divided into two steps.

In the first step, the interaction between the ion beam and the 102-mm thick liquid-hydrogen target is simulated. It calculates the energy loss in the target before (^{80}Zn) and after (^{79}Cu) the knockout reaction, and takes into account the half-life of the excited states before γ -ray emission. The inputs are the beam velocity, taken as $\beta_{in}^{Calc.}$ from table 3.2 with a distribution width corresponding to the experimental one, the energy of the different γ transitions to be simulated and the half-life of the de-exciting state.

The second step simulates the interaction of the γ rays from the first step with the DALI2 crystals. The geometry of DALI2 during the experiment is used. The experimental resolution of each crystal, measured with calibration sources at rest as described in section 3.3.1, is set as an input. The beam pipe is also included in the simulation as it can have an impact on low-energy transitions.

Finally, we perform the analysis of the simulated events exactly like in the treatment of real data, namely: (i) Doppler correction of the γ rays, (ii) add-back procedure and (iii) removal of defective crystals. The final output is the response function of DALI2 for a given simulated transition.

3.5.2 DALI2 energy resolution and efficiency

Once the simulations are performed, we can characterize the DALI2 response in experimental conditions. The shape of the response functions as a function of the energy is shown in figure 3.16(a), assuming emitting levels with a zero half-life. One can note that the photopeak progressively merges with the Compton edge because of the low resolution and that above 2.5 MeV there is no more a clear photopeak even with add-back. In figure 3.16(b) is plotted the σ energy resolution of the array. As regards the efficiency, shown in figure 3.16(c), we can see the clear improvement due to the add-back procedure. For example, there is a gain of more than 50% of photopeak efficiency for a γ ray of 2 MeV.

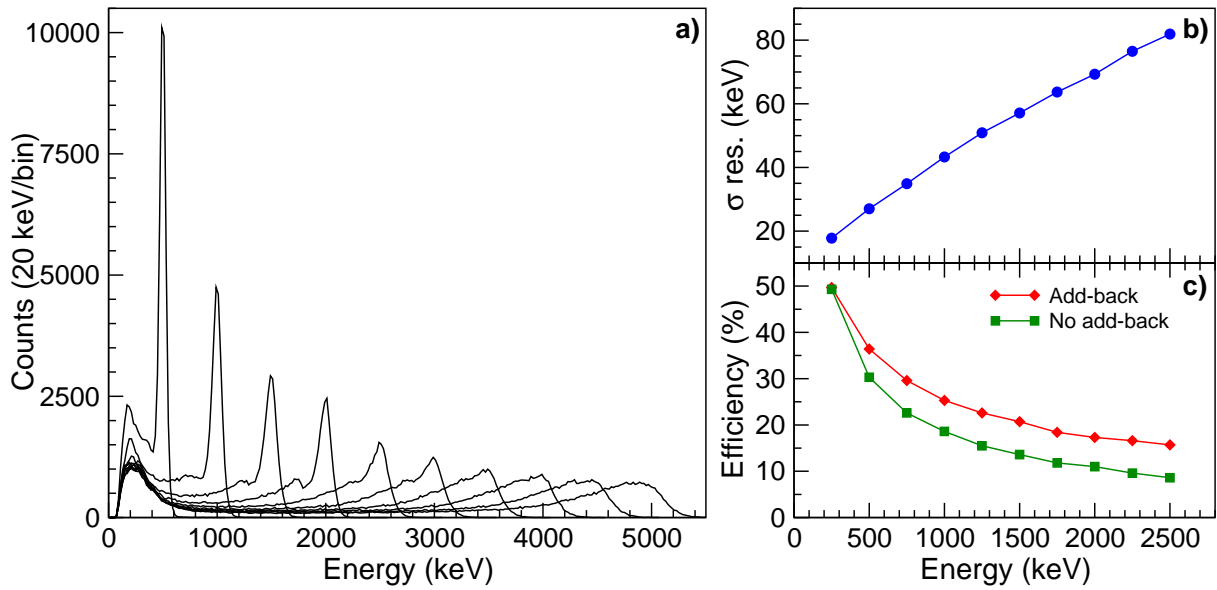


Figure 3.16 – Characteristics of DALI2 for γ rays emitted in experimental conditions. (a) DALI2 response functions with add-back for γ transitions between 0.5 and 5 MeV, by step of 0.5 MeV. (b) Energy resolution (σ) of the photopeaks, with add-back. (c) Efficiency with and without add-back.

The half-life of the emitting levels has an impact on the reconstructed energy as the residue travels before emitting the γ ray while the Doppler correction is applied at the interaction vertex. Considering the geometry of the setup, a half-life of several tens of picoseconds shifts the energy of the transitions towards lower energies by a few percent and also increases the width of the photopeak. The effect of different level half-lives on a γ ray of 1 MeV is shown in figure 3.17.

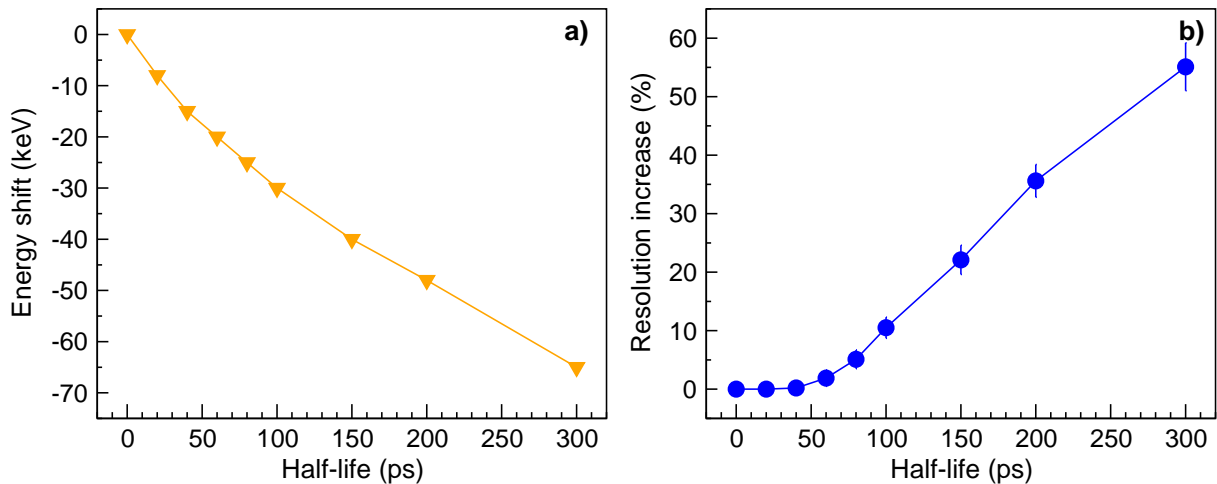


Figure 3.17 – Half-lives effect on a 1-MeV transition. (a) Energy shift of the photopeak. (b) Increase of the photopeak resolution compared to the case of a zero half-life. The resolution starts to increase only above a half-life of 50 ps.

3.5.3 Energy errors

Several sources of errors participate to the deterioration of the energy resolution. Once they are identified, it is possible to evaluate the contribution of each of them thanks to the simulations. From the Doppler-correction formula, given in equation 3.16, we see that there are three parameters that are subject to error measurement: E_γ , β , θ . The error on the corrected energy E_0 due to β and θ are given by

$$\sigma_E^\beta = \frac{\partial E_0}{\partial \beta} \sigma_\beta = E_\gamma \frac{\beta - \cos \theta}{(1 - \beta)^{3/2}} \sigma_\beta = E_0 \frac{\beta - \cos \theta}{(1 - \beta^2)(1 - \beta \cos \theta)} \sigma_\beta \quad (3.20)$$

$$\sigma_E^\theta = \frac{\partial E_0}{\partial \theta} \sigma_\theta = E_\gamma \frac{\beta \sin \theta}{\sqrt{1 - \beta^2}} \sigma_\theta = E_0 \frac{\beta \sin \theta}{(1 - \beta \cos \theta)} \sigma_\theta \quad (3.21)$$

with σ_β and σ_θ the errors on the velocity and the emission angle, respectively.

σ_β contains the resolution on the TOF measurement, i.e. the statistical error on β_{BR} and β_{ZD} , the error on the calculated β_{in} and β_{out} , and the error due to the linear interpolation discussed in section 3.4.1. The latter contribution dominates, as seen by comparing figure 3.15 and table 3.1, and we can estimate that at most $\sigma_\beta \sim 0.004$.

θ being the angle between the residue trajectory and the direction of γ -ray emission, σ_θ depends on the trajectory resolution, the vertex resolution and the error made by taking the average interaction point of each crystal instead of the real interaction point. For solid-target experiments, the average σ_θ is of the order of 3° [77]. In our case, we have a 102-mm thick target with a vertex resolution of 5-mm FWHM, meaning that the average σ_θ should be slightly higher.

A last source of statistical error comes from the intrinsic resolution of the crystal σ_E^{int} . The intrinsic resolution of each crystal has been determined in section 3.3.1, but the average σ_E^{int} of the whole array for a moving source can be determined only with the Geant4 simulations.

The total statistical error on the energy σ_E is the convolution of the three statistical-error sources:

$$\sigma_E = \sqrt{(\sigma_E^\beta)^2 + (\sigma_E^\theta)^2 + (\sigma_E^{int})^2} \quad (3.22)$$

and it should correspond to the energy resolution given in figure 3.16(b), found by fitting the photopeaks simulated in experimental conditions (with the three error sources included). The contribution to the energy resolution of each error source has been simulated for three different γ -ray energies and the results are given in table 3.3. The σ_E from equation 3.22 is compared to the resolution σ_{all} from figure 3.16(b).

One can note that the contribution of σ_E^β is negligible, while σ_E^θ and σ_E^{int} are in competition: up to 1 MeV, the intrinsic resolution dominates, while the angular resolution dominates for higher-energy γ rays. The compatibility of σ_E and σ_{all} simply shows the consistency of the procedure: taking the quadratic sum of each error is equivalent to consider all errors together.

	$E_0 = 500 \text{ keV}$	$E_0 = 1000 \text{ keV}$	$E_0 = 2000 \text{ keV}$
σ_E^β	2.7(1)	5.3(1)	10.3(2)
σ_E^θ	16.2(1)	28.5(6)	53.1(1.2)
σ_E^{int}	21.2(3)	31.0(5)	44.1(1.0)
σ_E	26.8(3)	42.4(8)	69.8(1.6)
σ_{all}	27.0(2)	42.3(4)	69.3(8)

Table 3.3 – Contribution to the total energy resolution of the three statistical error sources: β (σ_E^β), θ (σ_E^θ) and intrinsic (σ_E^{int}) resolutions. All values are given in keV. The energy resolution σ_E calculated from the three error sources is compared to the resolution σ_{all} from figure 3.16(b).

Concerning statistical errors, the error made on the mean value of a peak is given by σ_E/\sqrt{N} , with N the number of counts in the peak. When fitting a spectrum, the error on the mean value σ_E^{fit} can be higher: the fit is based on a statistical method, described in section 4.1.1, taking into account σ_E but also the function used for the fit, the error on N , etc. σ_E^{fit} will be even higher in the case of two peaks close to each other or if there is some background below the peak. Moreover, σ_E , defined as the resolution of the photopeak, is meaningless above 2.5 MeV, and only a fit with response functions can give an estimate of the energy error as it takes into account all statistical error sources at the same time.

Besides σ_E^{fit} , there is the 5-keV source of error σ_E^{cal} coming from the calibration and described in section 3.3.1. σ_E^{fit} and σ_E^{cal} are added quadratically in order to estimate the total error on the energy.

3.6 Two reference cases: $^{78,80}\text{Zn}$

The $^{78,80}\text{Zn}$ isotopes have been produced in different reaction channels during the experiment. Several of their γ transitions are already known [31,32,36] and these transitions are used to benchmark the overall analysis.

The γ -ray spectra of $^{80}\text{Zn}(p,p2n)^{78}\text{Zn}$ and $^{81}\text{Ga}(p,2p)^{80}\text{Zn}$, with and without add-back, are shown in figure 3.18. These channels have been chosen because they have large statistics. On the spectra, an important background can be observed at low energy. It corresponds mainly to atomic background [88]. Among this, there is Bremsstrahlung coming from electrons knocked-out in the collisions between the beam nuclei and the atoms of the target or some material of the beam line nearby the detection setup. There are also X-rays emitted during the rearrangement of electrons in the atoms of the materials after ionization. Of course, this region also contains the Compton continuum of the γ transitions. The add-back technique improves significantly the peak-to-total ratio as it induces a reduction of this continuum and an increase of the photopeak intensities.

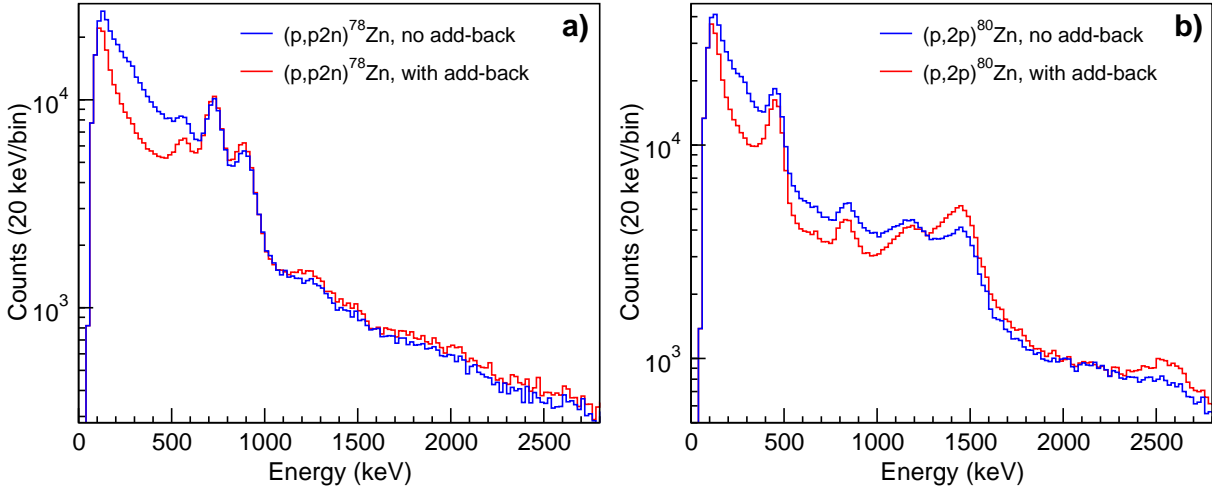


Figure 3.18 – γ -ray spectra of $^{80}\text{Zn}(p,p2n)^{78}\text{Zn}$ (a) and $^{81}\text{Ga}(p,2p)^{80}\text{Zn}$ (b), with and without add-back. The add-back technique improves significantly the signal-to-noise ratio and is necessary to identify the transition around 2.6 MeV in the ^{80}Zn spectrum.

Three peaks in the ^{78}Zn spectrum and five in the ^{80}Zn one have enough statistics to be fitted. The extracted energies are in good agreement within error bars with the literature values, as shown in table 3.4. In the case of ^{80}Zn , the 482-keV transition comes from a level having a half-life of 136^{+92}_{-67} ps [36], inducing a shift towards lower energies: the real emission point is further away from the interaction vertex, the Doppler correction is not correctly applied. From the simulation, such a half-life of 136 ps shifts a 482-keV peak by $-21(1)$ keV, which is compatible with the measured value of $456(5)$ keV. This 482-keV transition decays on top of the 1492-keV level, which itself decays directly to the ground state. Therefore, in the case of a 482-1492 γ -cascade, the 1492-keV transition is also subject to the 136-ps half-life: it is shifted by $-55(2)$ keV according to the simulation. The 1492-keV level can also be populated directly in the reaction, emitting a 1492-keV γ -ray with no lifetime shift. The superposition of both effects explains the measured value of $1460(6)$ keV. Finally, the 729.6-keV transition is emitted by a level having a half-life of $18.0(4)$ ps [89], but the effect is small enough to be within error bars.

As regards the resolution of these transitions, the simulated values are compatible with the measured ones, as shown in table 3.4. For lifetime reasons, the resolution of the 482-keV peak is worse than expected, as an incorrect Doppler correction increases the width of the photopeak. The increase is strong enough in the case of the 1492-keV peak so that it is not Gaussian anymore. Concerning the 1195-keV peak, it is indirectly affected by the lifetime: it is not possible to determine precisely its width as it overlaps with the large 1492-keV one.

Isotope	E_{tab} (keV)	E_{meas} (keV)	σ_{meas} (keV)	σ_{sim} (keV)
^{78}Zn	580(9)	571(5)	33(4)	31.2(5)
	729.6(5)	726(5)	34.8(9)	34.3(5)
	889.9(5)	884(5)	41(3)	39.3(7)
^{80}Zn	482(7)	456(5)*	32.7(6)*	27.0(2)
	841(13)	834(5)	37(2)	37.2(4)
	1195(18)	1199(8)	-*	50.4(6)
	1492(1)	1460(6)*	-*	57.1(5)
	2627(39)	2570(30)	88(10)	84(2)

Table 3.4 – Comparison between tabulated, measured and simulated observables for several transitions of $^{78,80}\text{Zn}$. Values inconsistent due to lifetime effects are marked with a star (*). Tabulated energies are taken from references [31, 32, 36].

3.7 Beam-line transmission

In order to calculate reaction cross sections, it is necessary to determine the overall transmission of the experimental beam line.

3.7.1 Principle

The overall transmission of the beam line is given by

$$T = \varepsilon_{line} \varepsilon_{loss} \varepsilon_{tr} \quad (3.23)$$

with ε_{line} the efficiency of the beam-line detectors, ε_{loss} the losses due to scattering in the MINOS target and ε_{tr} the transmission due to the $B\rho$ selection in the dipoles. Each of these three contributions depends on the considered reaction channel.

The calculation of T requires to know the total number of particles arriving from BigRIPS (F7) in order to compare it with the number of nuclei transmitted until the end of ZeroDegree (F11). Therefore, we use the F7DS (downscaled) trigger described in section 2.5, which records events passing through the F7 plastic, disregarding if they reach the end of the beam line.

We determine the transmission components using the x -position distribution of the isotopes in F5, named F5X, given by the PPAC detectors. The F5 plane is used because it belongs to BigRIPS and is momentum dispersive: looking at F5X allows to determine ε_{tr} , as a $B\rho$ selection is equivalent to a momentum selection.

3.7.2 Efficiency of the beam-line detectors

Before the experiment, a run without the liquid-hydrogen target was performed, with BigRIPS and ZeroDegree having the same central $B\rho$. In this case, we have $\varepsilon_{tr} = 1$ and for a given isotope, the number of particles in ZeroDegree N_{ZD} is simply the number of particles in BigRIPS N_{BR} multiplied by the efficiency of the beam-line detectors:

$$N_{ZD} = N_{BR} \varepsilon_{line} \quad (3.24)$$

The F5X distributions of ^{80}Zn and ^{79}Cu are shown in figure 3.19. In both cases the distribution with an isotope selection in BigRIPS only is compared to the distribution with a selection in both spectrometers. The scaling factor between both distributions gives ε_{line} for the isotope considered. We find $\varepsilon_{line}(^{80}\text{Zn}) = 80.6(5)\%$ and $\varepsilon_{line}(^{79}\text{Cu}) = 78(4)\%$.

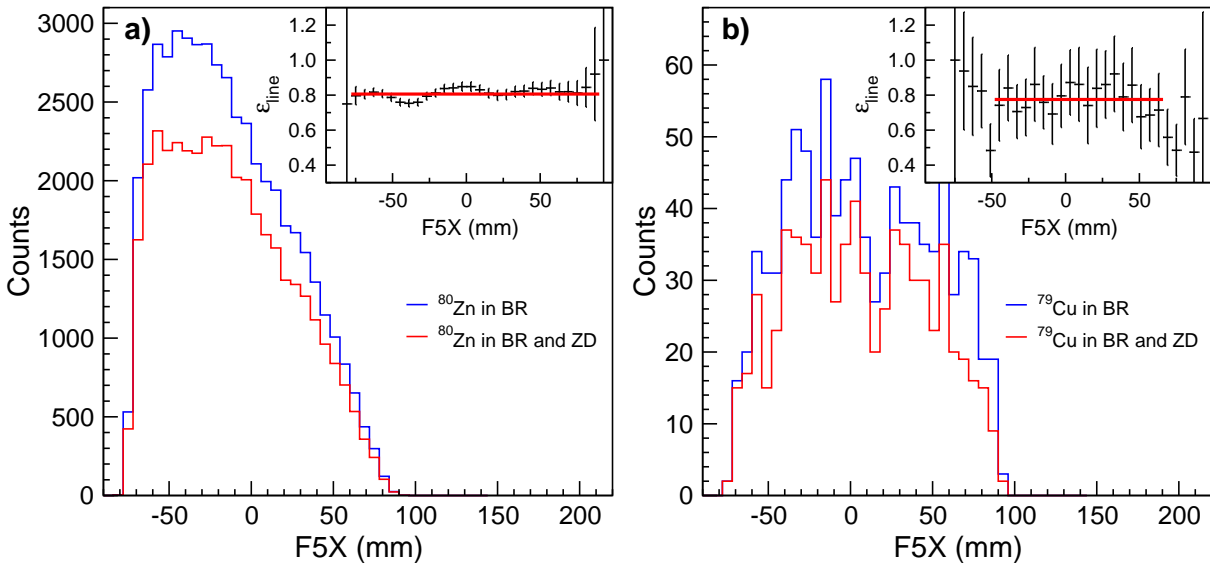


Figure 3.19 – F5X distributions for ^{80}Zn (a) and ^{79}Cu (b) without the liquid-hydrogen target, when the isotope is selected in BigRIPS only (blue) and in both BigRIPS and ZeroDegree (red). The insets show the ratio between the two distributions, which allow to extract ε_{line} by fitting the constant part.

3.7.3 Losses from scattering in the target

When using the physics runs, i.e. with the target, the relation between N_{ZD} and N_{BR} for a given isotope is

$$N_{ZD} = N_{BR} \varepsilon_{line} \varepsilon_{loss} \varepsilon_{tr} \quad (3.25)$$

with ε_{line} calculated above.

The corresponding F5X distributions of ^{80}Zn and ^{79}Cu are shown in figure 3.20. This time, a scale factor would not be enough to overlap both curves. ZeroDegree is centered

on $(A, Z-1)$ compared to BigRIPS and the liquid-hydrogen target induces a momentum spread. If the $B\rho$ of the isotopes varies too much from the central $B\rho$, they are stopped in the dipoles. This is the effect of ε_{tr} , which is not constant over F5X and which explains the cut on the left side of the F5X distributions. As regards ε_{line} and ε_{loss} , they are globally constant over F5X: the momentum spread induced by the target is not important enough for having large variations of the number of nuclei lost due to the beam-line efficiency and the scattering in the target. Therefore, on the right side of the distributions, where $\varepsilon_{tr} = 1$, the scaling factor between them corresponds to $\varepsilon_{line} \varepsilon_{loss}$ for ^{80}Zn . We obtain $\varepsilon_{line} \varepsilon_{loss} (^{80}\text{Zn}) = 60.3(2)\%$.

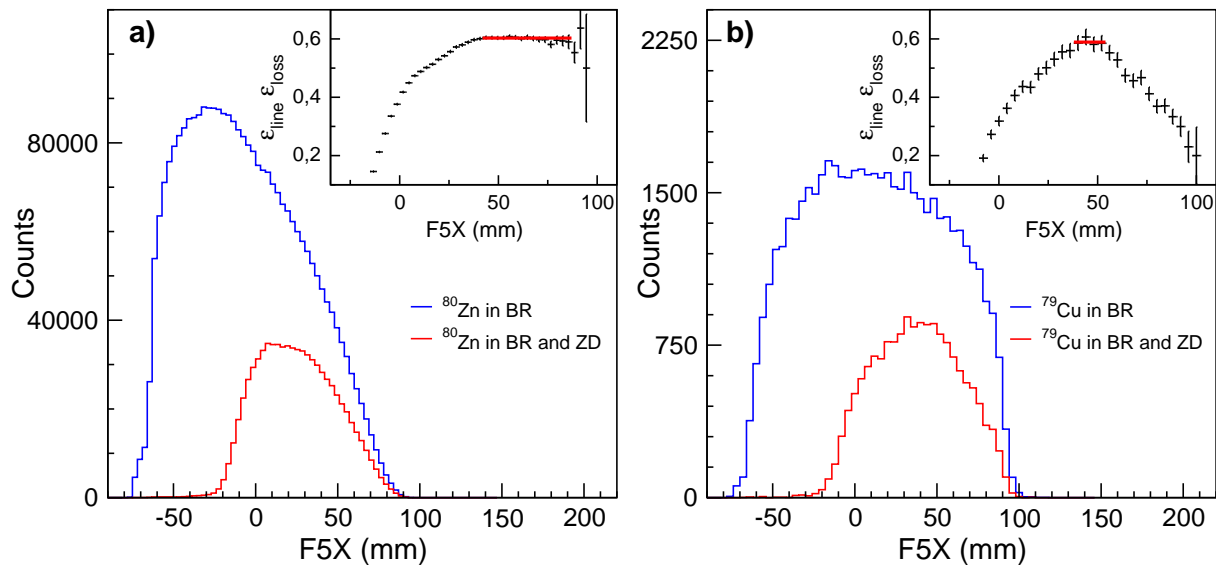


Figure 3.20 – F5X distributions for ^{80}Zn (a) and ^{79}Cu (b) with the liquid-hydrogen target, when the isotope is selected in BigRIPS only (blue) and in both BigRIPS and Zero-Degree (red). The insets show the ratio between the two distributions, which is not constant as the target induces a momentum change and reduces the transmission in the dipoles. $\varepsilon_{line} \varepsilon_{loss}$ can be determined by fitting the constant part of the ratio in the case of ^{80}Zn . For ^{79}Cu , the four maximum values are taken into account.

As regards ^{79}Cu , the effect of $\varepsilon_{tr} < 1$ can be seen on both sides. The origin of this cut is not fully understood but is observed only when the nucleus selected in BigRIPS is more exotic than ^{80}Zn . When selecting ^{79}Cu in ZeroDegree and ^{80}Zn in BigRIPS, this cut on the right disappears. We explain in the next section that this cut is therefore not a critical point for the calculation of cross section. If we take the small part in F5X where the ratio seems constant, for F5X between 38 and 54 mm, we find $\varepsilon_{line} \varepsilon_{loss} (^{79}\text{Cu}) = 58.9(1.6)\%$, which is compatible with the value for ^{80}Zn as expected: $\varepsilon_{line} \varepsilon_{loss}$ does not vary significantly between the different isotopes we produced because they have a high velocity and are close in (A, Z) . From the ε_{line} values found above, we can calculate the losses in the target: $\varepsilon_{loss} (^{80}\text{Zn}) = 74.8(5)\%$ and $\varepsilon_{loss} (^{79}\text{Cu}) = 76(4)\%$.

3.7.4 Number of nuclei

We calculated the ratio between the number of particles in BigRIPS and in Zero-Degree for the same isotope selected in both spectrometers. This ratio was equal to the transmission of the beam line. Now we focus on the reaction of interest, $^{80}\text{Zn}(p,2p)^{79}\text{Cu}$, with ^{80}Zn selected in BigRIPS and ^{79}Cu selected in ZeroDegree. The corresponding F5X distributions are shown in figure 3.21. The ratio between both distributions in the part where $\varepsilon_{tr} = 1$, i.e. where the ratio is constant, is proportional to $\varepsilon_{line} \varepsilon_{loss}$ but also to the reaction cross section. We find:

$$\frac{N_{ZD}(^{79}\text{Cu})}{N_{BR}(^{80}\text{Zn})} = 2.01(7) \times 10^{-3} \quad (3.26)$$

and this value will be used in section 5.4 for the cross section calculation.

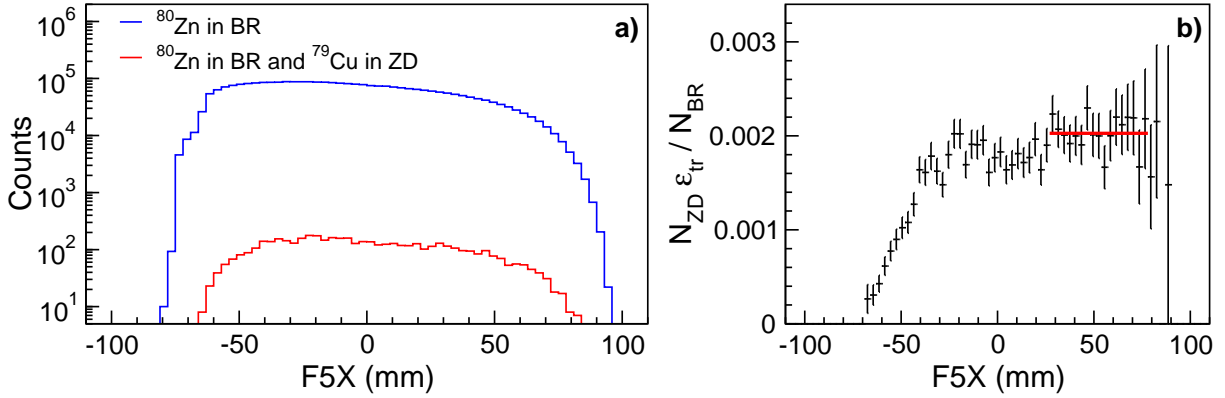


Figure 3.21 – (a) F5X distribution for ^{80}Zn selected in BigRIPS only (blue) and ^{80}Zn selected in BigRIPS plus ^{79}Cu selected in ZeroDegree (red). (b) Ratio between both distributions with a fit in the constant part for determining $N_{ZD}(^{79}\text{Cu})/N_{BR}(^{80}\text{Zn})$.

The cut observed in figure 3.20(b) does not affect this calculation because the $B\rho$ distribution in BigRIPS is that of ^{80}Zn and not of ^{79}Cu . As the effect of ε_{tr} is non-linear, we would see a decrease on the right part of the ratio in figure 3.21(b) if there was a cut. Moreover, as said before, we have $\varepsilon_{tr} = 1$ for F5X from 38 to 54 mm in figure 3.20(b): the same range in F5X in figure 3.21(b) corresponds to the constant part of the fit used for obtaining the ratio in equation 3.26, and using only this part would give the same value but with a larger error bar because there is less statistics: $N_{ZD}(^{79}\text{Cu})/N_{BR}(^{80}\text{Zn}) = 2.02(11) \times 10^{-3}$ in this case.

3.8 Limit of the analysis

By measuring the parallel momentum distribution of the residue after the (p,2p) knockout, one can access to the angular momentum l of the removed proton, i.e. of its orbital [62]. This gives a clue on the spin of the populated states. The total momentum p can be obtained by subtracting the momentum p_v^{out} of the $(A - 1)$ residue to the momentum of the incoming nucleus p_v^{in} at the reaction vertex. Unfortunately, several limitations happen and degrade the resolution of the momentum distribution:

- The energy straggling of the beam in the thick target increases the uncertainty on the velocities;
- The resolution on the reconstructed vertex in the target which also induce an uncertainty on the velocity calculation;
- The absence of residue-angle measurement prevents us from making a projection on the residue trajectory and access to the parallel momentum.

A study of these limitations was performed by C. Santamaria (CEA, France) [82] and the conclusions are that the poor resolution of the experimental momentum distribution does not allow to distinguish between a $l = 0$ and a $l = 3$ theoretical distributions. Moreover, in order to determine the momentum distribution for a given populated state, one must know the branching ratio to this state. We show in section 5.4.2 how large are the errors on the branching ratios in our case, which would make even worse the momentum distributions.

Chapter 4

Procedure for building level schemes

In this chapter, we describe the procedure we established for building level schemes from our data. We first present the method used for fitting the spectra and the different steps of the procedure, before to apply them to a known case, ^{81}Ga , for validation. These steps will be applied to ^{79}Cu in the next chapter.

4.1 General overview

4.1.1 Method of fit

The spectra shown in the following are always fitted in the same way: we use a double-exponential function, commonly used for reproducing the background in the DALI2 spectra [35–37,88], and for each suspected transition, we include a simulated response function of DALI2 at the corresponding energy in the fit. Each response function has two degrees of freedom, one for the energy and one for the intensity, as shown in figure 4.1(a).

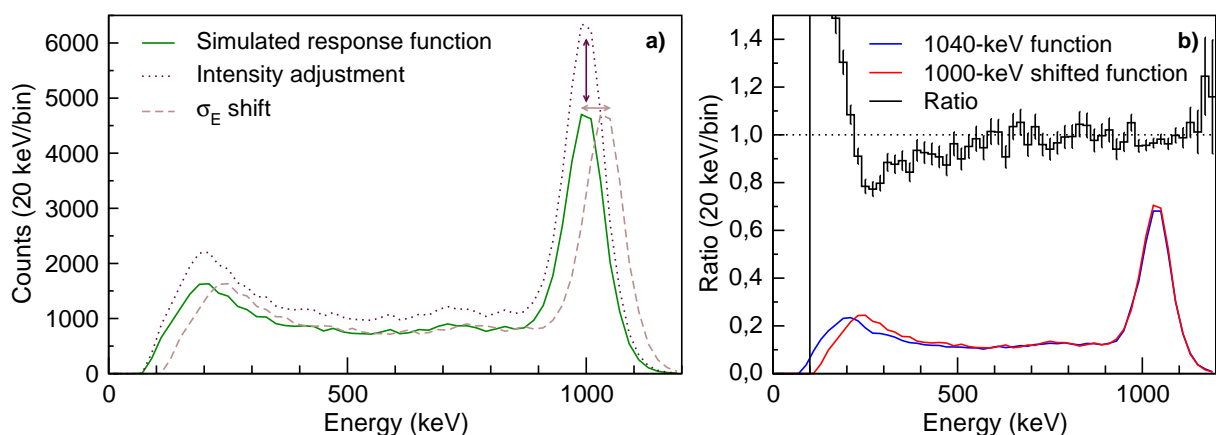


Figure 4.1 – (a) Energy and intensity degrees of freedom for each response function. (b) Ratio of the intensities for a response function at 1040 keV and another one at 1000 keV shifted by $\sigma_E = 40$ keV. Above 300 keV, i.e. after the backscattered peak, the difference is already less than 10%, and above 500 keV the ratio is 0.98(1).

Energies

In the fit, each response function is let free to shift in a range $\pm\sigma_E$, the energy resolution, around its simulated energy for a better agreement with the data. This is justified since the energy resolution does not vary rapidly with the energy, as shown in section 3.5.2, and so the response functions at E and $E \pm \sigma_E$ have similar shapes. The only limitation is at low energy, below 300 keV, because the backscattered peak will also be shifted while its location is almost independent on the energy, as explained in section 2.3.2. This issue can be bypassed by fitting the spectrum above 300 keV only or by using a smaller range of shift. The latter option is preferable in case of low-energy peaks.

Intensities

The intensity of each transition is simply given by the scale factor applied to its response function for reproducing the data, multiplied by the number of events simulated. By doing so, all detection-efficiency effects are taken into account by the simulation. The statistical error on this intensity depends on:

- The number of counts in the energy range of the transition;
- The intensity of the other transitions present in the spectrum;
- The background.

The efficiency given by the simulation agrees within 5% with the calibration-source measurements from previous experiments that used solid target. In our case, the large thickness of the target and its surrounding chamber makes impossible to perform precise efficiency measurements. Therefore, we allow a larger margin of 10% error to be safe. These 10% are added quadratically to the statistical error given by the fit.

The error made on the intensity due to the shift of the response functions is negligible compared to the other error sources because the change of efficiency between E and $E \pm \sigma_E$ is small, as shown in section 3.5.2. An example of such a difference is shown in figure 4.1(b).

Likelihood fits

We are dealing with low-statistics spectra obeying Poisson statistics and therefore we use the principle of maximum likelihood for fitting histograms. As described in reference [90], a likelihood χ^2 to be minimized can be defined as

$$\chi^2_\lambda = 2 \sum_i y_i - n_i + n_i \ln(n_i/y_i) \quad (4.1)$$

with n_i the true number of counts and y_i the number of counts estimated by the response function in the i^{th} bin.

This method takes into account empty bins and fits better histograms with low statistics than the Pearson's χ_P^2 minimization method, which assumes Gaussian-statistics histograms, while both methods give the same results in case of high statistics per bin. An example of simulated low-statistics histogram fitted using both methods is shown in figure 4.2.

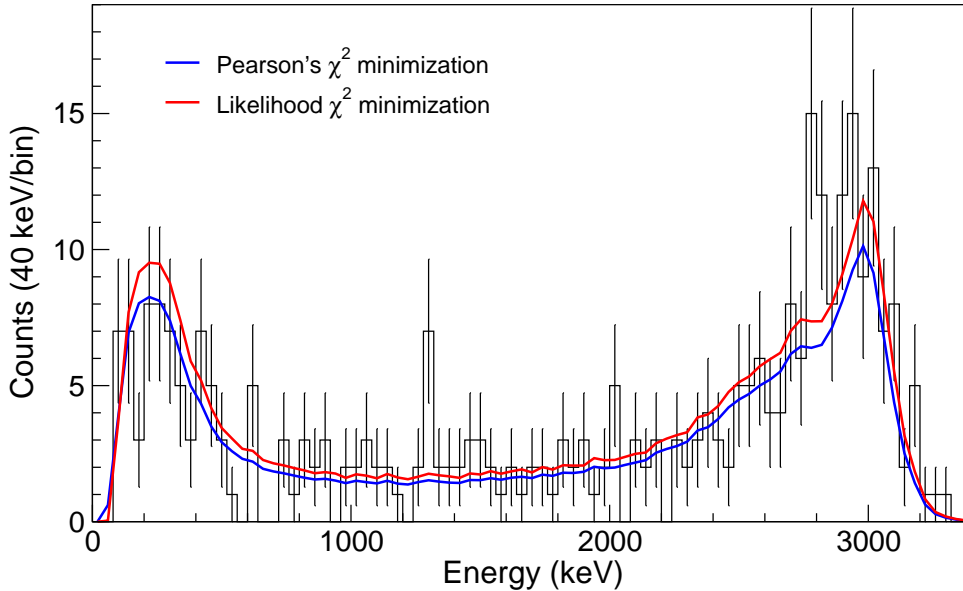


Figure 4.2 – Histogram resulting from the simulation of 500 γ rays of 3 MeV emitted in experimental conditions and fitted using both χ_P^2 and χ_λ^2 minimization methods. We find an intensity of 419(26) and 484(27), respectively.

We simulated γ rays of different energies emitted in experimental conditions with different intensities in order to quantify the limit of statistics that can be correctly fitted using simulated DALI2 response functions. The results are shown in table 4.1. We found that the likelihood method gives the correct intensity within the statistical error bars for intensities down to 200 counts, while the Pearson's χ_P^2 minimization method underestimates significantly the intensities for γ rays above 1 MeV.

Counts	0.5 MeV		1 MeV		2 MeV		3 MeV		4 MeV	
	I_P	I_λ	I_P	I_λ	I_P	I_λ	I_P	I_λ	I_P	I_λ
200	-4(9)	5(9)	-30(8)	1(9)	-13(10)	-8(9)	-13(9)	-1(9)	-2(11)	-7(9)
500	1(5)	4(6)	-2(6)	4(6)	-28(5)	-10(5)	-16(5)	-3(5)	-14(6)	-5(6)
1000	-1(4)	1(4)	-4(4)	2(4)	-17(4)	-5(5)	-15(4)	-3(4)	-20(4)	-5(4)

Table 4.1 – Results from χ_P^2 and χ_λ^2 fits of simulated low-statistics histograms, with 200, 500 and 1000 events. The difference between the true number of events and the intensity obtained from each method, respectively I_P and I_λ , is given in percent. The statistical uncertainty is also given.

Color code

We use a uniform color code for the different graphs we show. The data points are in black, the double-exponential background is a blue dashed-line, the simulated response functions are in indigo and the total fit, which is the sum of the background and all response functions, is in red.

4.1.2 Criteria for peaks identification

When dealing with low-statistics, the question of the significance of a peak arises. For the fits we performed, we consider a transition as real if it responds to the following criteria:

- Adding the corresponding response function in the fit improves χ^2_λ ;
- The width of the possible peak agrees with the resolution expected at this energy;
- The intensity of the peak obtained from the fit must be at least twice greater than its statistical uncertainty (criterion that we call “ 2σ significance”).

In the next pages, we fit the spectra with the minimum of transitions fulfilling these three criteria. Although this avoids to consider statistical artefacts as physical transitions, it also implies that we can miss some low-intensity γ rays. We discuss in more detail this point at the end of this chapter.

4.1.3 Steps of the procedure

The procedure we established for extracting as much information as possible from our data consists in performing a reliable identification of many transitions, determining their coincidence relations and estimating their intensities. With these information, we can then build level schemes. We can summarize the procedure as follow:

- Step 1: perform γ - γ coincidences without background subtraction;
- Step 2: use special multiplicity conditions in order to identify transitions to the ground state;
- Step 3: fit the spectrum with the γ transitions found in steps 1 and 2;
- Step 4: estimate the influence of the discrepancies between the fit and the data on the intensity of the transitions;
- Step 5: calculate the amount of background below each peak;
- Step 6: perform γ - γ coincidences with background subtraction, in order to confirm or invalidate the coincidence relations found in step 1.

4.2 Application to a known case: ^{81}Ga

Our procedure for building level schemes should be tested to a known case in order to verify its accuracy. The ideal case would be an even-odd nucleus, as such isotopes present a higher density of states and are closer to ^{79}Cu than even-even nuclei. In the data set, there is the same amount of statistics in the $^{82}\text{Ge}(p,2p)^{81}\text{Ga}$ channel than for copper. Moreover, the second Seastar campaign was performed in similar conditions (same setup) and offers a variety of channels leading to ^{81}Ga . We have therefore the possibility to carry out a last check that there is no bias in our analysis and that all steps described in the previous section are consistent, disregarding the data set we consider.

4.2.1 $^{82}\text{Ge}(p,2p)^{81}\text{Ga}$ from the first campaign

The γ -ray spectrum of $(p,2p)^{81}\text{Ga}$, coming from the same experiment than ^{79}Cu , is shown in figure 4.3. The add-back is done up to 15 cm and multiplicities below four are considered, for a better peak-to-total ratio. A peak is clearly visible around 350 keV, while several structures are present at higher energy, especially between 1 and 1.6 MeV. The peak below 200 keV is not a physical transition but corresponds to the background already described in section 3.6.

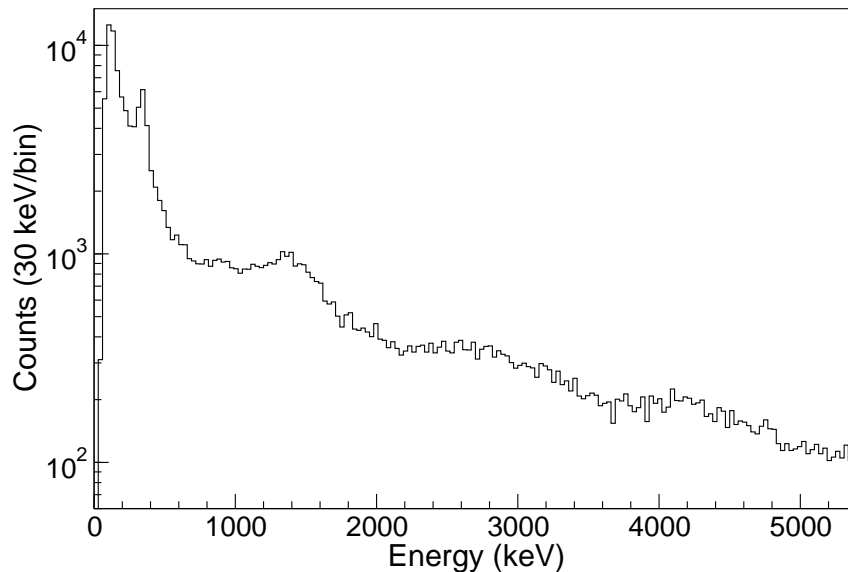


Figure 4.3 – γ -ray spectrum of $^{82}\text{Ge}(p,2p)^{81}\text{Ga}$ after add-back and Doppler correction.

Step 1 We start with the γ - γ coincidence spectrum for a gate set on the 350-keV peak, that we fit with a double-exponential background and several response functions that obey the criteria defined in section 4.1.2, as shown in figure 4.4. We identify five transitions at 460(8), 910(10), 1110(10), 1360(20) and 1600(20) keV, as well as the auto-coincidence. It is normal that the 350-keV transition is in coincidence with itself as no background

subtraction has been performed: the part of the Compton continuum of other peaks that is below the 350-keV peak induces false coincidences and is responsible of such an auto-coincidence. The spectrum is flat at higher energy than 1.6 MeV. Unfortunately, no other peak than the 350-keV one is resolved enough for performing γ - γ coincidences.

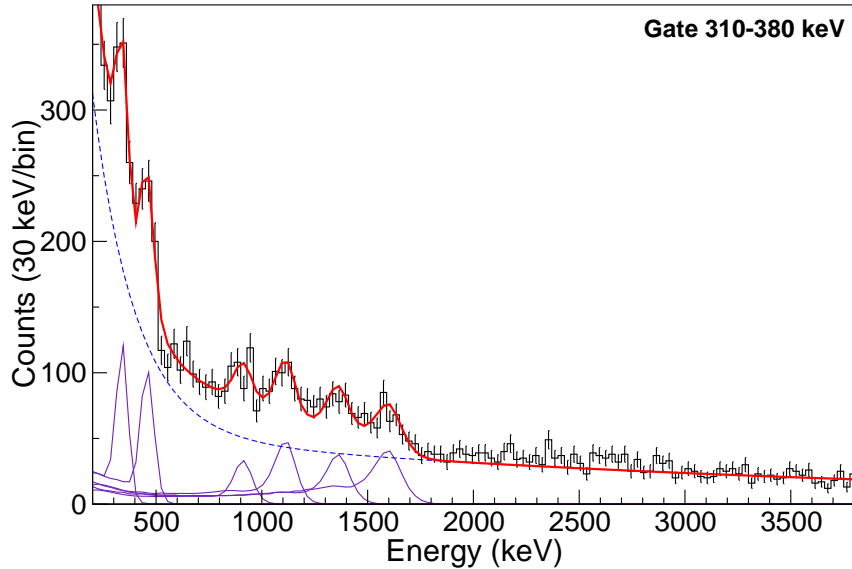


Figure 4.4 – Fit of the γ - γ coincidence spectrum for a gate set on the 350-keV transition.

Step 2 γ - γ coincidences are very powerful, but they do not allow to identify transitions that would directly go to the ground state. It is possible to observe such peaks using only events that have special conditions on the multiplicity. We select events with a multiplicity equal to one but with a number of fired crystals above one, giving the spectrum in figure 4.5. In this way, we favour:

- Transitions that are not in coincidence with other transitions, as a multiplicity equal to one means only one transition per event (after add-back);
- High-energy γ -rays, as a number of fired crystals above one means γ rays that have Compton-scattered.

This method is less precise than γ - γ coincidences, as we need to have 60 keV per bin due to the low statistics, but it is highly selective: as seen in figure 4.5, the statistics in the region from 1.2 to 1.6 MeV compared to the 350-keV peak is considerably higher than in figure 4.3. The 350-keV peak corresponds to only one bin as we use a low binning. An intense peak is observed around 1350 keV and a similar transition was seen in the γ - γ coincidence spectrum. Another peak is also present on its right side, around 1.5 MeV. Two structures are visible above 2 MeV, but they are too large to correspond to single peaks: it is not possible to identify any transitions there. Considering the spectrum in figure 4.3, the intensity of these transitions is low compared to the transitions below 2 MeV.

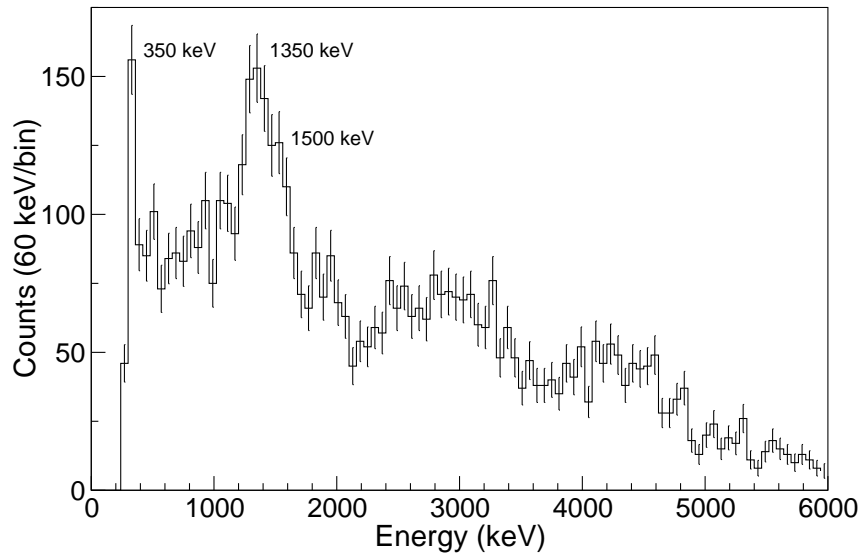


Figure 4.5 – γ -ray spectrum of $(p,2p)^{81}\text{Ga}$ for multiplicity = 1 and more than one crystal fired.

Step 3 In total, seven transitions have been found. We now use the seven corresponding response functions to fit the spectrum of ^{81}Ga , as shown in figure 4.6. There are slight discrepancies between the fit and the data around 600 keV and 1250 keV, as well as above 2 MeV due to high-energy transitions that are not identified. However, in the latter case, these transitions are far enough from the other peaks so that their contribution to the background below 2 MeV is a flat Compton tail that is taken into account by the exponential curve.

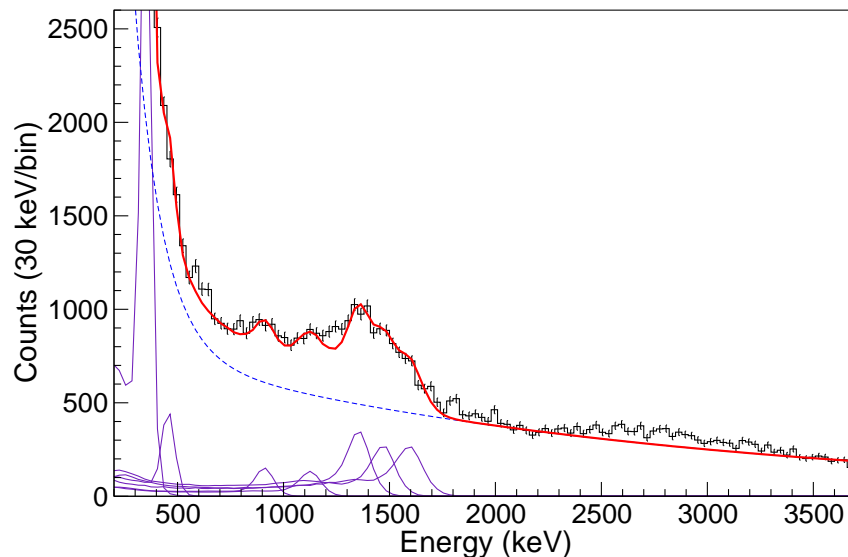


Figure 4.6 – Fit of the γ -ray spectrum of $^{82}\text{Ge}(p,2p)^{81}\text{Ga}$ after add-back and Doppler correction, for multiplicities below four. Discrepancies between the data and the fit are due to unidentified transitions.

Step 4 In order to estimate the effect of unidentified transitions on the intensities, two response functions are added in the fit at 600 and 1250 keV, i.e. where there are discrepancies, as shown in figure 4.7. The corresponding transitions do not appear to be intense. The intensities of the transitions identified in the ^{81}Ga spectrum are given in table 4.2, with (corrected intensities) and without (maximum intensities) the two additional response functions. One can see that the latter have a low impact on the intensities, within the error bars. The precise energy of the clear peak is found to be 344(5) keV.

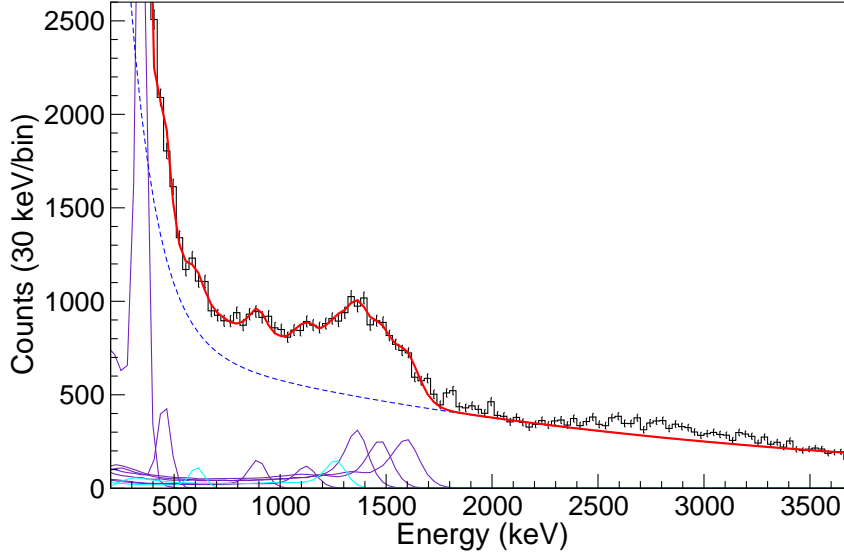


Figure 4.7 – Fit of γ -ray spectrum of $^{82}\text{Ge}(p,2p)^{81}\text{Ga}$ with two additional response functions (cyan) to remove the discrepancies observed previously below 2 MeV.

Energy (keV)	Maximum I_γ (%)	Corrected I_γ (%)
344(5)	94(10)	100(11)
456(6)	16(3)	16(3)
910(10)	11(2)	10(2)
1110(10)	13(2)	11(3)
1360(20)	39(6)	35(7)
1470(20)	33(5)	31(6)
1600(20)	41(6)	40(6)

Table 4.2 – Transitions seen in the $^{82}\text{Ge}(p,2p)^{81}\text{Ga}$ spectrum. The maximum intensities come from the fit of the spectrum with the identified transitions only, while the corrected intensities come from the fit taking into account the discrepancies. All intensities are normalized with respect to the corrected intensity of the 344-keV transition.

Step 5 The γ - γ relations found previously may not be all true coincidences as no background subtraction was performed so far. Now that we quantified the intensity of the 344-keV transition, we can determine the amount of background below this peak, as shown in figure 4.8. The false coincidences due to this background is estimated by setting

gates on both sides of each peak and the number of events contained in these two gates is normalized to the real amount of background. The spectra obtained from the gates are then added in order to obtain the background spectrum. The background gates are taken as a compromise between being close to the peak and not taking too much signal from the 344-keV peak itself nor the 456-keV one.

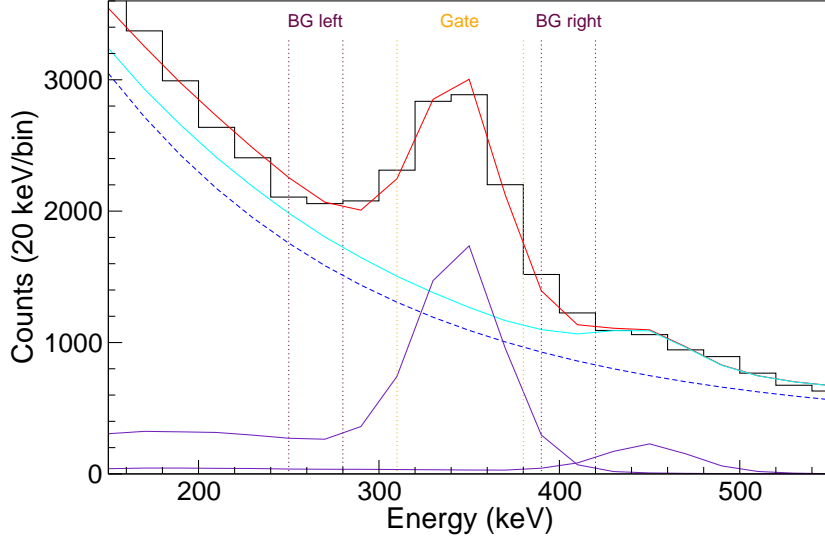


Figure 4.8 – Background below the 344-keV peak in the spectrum with multiplicities 2 and 3. In cyan, the double-exponential function plus the other response functions than the peak considered. In orange, the gate used for the γ - γ coincidences. In maroon, the gates for the background to subtract.

Step 6 As opposed to standard analysis of γ - γ coincidences, we do not extract information directly from the coincidence spectrum after background subtraction. Indeed, such a spectrum cannot be fitted as it does not obey Poisson statistics anymore (the likelihood fit described in section 4.1.1 cannot be used) and it has low statistics (the standard χ^2 method is not suitable). Moreover, there is no guarantee that the response functions after background subtraction have the same shape than the response functions simulated in a standard decay process. Therefore, in the same way than before, the background spectrum is fitted with response functions plus a double-exponential background, as shown in figure 4.9. Then, we can subtract the intensity of the transitions in the background spectrum to the intensity of the same transitions in the coincidence spectrum. Finally, the 2σ -significance criterion is applied: a transition is considered to be in coincidence with the peak for which the gate is set when its intensity after subtraction is at least two times greater than the statistical uncertainty.

After subtraction, we find that the 1360-keV transition is rejected ($I = 1.5\sigma$), it is not in coincidence with the 344-keV transition, as well as the auto-coincidence. As regards the other transitions, we find $I = 3.7\sigma$, 4.3σ , 3.0σ and 2.7σ for the 460, 910, 1110 and

1600-keV peaks, respectively. The coincidence spectrum after background subtraction is shown in figure 4.10, where the fit is given as an illustration but was not used to extract information.

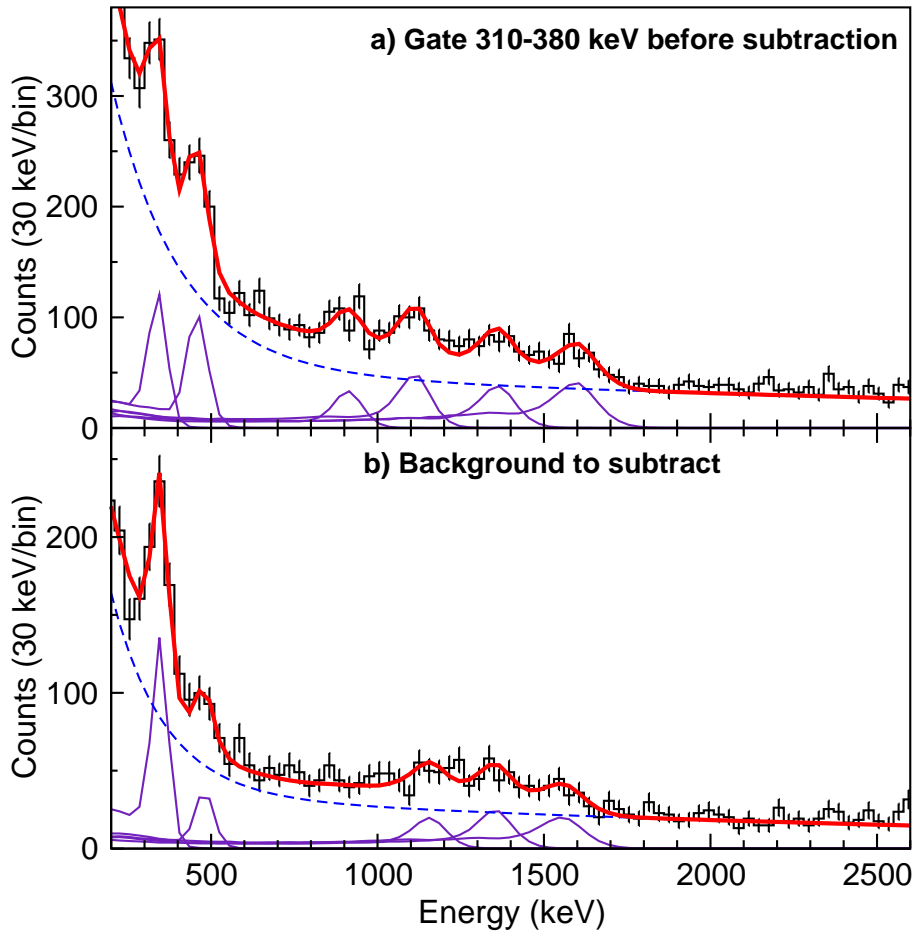


Figure 4.9 – (a) Coincidence spectrum before background subtraction for a gate set on the 344-keV peak and (b) the associated background spectra to subtract.

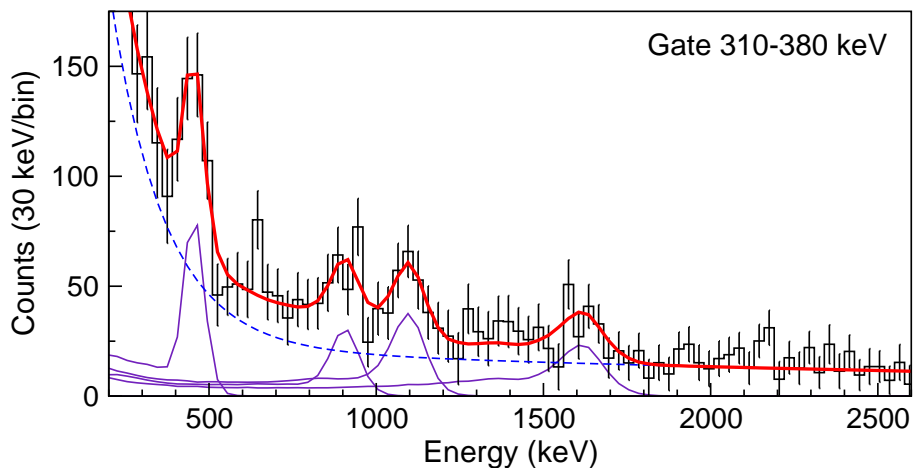


Figure 4.10 – γ - γ coincidence spectra after background subtraction for a gate set on the 344-keV peak. The fit is given as an illustration.

Summary The transitions identified in the $^{82}\text{Ge}(p,2p)^{81}\text{Ga}$ γ -ray spectrum are given in table 4.3, with their intensity and indicating whether they are in coincidence with the 344-keV transition.

Energy (keV)	Intensity (relative)
344(5)	100(11)
456(6)*	16(3)
910(10)*	10(2)
1110(10)*	11(3)
1360(20)	35(7)
1470(20)	31(6)
1600(20)*	40(6)

*Transitions in coincidence with the 344-keV transition.

Table 4.3 – Transitions seen in the $^{82}\text{Ge}(p,2p)^{81}\text{Ga}$ spectrum. The maximum intensities come from the fit of the spectrum with the identified transitions only, while the corrected intensities come from the fit taking into account the discrepancies. All intensities are normalized with respect to the corrected intensity of the 344-keV transition.

Building of the level scheme

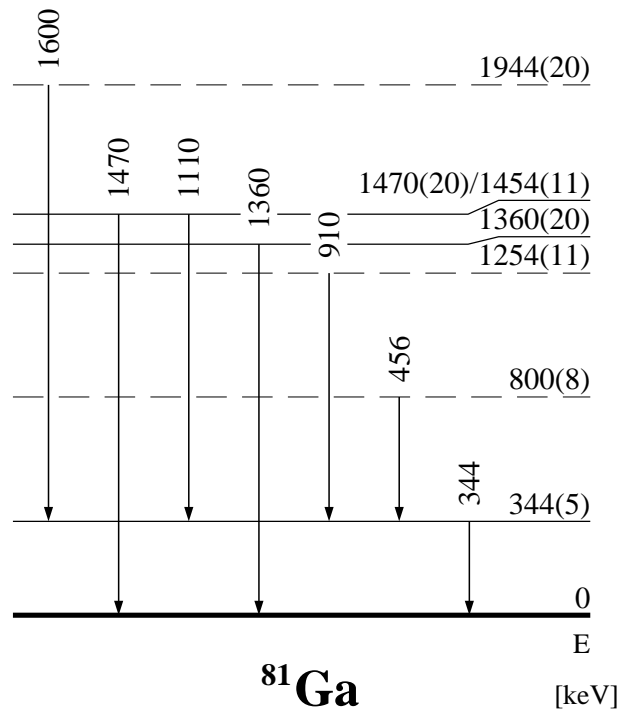


Figure 4.11 – Proposed level scheme for ^{81}Ga in this first analysis.

The level scheme built for ^{81}Ga from this analysis is shown in figure 4.11. The 344-keV transition is by far the most intense one and so we place a level at 344(5) keV. The 1360(20) and 1470(20)-keV transitions are not seen in coincidence with the 344-keV one and they are seen in the spectrum favoring the ground-state decays, in figure 4.5. As a consequence,

we place two levels at 1360(20) and 1470(20) keV. The 456 and 910-keV transitions are in coincidence with the 344-keV one, but as we cannot exclude them to be in coincidence with other transitions, we cannot place them firmly: we put them on top of the 344-keV and create two levels in dashed line at 800(8) and 1254(11) keV, respectively. The same reasoning works for the 1110(10)-keV transition, and we notice that the sum of the 344 and 1110-keV transitions gives 1454(11), which could correspond to the level at 1470(20) that we already built. Finally, the 1600(20)-keV transition can be either on top of the 355-keV level or on top of the 1470-keV one because of the 1110-keV transition. The coincidence of the 1600-keV transition with the 344-keV one would not be fulfilled if the former was on top of the 1360-keV level and its intensity is too large to place it somewhere else. A level in dashed line is then placed at 1944(20) keV.

4.2.2 Multi-channel to ^{81}Ga from the second campaign

The second seastar campaign took place one year after the first one, with the same experimental setup. We performed the data analysis for the second campaign following the same steps than described in chapter 3, taking into account the little changes (liquid-hydrogen target 3-mm thinner, DALI2 crystals organized in a different way, no DSSSD before the target, different energy thresholds). The ^{81}Ga isotope was not produced from the (p,2p) reaction but from several other channels: $^{87}\text{As}(p,3p4n)$, $^{86}\text{As}(p,3p3n)$, $^{86}\text{Ge}(p,2p4n)$, $^{85}\text{Ge}(p,2p3n)$, $^{84}\text{Ge}(p,2p2n)$, $^{84}\text{Ga}(p,p3n)$ and $^{83}\text{Ga}(p,p2n)$. As there is not enough statistics in each channel for performing γ - γ coincidences, we use all channels together. We have the risk to increase the density of states and this is therefore a good test case for the robustness of our procedure. The resulting γ -ray spectrum of ^{81}Ga is shown in figure 4.12, with multiplicities up to three.

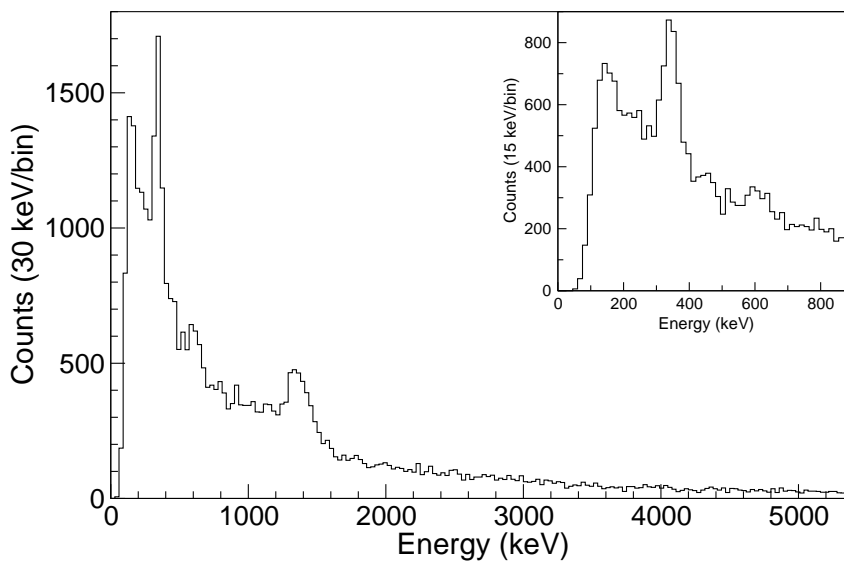


Figure 4.12 – γ -ray spectrum of ^{81}Ga after add-back and Doppler correction. (Inset) Low-energy part with a higher binning to show the peak at 450 keV.

At first, the spectrum looks simpler than in the case of (p,2p). There are two well-resolved peaks, at 350 and 600 keV, and another one at 450 keV that can be seen by increasing the binning, as shown in the inset of figure 4.12. There is also a structure between 1.2 and 1.6 MeV, but no transition seems to be present at higher energy.

Setp 1 The γ - γ coincidence spectra for a gate set on the 350, 450 and 600-keV peaks, shown in figure 4.13. In addition to the auto-coincidence, we identify seven transitions for a gate set on the 350-keV peak: 450(10), 550(10), 640(10), 930(20), 1130(20), 1310(20) and 1450(20) keV. For a gate set on the 450-keV peak, there are three transitions observed at 345(6), 630(20) and 1330(20) keV. Finally, for the last gate, we see peaks at 346(8), 480(20), 760(10), 990(20) and 1360(20) keV. Nothing is observed above 1.5 MeV in any of the three spectra.

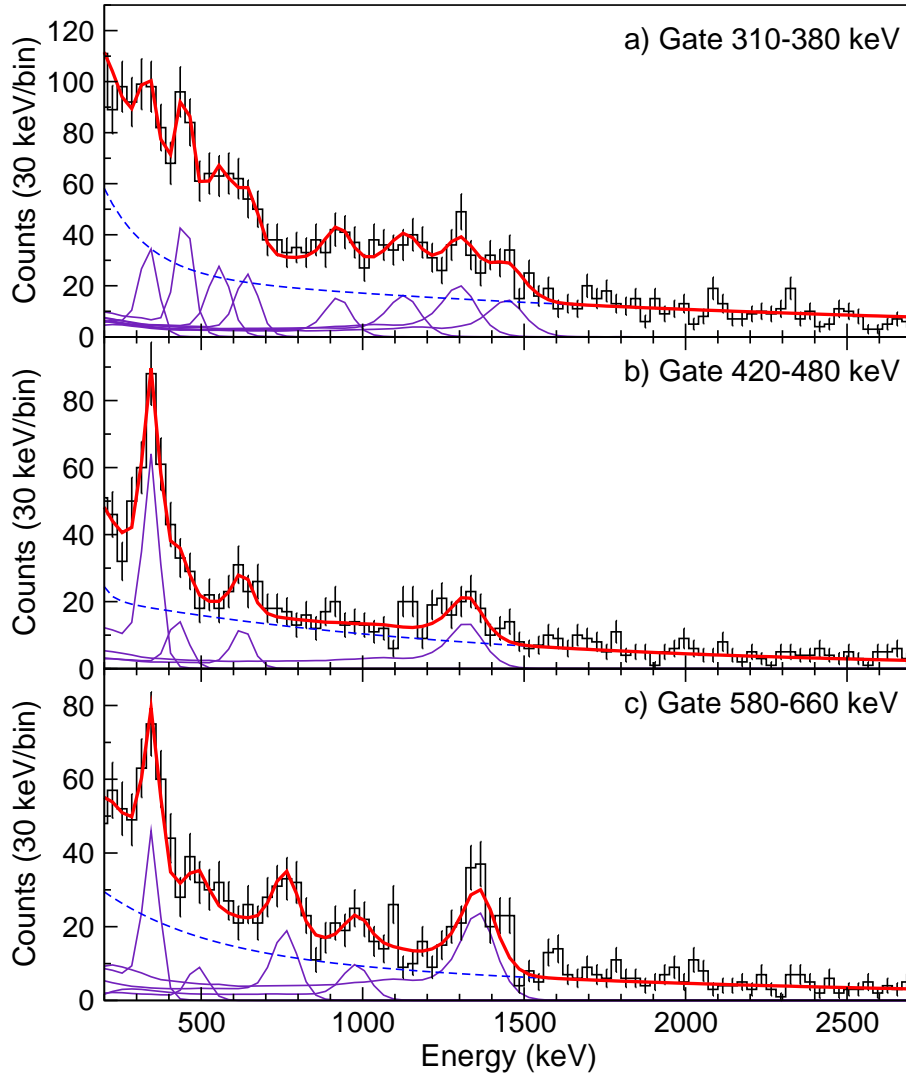


Figure 4.13 – Fit of the γ - γ coincidence spectra for a gate set on the (a) 350, (b) 450 and (c) 600-keV peaks.

Step 2 The γ -ray spectrum of ^{81}Ga for multiplicities limited to one and with at least two crystals fired is shown in figure 4.14. One can see a little accumulation of statistics at 600 keV and a very intense peak at 1350 keV. A structure is visible between 2 and 3 MeV, but nothing emerges clearly. As there is no indication for a peak at such energies in the spectrum shown in figure 4.12, and considering the low intensity of this region, we prefer not to draw any conclusion above 2 MeV.

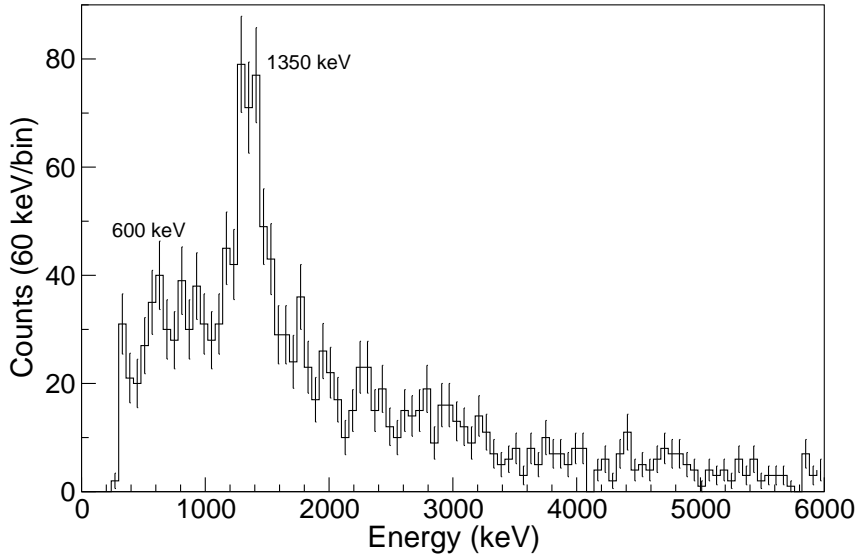


Figure 4.14 – γ -ray spectrum of ^{81}Ga for multiplicity = 1 and more than one crystal fired.

Steps 3 and 4 We now use the response functions corresponding to the nine transitions identified to fit the spectrum of ^{81}Ga , around 350, 450, 550, 630, 760, 950, 1130, 1330 and 1450 keV. The result is shown in figure 4.15. There is no discrepancies between the fit and the data, the whole spectrum is well reproduced. The intensities of the different transitions are shown in table 4.4, normalized to the intensity of the 344-keV transition, even if here this is not the most intense transition.

Energy (keV)	Intensity (relative)
344(5)	100(11)
445(9)	24(5)
540(20)	10(5)
620(10)	41(8)
770(10)	18(5)
930(10)	17(5)
1130(20)	19(5)
1340(20)	114(18)
1460(20)	74(13)

Table 4.4 – Transitions observed in the ^{81}Ga spectrum, with their intensity. Intensities are normalized with respect to the intensity of the 344-keV transition.

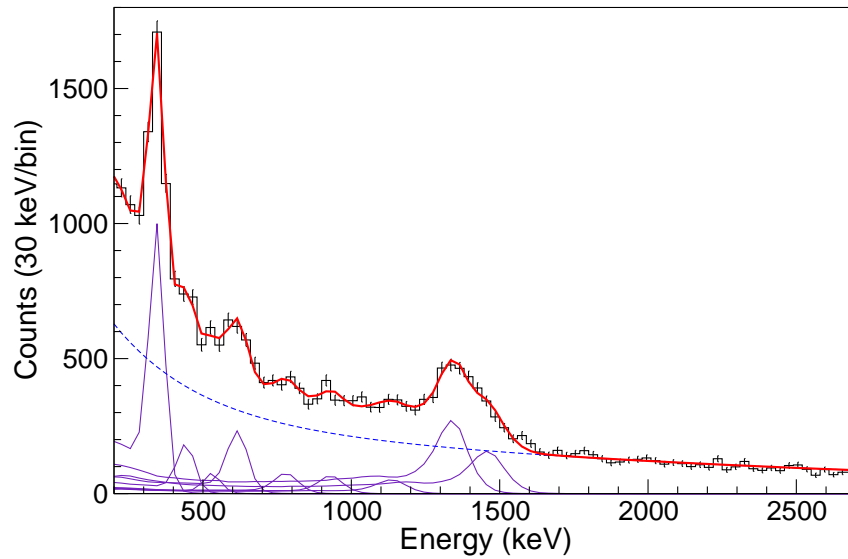


Figure 4.15 – Fit of the γ -ray spectrum of ^{81}Ga after add-back and Doppler correction, for multiplicities below four.

Step 5 The gates used for the γ - γ coincidences and the background subtraction are shown in figure 4.16, as well as the amount of background below the three peaks. One can see that several peaks in this range of energy are rather close to each other, which implies that the background gates for a given transition contain a part of the surrounding peaks. This could lead to the rejection of weak but true coincidences. Nevertheless, the background subtraction is essential to avoid false coincidences.

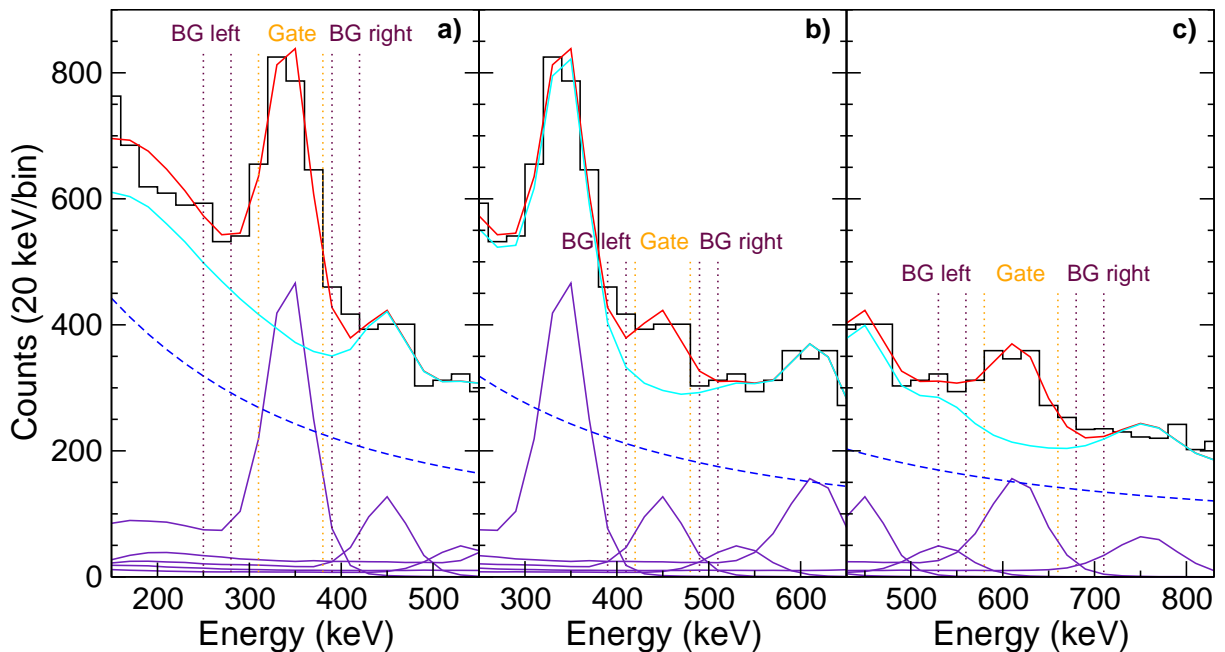


Figure 4.16 – Background below the (a) 344, (b) 445 and (c) 620-keV peaks in the spectrum with multiplicities 2 and 3. In cyan, the double-exponential function plus the other response functions than the peak considered. In orange, the gates used for the γ - γ coincidences. In maroon, the gates for the background to subtract.

Step 6 The γ - γ coincidence spectra corresponding to the three gates and their associated background spectra are shown in figure 4.17. The results of the subtraction is given in table 4.5. One can note that the 990(20)-keV peak in coincidence with the 620-keV transition is a bit far from the value found in the fit of the full spectrum, which is 930(10). Adding a peak at 990-keV does not improve the fit shown in figure 4.15, on the contrary, it is rejected by the 2σ -significance criterion. For now we consider that both energies correspond to the same peak and we will come back on this difference latter in this chapter. To finish, the coincidence spectrum after background subtraction is shown in figure 4.18.

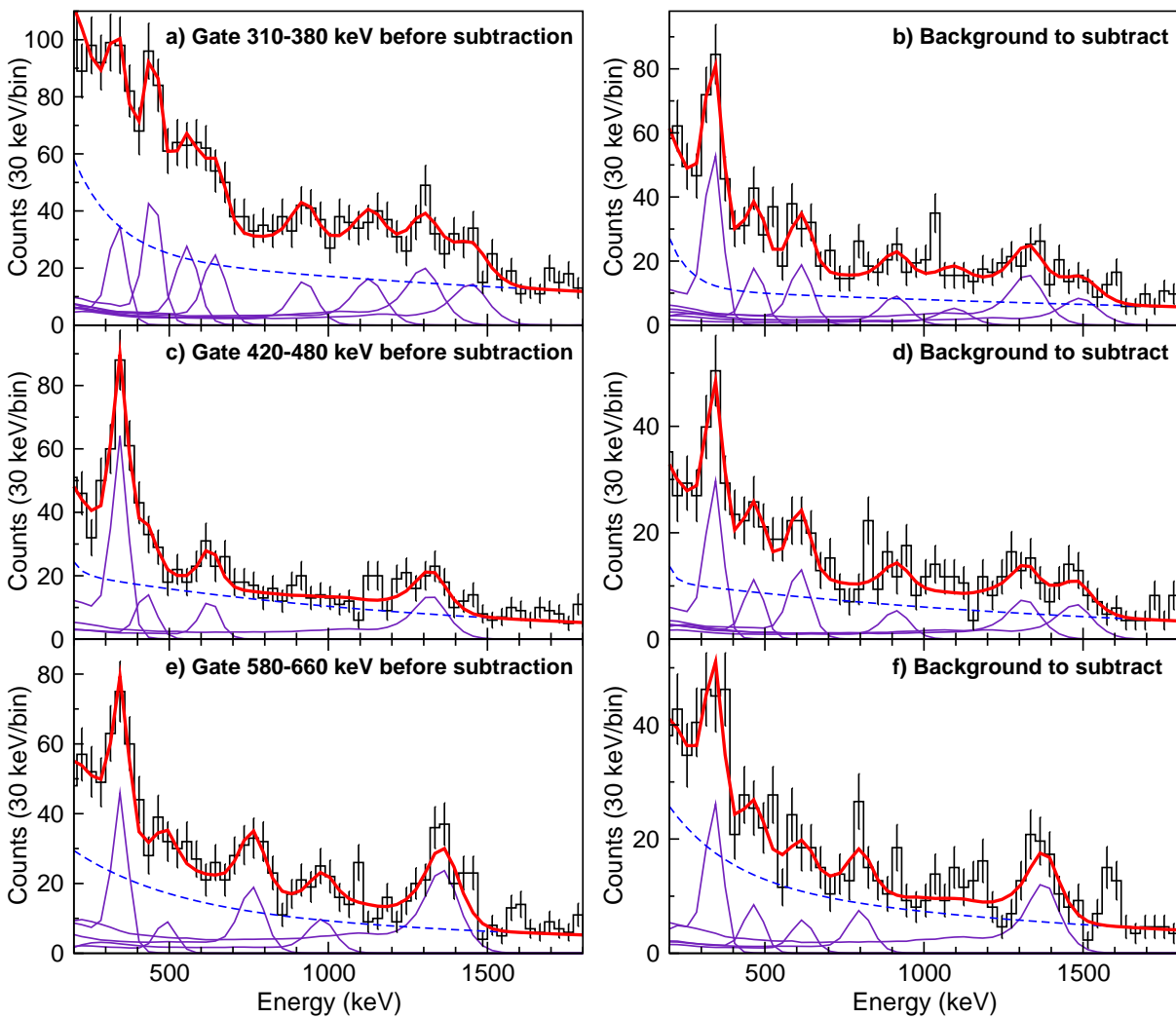


Figure 4.17 – Coincidence spectra before background subtraction for a gate set on the (a) 344, (c) 445 and (e) 620-keV peaks and their corresponding background spectra (b), (d), (f), respectively.

γ - γ	344 keV	445 keV	620 keV
344(5)	-	2.9	1.4
445(9)	2.4	-	0.2
540(20)	3.9	-	-
620(10)	0.7	0.0	-
770(10)	-	-	2.1
930(10)	1.1	-	2.9*
1130(20)	2.2	-	-
1340(20)	0.8	1.7	2.6
1460(20)	1.3	-	-

*Seen at 990(20) keV.

Table 4.5 – Intensity of the peaks in coincidence after background subtraction, given in terms of $I_\gamma/\sigma_{I_\gamma}$. Only values in bold type mean true coincidence (2σ -significance criterion).

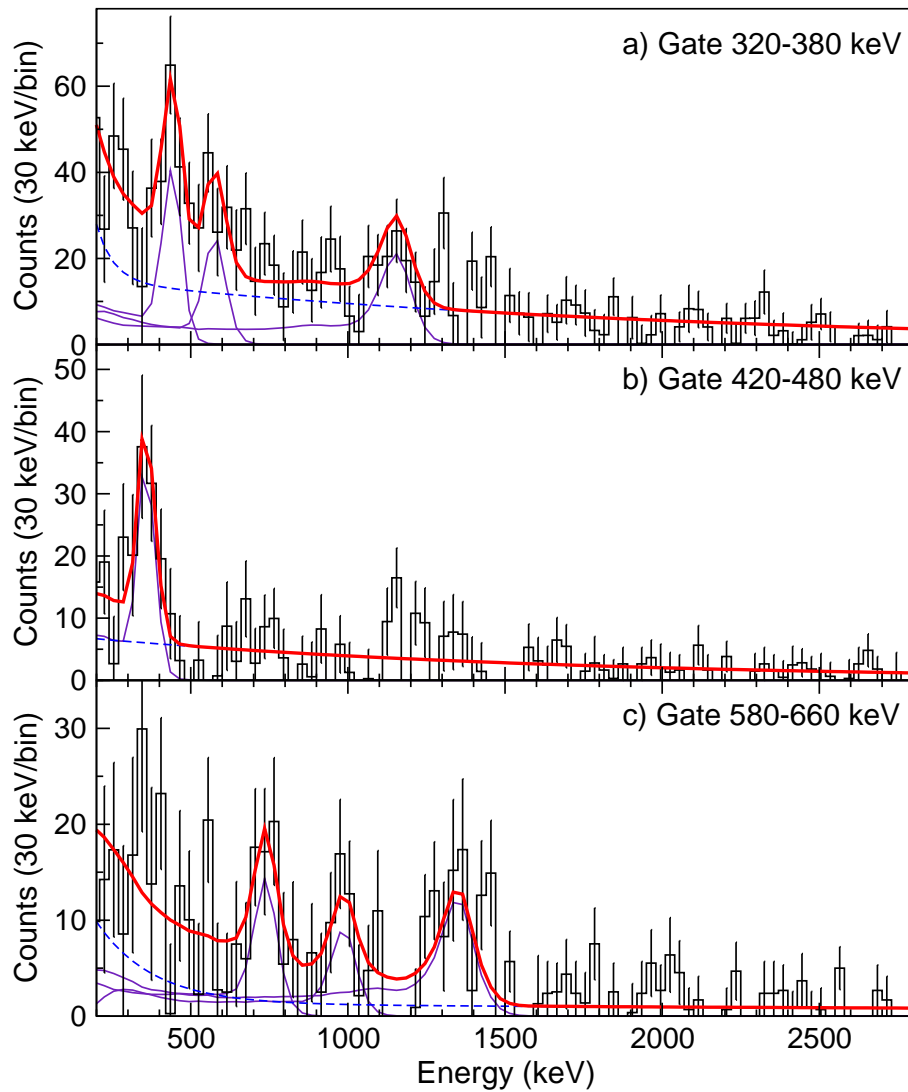


Figure 4.18 – γ - γ coincidence spectra after background subtraction for a gate set on the (a) 344, (c) 445 and (e) 620-keV peaks. The fit is given as an illustration.

Summary The transitions identified in the $^{82}\text{Ge}(p,2p)^{81}\text{Ga}$ γ -ray spectrum are given in table 4.6, with their intensity and indicating whether they are in coincidence with the 344-keV transition.

Energy (keV)	Intensity (relative)
344(5)	100(11) [†]
445(9)	24(5) [*]
540(20)	10(5) [*]
620(10)	41(8)
770(10)	18(5) [‡]
930(10)	17(5) [‡]
1130(20)	19(5) [*]
1340(20)	114(18) [‡]
1460(20)	74(13)

^{*}Transitions in coincidence with the 344-keV transition.

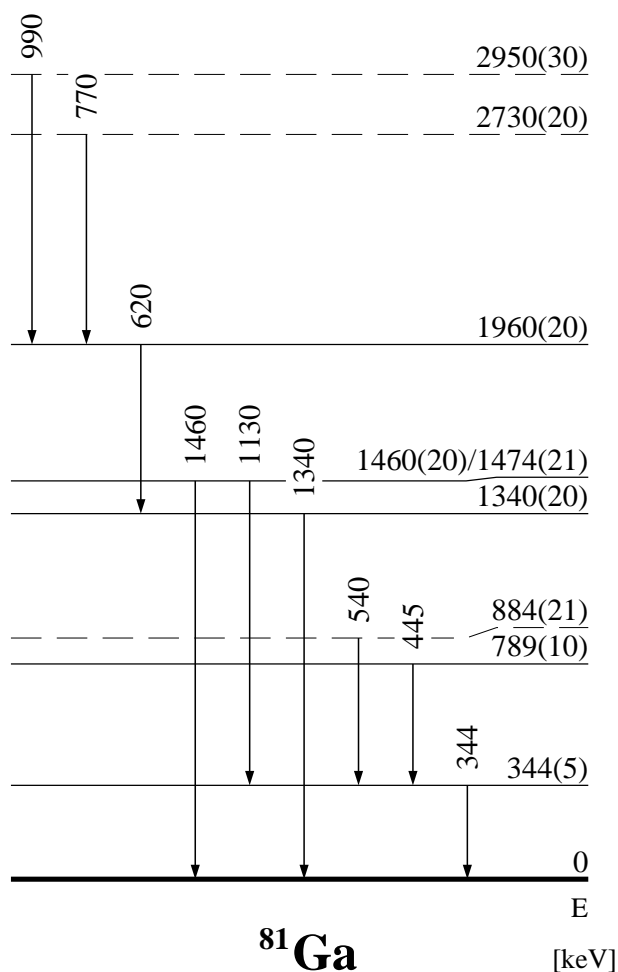
[†]Transitions in coincidence with the 445-keV transition.

[‡]Transitions in coincidence with the 620-keV transition.

Table 4.6 – Transitions observed in the ^{81}Ga spectrum, with their estimated intensity and coincidence relations. Intensities are normalized with respect to the intensity of the 344-keV transition.

Building of the level scheme

The level scheme built for ^{81}Ga from this analysis is shown in figure 4.19. The 344 and 1340-keV transitions are the most intense ones and are not in coincidence, so we place a level at 344(5) keV and another one at 1340(20) keV. The 445-keV transition is in coincidence only with the 355-keV one, we put it on top of the 344-keV level, creating a second excited state at 789(10) keV. Although the 540-keV transition is in coincidence with the 355-keV one, we put the level at 884(21) keV in dashed line because we cannot exclude that this transition happens higher in the level scheme: we cannot perform γ - γ coincidences with it and it is the weakest transition, which implies that it could be located above another transition also in coincidence with the 355-keV one. The 620-keV transition is placed on top of the 1340-keV state, considering their coincidence relations and their intensities. The 1460-keV transition is not in coincidence with any of the three transitions we looked at and this, together with its strong intensity, makes that it can either fall on the ground state or on the 1340-keV level. The 1130-keV transition is in coincidence with the 355-keV one but not with the one at 445-keV, and appears to be more intense than the 540-keV transition. We therefore place it on top of the 344-keV level, emitted from a state at 1474(21) keV. This value is very close to the 1460(20)-keV transition, favoring the placement of the latter as a direct decay to the ground state. Finally, two transitions at 770 and 990 keV are found to be in coincidence with the

Figure 4.19 – Proposed level scheme for ^{81}Ga in this second analysis.

620-keV one, but not with the 344 and 445-keV transitions. We place them on top of the 1960-keV state, emitted from two levels in dashed line: these transitions are unlikely to be emitted by the 1340-keV level, as we would otherwise have seen the complementary transitions to reach the ground state, but considering their similar intensity we cannot exclude that they are in coincidence with each other. The question whether the 930 and 990-keV transitions are the same, mentioned in step 6, rises here: if they are different, it is not possible to place the 930-keV transition on the level scheme as we cannot perform reliable γ - γ coincidences by setting a gate on it and it has not been seen in coincidence with any of the three transitions used in this analysis. The impossibility to disentangle this issue is not of primary importance, but shows the limitation of our method, probably due to the low statistics and the poor resolution.

4.3 Comparison with literature

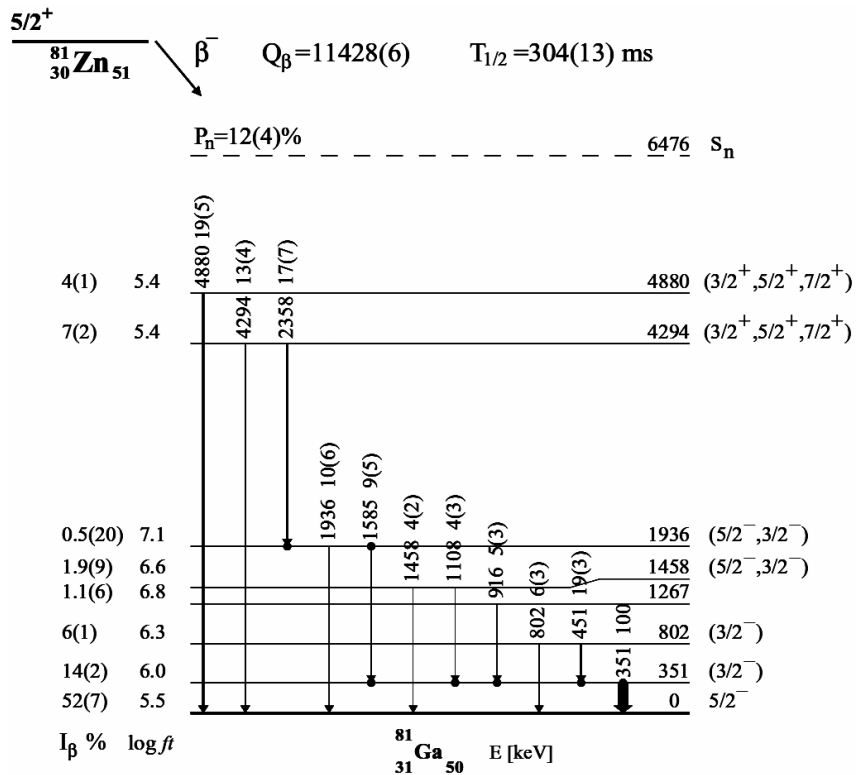


Figure 4.20 – Level scheme built from the β -decay study in reference [91].

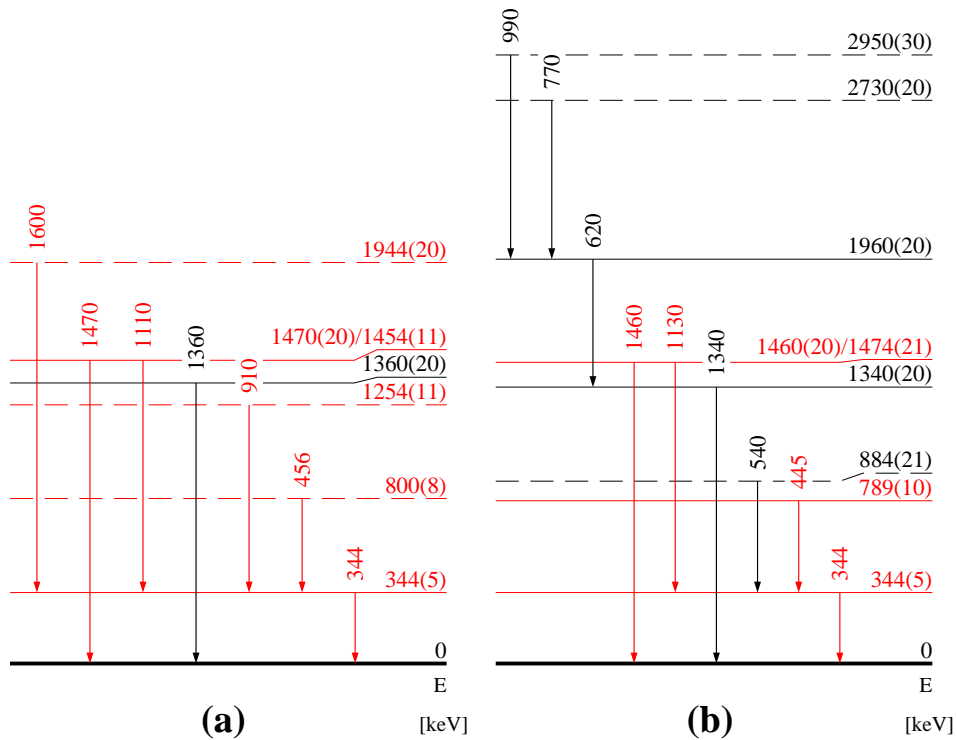


Figure 4.21 – Level schemes of ^{81}Ga obtained in the (a) first and (b) second analysis. In red, the levels already known from literature [91].

The ^{81}Ga nucleus has already been studied in several experiments, like for example in references [51, 52, 91, 92], and some of its excited states are already known. We show in figure 4.20 the level scheme published for ^{81}Ga from a β -decay study [91] and in figure 4.21 the level scheme obtained from the two analysis we performed, with in red the levels and transitions already known. The energy uncertainties in the literature scheme are lower than 2 keV for the states below 2 MeV, and the intensity of each transition is indicated.

To begin, we can make two observations. First, the three firm excited states and their four related decays in the scheme built from the first analysis are coherent with the corresponding ones found in the second analysis. Secondly, when the transitions are already known, the energies found in both analysis are in good agreement with the literature scheme, within error bars. The 344-keV transition is the exception, its value being slightly lower than expected even considering the uncertainty. This difference probably comes from lifetime effects, discussed in section 3.5.2, but we exclude a problem from the analysis as in both data sets we find the same shift. The non-linearity of the crystals below 400 keV can also be excluded because due to the Lorentz boost, most the γ -rays are emitted at forward angles, i.e. at higher energy than in the rest frame.

In the scheme (a), the three levels in dashed line correspond to excited states already observed. Although we could not be certain of their placement, because it would require to perform more γ - γ coincidences, we correctly identified the corresponding transitions and deduced their coincidence with the 344-keV one. We did not identify the decay of the 1944-keV level to the ground state, which exists according to figure 4.20. The intensities measured in reference [91] for the 1585 and 1936-keV transitions are similar but with important error bars, leading to a ratio between both intensities very large: 0.9(7). If the real value of this ratio is close to its upper limit (1.6), and as the efficiency and resolution for the photopeak are worse at 1.9 MeV than at 1.6 MeV, we can indeed miss it. Moreover, from the spectrum in figure 4.5, there is an accumulation of statistics around 1.9 MeV that could correspond to the 1936-keV transition.

In scheme (b), the possibility to perform γ - γ coincidences using the 445-keV transition allowed us to firmly place a state at 789 keV, in agreement with the level at 802 keV found in β decay. The difference between both values is explained with the statistical uncertainty and the slight shift of the first-transition energy mentioned above. The coincidence spectrum of the 620-keV transition was used to firmly place the latter on the scheme. The 990-keV transition does not correspond to the 916-keV one in figure 4.20 that would be shifted, as it is not in coincidence with the 344-keV transition.

Finally, the 1108 and 1458-keV transitions are emitted from the same level and we identified them in both cases. The ratio between their intensities should be the same disregarding how the 1458-keV level was populated. We found a ratio between the intensities of these two transitions equal to 0.35(12) and 0.26(8), respectively in the first and second analysis, which is coherent. In the literature, the intensity of both transitions has large error bars and the ratio is 1.0(9), meaning that our values are compatible.

As a conclusion, we performed two analysis of the same nucleus using different reaction channels and data sets coming from two independent experiments based on the same setup. In the first analysis, the statistics was similar than for ^{79}Cu and there was half as much in the second one. We therefore tested the procedure we established for building the level scheme a first time in similar conditions than for ^{79}Cu and a second time in different conditions, leading to results for ^{81}Ga that are coherent and compatible with what is known from previous studies. The limitations of this procedure, inherent to the low statistics and the poor resolution of the γ array, as well as to the large background, induce sometimes the impossibility to place some transitions on the level scheme. Our philosophy is to build a true level scheme even if it is not complete and this procedure appears to be robust enough for this purpose.

Chapter 5

Results

This chapter deals with the experimental results for the $^{80}\text{Zn}(p,2p)^{79}\text{Cu}$ reaction channel. The γ -ray spectrum of ^{79}Cu is presented and we apply the procedure described in the previous chapter for building its level scheme. The last part focuses on the calculation of inclusive and exclusive cross sections.

5.1 γ -ray energy spectrum

The γ -ray energy spectrum of ^{79}Cu obtained from the (p,2p) reaction channel after add-back and Doppler correction is shown in figure 5.1. The multiplicity is limited to a maximum of three γ rays per event for a better signal-to-noise ratio. Events with one or two protons detected in the MINOS TPC are taken into account.

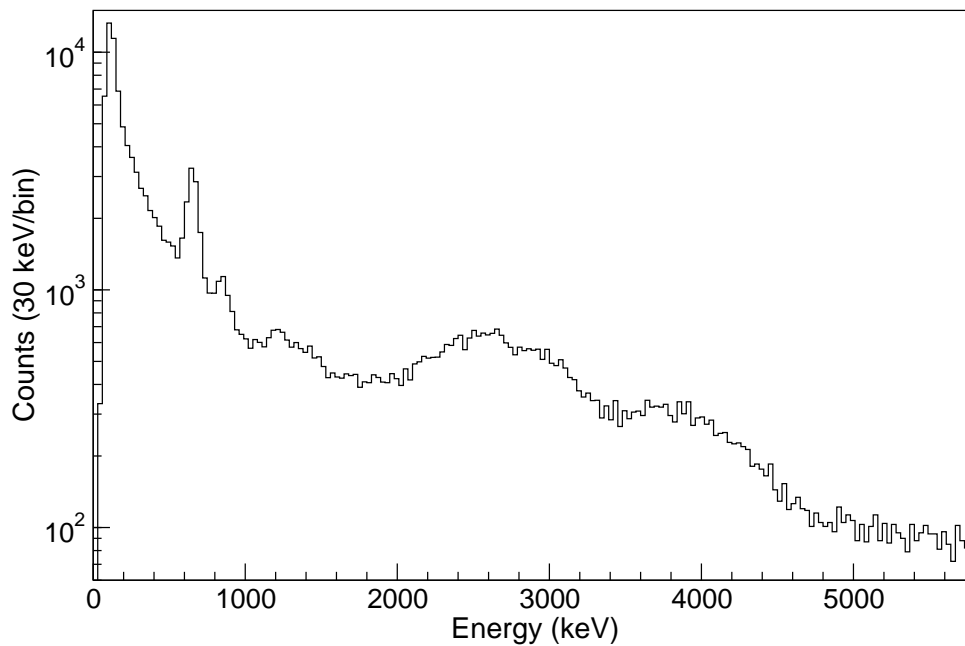


Figure 5.1 – γ -ray energy spectrum of $^{80}\text{Zn}(p,2p)^{79}\text{Cu}$ after add-back and Doppler correction. Multiplicities below four are considered.

Two clear transitions are found around 650 keV and 850 keV, while there are three structures in the ranges 1.0 to 1.5 MeV, 2.0 to 3.4 MeV and 3.4 to 4.5 MeV. Above 4.5 MeV, no transition is seen. The peak below 200 keV is not a physical transition but corresponds to the background already described in section 3.6.

5.2 Application of the procedure

We can now apply to the ^{79}Cu data the procedure that we established and validated in the last chapter.

5.2.1 γ - γ coincidences without background subtraction

In a first phase, we analyze the γ - γ coincidences. The γ - γ coincidences matrix, built for events with two or three γ rays detected in DALI2 after add-back, is shown in figure 5.2. As the 650 and 850-keV peaks are well separated from the other transitions and contain enough statistics, we can make projections of the γ - γ matrix with a gate set on these two peaks. The corresponding spectra can be fitted by the DALI2 response functions in order to extract the energy of the coincident transitions.

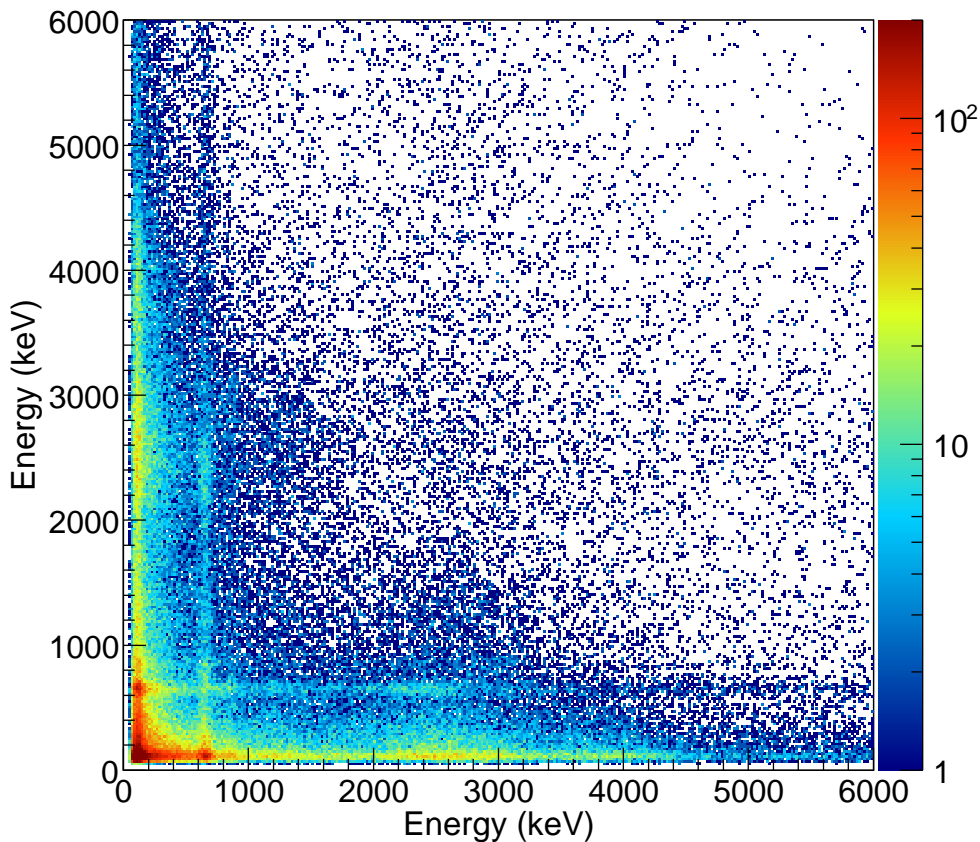


Figure 5.2 – γ - γ coincidences matrix of $(p,2p)^{79}\text{Cu}$, for multiplicities two and three.

Gate on the 650-keV peak

The coincidence spectrum obtained for a gate set on the 650-keV peak is shown in figure 5.3. First, we consider a double-exponential background, as shown with the blue dashed-line. The background at high energy is obtained by fitting an exponential function between 4 and 6 MeV. The exponential function for the low-energy background is fitted between 200 and 300 keV. Once the response functions are added, the Compton tail of the peaks contributing to the background at low energy, the exponential function have to be fitted again.

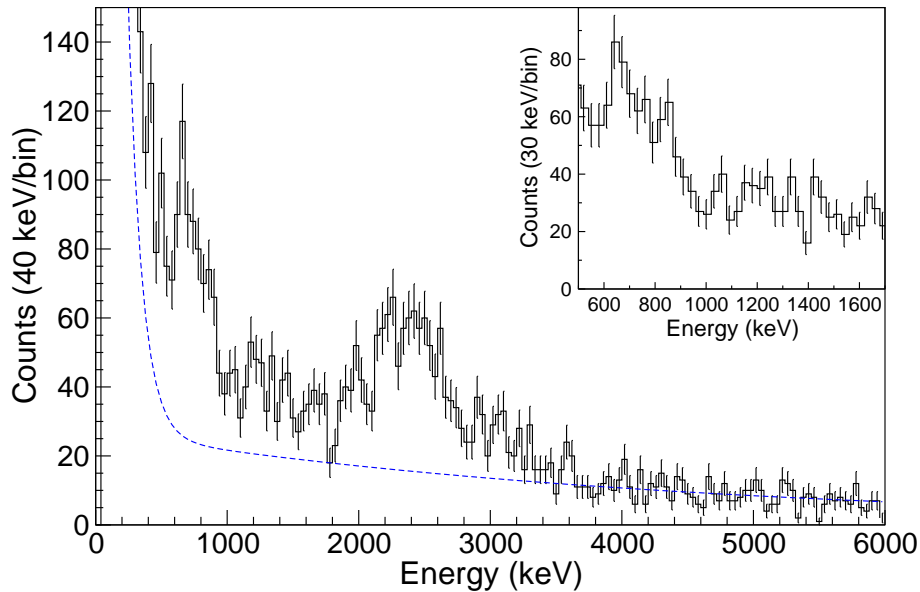


Figure 5.3 – γ - γ coincidence spectrum for a gate set on the 650-keV peak with a fitted double-exponential background. (Inset) Low-energy part with a higher binning.

A priori, there is sufficient statistics for having several peaks between 650 and 3100 keV. We start fitting the spectrum above 2.1 MeV in order to determine the number of peaks needed to reproduce the region between 2.1 and 2.8 MeV, and we include a response function fitting for the peak at 3.1 MeV as its Compton tail has an influence on the transitions at lower lower energy. The results of a fit with two and three response functions between 2.1 and 2.8 MeV are shown in figure 5.4.

The values of χ^2_λ divided by the number of degrees of freedom are given for different numbers of peaks in table 5.1. These values are an indicator of the goodness of fit: the closer to one it is, the better the fit is. The best fit is achieved for three transitions between 2.1 and 2.8 MeV and fulfills the criteria defined in section 4.1.2, while the second best fit does not respect the 2σ -significance criterion for one of the four transitions.

# of peaks	1	2	3	4
$\chi^2_\lambda/\text{NDF}$	2.31	1.46	1.03	1.14

Table 5.1 – Goodness of fit for different number of peaks between 2.1 and 2.8 MeV.

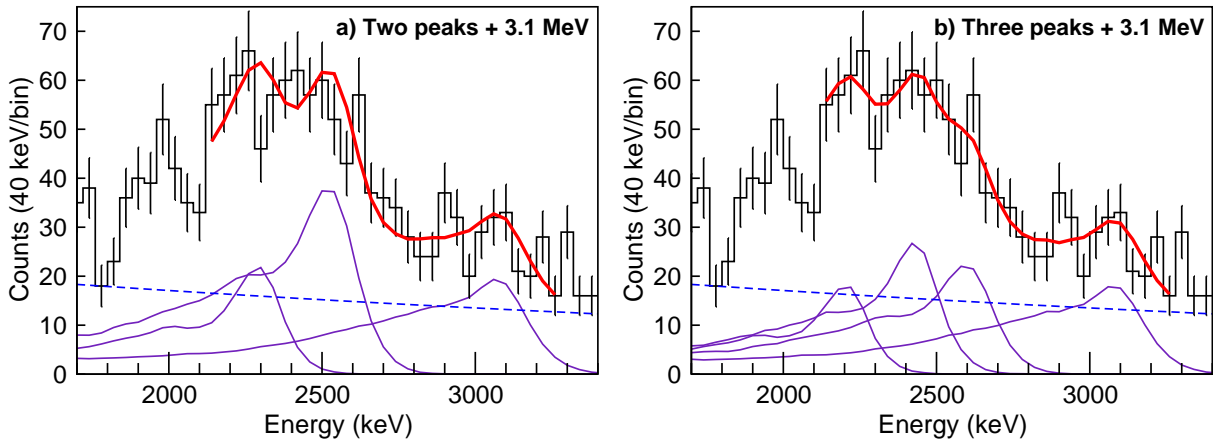


Figure 5.4 – Coincidence spectrum fitted between 2.1 and 3.3 MeV with two (a) and three (b) transitions plus a peak around 3.1 MeV.

Once the high-energy part of the coincidence spectrum is untangled, we can fit all the spectrum in order to complete the list of γ rays in coincidence with the 650-keV transition. The final fit is shown in figure 5.5, with in inset a focus on the low-energy part with a higher binning.

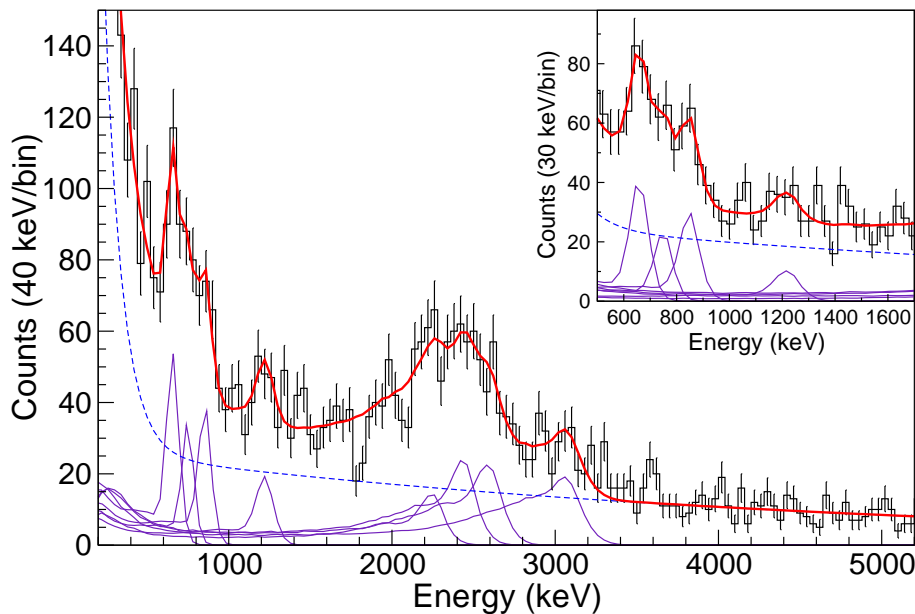


Figure 5.5 – Fit of the γ - γ coincidence spectrum for a gate set on the 650-keV peak. (Inset) Low-energy part with a higher binning.

At lower energy than 2.1 MeV, peaks around 650, 750, 860 and 1220 keV are needed for a good fit of the spectrum. It is normal that the 650-keV transition is in coincidence with itself as no background subtraction has been performed: the part of the Compton continuum of other peaks that is below the 650-keV peak induces false coincidences and is responsible of such an auto-coincidence.

The addition of other response functions than those shown in figure 5.5 would lead to the non-respect of at least one of the three criteria defined in section 4.1.2. For example, despite the apparent structures in the region between 1.4 and 2 MeV, the addition of peaks in this interval violates the 2σ -significance criterion as all the statistics is explained by the Compton tail of the higher-energy peaks.

To summarize the results of the fit, the following peaks are found in the γ - γ coincidence spectrum for a gate set on the 650-keV without background subtraction, besides the auto-coincidence: 750(20), 860(10), 1220(30), 2240(40), 2440(40), 2600(40) and 3070(30) keV. The significance of these transitions, defined as the intensity divided by the statistical uncertainty $I_\gamma/\sigma_{I_\gamma}$, is given in table 5.2.

Energy (keV)	750(20)	860(10)	1220(30)	2240(40)	2440(40)	2600(40)	3070(30)
Significance	3.7	5.6	4.6	3.3	3.8	4.6	8.8

Table 5.2 – Statistical significance of the transitions seen in the coincidence spectrum for a gate set on the 650-keV peak, defined as $I_\gamma/\sigma_{I_\gamma}$.

Gate on the 850-keV peak

The same method is applied on the γ - γ coincidence spectrum obtained with a gate on the peak at 850 keV. The result is shown in figure 5.6, with in inset a focus on the low-energy part with a higher binning. Peaks at 660(20), 760(30), 1250(30), 2360(30) and 3050(30) keV, as well as the auto-coincidence of the 850-keV transition, are observed. The significance of these transitions is given in table 5.3.

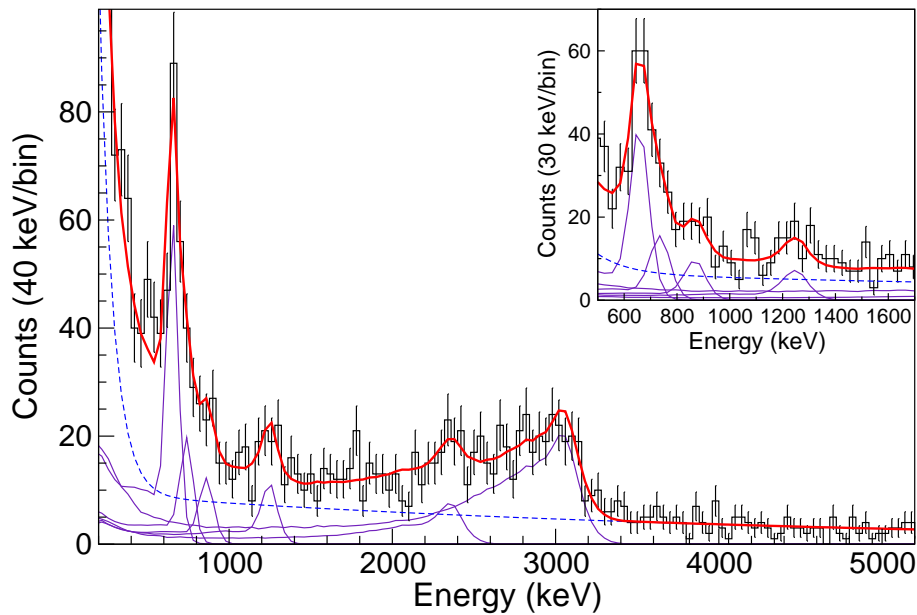


Figure 5.6 – Fit of the γ - γ coincidence spectrum for a gate set on the 850-keV peak. (Inset) Low-energy part with a higher binning.

Energy (keV)	660(20)	760(30)	1250(30)	2360(30)	3050(30)
Significance	8.0	3.5	3.9	3.9	12.4

Table 5.3 – Statistical significance of the transitions seen in the coincidence spectrum for a gate set on the 850-keV peak, defined as $I_\gamma/\sigma_{I_\gamma}$.

5.2.2 Decays to the ground state

It is possible to identify transitions that would directly go to the ground state, which cannot be observed with γ - γ coincidences, using only events that have special conditions on the multiplicity. We select events with a multiplicity equal to one but with a number of fired crystals above one, giving the spectrum in figure 5.7. In this way, we favour:

- Transitions that are not in coincidence with other transitions, as a multiplicity equal to one means only one transition per event (after add-back);
- High-energy γ -rays, as a number of fired crystals above one means γ rays that have Compton-scattered.

Although this method is less precise than γ - γ coincidences, due to the low statistics that require to have 60 keV per bin, it is highly selective: as seen in figure 5.7, the statistics in the region from 3.4 to 4.5 MeV compared to the 650-keV peak is considerably higher than in figure 5.1. Significant accumulation of statistics is found around 640, 840, 1220, 2580, 2940, 3800 and 4300 keV. The three last peaks were not identified in the coincidence spectra and are considered as coming from levels decaying directly to the ground state. The presence of the four other γ rays already identified in coincidence is normal since a γ cascade is sometimes only partially detected in DALI2.

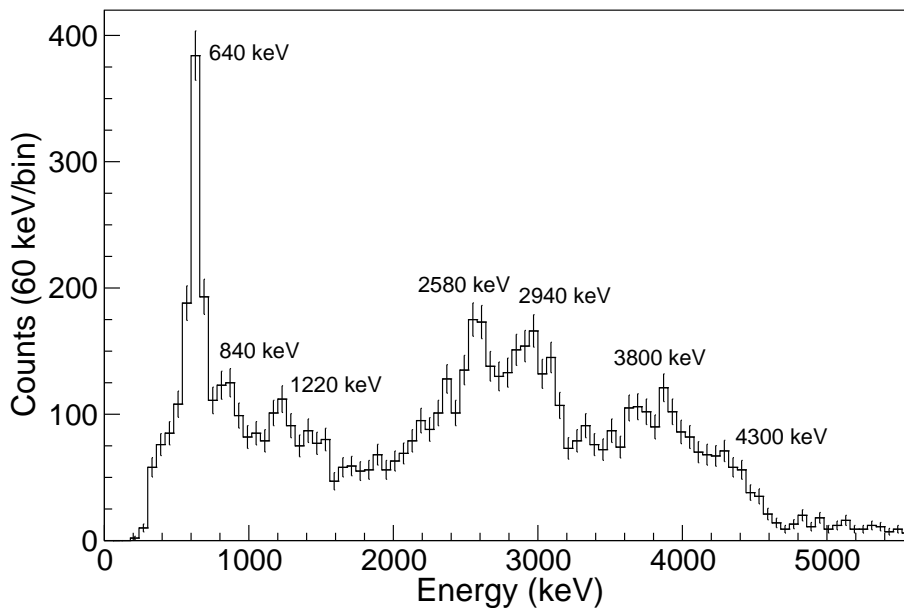


Figure 5.7 – γ -ray spectrum of $(p,2p)^{79}\text{Cu}$ for a multiplicity equal to one and a number of fired crystals above one.

5.2.3 Intensities estimation

In total, twelve transitions have been found. The spectrum of ^{79}Cu shown in figure 5.1 can then be fitted with the corresponding response functions plus a double-exponential background. It has to be noted that the 2360(30)-keV transition is in between the close 2240(40) and 2440(40)-keV transitions, with a separation of only 80(50) keV with the latter, i.e. $1.0(6) \sigma_E$ in terms of energy resolution. Such a proximity may imply difficulties for fitting accurately, like the rejection of one of the two transitions. Thus, we remove the 2360-keV transition from the fit and we justify this choice a posteriori in section 5.3.1.

The result of the fit with eleven response functions is shown in figure 5.8. The two response functions above 3.4 MeV are enough to fit the region between 3.4 and 4.5 MeV, so we let the intensity and energy parameters free in the fit: we find 3880(40) and 4300(40) keV. Below 3.4 MeV, there are discrepancies between the fit and the data due to non-identified transitions, so the intensities and energies of the response functions must be fixed manually. The intensities found for the transitions below 3.4 MeV using this procedure have to be seen as an upper limit.

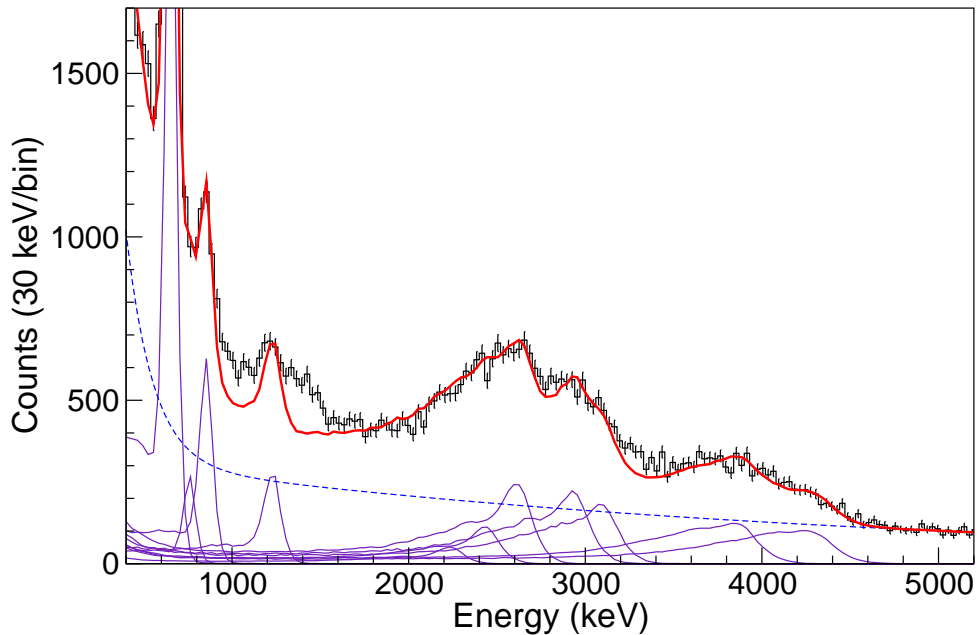


Figure 5.8 – Fit of the γ -ray spectrum of $(p,2p)^{79}\text{Cu}$ after add-back and Doppler correction, for multiplicities below four. The discrepancies between the data and the fit are due to unidentified transitions.

In order to estimate the effect of unidentified transitions on the intensities, we added response functions where there are discrepancies. The fit of the spectrum obtained from this exercise is shown in figure 5.9. Four transitions are needed at least to avoid discrepancies, including three transitions in the region between 1 and 1.5 MeV. This has to be taken carefully as it does not mean that we missed four transitions in the spectrum. Of course, this exercise cannot take into account any doublet, unresolved by DALI2.

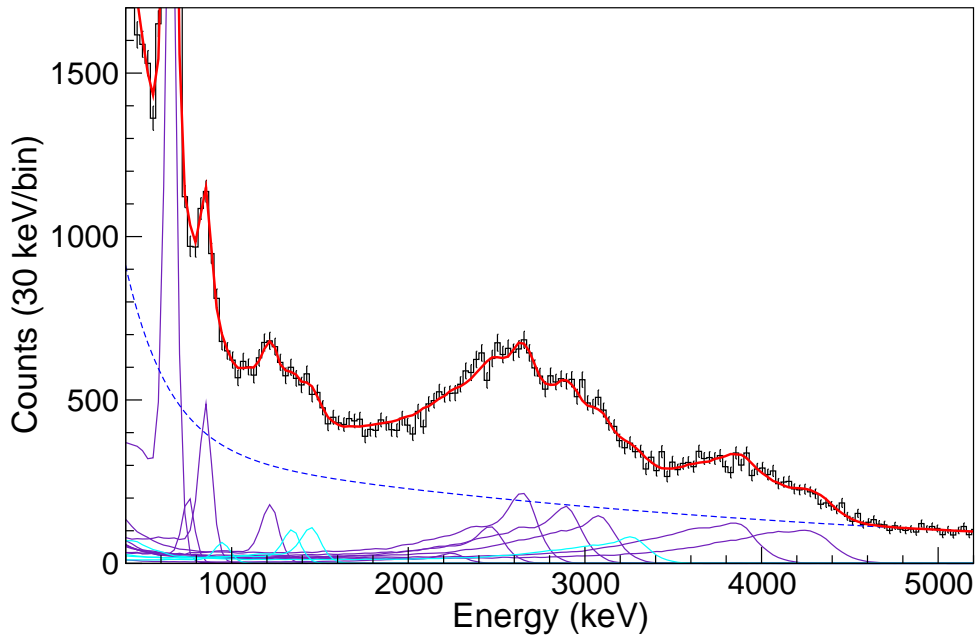


Figure 5.9 – Fit of the γ -ray spectrum of $(p,2p)^{79}\text{Cu}$ adding transitions (in cyan) where there were previously discrepancies.

The transitions identified in the $(p,2p)^{79}\text{Cu}$ spectrum and their respective intensities from the fits with (corrected intensities) and without (maximum intensities) the four added transitions are listed in table 5.4, taking into account all multiplicities. The uncertainty on the maximum intensities does not take into account any statistical uncertainty as they are fixed manually, except for the 3880 and 4300-keV transitions. The precise energy of the two clear peaks are found to be 656(5) and 855(6) keV, respectively.

Energy (keV)	Maximum I_γ (%)	Corrected I_γ (%)
656(5)	107(11)	100(11)
750(20)	11(1)	9(2)
855(6)	41(4)	33(4)
1220(30)	29(3)	16(4)
2240(40)	7(1)	4(2)
2440(40)	23(2)	21(3)
2600(40)	44(4)	40(7)
2940(60)	42(4)	33(6)
3070(30)	39(4)	28(6)
3880(40)	34(4)	34(4)
4300(40)	31(4)	31(4)

Table 5.4 – Transitions seen in the $^{80}\text{Zn}(p,2p)^{79}\text{Cu}$ spectrum. The maximum intensities come from the fit of the spectrum with the identified transitions only, while the corrected intensities come from the fit taking into account the discrepancies. The error bars for the intensity include the 10% uncertainty from the simulation. All intensities are normalized with respect to the corrected intensity of the 656-keV transition and take into account all multiplicities.

The intensity correction is very important for the 1220-keV transition as it is located in the region where there are the biggest discrepancies between the spectrum and the fit, as shown in figure 5.8. Moreover, several transitions are significantly affected by the addition of the response function at 3.3 MeV, due to the Compton tail of this transition that is important at such energies. The intensity of the 3880 and 4300-keV transitions remains unchanged as no discrepancy is found above 3.4 MeV.

5.2.4 γ - γ coincidences with background subtraction

Many transitions belonging to ^{79}Cu were found but the γ - γ relations from section 5.2.1 may not be all true coincidences as no background subtraction was performed so far. Now that we quantified the intensity of the 656 and 855-keV transitions, we can determine the amount of background below these two peaks, as shown in figure 5.10. The false coincidences due to this background are estimated by setting gates on both sides of each peak and the number of events contained in these two gates is normalized to the real amount of background. The spectra obtained from the gates are then added in order to obtain the background coincidence spectrum.

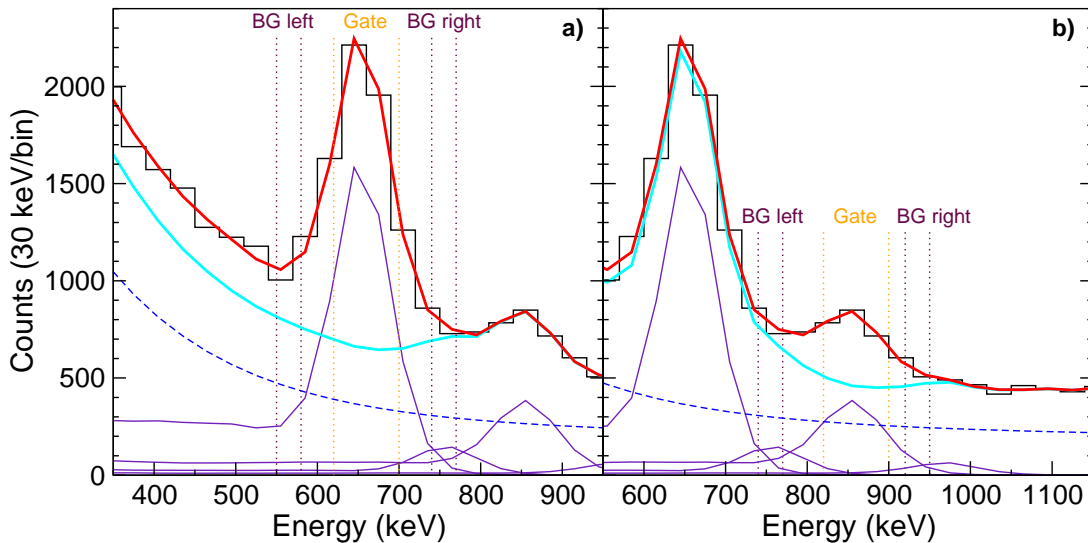


Figure 5.10 – Background below the (a) 656 and (b) 855-keV peaks in the spectrum with multiplicities 2 and 3. In cyan, the double-exponential function plus the other response functions than the peak considered, in orange, the gates used for the γ - γ coincidences and in maroon, the gates used for the background to subtract.

Contrary to standard analysis of γ - γ coincidences, we do not extract information directly from the coincidence spectrum after background subtraction: such a spectrum cannot be fitted as it does not obey Poisson statistics anymore (the likelihood fit described in section 4.1.1 cannot be used) and it has low statistics (the standard χ^2 method is not suitable). Moreover, there is no guarantee that the response functions after background

subtraction have the same shape than the response functions simulated in a standard decay process. Therefore, in the same way than in section 5.2.1, the background spectrum is fitted with response functions plus a double-exponential background, as shown in figure 5.11. Then, we can subtract the intensity of the transitions in the background spectrum to the intensity of the same transitions in the coincidence spectrum. Finally, the 2σ -significance criterion is applied: a transition is considered to be in coincidence with the peak for which the gate is set when its intensity after subtraction is at least two times greater than the statistical uncertainty.

The significance of each coincidence is given in table 5.5. The results show that all coincidences found in the coincidence spectra of section 5.2.1 are true coincidences, except the auto-coincidences and the 2360-keV transition in case of a gate on the 855-keV peak. The 750-keV peak is not seen in the two background spectra, which explains why the significance for this transition is the same before and after subtraction.

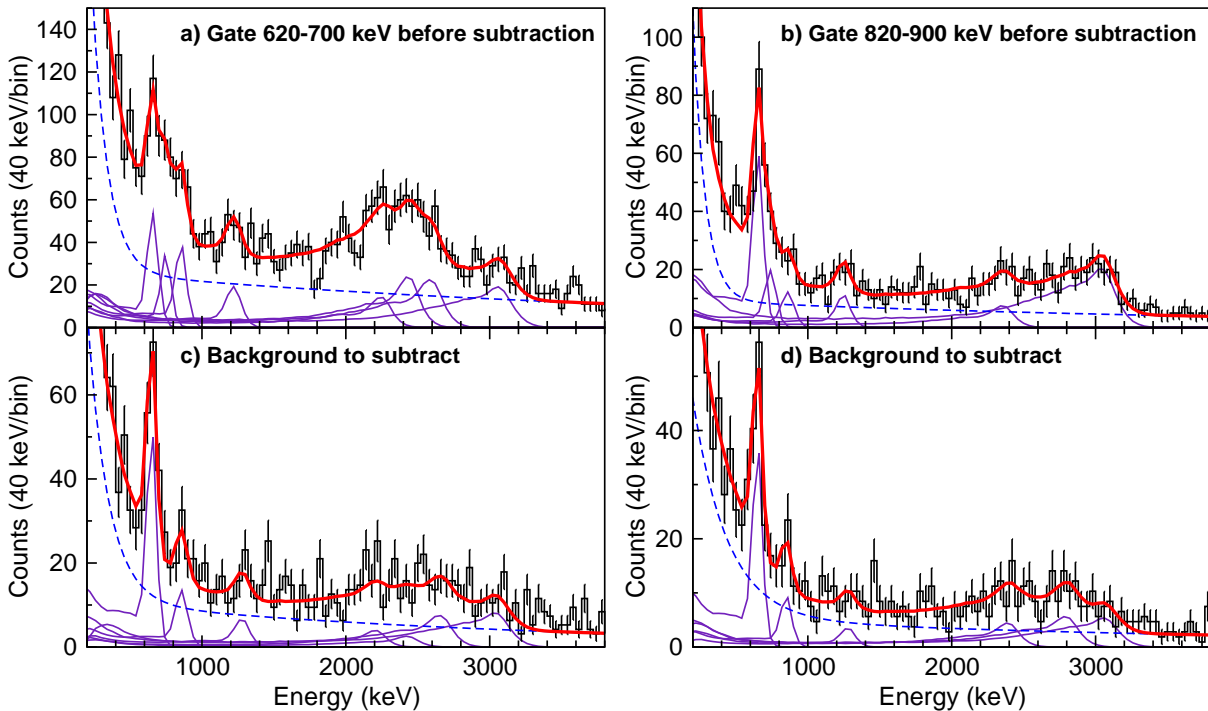


Figure 5.11 – Coincidence spectra before background subtraction for gates on the 656-keV (a) and the 855-keV (b) peaks and the associated background spectra to subtract, respectively (c) and (d).

E_γ (keV)	656	750	855	1220	2240	2360	2440	2600	3070
Coinc. 656	0.6	3.7	3.1	2.6	2.3	-	3.3	2.9	4.3
Coinc. 855	2.6	3.5	0.8	2.2	-	1.4	-	-	6.5

Table 5.5 – Statistical significance ($I_\gamma/\sigma_{I_\gamma}$) of the coincidences with the 656 and 855-keV transitions, after background subtraction. The coincidences rejected are in bold.

The coincidence spectrum after background subtraction is shown in figure 5.12. The fit is given as an illustration but is not used to extract information, as explained before.

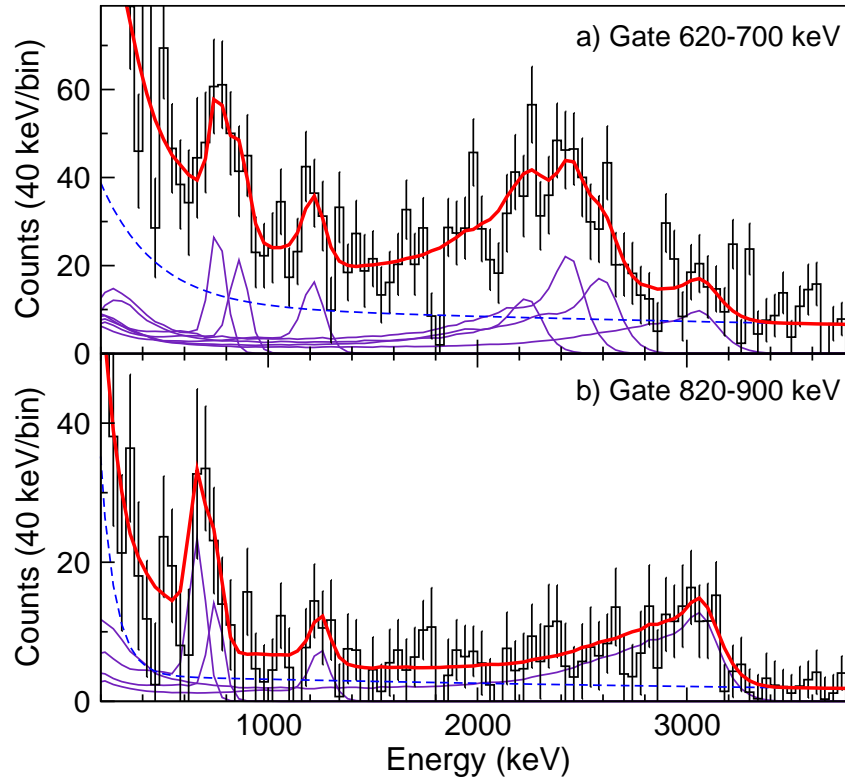


Figure 5.12 – γ - γ coincidence spectra after background subtraction for a gate set on the 656-keV (a) and 855-keV (b) transitions. The fit is given as an illustration.

Limitations

Taking the background on both sides of the peak in this case has two limitations. On the left side of the 656-keV peak, there is its own Compton tail that will induce true coincidences in the background spectrum, and on the right side, there is a part of the 750-keV peak that induces an excess of coincidences that are not linked to the background. These two limitations are present on the left side of the 855-keV peak, plus the possible presence of a peak on its right side. The consequence of such limitations is that it could overestimate the intensity of some peaks in the background coincidence spectrum and thus lead to the rejection of a weak but true coincidence.

Finally, due to the low statistics, we could have statistical fluctuations leading to the misidentification of coincidences that should normally be rejected. To prevent that, we tried different gates for the background to subtract, that we shifted up to 50 keV from the gates shown in figure 5.10. Some examples of coincidence spectra after subtraction are shown in figures 5.13 and 5.14. In each case, the coincidences previously established are confirmed, only the relative intensities between the transitions vary. We also tested different gate widths, and there is no impact on the conclusions.

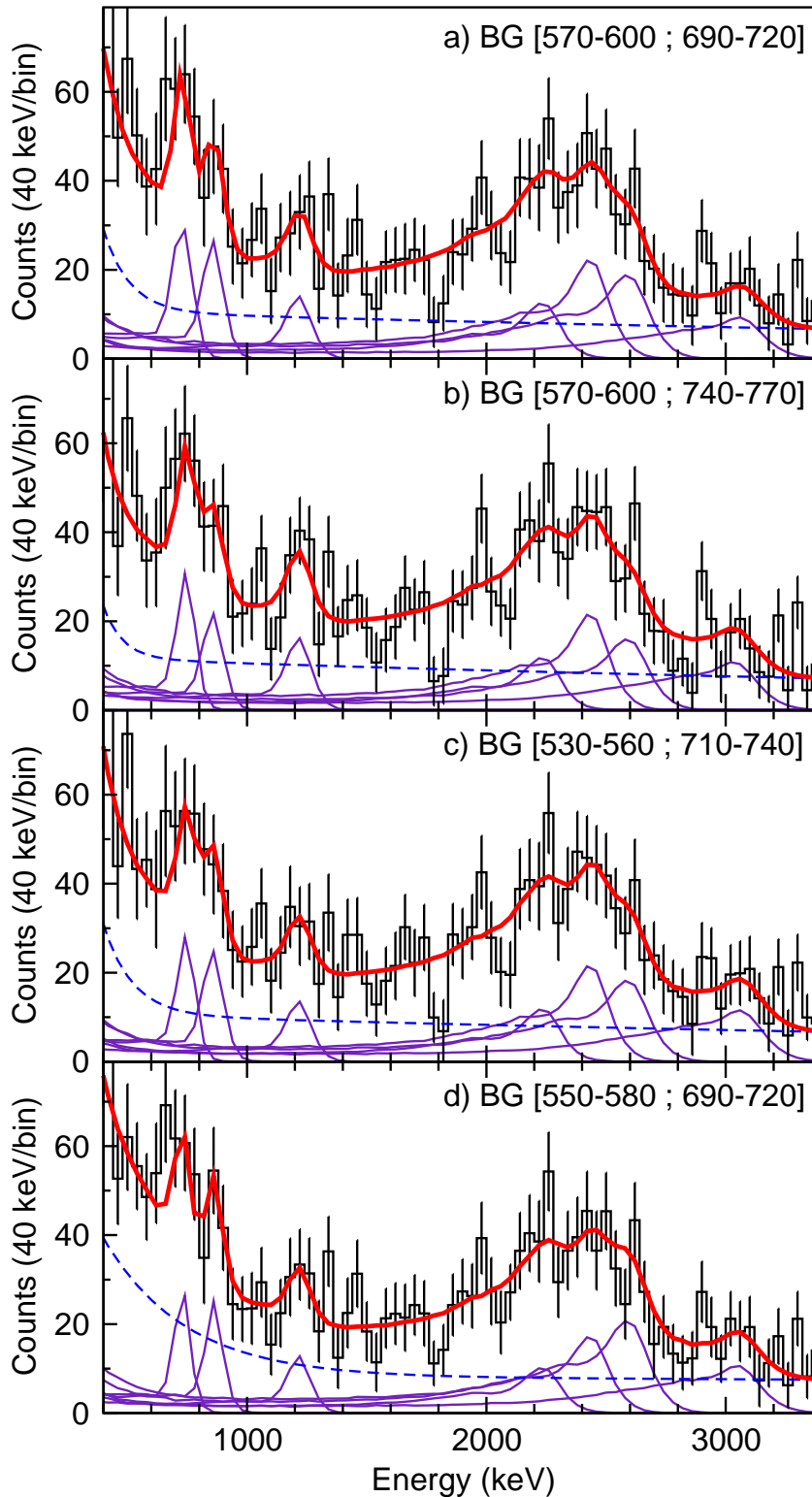


Figure 5.13 – γ - γ coincidence spectra after background subtraction for a gate set on the 656-keV peak, using different gates for the background. Although the intensities of the transitions in coincidence may vary, they remain present.

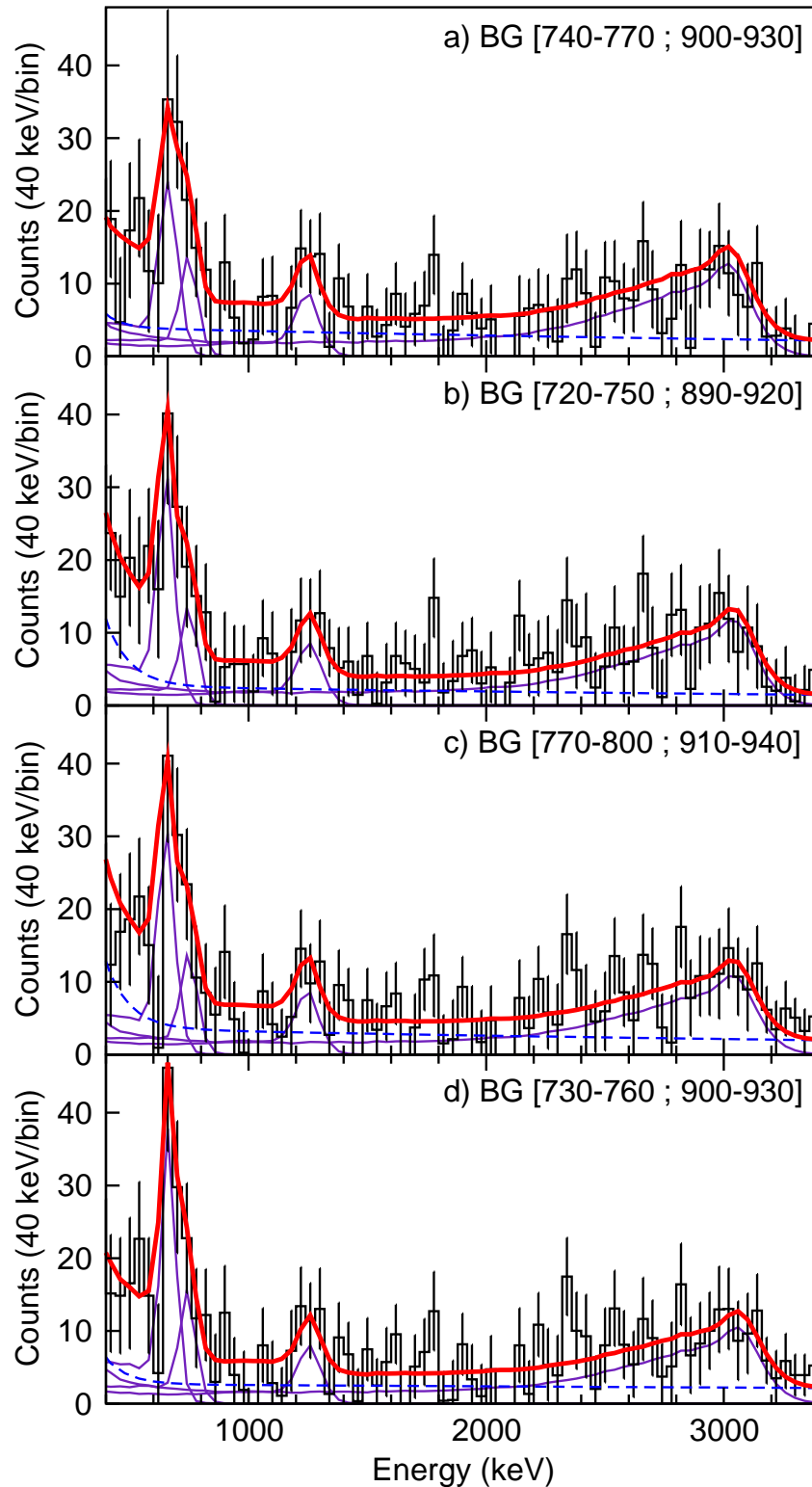


Figure 5.14 – γ - γ coincidence spectra after background subtraction for a gate set on the 855-keV peak, using different gates for the background. The coincidence with the 2360-keV transition always disappears while the other coincidences are confirmed.

5.2.5 Summary

The information extracted from this procedure is summed up in table 1 and will be used for building the level scheme in the next section. The discrepancies between the fit and the data indicate that other transitions are present in the spectrum. As it was not possible to identify them, and in order to avoid wrong guesses, we did not try to speculate on the number of missing peaks nor their energy.

Energy (keV)	Intensity (relative)
656(5) [†]	100(11)
750(20) ^{*,†}	9(2)
855(6) [*]	33(4)
1220(30) ^{*,†}	16(4)
2240(40) [*]	4(2)
2440(40) [*]	21(3)
2600(40) [*]	40(7)
2940(60)	33(6)
3070(30) ^{*,†}	28(6)
3880(40)	34(4)
4300(40)	31(4)

*Transitions in coincidence with the 656-keV transition.

†Transitions in coincidence with the 855-keV transition.

Table 5.6 – Transitions firmly identified in the $^{80}\text{Zn}(p,2p)^{79}\text{Cu}$ spectrum, with their estimated intensity and their coincidence relations. Intensities are normalized with respect to the intensity of the 656-keV transition.

5.3 Level scheme

The proposed level scheme for ^{79}Cu , based on the γ - γ coincidences and the intensities given in table 1, is shown in figure 5.15.

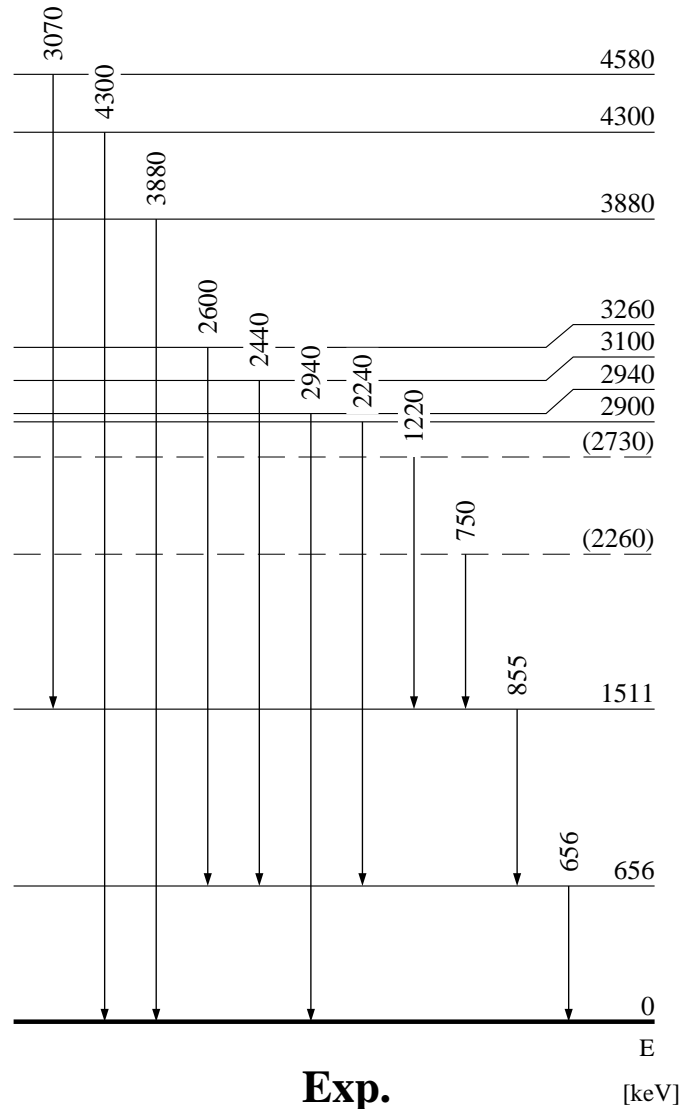


Figure 5.15 – Proposed level scheme for ^{79}Cu .

5.3.1 Placement of the transitions

656 and 855-keV transitions

Considering the intensities of the 656 and 855-keV transitions and their coincidence relations, the latter is placed on top of the former. No γ transition was seen below 656 keV, while it was possible elsewhere in the data set to detect peaks down to 200 keV, like for example in ^{77}Cu and ^{81}Ga as shown in figure 5.16. Therefore, we place the first excited state of ^{79}Cu at 656(5) keV and the second one at 1511(8) keV. A direct decay of the

1511-keV level to the ground state cannot be excluded but has not been observed: if such a transition exists, its intensity is at least three times smaller than the intensity of the 855-keV transition, considering the statistics around 1.5 MeV that we see the spectrum in figure 5.8. Such a transition could also explain the slight excess of statistics visible at 1.5 MeV in figure 5.7.

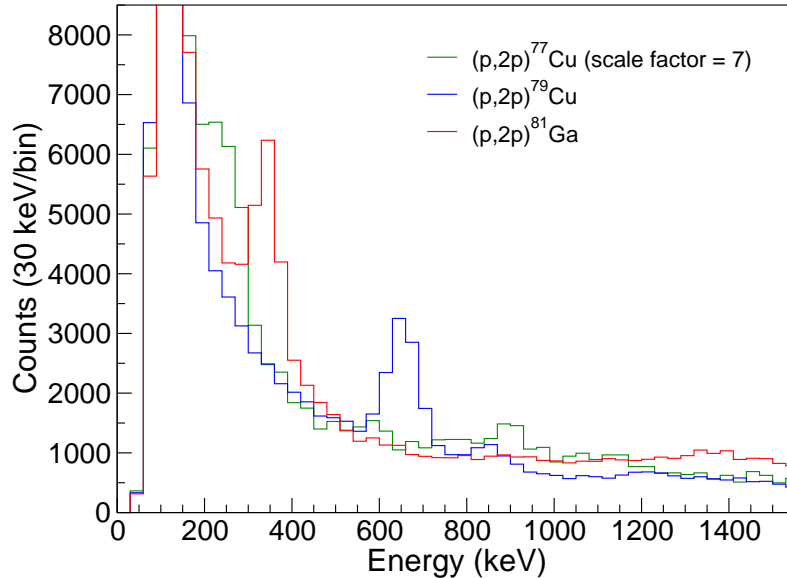


Figure 5.16 – Low-energy (p,2p) spectra of ^{77}Cu , ^{79}Cu and ^{81}Ga coming from the same data set. Despite the important background, peaks can be observed at low energy. A scale factor has been applied to the ^{77}Cu spectrum for the sake of clarity.

Transitions in coincidence with both the 656 and the 855-keV ones

The 750, 1220 and 3070-keV transitions, found in coincidence with both the 656 and 855-keV transitions, are placed on top of the 1511-keV level. This gives three levels at 2260(20), 2730(30) and 4580(30) keV respectively. The 2260 and 2730-keV levels are shown as dashed lines because they could be situated higher up in the level scheme since we cannot exclude the coincidence of the 750 and 1220-keV transitions with other γ rays due to low statistics and resolution: γ - γ coincidences with a gate on the 750-keV peak cannot be performed as it is mixed with the edges of the 656 and 855-keV peaks, and the 1220-keV peak is in a region where we cannot determine precisely the amount of background.

Looking at the γ - γ coincidences matrix in figure 5.2, we can see an accumulation of statistics at the junction of the 1.1-1.5 MeV and 2.4-3.0 MeV intervals. This could indicate a possible coincidence of the 1220-keV transition with some γ rays between 2.4 and 3 MeV. In figure 5.17, two coincidence spectra without background subtraction are shown, one with a gate on the 1220-keV peak and another one on its right side, around 1.4 MeV. There is no evidence for a 750-keV peak in the spectra, which excludes a 750-1220 coincidence. A transition at 2740(30) keV is observed but we cannot confirm this

coincidence relation as this transition is also seen for the gate set around 1.4 MeV and the background is not quantified below the 1220-keV peak, preventing us from making any reliable background subtraction. Although the energy of 2740 keV corresponds to the sum of 656+855+1220 keV within the error bars, we prefer not to place this transition in the level scheme because the coincidence relations are inconclusive.

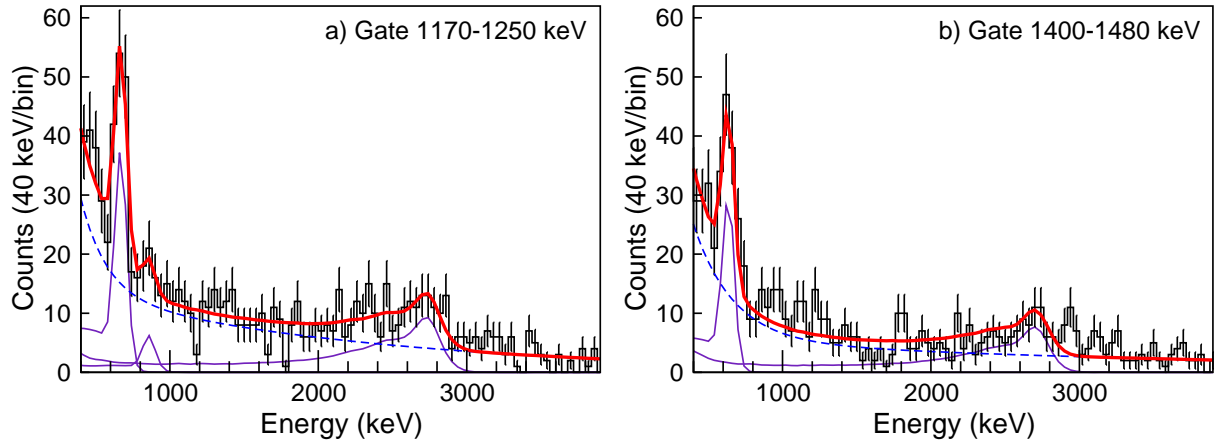


Figure 5.17 – γ - γ coincidence spectra for gates set on the 1220-keV transition (left) and around 1400 keV (right). A 2.7 MeV transition can be seen in both spectra.

Transitions to the ground state

The 2940, 3880 and 4300-keV transitions are not seen in the 656 and 855-keV coincidence spectra and were observed in the spectrum that favours high-energy transitions to the ground state shown in figure 5.7. Therefore, we place three levels at 2940(60), 3880(40) and 4300(40) keV that decay directly to the ground state.

Transitions in coincidence with the 656-keV one only

The 2240, 2440 and 2600-keV transitions were found in coincidence with the 656-keV transition only. No reverse gate can be set in this energy range of the spectrum because of the large overlap of the peaks. But according to the γ - γ coincidences matrix in figure 5.2, there is no coincidence between any of these three transitions and another transition than the 656-keV one: the accumulation of statistics at the junction of the 2.2-2.6 MeV and 0.8-1.5 MeV intervals is due to the Compton tail of other transitions, like the 2740 and 3070-keV ones that are mentioned in the previous paragraph, and no such accumulation is observed at higher energy than 1.5 MeV. Therefore, the 2240, 2440 and 2600-keV transitions are placed on top of the 656-keV level, creating excited states at 2900(40), 3100(40) and 3260(40) keV respectively. One can notice that the 2900(40)-keV level could correspond to the 2940(60)-keV one as the error bars are large.

2360-keV transition

Finally, a transition at 2360 keV was observed in the coincidence spectrum for a gate set on the 855-keV peak, but the coincidence relation between them was rejected after

background subtraction. Moreover, there is no 2360-keV peak observed in the spectrum favouring high-energy transitions to the ground state shown in figure 5.7. This means either that the transition is too weak to be observed in such a spectrum or that we missed coincidence relations with this 2360-keV transition. Therefore, its placement being too uncertain, we decided not to put it on the level scheme. This is also why we did not include this transition in the fit of the spectrum in figure 5.8, where we used only firm transitions that we can place on the level scheme, at least tentatively.

5.3.2 Influence of levels half-lives

No information about the half-lives of levels was available and therefore we considered all decays to be prompt: the Doppler correction is applied by taking the reaction vertex as the emission point. Considering the geometry of the setup, a half-life of several tens of picoseconds shifts the energy of the transitions toward lower energies by a few percent. It also increases the width of the photopeak. As an example, the effect of the half-life on a 650-keV transition was simulated and is shown in figure 5.18(a). In case of a perfect Doppler correction, the corrected energy should be the same whatever the angle of γ emission. Consequently, comparing the peaks from the spectra obtained with the DALI2 crystals at backward and forward angles can give hints on the half-life of the 656 and 855-keV peaks. From the spectra in figure 5.18(b), there is a difference of 8(7) keV between backward and forward angles for the 656-keV peak, and 11(9) keV for the 855 keV one. This corresponds respectively to a half-life of 50_{-50}^{+60} and 40_{-40}^{+50} ps according to the simulation and such large error bars prevent us from any conclusion. But if such a half-life effect could induce an energy-shift of a few percent, it would not affect the placement of the transitions in the level scheme.

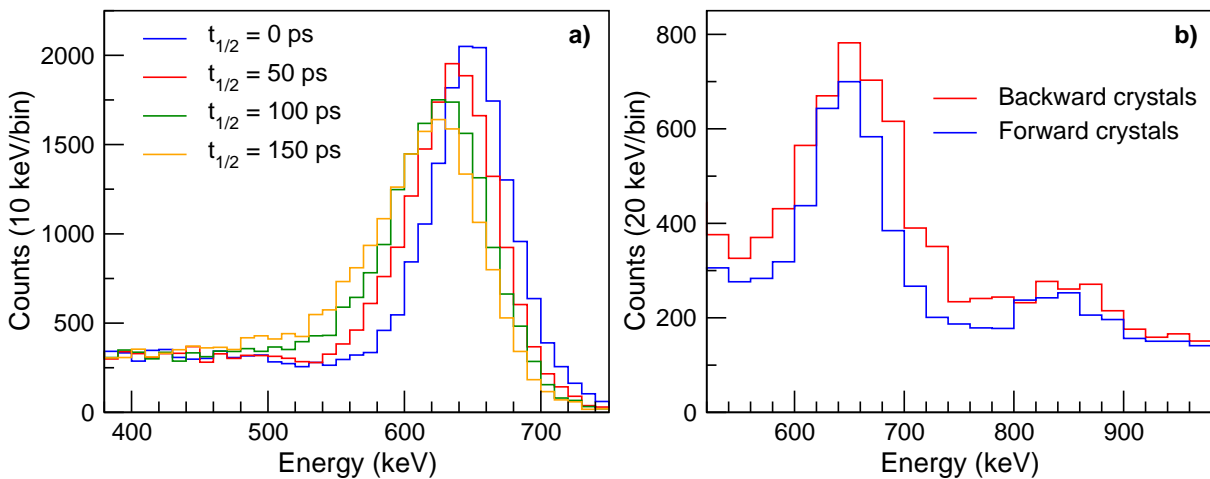


Figure 5.18 – (a) Simulated response functions of a 650-keV transition for different half-lives. (b) γ -ray spectrum of $(p,2p)^{79}\text{Cu}$ obtained with 60 backward (in red) and 60 forward (in blue) crystals of DALI2. The backward peaks have a larger width because backward crystals have a worse intrinsic resolution.

5.3.3 Knockout feeding

The knockout feeding of the 656-keV level, obtained by subtracting the intensities of the transitions going in (855, 2240, 2440 and 2600 keV) to the intensity of the 656-keV transition going out, is compatible with zero: we find 2(14), from the intensities given in table 1. Because of the large uncertainty, we cannot exclude direct knockout feeding to this level. A transition at 2360 keV and one at 2740 keV would imply a lower intensity for the 2440-keV and 2600-keV transitions, respectively, increasing the feeding value of the 656-keV level. In this perspective, the intensities of the 656 and 855-keV transitions are reliable as the peaks are well defined, but the intensities of the other transitions have to be seen as maximum values.

As regards the knockout feeding of the 1511-keV level, we obtain a negative value of -20(8). Three possibilities can explain the negative feeding. (i) There is possible existence of a 1511-keV transition to the ground state, for which we find an upper limit of 10(2) for its intensity if we include a 1.5-MeV response function to the fit in figure 5.8. (ii) If the 750 or 1220-keV transitions are located higher up in the level scheme, the knockout feeding would increase. (iii) As said before, the intensities of the 750, 1220 and 3070-keV transitions are maximum values that could be lowered by non-identified transitions. On the other hand, a strong knockout population of this level is unlikely as it is fed by the intense 3070-keV transition. We therefore consider that the 1511-keV level have a knockout feeding compatible with zero.

Concerning the states above 1.5 MeV, we do not observe any transition between them. The knockout feeding of each level is then taken as the intensity of its emitted γ -ray, keeping in mind that unidentified transitions could alter these values.

5.4 Cross sections calculation

5.4.1 Inclusive cross sections

The cross section is an effective area representing the probability of interaction between two particles. In the case of the $^{80}\text{Zn}(p,2p)^{79}\text{Cu}$ knockout reaction, its probability is given by the inclusive cross section:

$$N(^{79}\text{Cu}) = \sigma_{inc} n_t N(^{80}\text{Zn}) \quad (5.1)$$

with $N(^{80}\text{Zn})$ the number of ^{80}Zn nuclei entering the MINOS target, $N(^{79}\text{Cu})$ the number of ^{79}Cu nuclei produced in the target and n_t the number of target nuclei per cm^2 in the target, given as follow:

$$n_t = \frac{\rho_{target} L_{target} N_A}{M_H} = 4.32(4) \times 10^{23} \text{ cm}^{-2} \quad (5.2)$$

with $\rho_{target} = 70.97 \text{ kg/m}^3$ the target density, $L_{target} = 102(1) \text{ mm}$ the target length, $N_A = 6.02 \times 10^{23} \text{ atoms/mol}$ and $M_H = 1.008 \text{ g/mol}$ the hydrogen molar mass. As explained in section 3.7, $N(^{80}\text{Zn})$ and $N(^{79}\text{Cu})$ are not accessible directly as we measure only the number of ^{80}Zn nuclei in BigRIPS and the number of ^{79}Cu in ZeroDegree, and we have to take into account the transmission of the beam line. The inclusive cross section is therefore

$$\sigma_{inc} = \frac{N_{\text{ZD}}(^{79}\text{Cu})}{N_{\text{BR}}(^{80}\text{Zn})} \frac{1}{T} \frac{1}{n_t} \quad (5.3)$$

with $T = \varepsilon_{tr} \varepsilon_{line} \varepsilon_{loss}$ the total transmission of the beam line. We explained in section 3.7.4 how we measure $\varepsilon_{line} \varepsilon_{loss}$ as well as $N_{\text{ZD}}(^{79}\text{Cu})/N_{\text{BR}}(^{80}\text{Zn})$ when $\varepsilon_{tr} = 1$, and we obtain the following inclusive cross section for the $^{80}\text{Zn}(p,2p)^{79}\text{Cu}$ knockout reaction in our experiment:

$$\sigma_{inc} = 7.9(4) \text{ mb} \quad (5.4)$$

This value takes into account all final states populated in ^{79}Cu and is the starting point for calculating exclusive cross sections.

5.4.2 Exclusive cross sections

The exclusive cross section represents the probability to populate directly a given state in a reaction. It is therefore a fraction of the inclusive cross section, which is the total probability of the reaction disregarding the final state of the created nucleus. As explain in section 1.5.1, we can write it as

$$\sigma_{exc}(J^\pi) = b.r.(J^\pi) \sigma_{inc} = \frac{\sum_{\gamma_{out}} I_{\gamma_{out}}(J^\pi) - \sum_{\gamma_{in}} I_{\gamma_{in}}(J^\pi)}{N_{nuclei}} \sigma_{inc} \quad (5.5)$$

with I_γ^{in} and I_γ^{out} the intensity of the γ rays that feed and leave the J^π state, respectively, and N_{nuclei} the total number of ^{79}Cu nuclei produced in the (p,2p) channel, including events with a multiplicity equal to zero (no γ ray observed in DALI2). We immediately see that the exclusive cross-sections calculation requires a precise measurement of the γ -rays intensities, which is a limitation in our case. The exclusive cross sections of each state is given in table 5.7, and we put the value for the 1511-keV to zero. These values will be compared to theoretical calculations in the next chapter, but we can already make a few comments.

The exclusive cross sections of the 3880 and 4300-keV levels are the safest to calculate. Indeed, these states being close to the evaluated neutron separation energy (esimated $S_n = 5310(590) \text{ keV}$ [24]), they are less subject to feeding from states lying at higher energy. Moreover, the two transitions at 3880 and 4300-keV are enough to fit the spectrum in the interval between 3.4 and 4.5 MeV and are sufficiently separated for giving an intensity more precise than for example the 3070-keV transition which is close to the

2940-keV transition. For the other states that those at 3880 and 4300 keV, one has to be more careful about the exclusive cross sections since they are subject to all uncertainties discussed for γ -ray intensities. For the ground state, we can calculate an upper limit: in this case, the knockout feeding corresponds to the total number of ^{79}Cu nuclei minus the intensity of the 656, 2940, 3880 and 4300-keV transitions, and could be lower if we did not identify some transitions to the ground state.

Energy levels (keV)	σ_{exc} (mb)
0	< 3.8(8)
656(5)	0.04(29)
1511(8)	0
2260(20)	0.19(4)
2730(30)	0.33(9)
2900(40)	0.08(4)
2940(60)	0.69(13)
3100(40)	0.44(7)
3260(40)	0.84(15)
3880(40)	0.71(9)
4300(40)	0.65(9)
4580(30)	0.58(13)

Table 5.7 – Exclusive cross sections from the (p,2p) ^{79}Cu reaction for each state. The values are subject to be influenced by non-observed transitions.

Chapter 6

Interpretation and discussion

This last chapter deals with the comparison of our experimental results with shell-model calculations. The interpretation of the level scheme is done, as well as tentative calculations of spectroscopic factors. The final part summarizes both experimental and theoretical facts, and we conclude on the nature of the ^{79}Cu nucleus.

6.1 Monte-Carlo shell-model calculations

Monte-Carlo shell-model (MCSM) calculations [93,94] were performed by Y. Tsunoda and T. Otsuka (University of Tokyo, Japan). We present briefly the interaction used, before giving the results for the case of ^{79}Cu .

6.1.1 Valence space and interaction

The calculations were performed considering an inert core of ^{40}Ca plus 9 valence protons and 30 valence neutrons. The valence space, called $pf g_9 d_5$, was composed of the $1f_{7/2}$, $1f_{5/2}$, $2p_{3/2}$, $2p_{1/2}$, $1g_{9/2}$, $2d_{5/2}$ orbitals for both protons and neutrons, without any truncation within this space. This large valence space allows particle-hole excitations across the $Z = 28$ and $N = 50$ gaps, which were found to be needed for a correct description of experimental data, as explained in section 1.4.

The interaction used in this model space was the A3DA effective interaction [94], whose part of the two-body matrix elements (TBME) are taken from already existing interactions: the TBME of the pf shell come from the GXPF1A interaction [95], originally developed for light pf shell nuclei like neutron-rich titanium and calcium isotopes, and those of the $f_5 p g_9$ related to the $g_{9/2}$ orbital are taken from the JUN45 interaction [58], already mentioned in section 1.4. Previous experimental results obtained in the vicinity of ^{78}Ni are correctly reproduced within this theoretical framework, like the yrast states in the neutron-rich nickel isotopic chain [96] and the structure of $^{80,82}\text{Zn}$ [36] and of ^{77}Cu [49].

6.1.2 Results for ^{79}Cu

The energy levels obtained for ^{79}Cu by the MCSM calculations are compared to our experimental level scheme in figure 6.1.

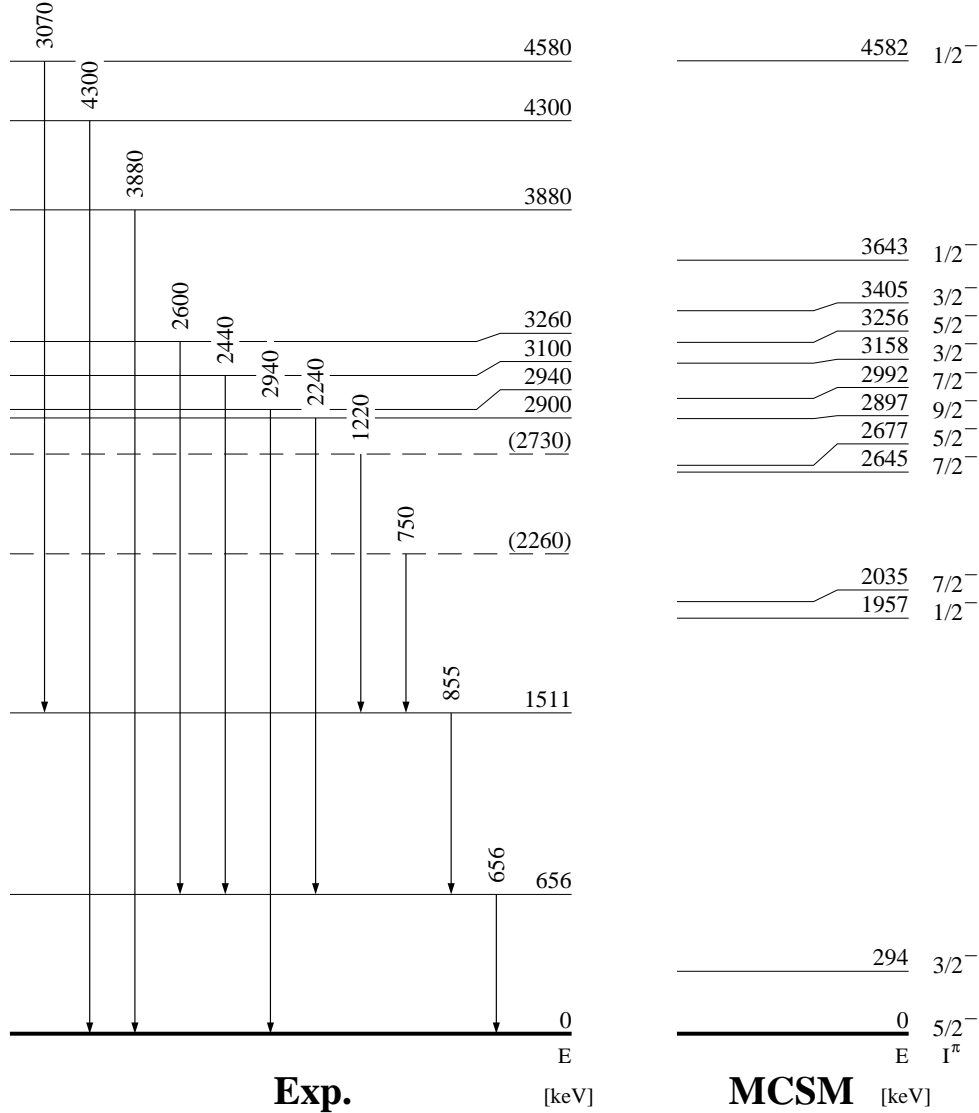


Figure 6.1 – Experimental level scheme (left) of ^{79}Cu compared to the Monte-Carlo shell-model (MCSM) calculations (right).

The calculated occupation numbers of neutron and proton orbits for the wave functions of the ground state of ^{80}Zn as well as for the lowest and the three first $7/2^-$ states in ^{79}Cu are given in table 6.1. Spectroscopic factors, defined in section 1.5.1 and corresponding in our case to the overlap between the ^{80}Zn (initial) and ^{79}Cu (final) wave functions, are also given. The ground state of ^{80}Zn has the $\nu g_{9/2}$ and $\pi f_{7/2}$ orbitals almost full, as expected in the extreme shell-model representation, and two protons located in the $\pi f_{5/2}$ and $\pi p_{3/2}$ orbitals.

	E (MeV)	J^π	$\pi f_{7/2}$	$\pi f_{5/2}$	$\pi p_{3/2}$	$\pi p_{1/2}$	$\pi g_{9/2}$	$\pi d_{5/2}$	$\nu g_{9/2}$	$\nu d_{5/2}$	S_{th}
^{79}Cu	0	$5/2^-$	7.73	1.05	0.15	0.02	0.03	0.01	9.83	0.21	1.33
	0.294	$3/2^-$	7.73	0.17	1.02	0.03	0.04	0.01	9.85	0.19	0.57
	1.957	$1/2^-$	7.57	0.47	0.29	0.62	0.03	0.01	9.06	0.97	0.04
	2.035	$7/2^-$	6.82	1.49	0.57	0.04	0.07	0.01	9.72	0.31	5.58
	2.645	$7/2^-$	7.22	1.09	0.61	0.03	0.04	0.01	9.26	0.78	0.15
	2.992	$7/2^-$	7.54	1.00	0.37	0.05	0.03	0.00	9.02	1.01	0.43
^{80}Zn	0	0^+	7.66	1.43	0.73	0.06	0.10	0.01	9.81	0.23	—

Table 6.1 – Occupation numbers of the $pf g_9 d_5$ proton orbits and $g_9 d_5$ neutron orbits, along with the calculated spectroscopic factors (S_{th}), for the lowest and the three first $7/2^-$ calculated states in ^{79}Cu , as well as for the ground state of ^{80}Zn .

The dominant configurations that compose the wave function of the ground state of ^{80}Zn and of the lowest states in ^{79}Cu are given in table 6.2. We can notice that 69% of the wave function of the ^{80}Zn ground-state is built from a pair of protons either in the $\pi f_{5/2}$ or the $\pi p_{3/2}$ orbitals. The 31% left contain many different configurations with particle-hole excitations across the $Z = 28$ and/or $N = 50$ gaps leading to a spin 0^+ , but none of these configurations taken individually exceeds 4% of the total wave function. The first four calculated states for ^{79}Cu have an important single-particle (single-hole) character, while the calculated states above 2.6 MeV shown in figure 6.1 are mainly core-coupling states, i.e. resulting from the coupling of a proton to an excited ^{78}Ni core.

	E (MeV)	J^π	Composition
^{79}Cu	0	$5/2^-$	75% $ 0^+ \otimes \pi f_{5/2}\rangle$
	0.294	$3/2^-$	74% $ 0^+ \otimes \pi p_{3/2}\rangle$
	1.948	$1/2^-$	48% $ 0^+ \otimes \pi p_{1/2}\rangle$
	2.043	$7/2^-$	64% $(\pi f_{5/2} p_{3/2})^2 \pi f_{7/2}^{-1}$
^{80}Zn	0	0^+	47% $ \pi f_{5/2}^2\rangle_{0^+}$
			22% $ \pi p_{3/2}^2\rangle_{0^+}$

Table 6.2 – Dominant component of the wave functions the lowest calculated states in ^{79}Cu and for the ground state of ^{80}Zn .

The evolution of the proton ESPE, defined in section 1.1.3, in the nickel chain when filling the $\nu g_{9/2}$ orbital is shown in figure 6.2. The inversion of ground-state spin measured in ^{75}Cu [46] is correctly reproduced by the MCSM calculations, but the inversion of the $\pi p_{3/2}$ and $\pi f_{5/2}$ ESPE is predicted to happen in ^{77}Cu . This means that the use of such a large valence space as $pf g_9 d_5$ includes further correlation effects, in comparison to the previous calculations described in section 1.4, which are reflected in the multipole inter-

action. In other words, the wave-function of the $5/2^-$ ground-state in ^{75}Cu is calculated to have a significant collective character. The calculations predict that this collectivity is reduced in $^{77,79}\text{Cu}$ and consequently, for these two isotopes, the first $3/2^-$ and $5/2^-$ are mainly single-particle states, as reflected in their wave function components given in table 6.2 for ^{79}Cu . As explained in section 1.4, this inversion of the $\pi p_{3/2}$ and $\pi f_{5/2}$ orbitals is found to be mainly due to the tensor force, which reduces the energy gap between the $\pi f_{7/2}$ and $\pi f_{5/2}$ orbitals when filling the $\nu g_{9/2}$ one.

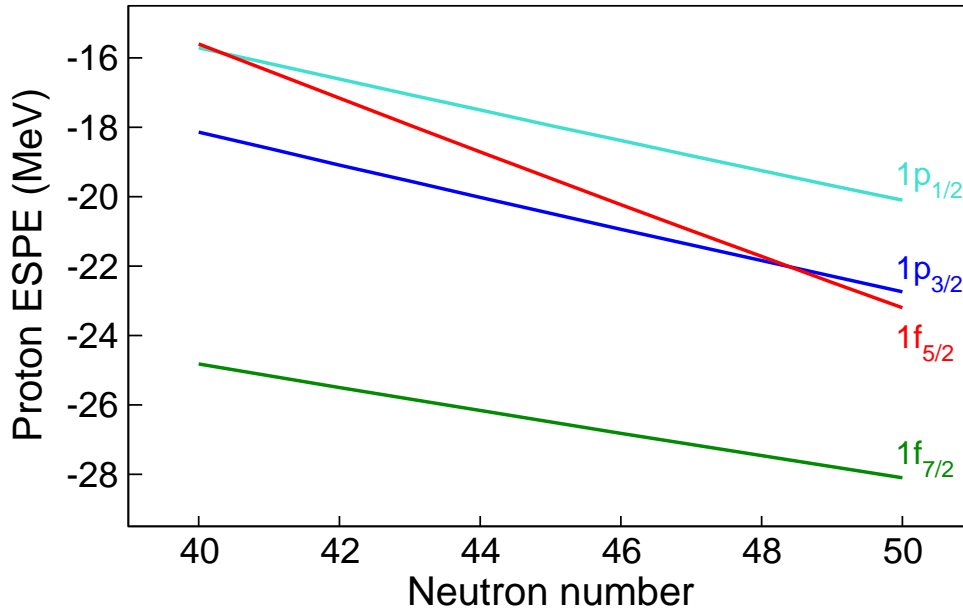


Figure 6.2 – Evolution of the proton ESPE as a function of the neutron number in the nickel isotopic chain.

6.2 Interpretation of the level scheme

As explained in section 3.8, it was not possible to measure the spin of the states in this experiment. Nevertheless, we can still derive an interpretation of the level scheme from both experimental arguments and shell-model calculations. As mentioned previously, the ground state of ^{80}Zn is characterised by a proton component distributed over the $\pi f_{5/2}$ and $\pi p_{3/2}$ orbitals in the calculations. The unpaired proton in ^{79}Cu is thus expected to reside mainly in the pf orbitals after one-proton removal from ^{80}Zn , and therefore generates negative-parity final states.

6.2.1 Ground state and first excited state

We propose a $5/2^-$ spin for the ground state of ^{79}Cu and a $3/2^-$ spin for the first excited state at 656 keV from the systematics of the copper isotopic chain, shown in figure 6.3, as well as the systematics of the $N = 50$ isotonic chain above ^{79}Cu [12, 51, 52].

The possibility to populate such a $3/2^-$ excited state in this experiment is confirmed by the observation in the same data set of the ground state transition of the first $3/2^-$ state in ^{77}Cu and ^{81}Ga , at 293 [49] and 351 keV [51] respectively, as shown in figure 5.16 in the previous chapter.

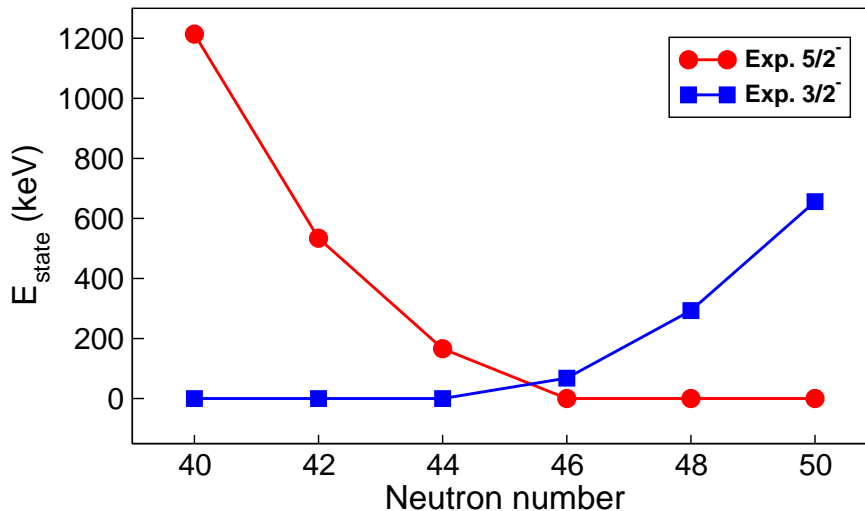


Figure 6.3 – Systematics of the first $3/2^-$ and $5/2^-$ states in neutron-rich copper isotopes from $N = 40$ to $N = 50$. The error bars are smaller than the data points. Data taken from references [43, 46–50] and this work.

The present MCSM calculations support this proposed assignment for the two lowest levels, as shown in figure 6.1. The calculated wave functions for these two $5/2^-$ and $3/2^-$ states, given in table 6.2, have a strong $\pi f_{5/2}$ (75%) and $\pi p_{3/2}$ (74%) single-particle character, respectively. The population of such a $\pi p_{3/2}$ single-particle state in the knock-out reaction is made possible by the wave function of the ^{80}Zn ground state that has a non-negligible component built from two protons in the $\pi p_{3/2}$ orbital, while it would be impossible in the extreme shell-model representation.

To conclude, from the comparison with ^{77}Cu [48, 49], the $3/2^-$ level is seen to rise, illustrating the continuation of the inversion between the $\pi p_{3/2}$ and $\pi f_{5/2}$ orbitals known from the preceding copper isotopes.

6.2.2 Second excited state

For the second excited state at 1511 keV, the MCSM calculations offer two possibilities: a $1/2^-$ state at 1957 keV, with a significant $\pi p_{1/2}$ single-particle character of 48%, or a $7/2^-$ state at 2035 keV, whose 64% of the wave function is built from a $\pi f_{7/2}^{-1}$ hole and two protons in $\pi f_{5/2} p_{3/2}$. The absence of direct feeding to the 1511 keV state in the knockout reaction disfavours the $7/2^-$ assignment, for which the calculated spectroscopic factor is very large: 5.58 over a total of 8 maximum. With such a high value, we would expect an

important knockout population that we do not observe. In addition, this absence of direct feeding is in agreement with the zero spectroscopic factor calculated for the $1/2^-$ state.

Another argument comes from the transition rates for a de-excitation of the 1511-keV state to the first $3/2^-$ level and the $5/2^-$ ground state. From the $B(M1)$ and $B(E2)$ values calculated by the MCSM and using equation 1.19 with both experimental and calculated energies, we obtain the expected transition rates given in table 6.3.

$i \rightarrow f$	$B(M1) (\mu_N^2)$	$B(E2) (e^2 \text{ fm}^4)$	$\lambda(E_{th}) (\text{ps}^{-1})$	$\lambda(E_{exp}) (\text{ps}^{-1})$
$1/2_1^- \rightarrow 5/2_{gs}^-$	—	317.3	10.91	3.06
$1/2_1^- \rightarrow 3/2_1^-$	0.078	166.9	8.74	0.95
$7/2_1^- \rightarrow 5/2_{gs}^-$	0.063	17.5	10.18	3.98
$7/2_1^- \rightarrow 3/2_1^-$	—	16.7	0.33	0.01

Table 6.3 – Reduced transition probabilities calculated by the MCSM and the corresponding transition rates, $\lambda = \lambda(M1) + \lambda(E2)$, using calculated and experimental energies.

The ratios of these calculated transition rates as well as the experimental value are given in table 6.4 for comparison. We also mention the ratios in case of pure single-particle states, obtained from the Weisskopf estimates given in equation 1.20. As already explained in section 5.3.3, a 1511-keV transition cannot be excluded and we found an upper limit of 10(2) for its intensity, compared to 33(4) for the 855-keV transition. This corresponds to a maximum ratio of 0.30(7), which is much closer to the expected value for $1/2^-$ than for $7/2^-$.

Ratio	MCSM (E_{th})	MCSM (E_{exp})	Pure s.p.	This work
$\frac{\lambda(1/2_1^- \rightarrow 5/2_{gs}^-)}{\lambda(1/2_1^- \rightarrow 3/2_1^-)}$	1.2	3.2	0.01	< 0.30(7)
$\frac{\lambda(7/2_1^- \rightarrow 5/2_{gs}^-)}{\lambda(7/2_1^- \rightarrow 3/2_1^-)}$	31	427	9393	

Table 6.4 – Ratio of the transition rates, considering the MCSM calculations, the Weisskopf estimates and the value from this work.

Thus, we suggest a spin $1/2^-$ for the 1511-keV state and the low ratio of 0.30(7) is compatible with the significant $\pi p_{1/2}$ single-particle character predicted by the MCSM. In the case of a collective $1/2^-$ state with a mixed wave function, we would not expect such a clear preference for the $1/2_1^- \rightarrow 3/2_1^-$ transition over the $1/2_1^- \rightarrow 5/2_{gs}^-$ one. This state is therefore unlikely to be of the same nature as the strongly collective $1/2^-$ state seen at low energy in $^{71,73,75}\text{Cu}$ [45, 47].

6.2.3 Multiplet of states

Between 2.3 and 3.3 MeV, we observe several levels rather close to each other. We interpret this multiplet of states as the coupling of a proton in the $\pi p_{3/2}$ or $\pi f_{5/2}$ orbital with the first 2^+ state of ^{78}Ni , in agreement with the MCSM calculations for which most of the calculated states shown above 2.6 MeV are core-coupling states. Such couplings to the core can lead to excited states having the following spins:

$$|2_1^+ \otimes \pi p_{3/2}\rangle \rightarrow \frac{1^-}{2}, \frac{3^-}{2}, \frac{5^-}{2}, \frac{7^-}{2} \quad \text{and} \quad |2_1^+ \otimes \pi f_{5/2}\rangle \rightarrow \frac{1^-}{2}, \frac{3^-}{2}, \frac{5^-}{2}, \frac{7^-}{2}, \frac{9^-}{2} \quad (6.1)$$

We did not necessarily populate all these nine states in the experiment and we cannot say firmly which ones we observed. The levels belonging to the $|2_1^+ \otimes \pi p_{3/2}\rangle$ coupling are more likely to decay through a transition to the first excited state ($\pi p_{3/2}$ character), analog to a de-excitation of the ^{78}Ni core from 2_1^+ to 0_1^+ . A transition to the ground state would require an additional de-excitation of the last proton from the $\pi p_{3/2}$ orbital to the $\pi f_{5/2}$ one. A similar reasoning works for the levels from the $|2_1^+ \otimes \pi f_{5/2}\rangle$ coupling that would rather de-excite through a transition to the ground state. The latter type of transition is more difficult to observe in our case: the energies are likely to be similar than those of the transitions already identified through γ - γ coincidences. It is therefore possible that we missed some transitions to the ground state in the range between 2.3 and 3.3 MeV that would belong to the multiplet.

In the extreme shell-model representation, it is not possible to populate such core-coupling states in the knockout reaction. But due to correlations, none of the levels observed has a pure wave function and we can have a mixing between both sets of states, as well as a mixing between the $7/2^-$ states of the multiplet and the $\pi f_{7/2}^{-1}$ single-particle wave function. Thus, we can access these multiplet states through the components of their wave function that overlap to those of the ^{80}Zn ground state wave function. Another possibility is the presence of transitions that we did not identify from the three states above 3.3 MeV, discussed after, to the multiplet. The region of the spectrum between 1.0 and 1.5 MeV could contain good candidates for such transitions. We also cannot exclude transitions within the multiplet.

In figure 6.4, we compare the spectrum of ^{79}Cu to the (p,2p) ones of ^{77}Cu and ^{81}Ga , respectively two neutrons less and two protons more than ^{79}Cu , obtained from the same data set. We notice that in both ^{77}Cu and ^{81}Ga spectra, there are several transitions next to the energy of the 2_1^+ state of ^{76}Ni and ^{80}Zn , respectively. Moreover, the intense transitions between 2.0 and 3.4 MeV are present only in ^{79}Cu , while there is no transition at this energy in the ^{77}Cu spectrum and at most some weak transitions in the ^{81}Ga one. These two facts show the possible observation of core-coupling states using the knockout reaction.

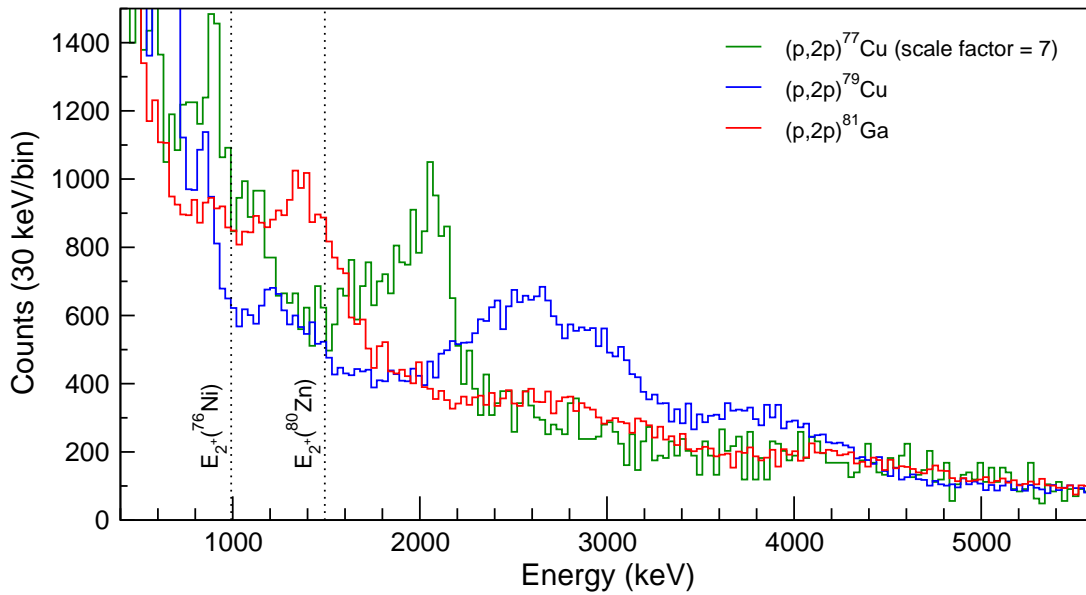


Figure 6.4 – γ -ray spectra of ^{77}Cu , ^{79}Cu and ^{81}Ga obtained from the $(p,2p)$ reaction in the same data set. In the ^{77}Cu and ^{81}Ga spectra, there are several transitions around the energy of the 2_1^+ state of ^{76}Ni and ^{80}Zn , respectively, indicating that we observed transitions from core-coupling states. In ^{79}Cu , such an accumulation of transitions is seen between 2.0 and 3.4 MeV. A scale factor has been applied to the ^{77}Cu spectrum for the sake of clarity.

Such core-coupling states between a proton in the $\pi p_{3/2}$ or $\pi f_{5/2}$ orbital with the 2_1^+ state of ^{78}Ni allow us to estimate the latter at about 3 MeV of excitation energy, in accordance with the MCSM calculation and other theoretical studies [23, 60, 96, 97]. As shown in figure 6.5, such a 3-MeV 2_1^+ -state in ^{78}Ni compared to the previous nickel isotopes indicates a good shell closure at $N = 50$. A direct spectroscopy of this state would be necessary for final confirmation.

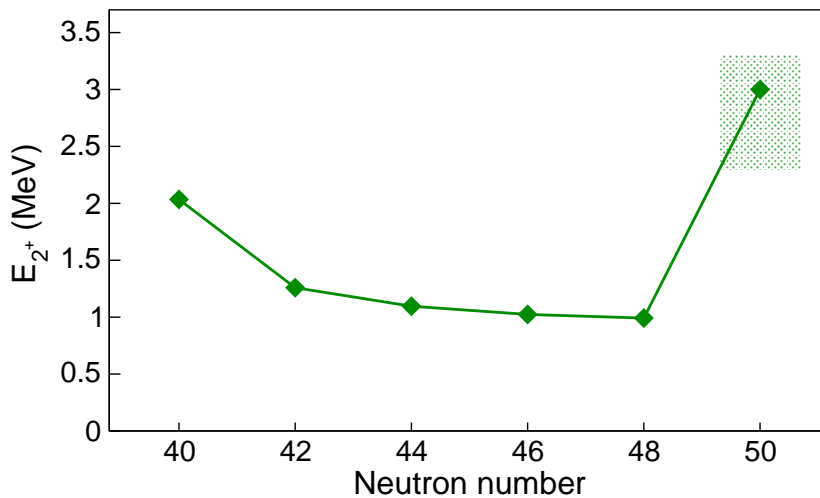


Figure 6.5 – Systematics of the first 2_1^+ -state in nickel isotopes, from $N = 40$ to $N = 50$. The value at $N = 50$ corresponds to an estimation based on this work, the limits being taken as the lower and upper states of the multiplet observed between 2.3 and 3.3 MeV. Data taken from references [27–30] up to $N = 48$.

6.2.4 Higher-energy levels

In the experimental level scheme, we find that the knockout of a proton results in a final ^{79}Cu nucleus at high excitation energy, populating several structures. Because of the composition of the wave function of the ^{80}Zn ground-state, we may expect the reaction to populate the $\pi f_{7/2}^{-1} f_{5/2}^2$ and $\pi f_{7/2}^{-1} p_{3/2}^2$ holes. As mentioned earlier, the $\pi f_{7/2}^{-1}$ single-particle wave function will mix with the $7/2^-$ members of the $\pi(f_{5/2}, p_{3/2}) \otimes 2^+$ multiplets, resulting in a fragmentation of the strength over different levels. This was already observed in $^{69,71}\text{Cu}$ where several states were found to have a significant $\pi f_{7/2}^{-1}$ hole character [50, 53, 55]. In ^{79}Cu , three states lie above 3.3 MeV and are clearly separated from the multiplet, two of them decaying directly to the ground state through the most energetic γ -rays identified in the spectrum, 3.9 and 4.3 MeV. Such states could be good candidates for carrying a part of the $\pi f_{7/2}^{-1}$ strength, but not the 4.6-MeV level as it decays to the $1/2^-$ one.

In the (p,2p) ^{77}Cu spectrum, as shown in figure 6.4, an intense peak can be seen around 2 MeV. It is the most intense transition in the spectrum and is well isolated from the others, meaning that it can be easily fitted with a response function and an exponential background. A quick look to its coincidence relations confirms that, besides its large intensity, there is no ambiguity in placing it to the ground state because it is not in coincidence with any other transition. We find an energy of 2070(10) keV, in very good agreement with the energy of 2068 keV observed very recently in a β -decay study [49]. The latter transition was placed directly the ground state and the authors assigned a tentative spin $7/2^-$ to the 2068-keV state, based on the $\log ft$ value, and considered it as a possible candidate for the $\pi f_{7/2}^{-1}$ hole state. The observation of such an intense $7/2^-$ state in the (p,2p) reaction is in favour of a $\pi f_{7/2}^{-1}$ hole character.

Assuming that the 2068-keV level in ^{77}Cu is a $\pi f_{7/2}^{-1}$ hole state and considering that it is strongly populated in the (p,2p) reaction, we can legitimately wonder where is such a state in ^{79}Cu , for which apparently nothing is populated so strongly. If we normalize the number of counts of (p,2p) ^{77}Cu to the one of (p,2p) ^{79}Cu , as made in figure 6.4, we find that the sum of the intensities of the 3.9 and 4.3-MeV transitions is equal to 72(12)% of the intensity of the 2068-keV one. If they do not emerge clearly in the spectrum, it is because of the low efficiency and the absence of photopeak at 4 MeV, as explained in section 3.5.2. Moreover, the transitions from core-coupling states are much below 2 MeV in ^{77}Cu while they go up to 3 MeV in ^{79}Cu , meaning that we can more easily have mixing of the core-coupling and single-hole characters in the multiplet. Therefore, the $\pi f_{7/2}^{-1}$ hole states are likely to be present, as expected, but we cannot firmly identify them. All we can say is that there is not a significant part of the strength below 2.2 MeV as the two first excited states and the ground state were assigned to be of different nature than $\pi f_{7/2}^{-1}$. It could be tempting to push the lower limit higher up, at 2.7 MeV, considering that the 2260 keV tentative state is unlikely to have a $\pi f_{7/2}^{-1}$ hole character as it de-excites through

a transition to the $1/2^-$ state, but above 2.2 MeV, i.e. at the rise of the second structure in the spectrum, we can have transitions to the ground state that we missed, like the 2360 keV one that we preferred not to place on the scheme.

In the MCSM calculations for ^{79}Cu , almost all the $\pi f_{7/2}^{-1}$ strength goes in one state, at 2 MeV. It has to be noted that in the case of ^{77}Cu , for which the same MCSM calculations have been performed, there is a also level carrying most of the strength at 1389 keV [49]. Such a low energy can be explained as follows: the calculations predict a pure 2 particles-1 hole (2p1h) $\pi f_{7/2}^{-1} f_{5/2}^2$ state at 3.38 MeV, but the mixing of the possible 2p1h configuration, e.g. the $J = 0^+$ pairing of the two protons in the $\pi f_{5/2}$ orbital, reduces it at 2.55 MeV. The addition of proton 3p2h, 4p3h, etc., and neutron 1p1h, etc., configurations pushes it down to 2 MeV. Experimentally, we find that the $\pi f_{7/2}^{-1}$ states are above this value and a possible explanation could be that such correlations are less important than predicted. However, the $\pi f_{7/2}^{-1}$ strength seems to be more fragmented than in the calculations. Further experimental work would be required to clarify this point.

As a conclusion, despite the impossibility to identify firmly a $\pi f_{7/2}^{-1}$ hole state in ^{79}Cu , we can put a lower limit of 2.2 MeV for the $\pi f_{7/2}^{-1}$ strength. The 3.9 and 4.3-MeV levels are good candidates to carry a part of this strength.

6.3 Exclusive cross sections

As explained in section 1.5.1, we can in principle extract spectroscopic factors from the exclusive cross sections. Although we cannot assign firmly spins to the different levels, we can do the two exercises presented here using the exclusive cross section given in table 5.7, to give some indications about the $\pi f_{7/2}^{-1}$ strength we may have observed. We shall stress that this part does not aim to establish firm conclusions beyond what is feasible.

First of all, single-particle cross sections for the (p,2p) reaction were calculated by K. Ogata (Osaka University, Japan), using the distorted-wave impulse approximation (DWIA) formalism [98]. The results are given in table 6.5 and are averaged over the beam energy covered by our target, like our experimental exclusive cross sections. In this calculation, the ground state and first excited state were assumed to have a spin $5/2^-$ and $3/2^-$, respectively, and a spin $7/2^-$ was considered for the states at 3880 and 4300 keV. We note that the single-particle cross section to remove a proton in the $f_{7/2}$ orbital does not appear to change much with the energy of the final state populated in ^{79}Cu .

Orbital	σ_{sp} (mb)
$\pi f_{5/2}$ (E = 0 keV)	2.07
$\pi p_{3/2}$ (E = 656 keV)	2.61
$\pi f_{7/2}$ (E = 3880 keV)	2.29
$\pi f_{7/2}$ (E = 4300 keV)	2.27

Table 6.5 – Single-particle cross sections calculated for the (p,2p) ^{79}Cu reaction with the DWIA formalism.

We can estimate the theoretical inclusive cross section of the $(p,2p)^{79}\text{Cu}$ reaction, considering that a proton is removed in the $f_{7/2}f_{5/2}p_{3/2}$ orbitals, as follows:

$$\sigma_{inc} = \sum_k S_k \sigma_{sp}^k = 18.3 \text{ mb} \quad (6.2)$$

where the spectroscopic factors S_k are taken from the MCSM calculations and are given in table 6.1. This value is significantly higher than the experimental inclusive cross section of 7.9(4) mb: we find a ratio experiment over theory equal to 0.43(2).

Such a reduction is common in knockout reactions. The difference between theoretical and experimental spectroscopic factors, referred as reduction factor R_s , has been much discussed in the literature over the past few years, like in references [99–102]. Although a pure argument of lack of short and long-range correlations in shell-model calculations was claimed at first, the trend of R_s over the proton-neutron asymmetry could also be explained by limits in reaction modeling [100]. For example, this trend was found to be different between knockout studies [99, 102] and transfer reactions [101]. No systematic study of R_s for $(p,2p)$ knockout studies using the DWIA formalism, employed for calculating the values in table 6.5, has been published so far, but such a reduction has to be expected at least due to the lack of correlations in the shell-model calculations [103]. Therefore, we use in the following $R_s \approx 0.55(15)$, corresponding to the reduction factor found in $(e,e'p)$ studies for stable nuclei.

We can now calculate the spectroscopic factors of the different levels mentioned in table 6.5 including this reduction factor:

$$S_{exp}(J^\pi) = \frac{\sigma_{exc}(J^\pi)}{\sigma_{sp}} \frac{1}{R_s} \quad (6.3)$$

and compare these values with the summed MCSM spectroscopic strength (for example for the $7/2^-$ states, $\sum S_{th}(7/2^-) = 5.58 + 0.15 + 0.43 = 6.16$ according to table 6.1). The results are shown in table 6.6.

Level	S_{exp}	$\sum S_{th}(J^\pi)$	Ratio exp/th (%)
$5/2^-$, E = 0 keV	< 3.30(1.12)	1.33	< 248(84)
$3/2^-$, E = 656 keV	0.03(22)	0.57	5(39)
$7/2^-$, E = 3880 keV	0.56(17)	6.16	9(4)
$7/2^-$, E = 4300 keV	0.52(16)	6.16	9(4)

Table 6.6 – Comparison between experimental, including the reduction factor R_s , and theoretical spectroscopic factors.

One can see that the value for the ground state is considerably overestimated: even taking the extreme shell-model value of 2 for the number of protons in the $\pi f_{5/2}$ orbital for the ground state of ^{80}Zn , the ratio would still be equal to 165(56)%. This is a strong indication that indeed we missed transitions to the ground state. As regards the two levels

at high energy, 3880 and 4300 keV, we find a total of 18(6)% of the expected spectroscopic strength calculated by the MCSM, which is not negligible.

We can try another exercise. Considering that all knockout feeding that does not go into the ground state and first excited state comes from a proton removed in the $\pi f_{7/2}$ orbital, we have at least $\sigma_{exc}(\pi f_{7/2}^{-1}) = 4.1(9)$ mb. Comparing this with the calculated $\sigma_{sp} = 2.29$ mb and taking into account the reduction factor, we find a spectroscopic strength of at least 3.3(1.2). This corresponds to 54(19)% of the MCSM strength, and this value would automatically increase if the ground state feeding was lower. This means that we surely populated the $\pi f_{7/2}^{-1}$ hole, but the strength seems to be more fragmented than expected, as said before.

In the case of (p,2p)⁸¹Ga, presented in section 4.2.1, we find an inclusive cross section of 8.3(1.8) mb, among which an upper limit of 68(21)% is found for the direct feeding to the ground state. This means that the important ground-state direct feeding of ⁷⁹Cu, with an upper limit of 48(10)% of the inclusive cross section, is not an isolated case. It is possible that in our analysis procedure we induce a systematic bias in the fit of the background, both at low and high energy: the minimization algorithm looks for the best agreement between the fit and the data, which can lead to an underestimation of the intensity for the numerous response functions that we include in the fit and an overestimation of the background. This mechanically favours the ground-state direct population. Another possibility, already mentioned in the case of ⁷⁹Cu, is the non-identification of some transitions to the ground state: such transitions would induce a decrease of the ground-state exclusive cross section.

These two exercises show that in our case it is difficult to discuss quantitatively the $\pi f_{7/2}^{-1}$ strength that we have populated and that the lower limit of 2.2 MeV mentioned in the previous section is more reliable. It would be interesting to study more in detail the ⁷⁷Cu nucleus from (p,2p) channel, and in particular to do the same exercises with the supposedly 7/2⁻ state at 2 MeV, in order to compare with ⁷⁹Cu. The analysis of this nucleus is ongoing and is currently performed by K. Hadynska-Klek (LNL, Italy) and E. Sahin (University of Oslo, Norway).

6.4 ⁷⁹Cu: a valence proton outside a ⁷⁸Ni core

The level scheme of ⁷⁹Cu established in this work shows a first excited state at 656 keV, with a proposed spin 3/2⁻, and second one at 1511 keV, with a proposed spin 1/2⁻, interpreted together with the 5/2⁻ ground state as having an important single-particle character from the experimentally observed feeding pattern and transition intensities as well as the present MCSM calculations. Together these results indicate that, while single-particle and collective states coexist at low energy in lighter copper isotopes, their single-particle character is restored in ⁷⁹Cu.

Above 2.2 MeV, we observe a multiplet of states up to 3.3 MeV, interpreted as levels coming from the coupling of the first 2^+ -state of ^{78}Ni and a proton in the $\pi f_{5/2}p_{3/2}$ orbitals to which $\pi f_{7/2}^{-1}$ hole-states probably mix. Several states were also observed in the spectra of ^{77}Cu and ^{81}Ga , produced by the same knockout reaction, around the value of the first 2^+ -state of ^{76}Ni and ^{80}Zn , respectively, meaning that we indeed have access to core-coupling states. We conclude that the first 2^+ -state of ^{78}Ni is located at around 3 MeV of excitation energy, which compared to previous nickel isotopes suggests a good shell-closure at $N = 50$.

The $Z = 28$ gap in ^{79}Cu corresponds to the ESPE splitting between the $\pi f_{5/2}$ and $\pi f_{7/2}$ orbitals, as the $\pi p_{3/2}$ and $\pi f_{5/2}$ ones are inverted. The MCSM calculations put this gap at 4.9 MeV compared to 6.7 MeV in ^{69}Cu , i.e. at $N = 40$, as it can be seen from figure 6.2. Experimentally, although we cannot assign firmly the spins, we determined a lower limit of 2.2 MeV for the $\pi f_{7/2}^{-1}$ strength, implying that it remains large. None of the excited states appears to be significantly more directly populated than the others, meaning that this strength appears to be fragmented, as it was observed in $^{69,71}\text{Cu}$ from transfer reactions, and we possibly have populated fragments up to 4.3 MeV. Thus, even if experimental levels are only first indications of the possible location of the ESPE because of the correlations in the nucleus, both experiment and theory show that despite the change of orbital content of the $Z = 28$ gap along the copper isotopic chain, its magicity persists.

Therefore, it appears that the ^{79}Cu nucleus is well depicted in terms of a valence proton outside a ^{78}Ni core, which presents us with an indirect evidence of the magic character of the latter.

Conclusion and outlook

In this work, we performed the first spectroscopy of the ^{79}Cu nucleus, having one proton more than ^{78}Ni , that was produced at RIKEN through proton knockout from a ^{80}Zn beam at 260 MeV per nucleon. An analysis procedure allowed us to build a level scheme up to 4.6 MeV and the results were compared to Monte-Carlo shell-model calculations. Firstly, we concluded on the restoration of the single-particle nature of the low-lying states in copper at $N = 50$. Secondly, we estimated the 2_1^+ (^{78}Ni)-state energy within an interval between 2.3 and 3.3 MeV from the multiplet of states we observe. Thirdly, we determined a lower limit of 2.2 MeV for the $\pi f_{7/2}^{-1}$ strength, indicating that the $Z = 28$ gap remains large at $N = 50$. These conclusions are fully in line with a ^{78}Ni nucleus that would be doubly magic.

One of the main limitations in the analysis was the intrinsic resolution of DALI2, which prevented us from a complete identification of the many transitions present in the spectrum. By coupling MINOS to a segmented germanium array such as AGATA [104], the photopeak efficiency would be reduced by about an order of magnitude, depending on the geometry and position of the array, but this would be largely compensated by the very high resolution. We also point out that the ^{238}U primary beam at RIKEN is now four times more intense than during our experiment, counterbalancing partially the low germanium efficiency.

This was a first spectroscopy of ^{79}Cu and further studies would be necessary for clarification, especially to answer the following question: where exactly does the $\pi f_{7/2}^{-1}$ strength lie? A transfer reaction from a beam of ^{80}Zn could bring many clues, following the example of the $^{70,72}\text{Zn}(d, ^3\text{He})^{69,71}\text{Cu}$ experiments [53, 55]. Some facilities can provide a ^{80}Zn beam with the energy required, up to a few tens of MeV per nucleon, like ISOLDE or RIKEN when the OEDO beam-line [105], developed for decelerating the fast beams coming from BigRIPS, will be ready. We can try to estimate the counting rate we would have in both cases.

A simple calculation was done using the TWOFNR code [106] in order to obtain the order of magnitude of the single-particle cross sections for the $^{80}\text{Zn}(d, ^3\text{He})^{79}\text{Cu}$ reaction, having a very negative Q -value equal to -11.6 MeV. The best beam-energy to populate $L = 3$ states was found to be 45 MeV per nucleon. With HIE-ISOLDE [107], we can

expect soon a ^{80}Zn beam at 10 MeV per nucleon with an intensity on target of around 10^4 pps. In the case of RIKEN, the deceleration of the ^{80}Zn beam down to 45(1) MeV per nucleon will be possible with an efficiency of 60%. The kinematic lines of the light ejectile for such beam energies is shown in figure 1. Considering the energy of the ^3He particles, we cannot use a thick target because of the energy-loss in it. We make the exercise both using a solid target of CD_2 with a thickness of 0.3 mg/cm^2 , like in the $^{72}\text{Zn}(d,^3\text{He})^{71}\text{Cu}$ experiment, and the MUST2 detector [108], or using instead the active target ACTAR [109], that we supposed to be 25-cm long and filled with a D_2 gas at atmospheric pressure.

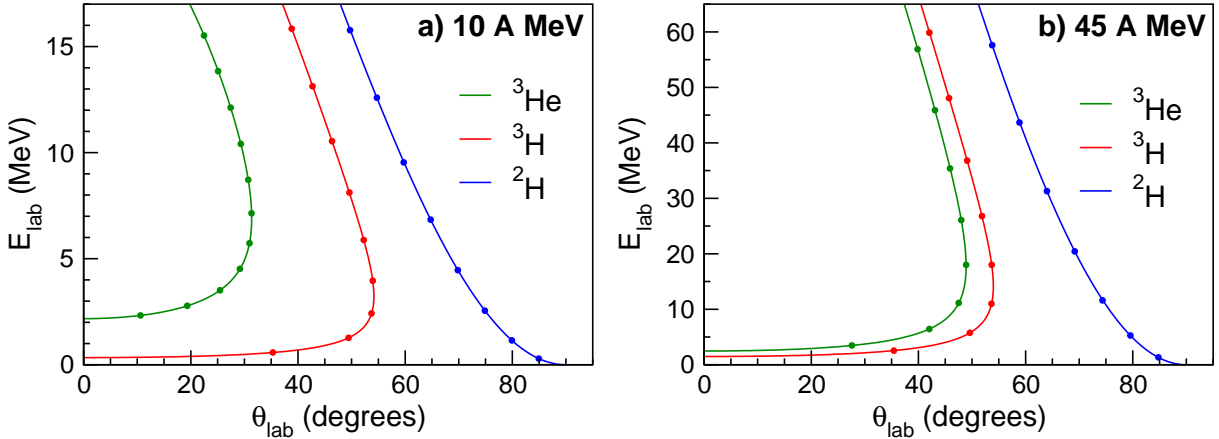


Figure 1 – Kinematics of the $(d,^3\text{He})^{79}\text{Cu}$, $(d,t)^{79}\text{Zn}$ and $(d,d)^{80}\text{Zn}$ reactions, using a ^{80}Zn beam at (a) 10 A MeV and (b) 45 A MeV. The dots correspond to the angle in the center-of-mass frame, by steps of 10° .

The angular distributions calculated using the TWOFNR code are given in figure 2. We consider a geometrical detection efficiency above 10° in the laboratory frame of 60% and 80% for MUST2 and ACTAR, respectively. This is a typical value for an array of four MUST2 telescopes at forward angles, while it is somehow approximate for ACTAR, as it depends on the reaction vertex, but we expect the active target to be efficient.

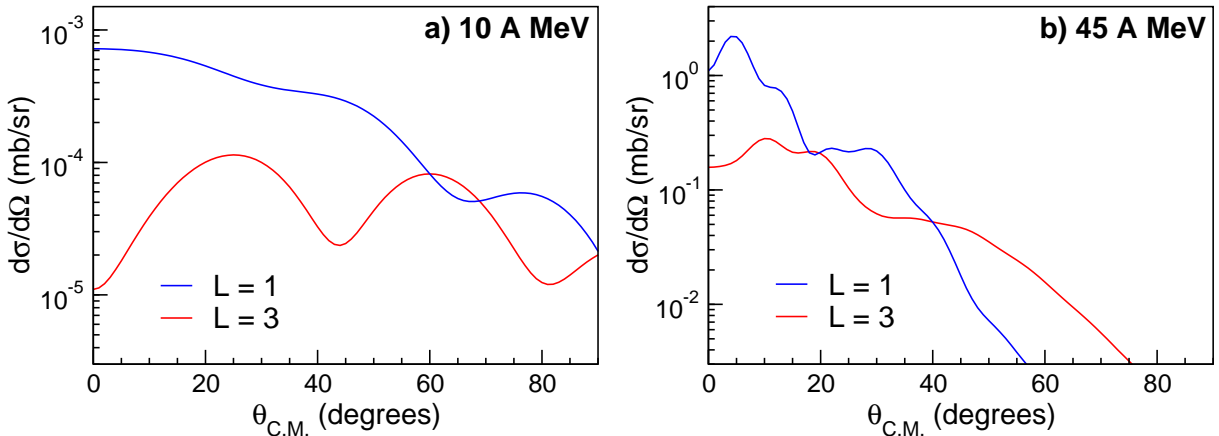


Figure 2 – Angular distributions for a proton removed in an orbital with $L = 1$ and $L = 3$, using a ^{80}Zn beam at (a) 10 A MeV and (b) 45 A MeV.

All these information are summarized in table 1, in which we calculate the number of counts expected after 5 days of experiment. We consider a $5/2^-$ spin for the ground state, $3/2^-$ for the state at 656 keV and a $7/2^-$ state at 4 MeV. We used the spectroscopic factors from the Monte-Carlo shell-model calculations.

$^{80}\text{Zn}(d, ^3\text{He})^{79}\text{Cu}$	ISOLDE		RIKEN	
Beam energy (A MeV)	10		45	
Beam intensity (pps)	$\sim 10^4$		$\sim 6 \times 10^2$	
Target type	CD ₂ (solid)	D ₂ (gas)	CD ₂ (solid)	D ₂ (gas)
Target thickness (mg/cm ²)	0.3	4.1	0.3	4.1
# target nuclei (cm ⁻²)	2.2×10^{19}	1.3×10^{21}	2.2×10^{19}	1.3×10^{21}
Detector	MUST2	ACTAR	MUST2	ACTAR
ε_{geo} ($> 10^\circ$ lab. frame)	$\sim 60\%$	$\sim 80\%$	$\sim 60\%$	$\sim 80\%$
$S_{th}\sigma_{sp}(f_{5/2})$ (mb)	5×10^{-4}		3×10^{-1}	
$S_{th}\sigma_{sp}(p_{3/2})$ (mb)	7×10^{-4}		2×10^{-1}	
$S_{th}\sigma_{sp}(f_{7/2})$ (mb)	2×10^{-8}		1.2	
Counts ($f_{5/2}$), 5 days	0	2	1	81
Counts ($p_{3/2}$), 5 days	0	3	1	54
Counts ($f_{7/2}$), 5 days	0	0	4	323
Total, 5 days	0	5	6	458

Table 1 – Information used for the calculation of the number of counts expected in the $^{80}\text{Zn}(d, ^3\text{He})^{79}\text{Cu}$ reaction, during 5 days of experiment. The number of counts may vary by an order of magnitude considering our approximations.

We clearly see that despite the high beam intensity, the energy provided by ISOLDE is too low for this reaction, due to the very negative Q -value. As regards RIKEN, the use of ACTAR seems to provide a sufficient number of counts in each state. But three remarks must be done. Firstly, if the $\pi f_{7/2}^{-1}$ strength is fragmented, as we found in our work, this will spread the counts over several peaks. Secondly, it also depends on the excitation-energy resolution, we cannot identify the $7/2^-$ peaks if they are too close to each other. Thirdly, this estimation may vary by an order of magnitude considering the approximations we made. But it seems that such a reaction is almost within reach.

Concerning the results that are not published yet but that should be available within the next months, we can mention three very interesting cases. The first one is the spectroscopy of ^{78}Ni that was also produced through proton knockout in the first Seastar campaign. There are still some discussions about the spin of the different levels populated but the final level scheme with the interpretation should be available soon. Secondly, a Coulomb-excitation experiment was performed at RIKEN to measure the reduced transition probabilities between low-lying states in ^{77}Cu . The results will be of great help to better quantify the evolution of the collectivity of these states. Finally, a proton-knockout experiment was performed at the NSCL in order to study the hole states in copper up to $N = 48$. The high resolution γ -array GRETINA [110] was used and the momentum distributions were measured. This will provide crucial information on the $\pi f_{7/2}^{-1}$ strength in $^{73,75,77}\text{Cu}$.

To finish, it would be also interesting to study the structure of ^{81}Cu , beyond the $N = 50$ shell gap, to see if the addition of two neutrons in the $\nu d_{5/2}g_{7/2}$ orbitals may induce an abrupt change like the sudden drop of the first $5/2^-$ level in ^{71}Cu , two protons above $N = 40$. The RIBF facility can deliver a ^{82}Zn beam with an intensity of 10 pps. Considering a similar setup and beam time than in our experiment, we would have 25 times less statistics for ^{81}Cu than for ^{79}Cu , allowing to identify only a transition such as the intense 656-keV one in ^{79}Cu . But there is still a lot of work to do in the copper isotopic chain up to $N = 50$ while waiting for future upgrades of worldwide facilities that will permit the study of more neutron-rich isotopes.

Appendices

Appendix A

Publication

PRL **119**, 192501 (2017)

Selected for a [Viewpoint](#) in *Physics*
PHYSICAL REVIEW LETTERS

week ending
10 NOVEMBER 2017



Persistence of the $Z = 28$ Shell Gap Around ^{78}Ni : First Spectroscopy of ^{79}Cu

L. Olivier,¹ S. Franchoo,¹ M. Niikura,² Z. Vajta,³ D. Sohler,³ P. Doornenbal,⁴ A. Obertelli,^{5,4} Y. Tsunoda,⁶ T. Otsuka,^{2,4,6} G. Authelet,⁵ H. Baba,⁴ D. Calvet,⁵ F. Château,⁵ A. Corsi,⁵ A. Delbart,⁵ J.-M. Gheller,⁵ A. Gillibert,⁵ T. Isobe,⁴ V. Lapoux,⁵ M. Matsushita,⁷ S. Momiyama,² T. Motobayashi,⁴ H. Otsu,⁴ C. Péron,⁵ A. Peyaud,⁵ E. C. Pollacco,⁵ J.-Y. Roussé,⁵ H. Sakurai,^{2,4} C. Santamaria,^{5,4} M. Sasano,⁴ Y. Shiga,^{4,8} S. Takeuchi,⁴ R. Taniuchi,^{2,4} T. Uesaka,⁴ H. Wang,⁴ K. Yoneda,⁴ F. Browne,⁹ L. X. Chung,¹⁰ Z. Dombradi,³ F. Flavigny,¹ F. Giacoppo,^{11,*} A. Gottardo,¹ K. Hadyńska-Klęk,¹¹ Z. Korkulu,³ S. Koyama,² Y. Kubota,^{4,7} J. Lee,¹² M. Lettmann,¹³ C. Louchart,¹³ R. Lozeva,^{14,†} K. Matsui,^{2,4} T. Miyazaki,² S. Nishimura,⁴ K. Ogata,¹⁵ S. Ota,⁷ Z. Patel,¹⁶ E. Sahin,¹¹ C. Shand,¹⁶ P.-A. Söderström,⁴ I. Stefan,¹ D. Steppenbeck,⁷ T. Sumikama,¹⁷ D. Suzuki,¹ V. Werner,¹³ J. Wu,^{4,18} and Z. Xu¹²

¹*Institut de Physique Nucléaire, IN2P3-CNRS, Université Paris-Sud, Université Paris-Saclay, 91406 Orsay Cedex, France*

²*Department of Physics, University of Tokyo, 7-3-1 Hongo, Bunkyo, Tokyo 113-0033, Japan*

³*MTA Atomki, P.O. Box 51, Debrecen H-4001, Hungary*

⁴*RIKEN Nishina Center, 2-1 Hirosawa, Wako, Saitama 351-0198, Japan*

⁵*IRFU, CEA, Université Paris-Saclay, F-91191 Gif-sur-Yvette, France*

⁶*Center for Nuclear Study, University of Tokyo, 7-3-1 Hongo, Bunkyo, Tokyo 113-0033, Japan*

⁷*Center for Nuclear Study, University of Tokyo, RIKEN campus, Wako, Saitama 351-0198, Japan*

⁸*Department of Physics, Rikkyo University, 3-34-1 Nishi-Ikebukuro, Toshima, Tokyo 172-8501, Japan*

⁹*School of Computing Engineering and Mathematics, University of Brighton, Brighton BN2 4GJ, United Kingdom*

¹⁰*Institute for Nuclear Science & Technology, VINATOM, P.O. Box 5T-160, Nghia Do, Hanoi, Vietnam*

¹¹*Department of Physics, University of Oslo, N-0316 Oslo, Norway*

¹²*Department of Physics, The University of Hong Kong, Pokfulam, Hong Kong*

¹³*Institut für Kernphysik, Technische Universität Darmstadt, 64289 Darmstadt, Germany*

¹⁴*IPHC, CNRS/IN2P3, Université de Strasbourg, F-67037 Strasbourg, France*

¹⁵*Research Center for Nuclear Physics (RCNP), Osaka University, Ibaraki 567-0047, Japan*

¹⁶*Department of Physics, University of Surrey, Guildford GU2 7XH, United Kingdom*

¹⁷*Department of Physics, Tohoku University, Sendai 980-8578, Japan*

¹⁸*State Key Laboratory of Nuclear Physics and Technology, Peking University, Beijing 100871, People's Republic of China*

(Received 1 February 2017; revised manuscript received 20 September 2017; published 6 November 2017)

In-beam γ -ray spectroscopy of ^{79}Cu is performed at the Radioactive Isotope Beam Factory of RIKEN. The nucleus of interest is produced through proton knockout from a ^{80}Zn beam at 270 MeV/nucleon. The level scheme up to 4.6 MeV is established for the first time and the results are compared to Monte Carlo shell-model calculations. We do not observe significant knockout feeding to the excited states below 2.2 MeV, which indicates that the $Z = 28$ gap at $N = 50$ remains large. The results show that the ^{79}Cu nucleus can be described in terms of a valence proton outside a ^{78}Ni core, implying the magic character of the latter.

DOI: 10.1103/PhysRevLett.119.192501

The shell model constitutes one of the main building blocks of our understanding of nuclear structure. Its robustness is well proven for nuclei close to the valley of stability, where it successfully predicts and explains the occurrence of magic numbers [1,2]. However, these magic numbers are not universal throughout the nuclear chart and their evolution far from stability, observed experimentally over the last decades, has generated much interest [3]. For example, the magic numbers $N = 20$ and 28 may disappear [4–7] while new magic numbers arise at $N = 14$, 16 and 32, 34, respectively [8–13]. Although shell gaps, defined within a given theoretical framework as differences of effective single-particle energies (ESPE), are not observables [14], they are useful quantities to assess the underlying structure of nuclei [15–17]. The nuclear potential acting on nuclei far from stability can induce drifts of

single-particle orbitals and their behavior as a function of isospin can be understood within the shell model [18–22]. Difficulties arise, however, when the single-particle properties are masked by correlations that stem from residual interactions and discriminating between the two effects is nontrivial.

In the shell model as it was initially formulated, the proton $\pi f_{7/2}$ orbital separates from the $3\hbar\omega$ harmonic oscillator shell because of the spin-orbit splitting and forms the $Z = 28$ gap. The neutron $\nu g_{9/2}$ orbital splits off from the $4\hbar\omega$ shell to join the $3\hbar\omega$ orbits and creates a magic number at $N = 50$. With 28 protons and 50 neutrons, the ^{78}Ni nucleus is thus expected to be one of the most neutron-rich doubly magic nuclei, making it of great interest for nuclear structure. Up to now, no evidence has been found for the disappearance of the shell closures at $Z = 28$

and $N = 50$, even if recent studies hint at a possible weakening of the $N = 50$ magic number below ^{78}Ni [23,24]. On the contrary, the half-life of ^{78}Ni was determined at 122.2(5.1) ms, suggesting a survival of magicity [25], and calculations predict a first excited state in ^{78}Ni above 2 MeV [24,26–28]. But so far no other information about ^{78}Ni is available, with the exception of indirect ones such as the mass of ^{79}Cu , measured recently [29].

The size of the $Z = 28$ gap might be affected by a drift of the single-particle energies. When adding neutrons in the $\nu g_{9/2}$ orbital above the $N = 40$ subshell gap, there is a sudden decrease of the energy of the first $5/2^-$ excited state relative to the $3/2^-$ ground state in $^{71,73}\text{Cu}$, which was established from β decay [30]. The subsequent inversion of these two states in ^{75}Cu was evidenced from collinear laser spectroscopy [31]. Theoretically, these $3/2^-$ and $5/2^-$ levels are linked through the main components in their respective wave functions with the $p_{3/2}$ and $f_{5/2}$ proton single-particle states [18,32,33].

The behavior of the $\pi f_{7/2}$ spin-orbit partner is more difficult to determine. This orbital is of primary importance as it is one of the two orbitals defining the $Z = 28$ gap. Access to this hole state is possible through proton transfer or knockout reactions [34]. While spectroscopic factors extracted in proton pickup reactions allow in principle for the measurement of strength functions, it is a challenge to identify the smallest components or those that are situated at high excitation energy. Moreover, away from the valley of stability, the resort to inverse kinematics with radioactive ion beams limits the count rate as well as the resolution that can be achieved. Today, data are available for the $^{70}\text{Zn}(d, ^3\text{He})^{69}\text{Cu}$ [35,36] and $^{72}\text{Zn}(d, ^3\text{He})^{71}\text{Cu}$ [37] reactions, on both sides of the $N = 40$ subshell gap. The measured part of the $\pi f_{7/2}^{-1}$ centroid was seen to remain at 3.8 MeV in ^{71}Cu , compared to a lower limit of 2.45 MeV in ^{69}Cu . While it is not possible to clarify in what direction or to what extent the energy of the centroid shifts, it remains sufficiently high and the $Z = 28$ gap does not appear to be appreciably affected.

In this Letter we report on our measurement of the proton knockout of ^{80}Zn into ^{79}Cu , at $N = 50$. The reaction mechanism favors proton hole states, including the $\pi f_{7/2}^{-1}$ one. It sheds the first light on the evolution of nuclear structure in the most neutron-rich copper isotopes available today, in the close vicinity of ^{78}Ni .

The experiment was performed at the Radioactive Isotope Beam Factory (RIBF), operated jointly by the RIKEN Nishina Center and the Center for Nuclear Study of the University of Tokyo. A ^{238}U beam with an energy of 345 MeV per nucleon and an average intensity of 12 pA was sent on a 3-mm thick ^9Be target for in-flight fission. The secondary ^{80}Zn beam was selected in the BigRIPS separator [38]. A secondary target was placed at the end of BigRIPS. The isotopes before and after the secondary

target were identified on an event-by-event basis in the BigRIPS and ZeroDegree spectrometers, respectively, with the TOF- $B\rho$ - ΔE method [39]. The average ^{80}Zn intensity was 260 particles per second. The detector setup installed between the two spectrometers was composed of the MINOS device [40] mounted inside the DALI2 γ -ray multidetector [41]. MINOS consists of a liquid-hydrogen target surrounded by a cylindrical time-projection chamber (TPC). The target was 102(1) mm long with a density of 70.97 kg/m³. The energy of the isotopes was 270 and 180 MeV per nucleon at the entrance and exit of MINOS, respectively. The ^{79}Cu nucleus was produced mainly through proton knockout from the incoming ^{80}Zn isotopes, the $(p, 3p)$ channel from ^{81}Ga contributing to only 8%. The emitted protons were tracked in the TPC, while the beam trajectory was given by two parallel-plate avalanche counters [42] before the target. For the events with at least one proton detected in the TPC, this ensured the reconstruction of the interaction-vertex position with 95% efficiency and a 5-mm uncertainty (full width at half maximum) along the beam axis. The DALI2 array consists of 186 NaI scintillator crystals that were calibrated with ^{60}Co , ^{137}Cs , and ^{88}Y sources. When several crystals separated by no more than 15 cm were hit by γ rays, the energies were summed before Doppler correction and the event was considered as one single γ ray, a method known as add back. The photopeak

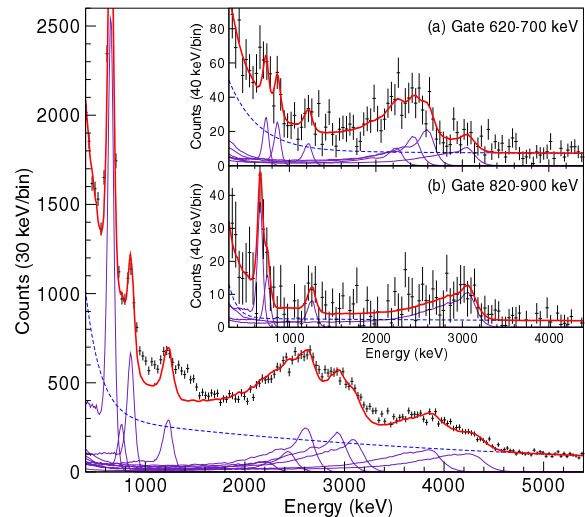


FIG. 1. γ -ray spectrum of $^{80}\text{Zn}(p, 2p)^{79}\text{Cu}$ after Doppler correction, with multiplicities below 4. The experimental data points are in black, with the double-exponential background as the blue dashed line, the simulated response function of each transition in purple, and the sum of the simulated response functions with the background in red. Discrepancies between the data and the fit are due to nonidentified transitions (see text). The inset shows γ - γ coincidences after background subtraction for a gate set on the 656-keV [subpanel (a)] and 855-keV [subpanel (b)] transitions.

TABLE II. Occupation numbers of proton orbits and spectroscopic factors (SF) for the lowest and the three first $7/2^-$ calculated states in ^{79}Cu , as well as for the ground state of ^{80}Zn .

	E (MeV)	J^π	$f_{7/2}$	$f_{5/2}$	$p_{3/2}$	$p_{1/2}$	$g_{9/2}$	$d_{5/2}$	SF
^{79}Cu	0	$5/2^-$	7.73	1.05	0.15	0.02	0.03	0.01	1.33
	0.294	$3/2^-$	7.73	0.17	1.02	0.03	0.04	0.01	0.57
	1.957	$1/2^-$	7.57	0.48	0.29	0.62	0.03	0.01	0.04
	2.035	$7/2^-$	6.82	1.49	0.57	0.04	0.07	0.01	5.58
	2.645	$7/2^-$	7.22	1.09	0.61	0.03	0.04	0.01	0.15
	2.992	$7/2^-$	7.54	1.00	0.37	0.05	0.03	0.00	0.43
^{80}Zn	0	0^+	7.66	1.43	0.73	0.06	0.10	0.01	—

Monte Carlo shell-model (MCSM) calculations were carried out in the $pf_{9/2}d_{5/2}$ model space of protons and neutrons with an A3DA Hamiltonian [27]. Previous results are reproduced within this theoretical framework, like the structure of $^{80,82}\text{Zn}$ [44] and ^{77}Cu [45]. Calculated occupation numbers of proton orbits for the wave functions of the ground state of ^{80}Zn as well as for the lowest calculated states in ^{79}Cu are given in Table II. Spectroscopic factors, corresponding to the overlap between the initial (^{80}Zn) and final (^{79}Cu) wave functions, are also given. The ground state of ^{80}Zn is characterized by a proton component that is distributed over the $\pi f_{5/2}$ and $\pi p_{3/2}$ orbitals. The unpaired proton in ^{79}Cu , after one-proton removal from ^{80}Zn , is expected to reside mainly in the pf orbitals and therefore generates negative-parity final states.

We propose a $5/2^-$ spin for the ground state of ^{79}Cu and a $3/2^-$ spin for the first excited state at 656 keV from the systematics of the copper isotopic chain, as shown in Fig. 3, as well as the systematics of the $N = 50$ isotonic chain above ^{79}Cu [48,49]. The present MCSM calculations support this conclusion. The calculated wave functions for the lowest $5/2^-$ and $3/2^-$ states correspond closely to those of the $\pi f_{5/2}$ (75.3%) and $\pi p_{3/2}$ (74.2%) single-particle states, respectively. From the comparison with ^{77}Cu

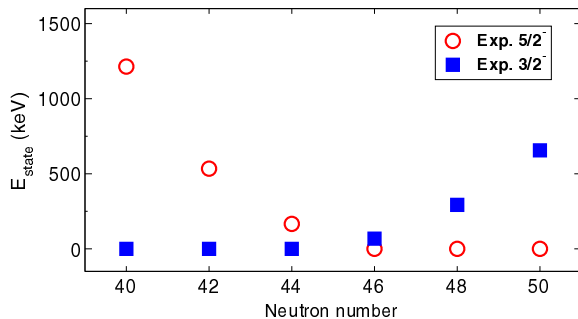


FIG. 3. Systematics of the first $3/2^-$ and $5/2^-$ states in copper isotopes. Data taken from Refs. [30,31,35,45–47] and this work. The error bars are smaller than the data points.

[45,46], the $3/2^-$ level is seen to rise and illustrates the continuation of the inversion of the $\pi p_{3/2}$ and $\pi f_{5/2}$ orbitals that is known from the preceding copper isotopes.

For the second excited state at 1511 keV, the calculation offers two possibilities: a $1/2^-$ state at 1957 keV, with 48.3% $\pi p_{1/2}$ single-particle character, or a $7/2^-$ state at 2035 keV, whose 64.1% of the wave function is built from a $\pi f_{7/2}^{-1}$ hole and two protons in $\pi f_{5/2}p_{3/2}$. The absence of direct feeding in the knockout reaction disfavors the $7/2^-$ assignment, for which the calculated spectroscopic factor is high. Comparing the transition strengths for $1/2^-$ and $7/2^-$ spins obtained from calculated $B(M1)$ and $B(E2)$ values and experimental energies, we find that the ratio $\lambda(1/2^- \rightarrow 5/2^-_{\text{gs}})/\lambda(1/2^- \rightarrow 3/2^-)$ equals 3.2 while $\lambda(7/2^- \rightarrow 5/2^-_{\text{gs}})/\lambda(7/2^- \rightarrow 3/2^-)$ is 427, so we would expect the 1511-keV transition to be stronger than the 855-keV one. We do not see a 1511-keV transition to the ground state because of the limited resolution, but we can put an upper limit of 10(2) for its intensity compared to 33(4) for the 855-keV one, namely, a ratio of 0.30(7). This is closer to the expected value for $1/2^-$ than for $7/2^-$. If this level is a $1/2^-$ state, the low ratio of 0.30(7) would rather support a $\pi p_{1/2}$ single-particle nature for this state, unlike the strongly collective $1/2^-$ state seen at low energy in $^{69,71,73,75}\text{Cu}$ [47,50].

The multiplet of states between 2.7 and 3.3 MeV is interpreted as the coupling of a proton in the $\pi f_{5/2}$ or $\pi p_{3/2}$ orbital with the first 2^+ state of ^{78}Ni , in agreement with the present MCSM calculations for which all calculated states shown above 2.6 MeV are core-coupling states. We can therefore estimate the first 2^+ state of ^{78}Ni at about 3 MeV excitation energy, in accordance with the MCSM calculations and other theoretical studies [24,26–28]. Such a 3-MeV 2^+ state in ^{78}Ni , compared to 992 keV in ^{76}Ni [51], indicates a good shell closure at $N = 50$.

In the experimental level scheme, we find that the knockout of a proton results in a final nucleus at high excitation energy, populating several configurations. Because of the structure of the wave function of the ^{80}Zn ground state, we may expect the reaction to populate the $\pi f_{7/2}^{-1}f_{5/2}^2$ hole but also the $\pi f_{7/2}^{-1}f_{5/2}p_{3/2}$ and $\pi f_{7/2}^{-1}p_{3/2}^2$ configurations. The $\pi f_{7/2}^{-1}$ single-particle wave function will mix with the $7/2^-$ members of the $\pi(f_{5/2}, p_{3/2}) \otimes 2^+$ multiplets, resulting in a fragmentation of the strength over several levels. We have no evidence for a strongly fed $7/2^-$ state below 2.2 MeV and we conclude on the absence of a significant part of the $\pi f_{7/2}^{-1}$ strength below this energy.

Concerning cross sections, we determined an inclusive cross section of 7.9(4) mb for the $^{80}\text{Zn}(p, 2p)^{79}\text{Cu}$ reaction, but reliable exclusive cross sections could not be extracted as the feeding ratio of each level could be affected by nonobserved transitions between high-energy levels. Only an upper limit of 3.8(8) mb for the ground state and a small

value of 0.04(29) mb for the first excited state were found, leaving at least 4.1(9) mb that will mainly belong to states that in their wave function contain a hole in the $\pi f_{7/2}$ orbital. Theoretical single-particle cross sections were calculated using the distorted-wave impulse approximation (DWIA) framework [52] and averaged along the thick target, the beam energy decreasing from 270 to 180 MeV per nucleon. The optical potentials for the incoming proton and the outgoing two protons are obtained by a microscopic framework; the Melbourne nucleon-nucleon G -matrix interaction [53] is folded by a nuclear density calculated with the Bohr-Mottelson single-particle potential [54]. For the ground state, the low-lying $\pi p_{3/2}$ state and the knockout of a $f_{7/2}$ proton, we obtained 2.1, 2.6, and 2.3 mb, respectively, and these numbers should be multiplied by the corresponding spectroscopic factors from the MCSM given in Table II. We did not identify a strongly populated $7/2^-$ state; our observation shows more fragmentation of the single-particle strength than predicted. Although this could be partly explained by the existence of unobserved γ rays, it is also possible that a part of the $\pi f_{7/2}^{-1}$ strength lies above the neutron-separation threshold. Somewhat discrepant with the presented shell-model calculations, this main result calls for further experimental and theoretical investigations.

The $Z = 28$ gap corresponds to the $\pi f_{5/2} f_{7/2}$ ESPE splitting, as the $\pi p_{3/2}$ and $\pi f_{5/2}$ orbitals are inverted and the MCSM calculations put it at 4.9 MeV. Experimentally, we found a lower limit of 2.2 MeV for the $\pi f_{7/2}^{-1}$ hole strength. Even if the latter cannot be directly related to the ESPE because of model-dependent correlations, both experiment and theory show that although the orbital content of the $Z = 28$ gap is changing along the copper isotopic chain, its magicity persists. Therefore, ^{79}Cu can be described as a ^{78}Ni core plus a valence proton. This is in line with the depiction of ^{80}Zn as two-proton configurations with a ^{78}Ni core [44].

In conclusion, we performed the first spectroscopy of ^{79}Cu and compared the results with MCSM calculations. These calculations show the restoration of the single-particle nature of the low-lying states, which is supported by the experiment. There is no significant knockout feeding to the excited states below 2.2 MeV, indicating that the $Z = 28$ gap remains large. The ability to describe the ^{79}Cu nucleus as a valence proton outside a ^{78}Ni core presents us with indirect evidence of the magic character of the latter. Spectroscopy and mass measurement of ^{78}Ni are the next steps for a direct proof of its double magicity.

The authors are thankful to the RIBF and BigRIPS teams for the stable operation and high intensity of the uranium primary beam, and production of secondary beams during the experiment. The development of MINOS and the core MINOS team have been supported by the

European Research Council through the ERC Grant No. MINOS-258567. A. O. was supported by JSPS long-term fellowship L-13520 from September 2013 to June 2014 at the RIKEN Nishina Center. A. O. deeply thanks the ERC and JSPS for their support. C. S. was supported by the IPA program at the RIKEN Nishina Center. A. O. and C. S. are grateful to the RIKEN Nishina Center for its hospitality. This work was supported by JSPS Grant-in-Aid for a JSPS Research Fellow (No. 268718). The MCSM calculations were performed on the K computer at RIKEN AICS (hp150224, hp160211). This work was supported in part by the HPCI Strategic Program (“The Origin of Matter and the Universe”) and the “Priority Issue on Post-K computer” (“Elucidation of the Fundamental Laws and Evolution of the Universe”) from MEXT and JICFuS. Z. D. and Z. V. were supported by the GINOP-2.3.3-15-2016-00034 contract. L. X. C. would like to thank MOST for its support. M. L. and V. W. acknowledge the German BMBF with the supporting No. 05P15RDFN1 and No. 05P12RDFN8. We thank N. Paul for her careful reading of the Letter.

*Present address: Helmholtz Institute Mainz, 55099 Mainz, Germany and GSI Helmholtzzentrum für Schwerionenforschung, 64291 Darmstadt, Germany.

†Present address: CSNSM, IN2P3-CNRS, Université Paris-Sud, Université Paris-Saclay, 91406 Orsay Cedex, France.

- [1] M. Goepfert-Meyer, *Phys. Rev.* **75**, 1969 (1949).
- [2] O. Haxel, J. H. D. Jensen, and H. E. Suess, *Phys. Rev.* **75**, 1766 (1949).
- [3] O. Sorlin and M.-G. Porquet, *Prog. Part. Nucl. Phys.* **61**, 602 (2008).
- [4] D. Guillemaud-Mueller, C. Detraz, M. Langevin, F. Naulin, M. de Saint-Simon, C. Thibault, F. Touchard, and M. Epherre, *Nucl. Phys.* **A426**, 37 (1984).
- [5] T. Motobayashi *et al.*, *Phys. Lett. B* **346**, 9 (1995).
- [6] C. M. Campbell *et al.*, *Phys. Rev. Lett.* **97**, 112501 (2006).
- [7] B. Bastin *et al.*, *Phys. Rev. Lett.* **99**, 022503 (2007).
- [8] A. Huck, G. Klotz, A. Knipper, C. Miede, C. Richard-Serre, G. Walter, A. Poves, H. L. Ravn, and G. Marguier, *Phys. Rev. C* **31**, 2226 (1985).
- [9] P. G. Thirolf *et al.*, *Phys. Lett. B* **485**, 16 (2000).
- [10] E. Becheva *et al.*, *Phys. Rev. Lett.* **96**, 012501 (2006).
- [11] A. Gade *et al.*, *Phys. Rev. C* **74**, 021302(R) (2006).
- [12] C. R. Hoffman *et al.*, *Phys. Lett. B* **672**, 17 (2009).
- [13] D. Steppenbeck *et al.*, *Nature (London)* **502**, 207 (2013).
- [14] T. Duguet, H. Hergert, J. D. Holt, and V. Somà, *Phys. Rev. C* **92**, 034313 (2015).
- [15] A. Poves and A. Zuker, *Phys. Rep.* **70**, 235 (1981).
- [16] T. Otsuka, R. Fujimoto, Y. Utsuno, B. A. Brown, M. Honma, and T. Mizusaki, *Phys. Rev. Lett.* **87**, 082502 (2001).
- [17] E. Caubier, G. Martínez-Pinedo, F. Nowacki, A. Poves, and A. P. Zuker, *Rev. Mod. Phys.* **77**, 427 (2005).

- PRL **119**, 192501 (2017) PHYSICAL REVIEW LETTERS week ending
10 NOVEMBER 2017
- [18] T. Otsuka, T. Suzuki, R. Fujimoto, H. Grawe, and Y. Akaishi, *Phys. Rev. Lett.* **95**, 232502 (2005).
[19] T. Otsuka, T. Suzuki, M. Honma, Y. Utsuno, N. Tsunoda, K. Tsukiyama, and M. Hjorth-Jensen, *Phys. Rev. Lett.* **104**, 012501 (2010).
[20] N. A. Smirnova, B. Bally, K. Heyde, F. Nowacki, and K. Sieja, *Phys. Lett. B* **686**, 109 (2010).
[21] T. Otsuka, *Phys. Scr.* **T152**, 014007 (2013).
[22] T. Otsuka and Y. Tsunoda, *J. Phys. G* **43**, 024009 (2016).
[23] C. Santamaria *et al.*, *Phys. Rev. Lett.* **115**, 192501 (2015).
[24] F. Nowacki, A. Poves, E. Caurier, and B. Bounthong, *Phys. Rev. Lett.* **117**, 272501 (2016).
[25] Z. Y. Xu *et al.*, *Phys. Rev. Lett.* **113**, 032505 (2014).
[26] K. Sieja and F. Nowacki, *Phys. Rev. C* **85**, 051301(R) (2012).
[27] Y. Tsunoda, T. Otsuka, N. Shimizu, M. Honma, and Y. Utsuno, *Phys. Rev. C* **89**, 031301(R) (2014).
[28] G. Hagen, G. R. Jansen, and T. Papenbrock, *Phys. Rev. Lett.* **117**, 172501 (2016).
[29] A. Welker *et al.*, following Letter, *Phys. Rev. Lett.* **119**, 192502 (2017).
[30] S. Franchoo, M. Huyse, K. Kruglov, Y. Kudryavtsev, W. F. Mueller, R. Raabe, I. Reusen, P. Van Duppen, J. Van Roosbroeck, L. Vermeeren, A. Wöhr, and K. L. Kratz, B. Pfeiffer, and W. B. Walters, *Phys. Rev. Lett.* **81**, 3100 (1998).
[31] K. T. Flanagan *et al.*, *Phys. Rev. Lett.* **103**, 142501 (2009).
[32] N. A. Smirnova, A. De Maesschalck, A. Van Dyck, and K. Heyde, *Phys. Rev. C* **69**, 044306 (2004).
[33] K. Sieja and F. Nowacki, *Phys. Rev. C* **81**, 061303(R) (2010).
[34] P. G. Hansen and J. A. Tostevin, *Annu. Rev. Nucl. Part. Sci.* **53**, 219 (2003).
[35] B. Zeidman and J. A. Nolen, *Phys. Rev. C* **18**, 2122 (1978).
[36] P. Morfouace *et al.*, *Phys. Rev. C* **93**, 064308 (2016).
[37] P. Morfouace *et al.*, *Phys. Lett. B* **751**, 306 (2015).
[38] T. Kubo *et al.*, *Prog. Theor. Exp. Phys.* **2012**, 03C003 (2012).
[39] N. Fukuda, T. Kubo, T. Ohnishi, N. Inabe, H. Takeda, D. Kameda, and H. Suzuki, *Nucl. Instrum. Methods Phys. Res., Sect. B* **317**, 323 (2013).
[40] A. Obertelli *et al.*, *Eur. Phys. J. A* **50**, 8 (2014).
[41] S. Takeuchi, T. Motobayashi, Y. Togano, M. Matsushita, N. Aoi, K. Demichi, H. Hasegawa, and H. Murakami, *Nucl. Instrum. Methods Phys. Res., Sect. A* **763**, 596 (2014).
[42] H. Kumagai, A. Ozawa, N. Fukuda, K. Sümmerer, and I. Tanihata, *Nucl. Instrum. Methods Phys. Res., Sect. A* **470**, 562 (2001).
[43] S. Agostinelli *et al.*, *Nucl. Instrum. Methods Phys. Res., Sect. A* **506**, 250 (2003).
[44] Y. Shiga *et al.*, *Phys. Rev. C* **93**, 024320 (2016).
[45] E. Sahin *et al.*, *Phys. Rev. Lett.* **118**, 242502 (2017).
[46] U. Köster, N. J. Stone, K. T. Flanagan, J. R. Stone, V. N. Fedosseev, K. L. Kratz, B. A. Marsh, T. Materna, L. Mathieu, P. L. Molkanov, M. D. Seliverstov, O. Serot, A. M. Sjödin, and Y. M. Volkov, *Phys. Rev. C* **84**, 034320 (2011).
[47] C. Petrone, J. M. Daugas, G. S. Simpson, M. Stanoiu, C. Plaisir, T. Faul, C. Borcea, R. Borcea, L. Caceres, S. Calinescu, R. Chevrier, L. Gaudefroy, G. Georgiev, G. Gey, O. Kamalou, F. Negoita, F. Rotaru, O. Sorlin, and J. C. Thomas, *Phys. Rev. C* **94**, 024319 (2016).
[48] D. Verney, F. Ibrahim, C. Bourgeois, S. Essabaa, S. Gales, L. Gaudefroy, D. Guillemaud-Mueller, F. Hammache, C. Lau, F. LeBlanc, A. C. Mueller, O. Perru, F. Pougheon, B. Roussiere, J. Sauvage, and O. Sorlin, *Phys. Rev. C* **76**, 054312 (2007).
[49] B. Cheal *et al.*, *Phys. Rev. Lett.* **104**, 252502 (2010).
[50] I. Stefanescu *et al.*, *Phys. Rev. Lett.* **100**, 112502 (2008).
[51] C. Mazzocchi *et al.*, *Phys. Lett. B* **622**, 45 (2005).
[52] T. Wakasa, K. Ogata, and T. Noro, *Prog. Part. Nucl. Phys.* **96**, 32 (2017).
[53] K. Amos, P. J. Dortmans, H. V. von Geramb, S. Karataglidis, and J. Raynal, *Adv. Nucl. Phys.* **25**, 276 (2000).
[54] A. Bohr and B. R. Mottelson, *Nuclear Structure* (Benjamin, New York, 1969), Vol. I.

Appendix B

Résumé en français

Le noyau atomique est un des systèmes physiques les plus complexes et les plus fascinants, présentant une grande variété de comportements tels que la déformation, les excitations collectives ou encore l'émission de particules. Il est le théâtre d'une intense compétition entre les interactions forte, faible et Coulombienne. Depuis sa découverte par E. Rutherford [1] il y a plus d'un siècle, de nombreuses études expérimentales et théoriques ont été menées pour tenter de comprendre ses nombreuses propriétés. Pourtant, aujourd'hui encore, il n'existe pas de théorie unifiée qui rendrait compte de tous les phénomènes nucléaires et de nombreuses questions restent au mieux partiellement résolues. Un des problèmes majeurs est celui de la compréhension du comportement de la matière nucléaire loin de la vallée de stabilité.

Il fut observé il y a près de 80 ans que certains noyaux ayant un nombre spécial de protons et/ou de neutrons présentent d'intéressantes propriétés telles qu'un excès d'énergie de liaison. Ces nombres, aujourd'hui appelés "nombres magiques", sont 2, 8, 20, 28, 50, 82, 126. Cette observation fut interprétée comme une indication que le noyau pouvait être décrit en termes d'orbitales et de couches, à l'instar des électrons dans l'atome. Différents modèles de particules individuelles furent rapidement proposés mais tous échouèrent à reproduire la suite des nombres magiques. Il fallut attendre 1949 pour que ce problème soit résolu, avec l'introduction dans le potentiel nucléaire d'un terme empirique de spin-orbite par Goeppert Mayer [4] et Haxel, Jensen et Suess [5]. Néanmoins, avec le développement des faisceaux radioactifs durant les dernières décennies, il fut observé qu'il peut y avoir d'importants réarrangements de la structure nucléaire. Les nombres magiques mentionnés ci-dessus, valides aux alentours de la vallée de stabilité, ne sont pas universels : loin de la stabilité, certains peuvent disparaître et de nouveaux nombres magiques peuvent apparaître. Ceci mène naturellement à un autre problème majeur, celui des forces en jeu dans l'évolution des couches loin de la stabilité.

Dans cette thèse, nous nous focalisons sur l'évolution de la structure nucléaire côté protons en allant vers le noyau de ^{78}Ni ($Z = 28$, $N = 50$), un des noyaux les plus exotiques possédant deux nombres magiques conventionnels. L'évolution du gap $Z = 28$ vers $N = 50$ peut être étudié en sondant le caractère de particule individuelle des niveaux d'énergie

dans la chaîne isotopique de cuivre, ayant un proton de plus que le nickel. Ce travail porte sur le ^{79}Cu , à $N = 50$, produit par la réaction de knockout proton (p,2p) et étudié par spectroscopie γ en ligne.

B.1 Motivation physique

Jusqu'à présent, il n'y a pas eu d'observation d'une disparition des fermetures de couche à $Z = 28$ et $N = 50$. En revanche, certaines études indiquent un possible affaiblissement de ces gaps [19, 23, 38, 59] autour du ^{78}Ni . Comme expliqué dans le chapitre 1, peu de données expérimentales concernant le ^{78}Ni lui-même existent, seul son temps de demi-vie est connu [25]. Les isotopes de cuivre permettent de sonder la structure nucléaire côté protons dans cette région et en particulier de caractériser sa nature de particule individuelle. Les orbitales d'intérêt pour les protons sont $1f_{7/2}$, supposément remplie, et $2p_{3/2}$, $1f_{5/2}$, $2p_{3/2}$. Concernant les neutrons, il s'agit de l'orbitale $1g_{9/2}$ qui est pleine à $N = 50$.

La taille du gap $Z = 28$ peut être affectée par des dérives monopolaires. En ajoutant des neutrons dans l'orbitale $\nu g_{9/2}$, au delà de $N = 40$, l'énergie du premier état excité $5/2^-$ baisse brutalement par rapport à l'état fondamental $3/2^-$ dans les noyaux de $^{71,73}\text{Cu}$ [43, 44]. L'inversion de ces deux états fut ensuite observée dans le ^{75}Cu , où le spin de l'état fondamental est $5/2^-$ [46]. Théoriquement, ces niveaux $3/2^-$ et $5/2^-$ correspondent principalement aux états de particule individuelle $p_{3/2}$ et $f_{5/2}$, respectivement [19, 57, 59]. Le comportement de l'orbitale $\pi f_{7/2}$, partenaire de spin-orbite de l'orbitale $\pi f_{5/2}$, est plus difficile à déterminer. Cette orbitale est d'une importance majeure puisqu'il s'agit d'une des deux orbitales délimitant le gap $Z = 28$. L'accès à cet état trou est possible par réaction de transfert ou de knockout [63]. Bien que les facteurs spectroscopiques extraits dans les réactions de pick-up proton permettent en principe d'accéder au barycentre de la force $\pi f_{7/2}$, c'est un défi d'identifier les plus petites composantes ou celles situées à haute énergie. Aujourd'hui, des données sont disponibles concernant les réactions $^{70}\text{Zn}(d,^3\text{He})^{69}\text{Cu}$ [50, 53] et $^{72}\text{Zn}(d,^3\text{He})^{71}\text{Cu}$ [55], autour de $N = 40$. Le barycentre de la force $\pi f_{7/2}$ fut déterminé à 3.8 MeV dans le ^{71}Cu , comparé à une valeur limite de 2.45 MeV dans le ^{69}Cu . Bien qu'il soit impossible de clarifier dans quelle direction le barycentre se déplace, il reste suffisamment haut et le gap $Z = 28$ n'apparaît pas fortement affecté. A l'autre bout de la chaîne, dans le ^{79}Cu , aucune information spectroscopique n'est connue. Étudier le comportement de l'orbitale $\pi f_{7/2}$ à $N = 50$ permettrait d'obtenir des informations sur la magie du ^{78}Ni .

B.2 Dispositif expérimental

L'expérience étudiée ici faisait partie la première campagne Seastar (signifiant en anglais *Shell evolution and search for two-plus energies at the RIBF*), un programme

expérimental visant à étudier par spectroscopie γ en ligne des noyaux riches en neutrons produits par réaction de knockout proton. Elle s'est déroulée pendant 5 jours au laboratoire RIKEN, au Japon. Le dispositif expérimental est décrit dans le chapitre 2.

Un faisceau primaire d' ^{238}U , accéléré à une énergie de 345 MeV/nucléon et d'une intensité de 12 pnA, fut envoyé sur une cible de ^9Be . La fission en vol des noyaux d'uranium engendra un cocktail d'isotopes radioactifs, identifiés et sélectionnés en vol par le spectromètre BigRIPS [67] pour former le faisceau secondaire. Les noyaux d'intérêts furent ensuite envoyés sur le dispositif MINOS (*MagIc Numbers Off Stability*) [74] avec une vitesse $\beta \sim 0.6$. MINOS est composé d'une cible d'hydrogène liquide de 10 cm de long, où se déroulent les réactions de knockout, entourée d'une chambre à projection temporelle (TPC en anglais) servant à reconstruire la trajectoire des protons issus de la réaction. Cette reconstruction permet de déterminer le vertex d'interaction dans la cible, afin de corriger le plus efficacement possible l'important effet Doppler affectant les rayons γ prompts émis par le résidu et détectés par le spectromètre γ DALI2 (*Detector Array for Low Intensity radiation 2*) [77]. Les résidus furent identifiés par le spectromètre ZeroDegree [67] situé en sortie de MINOS.

L'intensité moyenne du faisceau secondaire de ^{80}Zn était de 260 particules par seconde (pps) tandis que le nombre d'événements correspondant à la réaction $(p,2p)^{79}\text{Cu}$ était de 0.5 pps. Ce faible taux de comptage explique le choix d'un détecteur γ tel que DALI2, caractérisé par une grande segmentation (186 cristaux) et une grande efficacité (scintillateurs). La contrepartie est la faible résolution en énergie du détecteur. À 1 MeV, la résolution était de $\sigma_E/E = 4.3\%$ pour une efficacité de 27%.

B.3 Analyse et construction des schémas de niveaux

L'analyse des données issues de l'expérience se déroule principalement en effectuant les étapes suivantes, détaillées dans le chapitre 3 :

- Corrections empiriques pour améliorer l'identification des isotopes dans les spectromètres BigRIPS et ZeroDegree ;
- Étalonnage en temps et en énergie de DALI2 ;
- Étalonnage de la vitesse de dérive des électrons dans la TPC de MINOS ;
- Procédure dite d'*add-back*, pour reconstruire l'énergie des rayons γ ayant subi une diffusion Compton ;
- Correction de l'effet Doppler.

Ces étapes, bien que standardes dans une telle expérience, sont cruciales afin d'obtenir des spectres en énergie fiables. Pour s'assurer de la qualité de l'analyse, une validation est

effectuée en utilisant des transitions déjà connues [31, 32, 36] des isotopes de $^{78,80}\text{Zn}$, produits par différentes voies de réaction durant l'expérience. Nous identifions trois pics dans le spectre de ^{78}Zn et cinq dans celui de ^{80}Zn : les énergies mesurées sont compatibles avec celles existantes dans la littérature, à deux exceptions près dues au temps de vie d'un des niveaux émetteurs dans le ^{80}Zn qui induit fatalement une mauvaise correction de l'effet Doppler. L'analyse est donc validée mais il faut mentionner que l'énergie mesurée des transitions peut être décalée de quelques pourcents à cause du temps de vie des niveaux émetteurs.

Les spectres en énergie sont ajustés par une fonction correspondant à la somme des fonctions de réponse de DALI2 aux différentes énergies où se trouvent les transitions ainsi que de deux fonctions exponentielles servant à reproduire le bruit de fond à basse et haute énergie. Dans le cas du ^{79}Cu , la densité de transition dans le spectre est telle qu'il n'est pas possible d'identifier a priori le nombre de transitions présentes, ni leur énergie. Nous avons donc établi une procédure, expliquée dans le chapitre 4, afin d'extraire un maximum d'information des données. Elle comporte les six étapes suivantes :

1. Coïncidences γ - γ sans soustraction du bruit de fond ;
2. Identification des transitions allant directement sur l'état fondamental ;
3. Ajustement du spectre en énergie avec les transitions trouvées lors des étapes 1 et 2 ;
4. Estimation des différences entre l'ajustement et le spectre ;
5. Calcul de la quantité de bruit de fond sous chaque pic utilisé en étape 1 ;
6. Coïncidences γ - γ avec soustraction du bruit de fond, pour confirmer ou invalider les relations trouvées en étape 1.

Nous avons validé cette procédure en utilisant le noyau de ^{81}Ga , produit par la réaction (p,2p) pendant la première campagne Seastar et par différentes voies de réaction lors de la seconde campagne qui s'est déroulée un an après. Ceci nous a permis de tester notre méthode sur deux jeux de données indépendants. Les deux schémas de niveaux construits sont cohérents entre eux et compatibles avec ce qui existe dans la littérature [91], nous avons donc appliqué cette procédure sur le ^{79}Cu .

B.4 Résultats et interprétation

Le spectre en énergie du ^{79}Cu montre deux pics suffisamment isolés pour effectuer des coïncidences γ - γ , à 650 et 850 keV. Ceux-ci nous ont donc servi de point de départ pour appliquer la procédure décrite précédemment et les résultats sont présentés dans le chapitre 5. Le schéma de niveaux du ^{79}Cu fut établi pour la première fois, jusqu'à une énergie de 4.6 MeV, et nous avons pu y placer 11 transitions. Deux autres transitions furent identifiées mais n'ont pas pu être placées, et quelques autres transitions sont susceptibles d'exister mais n'ont pas pu être identifiées à cause de la faible statistique et de la mauvaise résolution propre aux scintillateurs.

Le schéma de niveaux obtenu fut ensuite comparé à des calculs théoriques de modèle en couche Monte Carlo (MCSM) [93, 94]. L'interprétation des résultats est détaillée dans le chapitre 6. À partir de la systématique des premiers niveaux $3/2^-$ et $5/2^-$ dans la chaîne isotopique de cuivre [43, 46–50], nous avons proposé un spin $5/2^-$ pour l'état fondamental et un spin $3/2^-$ pour le premier état excité, à 656 keV, ce qui est en accord avec les calculs du MCSM. Ce dernier prédit un caractère de particule individuelle pour les deux états. Nous avons suggéré un spin $1/2^-$ pour le deuxième état excité, à partir de l'absence de population directe de cet état ainsi que par les taux de transitions estimés expérimentalement et ceux obtenus théoriquement. Nous avons interprété le multiplet d'états entre 2.3 et 3.3 MeV comme venant du couplage entre le premier état 2^+ du ^{78}Ni avec un proton dans l'orbitale $\pi f_{5/2}$ ou $\pi p_{3/2}$. Les spectres de ^{77}Cu et ^{81}Ga obtenus par réaction de (p,2p) au cours de la même expérience présentent plusieurs transitions autour de l'énergie du premier état 2^+ du ^{76}Ni et ^{80}Zn , respectivement, indiquant qu'il est effectivement possible d'observer des niveaux dus au couplage. Nous avons donc pu estimer l'énergie d'excitation du premier état 2^+ du ^{78}Ni à environ 3 MeV. Comparée à l'énergie du même niveau dans les isotopes de nickel moins riches en neutrons [27–30], cette valeur semble indiquer une bonne fermeture de couche à $N = 50$. Pour finir, deux niveaux à 3.9 et 4.3 MeV décroissent directement vers l'état fondamental, ce qui en fait de bons candidats pour porter une partie de la force $\pi f_{7/2}^{-1}$. Bien qu'il ne soit pas possible d'identifier formellement un état trou $\pi f_{7/2}^{-1}$ dans le ^{79}Cu , nous trouvons une limite inférieure égale à 2.2 MeV pour le barycentre de la force $\pi f_{7/2}^{-1}$ puisque nous n'avons aucune indication de la présence d'un état fortement peuplé en dessous. Le nombre de niveaux indique que la force est probablement fragmentée, même si une partie de cette fragmentation observée pourrait être due à des transitions non-identifiées dans le spectre en énergie. Ce résultat semble être en désaccord avec les calculs théoriques et nécessiterait d'effectuer d'autres études expérimentales et théoriques pour clarifier la situation.

Il apparaît donc que le noyau de ^{79}Cu est bien décrit en termes d'un proton de valence au-dessus d'un coeur de ^{78}Ni , ce qui nous donne une preuve indirecte du caractère magique de ce dernier.

B.5 Conclusion

Dans ce travail, nous avons réalisé la première spectroscopie γ en ligne du noyau de ^{79}Cu , qui fut produit au RIKEN par réaction de knockout proton à partir d'un faisceau de ^{80}Zn à 260 MeV/nucléon. Nous avons déterminé une limite inférieure de 2.2 MeV pour la force $\pi f_{7/2}^{-1}$, ce qui indique que le gap $Z = 28$ reste important à $N = 50$. De futures études seront nécessaires pour savoir où se situe précisément cette force $\pi f_{7/2}^{-1}$. Plusieurs pistes sont possibles : une partie pourrait être au-delà du seuil de séparation d'un neutron, une autre dans le multiplet d'états observés. Une réaction de transfert telle que $^{80}\text{Zn}(d, ^3\text{He})^{79}\text{Cu}$ pourrait apporter de nombreuses réponses, à l'instar des expériences utilisant les réactions $^{70,72}\text{Zn}(d, ^3\text{He})^{69,71}\text{Cu}$ [53, 55]. En utilisant le faisceau de ^{80}Zn du RIKEN, aujourd'hui quatre fois plus intense que lors de notre expérience, il serait possible d'obtenir quelques dizaines d'événements pour chaque état d'intérêt. Une campagne $^{74-80}\text{Zn}(d, ^3\text{He})$ est donc envisageable dans peu de temps. De même, une expérience d'excitation Coulombienne du ^{79}Cu aiderait à quantifier le degré de collectivité des différents niveaux d'énergie. Une telle expérience fut réalisée au RIKEN pour le ^{77}Cu et les futures améliorations du système d'accélération visant à augmenter l'intensité du faisceau incident devraient permettre d'atteindre rapidement le ^{79}Cu . Enfin, la spectroscopie du ^{78}Ni apportera des informations clés.

Bibliography

- [1] E. Rutherford. *The scattering of α and β particles by matter and the structure of the atom*. Philosophical Magazine **21**, 669 (1911).
- [2] K. Guggenheimer. *Remarques sur la constitution des noyaux atomiques - I*. Journal de Physique et le Radium **5**, 253 (1934).
- [3] W. M. Elsasser. *Sur le principe de Pauli dans les noyaux. I, II and III*. Journal de Physique et le Radium **4**, 549 (1933) ; **5**, 389 (1934) ; **5**, 635 (1934).
- [4] M. Goeppert Mayer. *On closed shells in nuclei II*. Physical Review **75**, 1969 (1949).
- [5] O. Haxel, J. H. D. Jensen, and H. E. Suess. *On the ‘magic numbers’ in nuclear structure*. Physical Review **75**, 1766 (1949).
- [6] O. Sorlin and M.-G. Porquet. *Nuclear magic numbers: new features far from stability*. Progress in Particle and Nuclear Physics **61**, 602 (2008).
- [7] B. Bastin *et al.* *Collapse of the $N = 28$ shell closure in ^{42}Si* . Physical Review Letter **99**, 022503 (2007).
- [8] D. Steppenbeck *et al.* *Evidence for a new nuclear ‘magic number’ from the level structure of ^{54}Ca* . Nature **502**, 207 (2013).
- [9] N. A. Smirnova. *Shell structure evolution and effective in-medium NN interaction*. Ecole Joliot-Curie, 2009.
- [10] A. P. Zuker. *Three-body monopole corrections to realistic interactions*. Physical Review Letter **90**, 042502 (2003).
- [11] T. Otsuka *et al.* *Three-body forces and the limit of oxygen isotopes*. Physical Review Letter **105**, 032501 (2010).
- [12] D. Verney. *Etude de l’effet de couche $N=50$ en direction de ^{78}Ni : contribution des études de radioactivité auprès du séparateur en ligne PARRNe*. Habilitation à diriger des recherches, Université Paris-Sud XI (2013).

- [13] M. Dufour and A. P. Zuker. *Realistic collective nuclear Hamiltonian*. Physical Review C **54**, 1641 (1996).
- [14] N. A. Smirnova *et al.* *Nuclear shell evolution and in-medium NN interaction*. Physical Review C **86**, 034314 (2012).
- [15] T. Otsuka *et al.* *Magic numbers in exotic nuclei and spin-isospin properties of the NN interaction*. Physical Review Letter **87**, 082502 (2001).
- [16] A. Ozawa *et al.* *New magic number, $N=16$, near the neutron drip line*. Physical Review Letter **84**, 5493 (2000).
- [17] T. Duguet and G. Hagen. *Ab initio approach to effective single-particle energies in doubly closed shell nuclei*. Physical Review C **85**, 034330 (2012).
- [18] A. Umeya and K. Muto. *Triplet-even channel attraction for shell gaps*. Physical Review C **69**, 024306 (2004).
- [19] T. Otsuka *et al.* *Evolution of nuclear shells due to the tensor force*. Physical Review Letter **95**, 232502 (2005).
- [20] T. Otsuka *et al.* *Novel features of nuclear forces and shell evolution in exotic nuclei*. Physical Review Letter **104**, 012501 (2010).
- [21] N. A. Smirnova *et al.* *Shell evolution and nuclear forces*. Physics Letters B **686**, 109 (2010).
- [22] T. Otsuka. *Exotic nuclei and nuclear forces*. Physica Scripta **T152**, 014007 (2013).
- [23] F. Nowacki *et al.* *Shape coexistence in ^{78}Ni as the portal of the fifth island of inversion*. Physical Review Letter **117**, 272501 (2016).
- [24] M. Wang *et al.* *The AME2016 atomic mass evaluation. (II) Tables, graphs and references*. Chinese Physics C **41**, 030003 (2017).
- [25] Z. Y. Xu *et al.* *β -decay half-lives of $^{76,77}\text{Co}$, $^{79,80}\text{Ni}$, and ^{81}Cu : experimental indication of a doubly magic ^{78}Ni* . Physical Review Letter **113**, 032505 (2014).
- [26] National Nuclear Data Center. www.nndc.bnl.gov.
- [27] R. Broda *et al.* *$N = 40$ neutron subshell closure in the ^{68}Ni nucleus*. Physical Review Letters **74**, 868 (1995).
- [28] R. Grzywacz *et al.* *New island of μs isomers in neutron-rich nuclei around the $Z = 28$ and $N = 40$ shell closures*. Physical Review Letter **81**, 766 (1998).

-
- [29] M. Sawicka *et al.* *Low energy levels in ^{72}Ni* . *Physical Review C* **68**, 044304 (2003).
- [30] C. Mazzocchi *et al.* *Low energy structure of even-even Ni isotopes close to ^{78}Ni* . *Physics Letters B* **622**, 45 (2005).
- [31] J. M. Daugas *et al.* *The 8^+ isomer in ^{78}Zn and the doubly magic character of ^{78}Ni* . *Physics Letters B* **476**, 213 (2000).
- [32] J. Van de Walle *et al.* *Coulomb excitation of neutron-rich Zn isotopes: first observation of the 2_1^+ state in ^{80}Zn* . *Physical Review Letter* **99**, 142501 (2007).
- [33] M. Lebois *et al.* *Experimental study of ^{84}Ga β decay: evidence for a rapid onset of collectivity in the vicinity of ^{78}Ni* . *Physical Review C* **80**, 044308 (2009).
- [34] K. Miernik *et al.* *Large β -delayed one and two neutron emission rates in the decay of ^{86}Ga* . *Physical Review Letter* **111**, 132502 (2013).
- [35] C. Santamaria *et al.* *Extension of the $N = 40$ island of inversion towards $N = 50$: spectroscopy of ^{66}Cr , $^{70,72}\text{Fe}$* . *Physical Review Letter* **115**, 192501 (2015).
- [36] Y. Shiga *et al.* *Investigating nuclear shell structure in the vicinity of ^{78}Ni : low-lying excited states in the neutron-rich isotopes $^{80,82}\text{Zn}$* . *Physical Review C* **93**, 024320 (2016).
- [37] S. Chen *et al.* *Low-lying structure and shape evolution in neutron-rich Se isotopes*. *Physical Review C* **95**, 041302(R) (2017).
- [38] O. Perru *et al.* *Enhanced core polarization in ^{70}Ni and ^{74}Zn* . *Physical Review Letter* **96**, 232501 (2006).
- [39] O. Sorlin *et al.* *$^{68}\text{Ni}_{40}$: magicity versus superfluidity*. *Physical Review Letter* **88**, 092501 (2002).
- [40] N. Aoi *et al.* *Enhanced collectivity in ^{74}Ni* . *Physics Letters B* **692**, 302 (2010).
- [41] T. Marchi *et al.* *Quadrupole transition strength in the ^{74}Ni nucleus and core polarization effects in the neutron-rich Ni isotopes*. *Physical Review Letter* **113**, 182501 (2014).
- [42] K. Kolos *et al.* *Direct lifetime measurements of the excited states in ^{72}Ni* . *Physical Review Letter* **116**, 122502 (2016).
- [43] S. Franchoo *et al.* *Beta decay of $^{68-74}\text{Ni}$ and level structure of neutron-rich Cu isotopes*. *Physical Review Letter* **81**, 3100 (1998).

- [44] S. Franchoo *et al.* *Monopole migration in $^{69,71,73}\text{Cu}$ observed from β decay of laser-ionized $^{68-74}\text{Ni}$.* Physical Review C **64**, 054308 (2001).
- [45] I. Stefanescu *et al.* *Interplay between single-particle and collective effects in the odd- A Cu isotopes beyond $N = 40$.* Physical Review Letter **100**, 112502 (2008).
- [46] K. T. Flanagan *et al.* *Nuclear spins and magnetic moments of $^{71,73,75}\text{Cu}$: inversion of $\pi 2p_{3/2}$ and $\pi 1f_{5/2}$ levels in ^{75}Cu .* Physical Review Letter **103**, 142501 (2009).
- [47] C. Petrone *et al.* *Nearly degenerate isomeric states of ^{75}Cu .* Physical Review C **94**, 024319 (2016).
- [48] U. Köster *et al.* *In-source laser spectroscopy of $^{75,77,78}\text{Cu}$: direct evidence for a change in the quasiparticle energy sequence in $^{75,77}\text{Cu}$ and an absence of longer-lived isomers in ^{78}Cu .* Physical Review C **84**, 034320 (2011).
- [49] E. Sahin *et al.* *Shell evolution towards ^{78}Ni : low-lying states in ^{77}Cu .* Physical Review Letter **118**, 242502 (2017).
- [50] B. Zeidman and J. A. Nolen Jr. *Mass and low-lying energy levels of ^{69}Cu .* Physical Review C **18**, 2122 (1978).
- [51] D. Verney *et al.* *Low-energy states of $^{81}_{31}\text{Ga}_{50}$: proton structure of the nuclei close to ^{78}Ni .* Physical Review C **76**, 054312 (2007).
- [52] B. Cheal *et al.* *Nuclear spins and moments of Ga isotopes reveal sudden structural changes between $N=40$ and $N=50$.* Physical Review Letters **104**, 252502 (2010).
- [53] P. Morfouace *et al.* *Single-particle strength in neutron-rich ^{69}Cu from the $^{80}\text{Zn}(d, ^3\text{He})^{69}\text{Cu}$ proton pick-up reaction.* Physical Review C **93**, 064308 (2016).
- [54] T. Ishii *et al.* *The $(\nu g_{9/2}^2 \pi p_{3/2})_{19/2^-}$ isomer in ^{71}Cu and the prediction of its $E2$ decay from the shell model.* Physical Review Letter **81**, 4100 (1998).
- [55] P. Morfouace *et al.* *Evolution of single-particle strength in neutron-rich ^{71}Cu .* Physics Letters B **751**, 306 (2015).
- [56] E. Sahin *et al.* *Shell evolution beyond $N = 40$: $^{69,71,73}\text{Cu}$.* Physical Review C **91**, 034302 (2015).
- [57] N. A. Smirnova *et al.* *Shell-model description of monopole shift in neutron-rich Cu.* Physical Review C **69**, 044306 (2004).
- [58] M. Honma *et al.* *New effective interaction for f_5pg_9 -shell nuclei.* Physical Review C, **80** 064323 (2009).

-
- [59] K. Sieja and F. Nowacki. *Shell quenching in ^{78}Ni : a hint from the structure of neutron-rich copper isotopes*. *Physical Review C* **81**, 061303(R) (2010).
- [60] K. Sieja and F. Nowacki. *Three-body forces and persistence of spin-orbit shell gaps in medium-mass nuclei: toward the doubly magic ^{78}Ni* . *Physical Review C* **85**, 051301(R) (2012).
- [61] S. Lenzi *et al.* *Island of inversion around ^{64}Cr* . *Physical Review C* **82**, 054301 (2010).
- [62] A. Obertelli. *Nuclear structure from direct reactions with rare isotopes: observables, methods and highlights*. *European Physical Journal Plus* **131**, 319 (2016).
- [63] P. G. Hansen and J. A. Tostevin. *Direct reactions with exotic nuclei*. *Annual Review of Nuclear and Particle Science* **53**, 219 (2003).
- [64] A. deShalit and H. Feshbach. *Theoretical nuclear physics – Volume 1: nuclear structure*. John Wiley & Sons, Inc. (1974).
- [65] H. Okuno, N. Fukunishi, and O. Kamigaito. *Progress of RIBF accelerators*. *Progress of Theoretical and Experimental Physics* **2012**, 03C002 (2012).
- [66] RIBF website. www.nishina.riken.jp/RIBF/accelerator/concept.html. Visited on May 4th, 2017.
- [67] T. Kubo *et al.* *BigRIPS separator and ZeroDegree spectrometer at RIKEN RI Beam Factory*. *Progress of Theoretical and Experimental Physics* **2012**, 03C003 (2012).
- [68] K.-H. Schmidt *et al.* *The momentum-loss achromat - A new method for the isotopical separation of relativistic heavy ions*. *Nuclear Instruments and Methods in Physics Research A* **260**, 287 (1987).
- [69] D. J. Morissey and B. M. Sherrill. *In-flight separation of projectile fragments*. *The Euroschool Lectures on Physics with Exotic Beams, Vol. 1*, Springer-Verlag (2004).
- [70] N. Fukuda *et al.* *Identification and separation of radioactive isotope beams by the Big-RIPS separator at the RIKEN RI Beam Factory*. *Nuclear Instruments and Methods in Physics Research B* **317**, 323 (2013).
- [71] H. Kumagai *et al.* *Delay-line PPAC for high-energy light ions*. *Nuclear Instruments and Methods in Physics Research A* **470**, 562 (2001).
- [72] H. Kumagai *et al.* *Development of Parallel Plate Avalanche Counter (PPAC) for BigRIPS fragment separator*. *Nuclear Instruments and Methods in Physics Research B* **317**, 717 (2013).

- [73] K. Kimura *et al.* *High-rate particle identification of high-energy heavy ions using a tilted electrode gas ionization chamber.* Nuclear Instruments and Methods in Physics Research A **538**, 608 (2005).
- [74] A. Obertelli *et al.* *MINOS: A vertex tracker coupled to a thick liquid-hydrogen target for in-beam spectroscopy of exotic nuclei.* European Physical Journal A **50**, 8 (2014).
- [75] I. Giomataris *et al.* *MICROMEGAS: a high-granularity position-sensitive gaseous detector for high particle-flux environments.* Nuclear Instruments and Methods in Physics Research A **376**, 29 (1996).
- [76] I. Giomataris *et al.* *Micromegas in a bulk.* Nuclear Instruments and Methods in Physics Research A **560**, 405 (2006).
- [77] S. Takeuchi *et al.* *DALI2: A NaI(Tl) detector array for measurements of γ rays from fast nuclei.* Nuclear Instruments and Methods in Physics Research A **763**, 596 (2014).
- [78] S. Agostinelli *et al.* *Geant4 - a simulation toolkit.* Nuclear Instruments and Methods in Physics Research A **506**, 250 (2003).
- [79] H. Baba *et al.* *New data acquisition system for the RIKEN Radioactive Isotope Beam Factory.* Nuclear Instruments and Methods in Physics Research A **616**, 65 (2010).
- [80] G. F. Knoll. *Radiation detection and measurement.* John Wiley & Sons, Inc., Fourth edition (2010).
- [81] H. Blok *et al.* *Path reconstruction and resolution improvement in magnetic spectrometers.* Nuclear Instruments and Methods in Physics Research A **262**, 291 (1987).
- [82] C. Santamaria. *Quest for new nuclear magic numbers with MINOS.* PhD thesis, Université Paris-Sud XI (2015).
- [83] P. Hough. *Method and means for recognizing complex patterns.* U.S. Patent 3,009,654 (1962).
- [84] W. R. Leo. *Techniques for nuclear and particle physics experiments.* Springer-Verlag, Second revised edition (1994).
- [85] S. Takeuchi *et al.* *Low-lying states in ^{32}Mg studied by proton inelastic scattering.* Physical Review C **79**, 054319 (2009).
- [86] O. B. Tarasov and D. Bazin. *LISE++: Radioactive beam production with in-flight separators.* Nuclear Instruments and Methods in Physics Research B **266**, 4657 (2008).

-
- [87] P. Doornenbal. *Manual of a GEANT4 simulation code for γ -ray detectors used in the RIKEN-RIBF facility*. Unpublished (2011). Available on www.nishina.riken.jp/collaboration/SUNFLOWER/misc/download/simulation.html. Visited on April 21th, 2017.
- [88] P. Doornenbal. *In-beam gamma-ray spectroscopy at the RIBF*. Progress of Theoretical and Experimental Physics **2012**, 03C004 (2012).
- [89] J. Van de Walle *et al.* *Low-energy Coulomb excitation of neutron-rich zinc isotopes*. Physical Review C **79**, 014309 (2009).
- [90] S. Baker and R. D. Cousins. *Clarification of the use of chi-square and likelihood functions in fits of histograms*. Nuclear Instruments and Methods in Physics Research **221**, 437 (1984).
- [91] S. Padgett *et al.* *β decay of ^{81}Zn and migrations of states observed near the $N = 50$ closed shell*. Physical Review C **82**, 064314 (2010).
- [92] E. Sahin *et al.* *Structure of the $N = 50$ As, Ge, Ga nuclei*. Nuclear Physics A **893**, 1 (2012).
- [93] T. Otsuka *et al.* *Monte Carlo shell model for atomic nuclei*. Progress in Particle and Nuclear Physics **47**, 319 (2001).
- [94] N. Shimizu *et al.* *New-generation Monte Carlo shell model for the K computer era*. Progress of Theoretical and Experimental Physics **2012**, 01A205 (2012).
- [95] M. Honma *et al.* *Shell-model description of neutron-rich pf-shell nuclei with a new effective interaction GXPF1*. European Physical Journal A **25**, 499 (2005).
- [96] Y. Tsunoda *et al.* *Novel shape evolution in exotic Ni isotopes and configuration-dependent shell structure*. Physical Review C **89**, 031301(R) (2014).
- [97] G. Hagen, G. R. Jansen, and T. Papenbrock. *Structure of ^{78}Ni from first-principles computations*. Physical Review Letters **117**, 172501 (2016).
- [98] T. Wakasa, K. Ogata, and T. Noro. *Proton-induced knockout reactions with polarized and unpolarized beams*. Progress in Particle and Nuclear Physics **96**, 32 (2017).
- [99] A. Gade *et al.* *Reduction of spectroscopic strength: weakly-bound and strongly-bound single-particle states studied using one-nucleon knockout reactions*. Physical Review C **77**, 044306 (2008).
- [100] F. Flavigny *et al.* *Nonsudden limits of heavy-ion induced knockout reactions*. Physical Review Letter **108**, 252501 (2012).

- [101] F. Flavigny *et al.* *Limited asymmetry dependence of correlations from single nucleon transfer*. Physical Review Letter **110**, 122503 (2013).
- [102] J. A. Tostevin and A. Gade. *Systematics of intermediate-energy single-nucleon removal cross sections*. Physical Review C **90**, 057602 (2014).
- [103] K. Ogata. Private communication.
- [104] S. Akkoyun *et al.* *AGATA - Advanced GAMMA Tracking Array*. Nuclear Instruments and Methods in Physics Research A **668**, 26 (2012).
- [105] OEDO website. www.cns.s.u-tokyo.ac.jp/oedo/wiki. Visited on July 12th, 2017.
- [106] J. A. Tostevin. *University of Surrey version of the code TWOFNR (of M. Toyama, M. Igarashi and N. Kishida) and code FRONT*. www.nucleartheory.net/NPG/code.htm. Visited on July 12th, 2017.
- [107] M. J. G. Borge and K. Riisager. *HIE-ISOLDE, the project and the physics opportunities*. European Physical Journal A **52**, 334 (2016).
- [108] E. Pollacco *et al.* *MUST2: a new generation array for direct reaction studies*. European Physical Journal A **25**, 287 (2005).
- [109] ACTAR TPC. pro.ganil-spiral2.eu/laboratory/detectors/actartpc. Visited on July 12th, 2017.
- [110] D. Weisshaar *et al.* *The performance of the γ -ray tracking array GRETINA for γ -ray spectroscopy with fast beams of rare isotopes*. Nuclear Instruments and Methods in Physics Research A **847**, 187 (2017).

Titre : Structure nucléaire dans la région du ^{78}Ni : spectroscopie γ en ligne du ^{79}Cu par réaction de knockout proton

Mots clés : Structure nucléaire, noyaux exotiques, ^{78}Ni , spectroscopie γ en ligne, knockout proton

Résumé : La structure nucléaire en couches évolue en allant vers des régions de plus en plus exotiques de la carte des noyaux. Par conséquent, les nombres magiques conventionnels (8, 20, 28, 50, 82, 126) peuvent disparaître loin de la stabilité, tandis que de nouveaux nombres magiques peuvent apparaître. Le noyau de ^{78}Ni , avec 28 protons et 50 neutrons, est un des noyaux supposés doublement magiques les plus exotiques et est donc d'un grand intérêt. L'évolution de la fermeture de couche à $Z = 28$ en allant vers $N = 50$ peut être étudiée en sondant le caractère de particule individuelle des niveaux dans la chaîne isotopique de cuivre, ayant un proton de plus que le nickel. Ce travail porte sur le ^{79}Cu , à $N = 50$.

Afin d'effectuer la première spectroscopie γ en ligne des noyaux autour du ^{78}Ni , une expérience a été réalisée à la Radioactive Ion Beam Factory du RIKEN,

au Japon. Le noyau de ^{79}Cu était produit par la réaction de knockout (p,2p) à partir d'un faisceau de ^{80}Zn envoyé sur le dispositif MINOS, une cible d'hydrogène liquide couplée à une TPC servant à reconstruire la trajectoire des protons. L'émission de rayons gamma subséquente était détectée en vol par le scintillateur segmenté DALI2. Les spectromètres BigRIPS et Zero-Degree permettaient, respectivement, une identification sans ambiguïté des noyaux entrants et sortants.

Une procédure d'analyse basée sur des coïncidences γ - γ a permis de construire le premier schéma de niveau du ^{79}Cu , avec des états jusqu'à 4.6 MeV, et les résultats ont été comparés à des calculs de modèle en couches Monte Carlo. Les conclusions montrent que le noyau de ^{79}Cu est bien décrit en termes d'un proton de valence en dehors d'un coeur fermé de ^{78}Ni , ce qui implique le caractère magique de ce dernier.

Title : Nuclear structure in the vicinity of ^{78}Ni : In-beam γ -ray spectroscopy of ^{79}Cu through proton knockout

Keywords : Nuclear structure, exotic nuclei, ^{78}Ni , in-beam γ -ray spectroscopy, proton knockout

Abstract : The nuclear shell structure is evolving when going into more and more exotic regions of the chart of isotopes and consequently, the conventional magic numbers (8, 20, 28, 50, 82, 126) may disappear far from stability, while some new magic numbers can appear. The ^{78}Ni nucleus, with its 28 protons and 50 neutrons, is one of the most exotic supposedly doubly-magic nuclei, making it of great interest. The evolution of the $Z = 28$ gap towards $N = 50$ can be studied by probing the single-particle character of the states in the copper isotopic chain, having one proton more than nickel. This work focuses on ^{79}Cu , at $N = 50$.

In the aim of performing the first in-beam γ -ray spectroscopy of nuclei in the close vicinity of ^{78}Ni , an experiment was carried out at the Radioactive Isotope Beam Factory of RIKEN, in Japan. The ^{79}Cu nu-

cleus was produced through the (p,2p) knockout reaction from a ^{80}Zn beam sent on the MINOS device, a liquid-hydrogen target coupled to a TPC used for proton tracking. The subsequent γ -decay was detected in-beam with the DALI2 scintillator array. The BigRIPS and ZeroDegree spectrometers allowed an unambiguous identification of the incoming and outgoing nuclei, respectively.

An analysis procedure based on γ - γ coincidences permitted to build the first level scheme of ^{79}Cu , with levels up to 4.6 MeV, and the results were compared to Monte-Carlo shell-model calculations for interpretation. The conclusions show that the ^{79}Cu nucleus is well described in terms of a valence proton outside a closed ^{78}Ni core, implying the magic character of the latter.